**NTNU – Trondheim**
Norwegian University of
Science and Technology

# EBSD Microstructure Characterization of 9% Nickel Steel during In Situ Heat Treatment

Gøril Jahrsengene

Chemical Engineering and Biotechnology
Submission date: June 2015
Supervisor: Ida Westermann, IMTE
Co-supervisor: Morten Karlsen, Statoil

Norwegian University of Science and Technology
Department of Materials Science and Engineering

# Preface

This master's thesis was conducted at the Institute of Materials Science and Engineering at the Norwegian University of Science and Technology (NTNU) during the spring of 2015. Parts of the results together with the pre-study done during project work conducted the autumn of 2014 will be presented on the 25th ISOPE Conference 2015, which takes place at Hawaii, USA.

I wish to thank my supervisors Associate Professor Ida Westermann, Professor II Morten Karlsen and Professor Jarle Hjelen for motivation and guidance during the thesis work. They also deserve thanks, as well as Professor II Odd Magne Akselsen and Maia Wenn, concerning the writing of the ISOPE conference proceedings. Senior engineers Wilhelm Dall and Sergey Khromov have provided technical guidance concerning the in situ SEM and EBSD work. Senior engineer Trygve Schanche advised during the preparation of the steel. A thank you also goes to Arne Gellein who provided the steel and Solveig Kirknes for help with the weld simulation, both from SINTEF.

June 2015

Gøril Jahrsengene

# Abstract

Arctic steels are developed to withstand very low temperatures with a ductile-to-brittle transition temperature below -60°C. 9% nickel steels are today used for storage of liquefied natural gases (LNG) at cryogenic temperatures, and are therefore feasible steels for use in arctic regions. The good low temperature properties are hypothesized to originate from stable retained austenite formed as a consequence of a tempering process during the production of the steel. However, during welding the microstructure is changed in the heat affected zone (HAZ) close to the weld, which will affect the austenite content. In situ heating in combination with electron backscatter diffraction (EBSD) inside a field emission scanning electron microscope (FESEM) has been used in this master's thesis to investigate the austenite development and stabilization when holding the temperature stable in the $\alpha + \gamma$-region of the phase diagram after first conducting a single cycle weld simulation ex situ.

During the in situ experiments it was discovered that the formation of austenite was very dependent on the prior austenite grain obtained at the peak temperature during the first weld simulation. Growth rate, stabilization of formed austenite and total amount retained austenite all varied depending on the prior grain structure and orientation. This was evident both during the in situ experiment and after storing the samples at room temperature. Austenite formed on previous grain boundaries and lath boundaries, and the location of the phase also affected the growth rates. The austenite formed on lath boundaries grew much faster than on previous grain boundaries.

Austenite formed at 590°C was very stable and was retained after cooling, and the amount retained austenite varied from 5 to 25% depending on the grain investigated. More austenite formed with increasingly higher temperatures, but most of this austenite was not retained at room temperature. The austenite showed an orientation memory effect during the phase transformation, as it reformed to its original orientation after cooling. Partial or full recrystallization was observed in the samples heated to 640°C and higher, indicating that the temperatures reached the pure $\gamma$-region. This temperature was much lower than during fast heating.

# Sammendrag

Arktiske stål er utviklet for å motstå lave temperaturer med en "duktil-til-sprø" omslagstemperatur under -60 °C. 9 % nikkelstål blir i dag brukt for oppbevaring av flytende gasser på kryogenske temperaturer, og er derfor et materiale det kan være gunstig å bruke i arktiske strøk. Hypotesene bak lavtemperaturegenskapene antar at det er et resultat av stabil restaustenitt i stålet, en fase som blir dannet under herding under vanlig produksjon. Under sveising vil mikrostrukturen endre seg i områdene nærme sveisen, som igjen vil påvirke austenittinnholdet. In situ-oppvarming i kombinasjon med EBSD (Electron Backscatter Diffraction) i et FESEM (feltemisjon skanning elektronmikroskop) har i masteroppgaven blitt brukt til å granske vekst og stabilisering av austenitten ved å holde temperaturen stabil over lengre tid i $\alpha + \gamma$-området i fasediagrammet, etter først å ha utført en enkel sveisesimulering på materialet.

Under in situ-eksperimentene ble det oppdaget at dannelse av austenitt var veldig avhengig av den tidligere grovkornede austenitten som ble dannet ved makstemperaturen under den første sveisesimuleringen. Veksthastighet, hvor stabil austenitten som ble dannet var og den totale mengden restaustenitt var påvirket av den tidligere kornstrukturen og orienteringen. Dette var tydelig både under in situ-eksperimentene og ved undersøkelser ved romtemperatur etter oppvarmingseksperimentet. Austenitt ble dannet både på tidligere austenittkorngrenser og mellom martensittstavene (lath martensite), og veksthastigheten var forskjellig på disse to stedene. Austenitten som ble dannet mellom stavene vokste mye raskere enn de som vokste på tidligere austenittkorngrenser.

Austenitten som ble dannet ved 590 °C var meget stabil og ble beholdt etter avkjøling, og mengden austenitt varierte mellom 5 og 25 % avhengig av kornet som ble undersøkt. Mer austenitt ble dannet ved økende temperaturer, men mesteparten av denne austenitten var ikke stabil og mengden restaustenitt var lav etter avkjøling. Austenitten returnerte til en krystallografisk identisk orientering etter avkjøling som den hadde før oppvarming. Delvis eller full rekrystallisering ble observert i prøvene oppvarmet til 640 °C, som indikerer at prøvene har oppnådd en temperatur i det rene $\gamma$-området. Denne temperaturen var mye lavere enn observert ved rask oppvarming.

# Abbreviations and Symbols

| Abbreviation / Symbol | Explanation |
|---|---|
| A3 | Electrolyte used for electropolishing |
| $Ac_1$ | Austenite start temperature during fast heating |
| $Ac_3$ | Austenite finish temperature during fast heating |
| $Ae_1$ | Austenite start temperature during equilibrium heating |
| $Ae_3$ | Austenite finish temperature during equilibrium heating |
| ASTM | American Society for Testing and Materials |
| BCC | Body Centered Cubic |
| BCT | Body Centered Tetragonal |
| CCD | Charge Couple Device |
| CCT | Continuous Cooling Transformation |
| CGHAZ | Coarse Grained HAZ |
| CI | Confidence Index |
| $d_{hkl}$ | Interplanar distance between atom plane |
| $E_0$ | Accelerating voltage |
| EBSD | Electron BackScatter Diffraction |
| EBSP | Electron BackScatter Pattern |
| EDS | Energy-Dispersive (X-ray) Spectroscopy |
| FCC | Face Centered Cubic |
| FESEM | Field Emission SEM |
| fps | Frames Per Second |
| HAZ | Heat Affected Zone |
| HSLA | High Strength Low Alloy |
| ICCGHAZ | InterCritical Coarse Grained HAZ |
| $i_p$ | Beam current (in SEM) |
| IPF | Inverse Pole Figure |
| IQ | Image Quality |
| ISOPE | International Society of Offshore and Polar Engineering |
| I-T | Instantaneous Transformation |
| KS | Kurdjumov-Sachs (orientation relationship) |
| LNG | Liquid Natural Gas |
| $M_f$ | Martensite finish temperature during cooling |
| $M_s$ | Martensite start temperature during cooling |
| OIM | Orientation Imaging Microscopy |

| | |
|---|---|
| PC | Pattern Center |
| RT | Room Temperature |
| SEM | Scanning Electron Microscopy/Microscope |
| TEM | Transmission Electron Microscopy |
| $T_p$ | Peak temperature during e.g. weld simulation |
| TTT | Time Temperature Transformation |
| XRD | X-Ray Diffraction |
| ZAF | Algorithm for quantification using EDS |
| α | Ferrite |
| α | Beam divergence (in formula for resolution in SEM) |
| α' | Martensite |
| γ | Austenite |
| $\Delta t_{8/5}$ | Time to cool from 800 to 500°C during e.g. weld simulation |
| $\theta_B$ | Bragg's angle |
| λ | Wavelength of electron |

# Contents

# Chapter 1 Introduction

Materials with low design temperature are of great interest because, in recent years, oil and gas production in arctic environments has become an interesting target for oil companies worldwide. United States Geological Survey assessed the area north of the Arctic Circle, and concluded that approximately 30% of the remaining global gas reserves and 13% of oil reserves may be found in this region of the world [1]. The two most important environmental requirements in the Arctic are the air temperature and the possibility of large deformations. In the extreme Arctic environment the ambient temperature can be expected to reach below -40°C, which will lead to a design temperature of -60°C. This can be a problem because most steels exhibit a ductile-to-brittle transition at lower temperatures [2]. Constructions will be exposed to thawing, frost heaving, landslides, and in marine environments also heavy winds and drifting ice bergs [3]. Both temperature and deformation parameters will, from a material design perspective, be essential for the choice of material to be used in Arctic environments.

This thesis investigates a low carbon steel containing 9% nickel. The steel of current interest has very good mechanical properties at low temperatures, and has shown to retain its ductility at -196°C. This particular steel is today used to store liquefied natural gases (LNG) in large tanks [4], and possesses high strength and suitable fracture toughness at cryogenic temperatures [5]. As LNG is stored at, or below, its -162°C boiling temperature, this steel is extremely relevant to consider using in arctic conditions. Because of the good low temperature properties it is very interesting to examine closer and find out what makes this steel usable at these temperatures, and evaluate if it will be acceptable to use in arctic environments.

The good low temperature toughness is believed to originate from stable retained austenite present in an otherwise tempered martensitic matrix. 9% nickel steel has, depending on precise production parameters, 5-15 volume% retained austenite [4-6]. In order to be used in arctic environments it is important that the low temperature properties are not lost during welding. It is well known how the mechanical properties are affected by changes in the microstructure during welding of the material [5, 7], and this might possibly influence the good low temperature properties. Literature has shown that thermal cycling to different peak temperatures significantly decreases the retained austenite content, and this will reduce the impact toughness at cryogenic temperatures [5].

During earlier characterization projects with scanning electron microscopy (SEM) it has been difficult to identify the large amount of retained austenite predicted by theory by using the electron backscatter diffraction (EBSD) technique [8, 9] on the not-welded steel. This might indicate that the preparation method will compromise the microstructure, that it is not as much austenite present in the steel as predicted by literature, or that the phase is too finely dispersed to be detected with the chosen acquisition settings. Previous investigations done by the author revealed that the steel weld simulated to obtain a structure responding to the intercritically reheated coarse grained heat affected zone (ICCGHAZ) showed a significantly larger amount of austenite than the as-received material with the same preparation method and acquisition settings.

With this result in mind the project objectives are twofold. It is wished to further develop the in situ hot stage and controlling equipment with the goal to update the user manuals. The main task is to study the microstructure of 9% Ni steel during in situ heating using the previously mentioned hot stage in combination with the EBSD technique regarding

- quantification of the austenite phase before and during heating and after cooling to room temperature using different holding temperatures
- where the austenite forms during heating
- if there is any preferred orientations of the austenite concerning orientation and grain size, and whether this affects the formation at elevated temperatures and stability after cooling

Several temperature evaluations were also conducted, concerning both the in situ equipment and generally during heating. The theory behind the metallurgy and properties of the steel is also investigated, and how welding affects the microstructure. Additionally, some theory regarding the EBSD technique when used in combination with in situ investigations, and how in situ heating can be used to evaluate the phase transformation is investigated in the report.

# Chapter 2 Theory

## 2.1 Metallurgy of 9% Nickel Steel

The mechanical properties of steels are decided by the alloying elements and the production process regarding deformation and heat treatment parameters. The 9% nickel steel used for LNG-storage has a microstructure consisting of tempered martensite with 5-15% metallurgically stable retained austenite [4-6].

Austenite has a face centered cubic crystal structure (FCC) and is called gamma iron (γ). This phase is soft and ductile. In pure iron the austenite phase is stable in the temperature interval 912-1394°C, but it can be expanded or narrowed by adding alloying elements. By adding nickel as an alloying element the austenite phase will be stable at much lower temperatures than with pure iron, depending on the composition of the steel [2]. This expansion can clearly be observed in the binary phase diagram of iron and nickel in Figure 2.1. The equilibrium phase diagram does not say anything about the kinetics of the phase transformations.

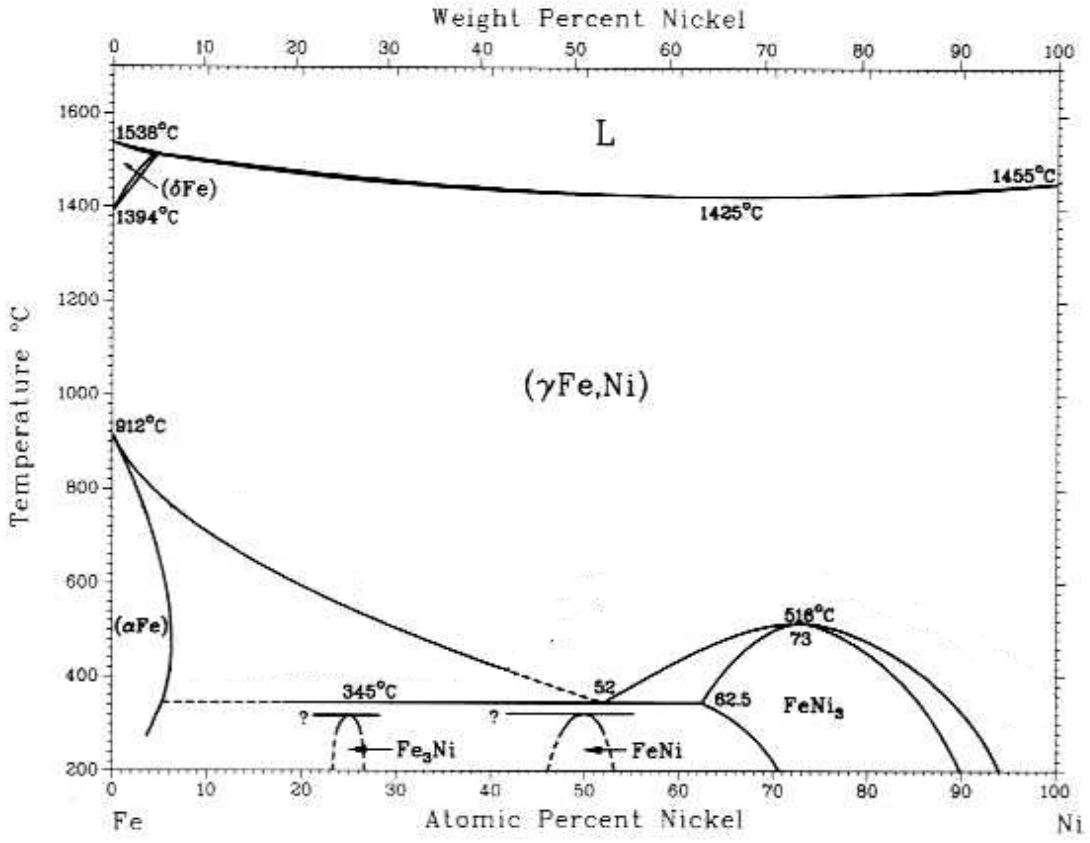


**Figure 2.1: Binary phase diagram of iron and nickel [10]. With addition of nickel the transformation temperature at 912°C decreases and the γ-phase is stable at lower temperatures. Note that the weight% is the upper axis, and atom% the lower axis.**

Martensite is a metastable phase formed when steel is quenched from a temperature in the γ-region with a high cooling rate. The transition from austenite to martensite is a diffusionless transformation referred to as a displacive transformation, resulting in a microstructure with the same carbon content as the original austenite. Considering pure carbon steel with no other alloying elements the carbon, formerly in solid solution in the austenite, remains in solution in what looks like a ferrite phase, also called alpha iron (α). The ferrite has a body-centered cubic crystal structure (BCC), but the displacive transformation to martensite will alter the geometry slightly and the crystal structure is referred to as a body-centered tetragonal structure (BCT) [7]. The martensite is referred to as α'. Since the martensitic transformation is diffusionless there are no lower temperature limitations, but the transformation is athermal and will require a continuous cooling process. $M_s$ and $M_f$ is defined as the start and finish temperature of the austenite to martensite transformation, and both are dependent on the alloying elements of the steel. If the cooling stops and the temperature is kept constant the carbon will start to diffuse to dislocations, and the martensitic transformation stops due to carbon making the austenite stable [2].

Because the metastable phases are absent in the regular equilibrium phase diagrams the transformation between the different phases can be presented in a temperature-time-transformation (TTT)-diagram. These can be used to determine the cooling rate required to obtain martensite [2]. A TTT-diagram is unique for every steel. It can be presented in an I-T (instantaneous transformation)-diagram, where lines indicate beginning and end on an isothermal transformation assuming quenching from the austenite area and down to a temperature which is held constant during the transformation, or a CCT (continuous cooling transformation)-diagram. Figure 2.2 shows a CCT-diagram for a 9% nickel steel with different cooling rates and its resulting hardness as an example. This steel has a martensite finish temperature $M_f$ at approximately 100°C, but for 9% Ni steel it is not unusual to observe a finish temperature is below 0°C. If a fully martensitic structure is desired, quenching below this temperature will have to be used. What is referred to as retained austenite will still be present in the otherwise martensitic structure if the $M_f$ temperature is not achieved [7].

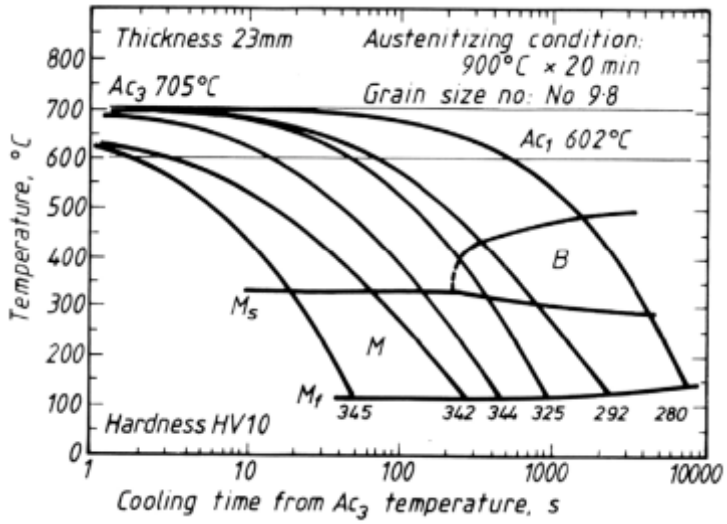


**Figure 2.2: CCT-diagram of one specific 9% nickel steel [11] with specifications concerning thickness, grain size and austenitizing conditions. The diagram can be used to calculate the critical cooling rate necessary to avoid formation of unwanted phases.**

Low carbon martensite is often referred to as lath martensite, where the laths are long and about 0.5 μm wide. The laths are grouped together in packets with low angle boundaries between each lath [7]. Higher quantity of carbon leads to a more brittle material than with low amounts of carbon because the carbon deforms the crystal structure elastically and binds itself to the dislocations to achieve lower stress in the microstructure. This locks the dislocations, and the structure appear brittle [2, 7]. Factors that determine the hardness of the martensite are grain boundaries, dislocation density and original austenite grain size. With nickel present in the steel this will affect several of these factors as well as lowering the $M_s$ temperature, thus giving more retained austenite in the finished material. Nickel has a refining effect on the grain size, it suppresses the formation of ferrite, and is also shown to facilitate dislocation generation at lower temperatures resulting in better toughness [12].

The martensite in the 9% nickel steel used for LNG storage is produced by quenching from the lower part of the austenite region of the phase diagram resulting in relatively small grains. Subsequent tempering of the steel in the lower part of the two phase region results in precipitation of austenite as small elongated particles along martensite lath boundaries and prior austenite grain boundaries [6]. The high amount of nickel stabilizes the austenite, resulting in 5-15 volume% stable retained austenite after cooling to room temperature. During tempering the diffusion of carbon and nickel from the martensitic phase to the austenite phase makes the martensite less hard and brittle, and the ductility will increase [2, 5].

### 2.1.1 Chemical and Mechanical Requirements

The investigated material is categorized as a low carbon steel containing 9% nickel. Today this steel is most commonly used to store liquefied natural gas (LNG) and other liquefied gases because of its high brittle crack arrestability at low temperatures [13]. Because of the good low temperature properties the steel is a very relevant material to consider using in arctic regions. The standards used for 9% nickel steels are ASTM A353 and ASTM A553 [4]. The chemical composition requirements of 9% nickel steel used for LNG storage are presented in Table 2.1.

**Table 2.1: Restrictions and requirements for the chemical composition of 9% nickel steel [14].**

| Element | C (max.) | Mn (max.) | P (max.) | S (max.) | Si | Ni |
|---|---|---|---|---|---|---|
| **weight%** | 0.13 | 0.90 | 0.015 | 0.015 | 0.15-0.40 | 8.50-9.50 |

Examples of the mechanical properties of 9% nickel steel are listed in Table 2.2. The design temperature is -196°C, corresponding to the temperature of liquid nitrogen. The retained austenite present in the microstructure is thermally stable and will not transform to martensite even at this temperature [6]. Charpy V-Notch impact absorption energy should be, at the design temperature of -196°C, 34 J in longitudinal direction and 29 J in transversal direction (average of three specimen) [4, 14]. The toughness requirements after welding are the same as for the base material.

**Table 2.2: A selection of mechanical requirements for 9% nickel steel [4, 14]. Most of the values are defined at room temperature (RT), but the modulus of elasticity is also evaluated at -196°C.**

| Tensile Strength, RT [*MPa*] | Yield Strength, RT [*MPa*] | Elongation in 2'', 50 mm, RT [*%*] | Modulus of Elasticity, 21°C [*GPa*] | Modulus of Elasticity, -196°C [*GPa*] |
|---|---|---|---|---|
| 690-825 | 515 | 20 | 185 | 209 |

## 2.2 Welding

Welding is a fabrication process that joins materials together. The process involves a source of heat, the prime purpose of which is to cause melting. Fusion welding involves deposition of a small amount of molten material within the gap between the components to be joined. Heat manages to diffuse from the fusion zone, the area with deposited material and part of the steel component melted during the process, into adjacent non-melted regions. As a consequence

these regions experience a heating and cooling cycle [7]. This region is called the heat affected zone (HAZ) and because of heat diffusion the microstructure will change. This results in new mechanical properties close to the weld, or the fusion zone as it is presented in the schematic in Figure 2.3.

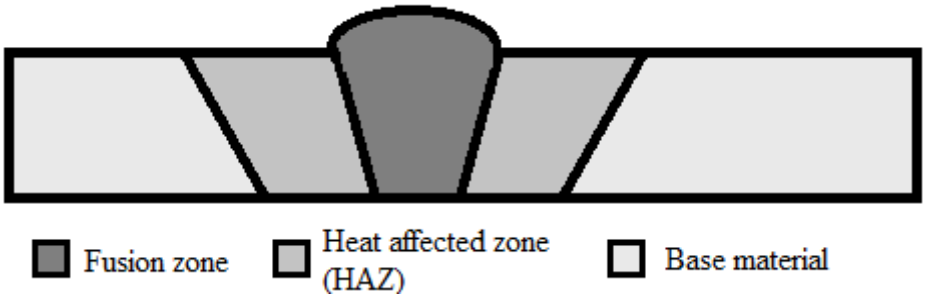


**Figure 2.3: Welding with fusion zone, heat affected zone (HAZ) and base material.**

Depending on the position in the HAZ the nature of the thermal cycle can be described by two parameters. Both the peak temperature, $T_p$, and the cooling rate $\Delta t_{8/5}$, the time it takes to cool over the temperature range 800-500°C (usually the temperature interval where austenite decomposes by solid state transformation), decrease with distance from the weld and increase with heat input [7]. Thermal weld simulation is a way of reconstructing the microstructural changes during welding, and these two parameters together with the heat input can be chosen to simulate the true heat flow during welding.

During fast heating and cooling the phase transformation does not occur in equilibrium and the transformation temperatures with fast heating are denoted $Ac_1$ and $Ac_3$. Both of these increase with increasing heat input, although generally the $Ac_1$ temperature is less affected by the heat input parameter [15]. The HAZ formed after one-cycle welding can be divided into four zones depending on the peak temperature. A coarse-grained austenite zone is formed in the region closest to the fusion boundary. When the peak temperature is above $Ac_3$ a fully austenitic microstructure is formed and the annealing effect result in coarse grains and low toughness. The grain size of the austenite decreases with the distance from the fusion boundary because the peak temperature decreases. In the fine grained zone the mechanical properties are usually superior to the coarse grained zone. Further away from the fusion boundary the steel becomes partially austenitic due to intercritical heating in the two-phase region, and the phase that do not transform to austenite at all experience a tempering effect. When the peak temperature is less than $Ac_1$ the only effect on the steel is tempering [7, 16]. The different regions are presented in Figure 2.4 for a regular carbon steel with 0.15 wt% C; however, this figure does not take into consideration the fast heating rates and use the

equilibrium transformation temperatures $Ae_1$ and $Ae_3$ instead of $Ac_1$ and $Ac_3$ as dividers for the zones.

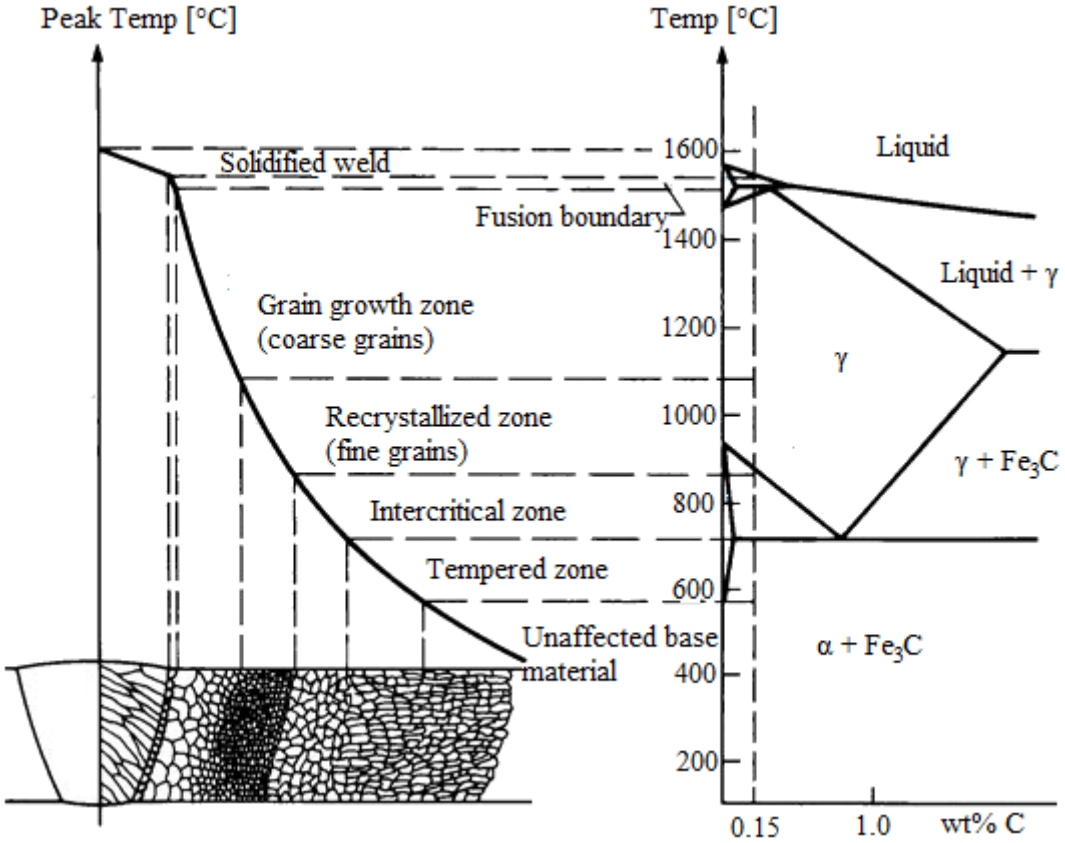


**Figure 2.4: The figure gives the relationship between the (HAZ) and the equilibrium phase diagram [17]. With decreasing peak temperature the microstructure changes to give very different properties. During welding the zones are usually moved upwards because of increasing $Ac_1$ and $Ac_3$ temperatures caused by the high heat input.**

As previously mentioned, during welding and in weld simulations the phase transformation will not occur in equilibrium because the heating and cooling rates are too high. The transformation temperatures $Ac_1$ and $Ac_3$ can be identified by investigating how the volume changes during heating. This can be done experimentally by the use of a dilatometer.

Kinetically, in a lattice the atoms vibrate in place, and with an increase in temperature the atoms will move more due to an increase in kinetic energy. This will usually give a larger average separation between each atom, thus also an increase in volume [18]. It is a linear relationship between the volume change and temperature, and a phase transformation will correspond to a change in the slope. A transformation from martensite (BCT) to the more closed-packed austenite (FCC) will give a change in crystal lattice, and because of the reducing lattice parameter the volume will decrease. When the transformation is complete the

thermal expansion of the new, pure phase will resume its linearity. Part of an experimental graph of the relative expansion given by temperature is presented in Figure 2.5.

The true transformation temperatures can often be calculated based on the composition of the steel [15]. When the composition exceeds 5% nickel the most used equations are no longer valid, and empirical equations with increasing amount of nickel are not established. However, austenite stabilizers like nickel, carbon, and manganese will lower the transformation temperatures, and ferrite stabilizers will have the opposite effect. The heating rate will also affect the temperatures.

Based on earlier dilatometric analysis done by the author during ex situ weld simulation, the intercritical temperature interval is evaluated to be approximately from 660 to 750°C. This is a much more narrow temperature interval than the equilibrium transformation temperatures in Figure 2.1. The experimental dilatometric curves are presented in Figure 2.5, with the experimental $Ac_1$ and $Ac_3$ temperatures marked with lines.

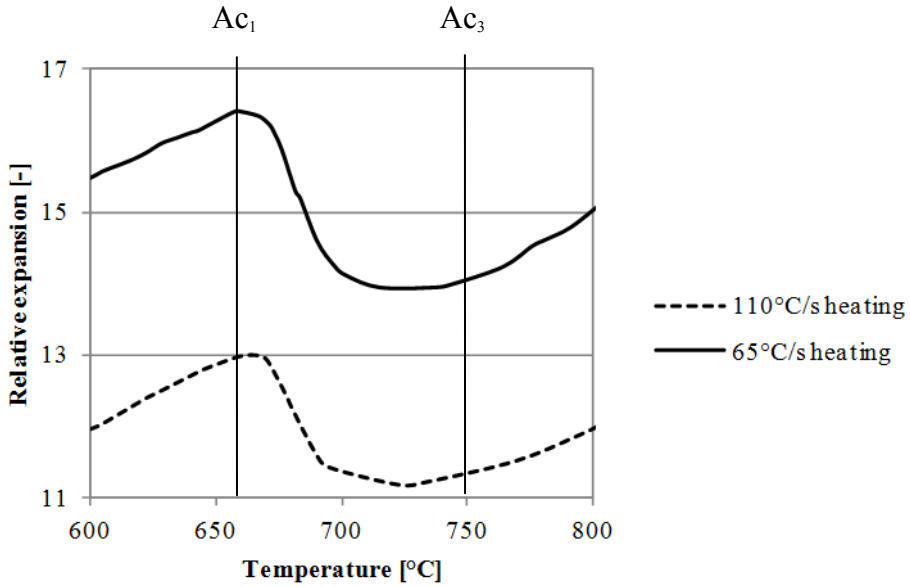


**Figure 2.5: Result of dilatometric analysis showing the relative expansion during weld simulation with two fast heating rates. The relevant temperature interval show that the $Ac_1$ and $Ac_3$ temperature for the slowest heating rate being approximately 660°C and 750°C, with a small difference for the higher rate. Note that the values of the expansion is not comparable.**

Dilatometry done by Nippes revealed the transformation temperatures using 350°C/s heating rate to be 618°C and 666°C [5]. This is lower than the temperatures identified in Figure 2.5, even with higher heating rate (thus more heat input). The CCT-diagram in Figure 2.2 defined its $Ac_1$ and $Ac_3$ temperatures to be 602 and 705°C, but it is not defined with corresponding heating rates.

### 2.2.1 Multipass Welding

During multipass welding the four distinctive zones in the HAZ are modified by subsequent thermal cycles, and the microstructures obtained after the first cycle will change even more. The different localized and discontinuous zones are presented in Figure 2.6. In low carbon steels it is often found that the intercritically reheated coarse grained HAZ (ICCGHAZ) is the one exhibiting the lowest toughness (Figure 2.6b, zone C) [16].

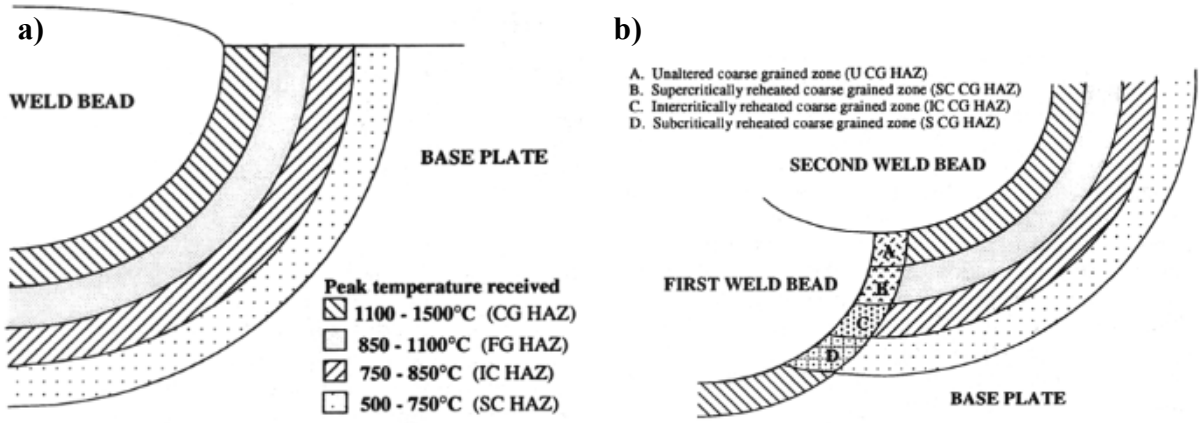


**Figure 2.6: Schematic representation of the HAZ [16]. a) Single-pass weld with four distinctive regions. b) Multipass welding presenting how the original coarse grained region changes with the second cycle.**

MA-phases are a mixture of martensite (M) and retained austenite (A). The phase appears in the microstructure after welding when the peak temperature is so low that only some of the steel transform into austenite, e.g. in the two-phase region of the phase diagram. Due to diffusion the austenite will get a larger concentration of carbon and in the case of the relevant steel also nickel, and thus get more stable. If the cooling rate is sufficiently large this austenite will transform partially to a hard martensite, while the rest of the austenite will remain in an otherwise tempered structure [7] (e.g. tempered martensite). This is especially problematic in the intercritically reheated coarse grained zone (Figure 2.6b, area C). The "ductile to brittle" transition temperature for steels will generally increase with increasing amount of MA-phases present in the steel [19], thus making it a huge problem considering arctic use.

The dilatometric results in Figure 2.5 indicate that a 9% Ni sample heated to 1350°C on its first cycle, and 700°C on its second cycle, will get a microstructure corresponding to what occurs in true ICCGHAZ. Microhardness results indicate that the intercritical temperature range is in the same area. Figure 2.7 gives the hardness with respect to the second peak temperature during a two cycle weld simulation, and a significant change is observed between 600 and 700°C. This increase in hardness at 700°C indicates a partial phase transformation at the peak temperature resulting in smaller grains and high hardness. Comparing to the lower

second peak temperatures, the coarse grained microstructure obtained after the first cycle is most likely only tempered, and get softer with increasing second peak temperature (shown by decreasing hardness).

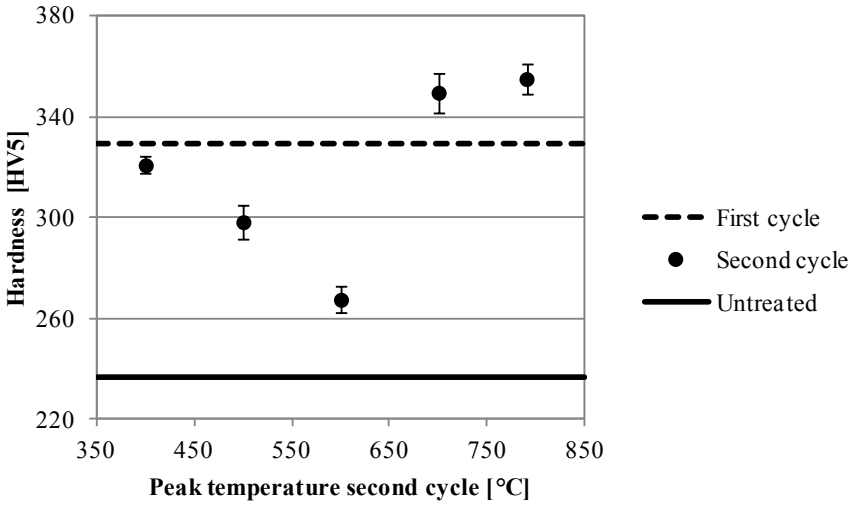


**Figure 2.7: The hardness of the samples with respect to the peak temperature of the second welding cycle. The hardness of the untreated material and the hardness after the first welding cycle can be used as references. The hardness decrease with increasing temperature in the 400-600°C interval, and for peak temperatures of 700°C and higher it increase from the original first cycle hardness, an indication of a significant change in microstructure in this temperature region.**

### 2.2.2 Microstructure of 9% Ni Steel after Weld Simulations

Several investigations concerning the microstructure of lath martensite produced after annealing a 9% nickel steel at high temperatures have been completed by Morris et al. [20]. The investigations show that inside one prior austenite grain formed at the peak temperature there are several packets, the packets are subdivided into blocks, and the blocks contain laths with several Kurdjumov-Sachs relationships (which is described in more detail in section 2.3.5). A typical presentation of electron backscatter diffraction (EBSD) results of this microstructure is presented in Figure 2.8. Each of the different-colored packets in Figure 2.8b can be investigated further in Figure 2.8c. During this heat treatment it is well known that the amount of austenite decrease drastically and thus will change the mechanical properties [5], but it is few publications on further investigations of the more critical ICCGHAZ microstructure. The EBSD-technique is presented in section 2.3.

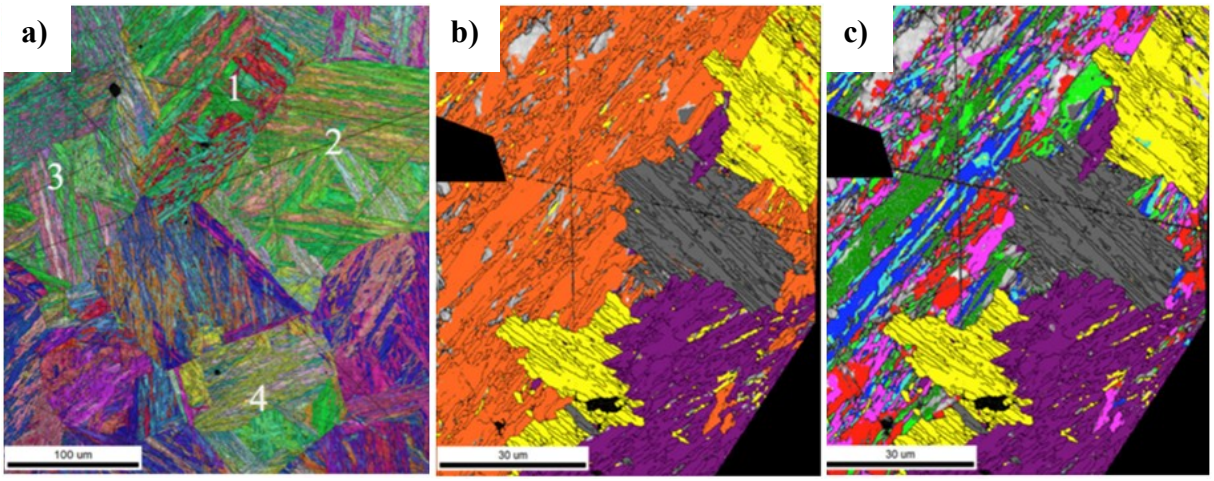


**Figure 2.8: a) Original EBSD image of coarse grained 9% Ni steel, with numbered prior austenite grains. b) Packet structure of grain 1. Each color corresponds to one packet. c) Lath structure of the orange packet in b), with two and two colors interleaving giving longer and wider blocks: red and pink, the two greens and the two blues [20].**

As a pre-study to the master's thesis the author did experiments with the relevant 9% Ni steel using EBSD and weld simulation with the goal to investigate the amount of austenite and microstructure after different thermal treatments. The EBSD data was presented with IPF maps and phase maps. The as-received material had surprisingly low amount of austenite compared to theory, with almost negligible amounts detected. The most relevant investigations on the ex situ weld simulated material is presented in the conference proceedings for the ISOPE conference in Appendix A. The treatment resulting in ICCGHAZ was the only one exhibiting not negligible amounts of austenite. Otherwise the structure is martensite, comparable to other results (e.g. Figure 2.8).

Looking at the IPF map Figure 2.9b, some smaller and some larger grains can be detected after the second weld cycle compared to the first cycle in Figure 2.9a. This indicates that a phase transformation occurred at the peak temperature, as well as a partial recrystallization. In Figure 2.10 it can be observed that the austenite is detectable in the sample having been reheated to 700°C. This was not evident with any other heat treatments or the as-received material. Approximately 1.5% austenite with good quality was detected after a second peak temperature of 700°C.

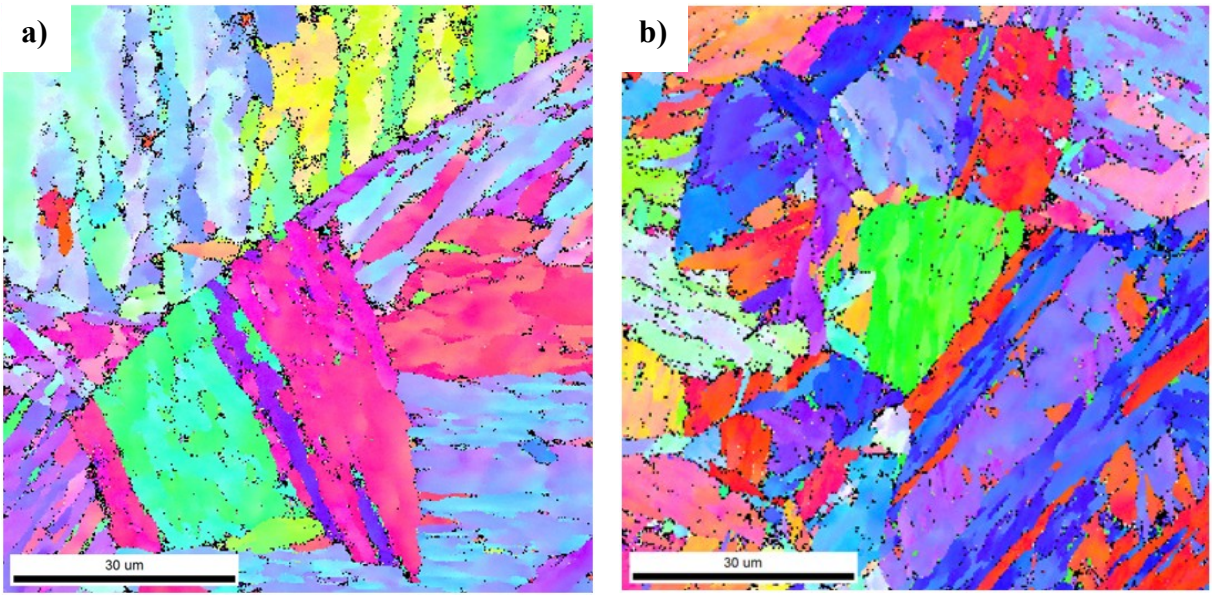


**Figure 2.9: IPF of representative area after a) the first cycle, peak temperature 1350°C, and b) after second cycle with second peak temperature of 700°C. The step size was 0.2 µm.**

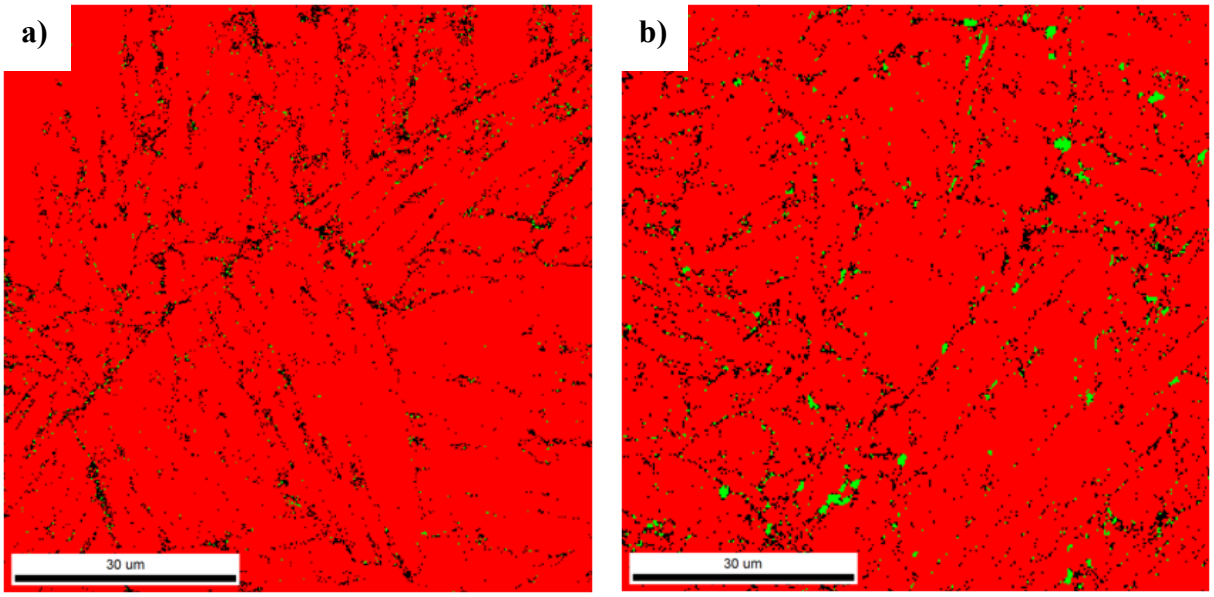


**Figure 2.10: Phase map of representative area after a) the first cycle, peak temperature 1350°C, and b) after second cycle with second peak temperature of 700°C. The step size was 0.2 µm.**

## 2.3 EBSD

The Electron Backscatter Diffraction (EBSD) technique used in a scanning electron microscope (SEM) has developed into a very recognized and employed technique to characterize crystalline materials. EBSD enables, among other things, individual grain orientations, local texture, point-to-point orientation correlations, phase identification and distribution to be determined on the surface of polycrystals [21].

The EBSD signal originates from accelerated primary electrons exhibiting a high-angle backscatter when they interact with specific atom planes at an angle that satisfy Bragg's law [21]:

$$2d_{hkl} \sin \theta_B = n\lambda$$

$d_{hkl}$ is the interplanar spacing between the diffracting planes, $\theta_B$ is the Bragg angle, $\lambda$ is the wavelength of the primary electrons, and $n$ is an integer. This is presented in Figure 2.11, where the different paths I and II interacts with planes of atoms with distance $d$. Bragg's law states that this must give a path difference of a whole number of wavelengths to produce a diffraction pattern.

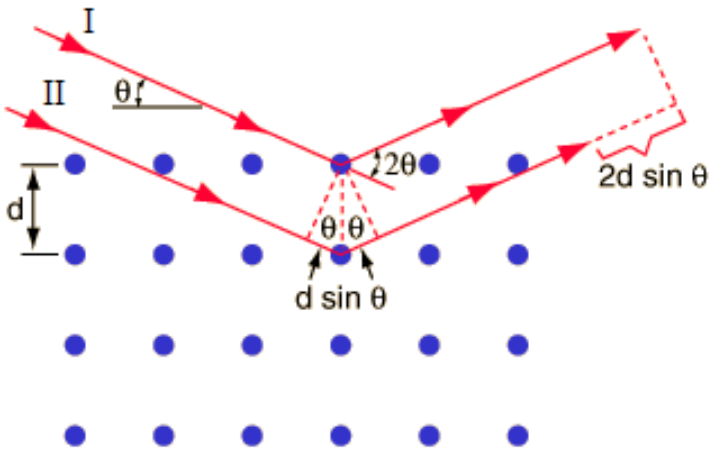


**Figure 2.11: Representation of path difference between two incident beams diffracting from planes of atoms with interplanar distance *d*. Bragg's law states that the path difference must be a whole number of wavelengths of the elastically backscattered electron to produce a diffraction pattern.**

A typical pattern resulting from the backscatter phenomena, commonly called Electron Backscatter Pattern (EBSP), is presented in Figure 2.12a. The bands in the figure are called Kikuchi-lines, and each line corresponds to one atom plane in the crystal lattice. Bragg's law is satisfied at the band edges, because the backscattered electrons interact with the atom planes and form two cones, presented in Figure 2.12b, visible as two parallel lines on the screen. Each cone has an angle opening equal to 180° - $2\theta_B$, giving the distance between the two lines in the EBSP equal to $2\theta_B$. In the centre of the band the crystal planes virtually intersect the screen. The intersections between two bands give a specific crystallographic direction. The orientation based on the EBSP is determined by identifying three independent directions (zone axis), giving the direction perpendicular to the surface of the crystal the pattern originates from [21, 22].

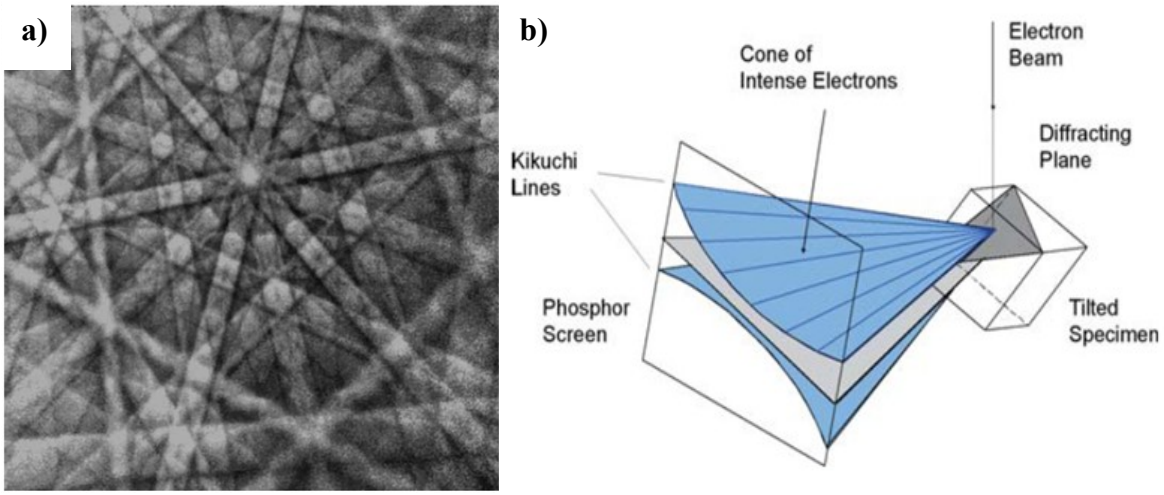


**Figure 2.12: a) Example of an electron backscatter diffraction pattern showing the Kikuchi-lines. b) Presentation of the diffraction cones with respect to the reflecting plane, the specimen, and the phosphor screen. These lines can be used to calculate the crystallographic orientation the pattern originates from [21].**

EBSD signals are generated from a very small volume of the sample, typically a top layer of 20-50 nm [21]. A phosphor screen registers the backscatter diffraction electrons from a stationary beam of high-energy electrons. The sample is usually tilted 70 degrees to increase the backscatter signal [23]. However, about 95% of the electrons registering on the phosphor screen have been inelastically scattered and contribute only to noise in the image [24]. A typical experimental setup is presented in Figure 2.13.

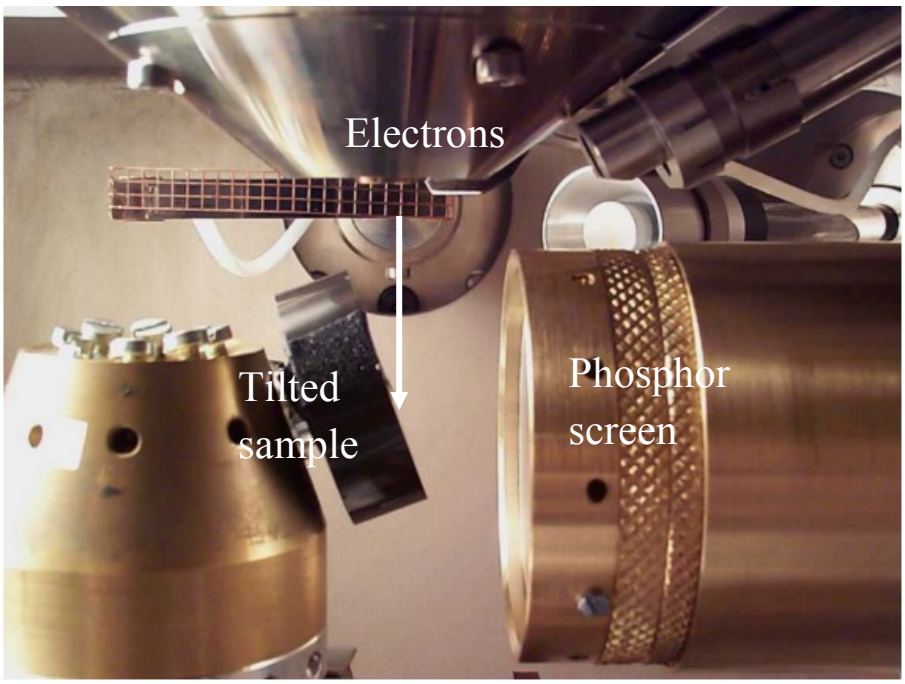


**Figure 2.13: Experimental setup for detecting electron backscatter diffraction patterns [22].**

### 2.3.1 Operational Parameters in SEM

Good diffraction patterns are achieved by using the appropriate operational parameters in combination with the SEM. The goal is to scan the area of interest and obtain good patterns in the shortest amount of time. Other than the tilt angle mentioned earlier there are several other important parameters to consider. The general equation of the secondary electron resolution in SEM given by the diameter ($d$) of the beam:

$$d = k \cdot \sqrt{\frac{i_p}{E_0}} \cdot \frac{1}{\alpha}$$

can be used when considering several of the parameters. The diameter is given by a constant ($k$) depending on the cathode emitting the electrons, the beam current ($i_p$), the accelerating voltage ($E_0$) and beam divergence ($\alpha$). This general equation does not consider aberrations (deviations) in the system.

Figure 2.14a shows that from 10 to 100 nA the effective spatial resolution tends to only increase slightly when using a Field Emission (FE) SEM [21, 25, 26]. Affectively, one can both have a large aperture diameter and a high beam current. Both parameters result in a higher current hitting the sample, and higher current give a lower resolution according to the equation for regular SEM. When considering EBSD, a larger beam current will contribute to a better and faster scan due to more electrons contributing to the individual patterns. Thus, for optimization of the EBSD parameters, the SEM is run in high current mode and with the largest aperture diameter.

Resolution of the patterns will increase with a short working distance. However, this will lead to a Pattern Center (PC, explained in more detail in section 2.3.3) out in the edges of the phosphor screen, and the diffraction patterns will be insufficient for indexing because parts of the pattern are not recorded. The working distance will be affected by the size and position of the screen, as well as decide how many of the patterns that are correct indexed [26]. As seen in Figure 2.14b, the percentage of correct indexed patterns increase with increasing working distance up to 22 mm before it flattens out and decreases. The optimum working distance is usually 20-24 mm (depending on the EBSD detector position). The effect of a retracted detector is presented in Figure 2.15.

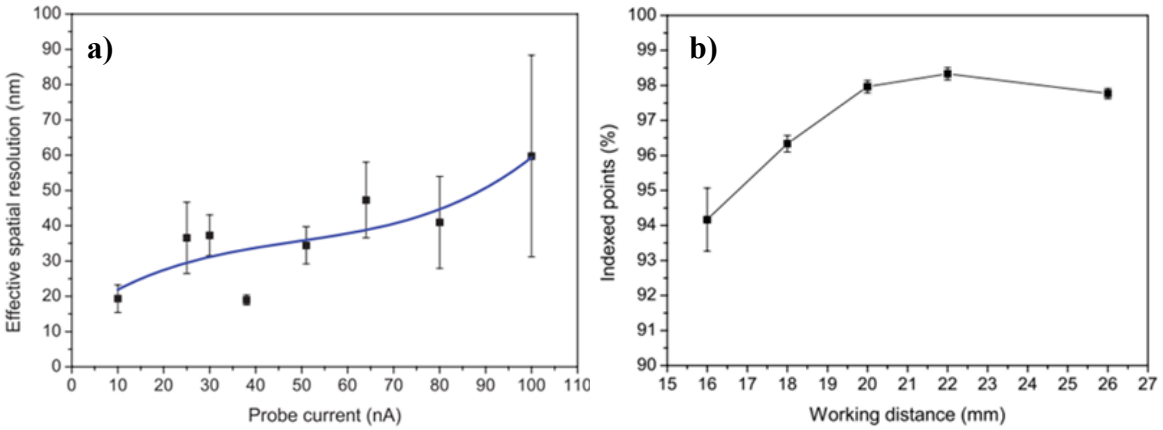


**Figure 2.14: a) The effect of probe current on the effective spatial resolution in a coarse-grained titanium sample. b) The percentage of indexed points with respect to the working distance. The maximal percentage of indexed points is in the 20-24 mm interval [26].**

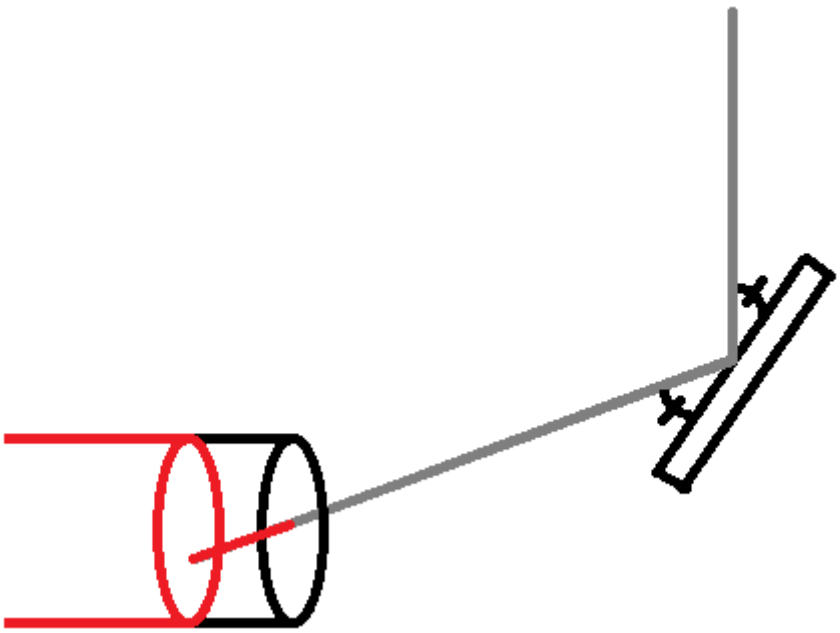

**Figure 2.15: If the position of the EBSD detector changes, the working distance parameter will be optimized at different values. The red detector is retracted from its original black position, giving a pattern center (PC), where the beam from the specimen hit the screen, much lower on the new screen. To obtain a PC in the middle of the new position, the beam must be moved higher, thus the sample position must be closer to the lenses and the working distance smaller.**

High accelerating voltage will give a lower wavelength of the electron [23]:

$$\lambda = \frac{1.24}{\sqrt{E_0}}$$

According to Bragg's law the width of the Kikuchi patterns will decrease (as the Bragg angle decrease) and be easier to detect by increasing the accelerating voltage (because of decreasing wavelength). However, in EBSD the penetration depth of the electron beam should be as small as possible, and considering this a low accelerating voltage is favored. A lower accelerating voltage will also reduce the efficiency of the phosphor screen. A compromise is usually an accelerating voltage of 20 kV, giving sufficient thin Kikuchi bands to detect and not too deep penetration of the sample [22].

To avoid contamination in the sample chamber it is important to have clean vacuum. When an area is scanned the electron current can deposit hydrocarbons on the surface, resulting in bad diffraction patterns. As long as the vacuum is better than $6.1 \cdot 10^{-5}$ Pa this should not be a problem [26]. The effect of contamination of repeated scans is explored further in section 2.4.

Another important parameter is the step size. This decides how many registered points there will be over a chosen area during acquisition. More registered points take a longer time, but the results are usually more precise. The correspondence between step size and magnification is presented in Figure 2.16. Using 1000X magnification the optimum step size is 80 nm [26].

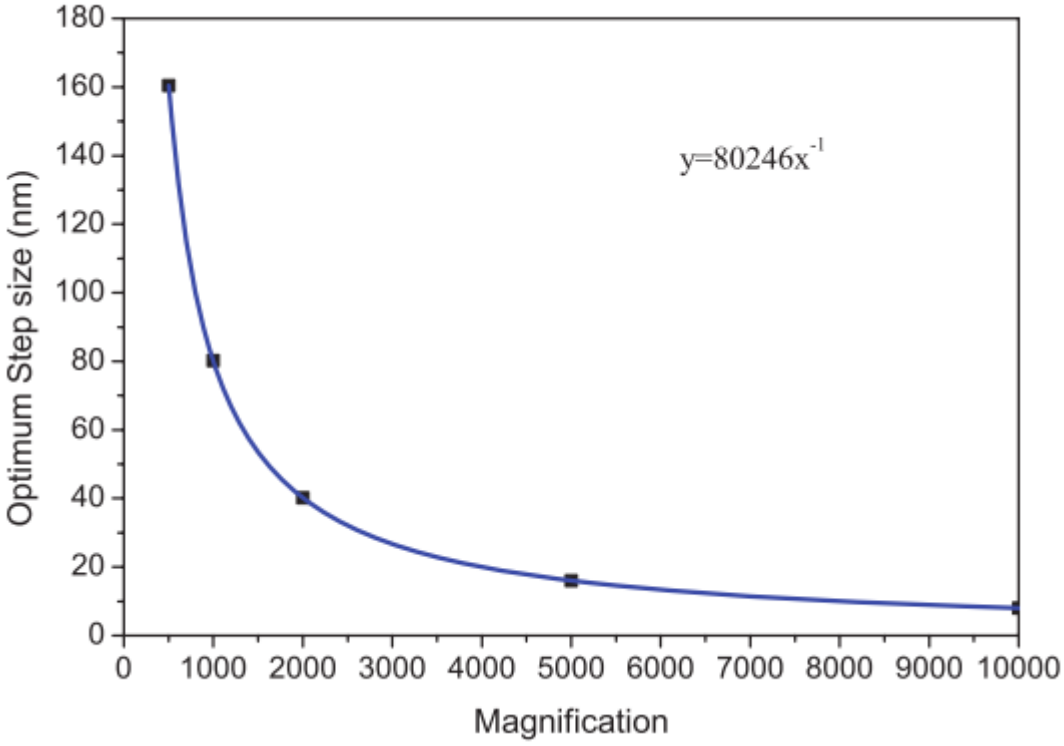


**Figure 2.16: The optimum step size as a function of magnification [26].**

### 2.3.2 Operational Parameters and Settings in NORDIF

NORDIF is the program used for acquisition of the patterns. Figure 2.17a shows the interface of the NORDIF program, where the parameters accelerating voltage, working distance, tilt angle and magnification are entered before a secondary electron image of the chosen area is extracted. The left side window gives the opportunity to select these different settings and is further examined in Figure 2.17b.

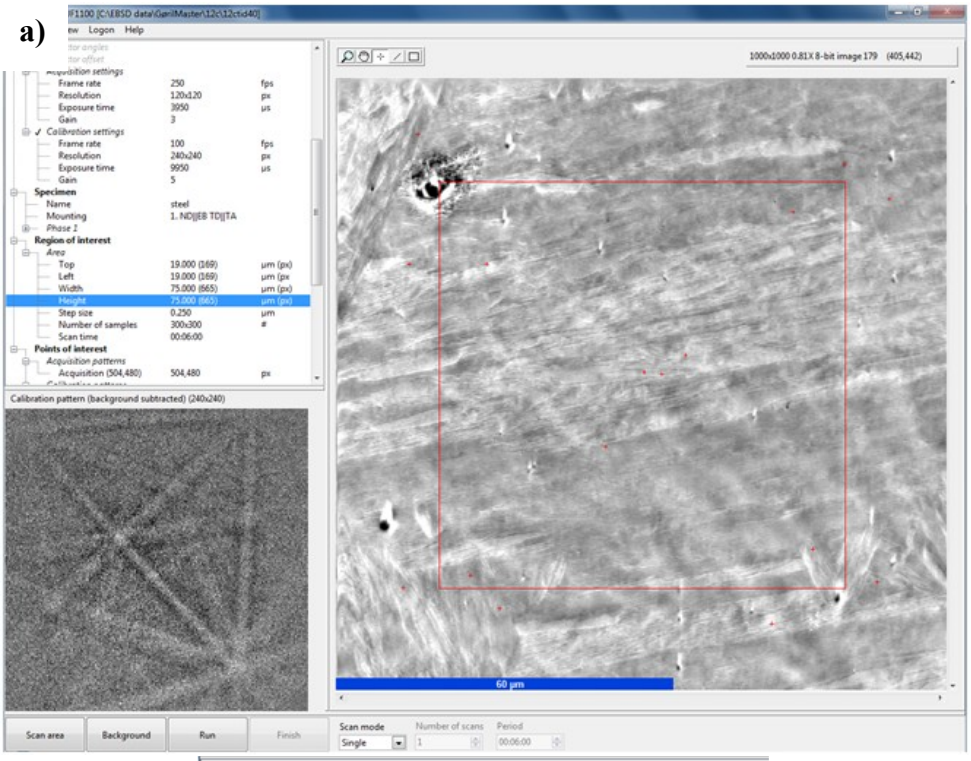


b)

| | | |
|---|---|---|
| **Microscope** | | |
| Manufacturer | ZEISS | |
| Model | Supra | |
| Magnification | 1000 | # |
| Accelerating voltage | 20.0 | kV |
| Working distance | 19.7 | mm |
| Tilt angle | 70.0 | ° |
| *Signal voltages* | | |
| *Deflection voltages* | | |
| *Electron image* | | |
| Frame rate | 0.15 | fps |
| Resolution | 1000x1000 | px |
| Calibration factor | 5636.3 | µm/V |
| *Aspect ratio* | | |
| **EBSD detector** | | |
| Port position | 270 | ° |
| *Detector angles* | | |
| *Detector offset* | | |
| ✓ *Acquisition settings* | | |
| Frame rate | 250 | fps |
| Resolution | 120x120 | px |
| Exposure time | 3950 | µs |
| Gain | 3 | |
| *Calibration settings* | | |
| Frame rate | 100 | fps |
| Resolution | 240x240 | px |
| Exposure time | 9950 | µs |
| Gain | 5 | |

**Figure 2.17: The NORDIF software, with a) the whole interface with example of secondary electron image, region of interest and one calibration pattern, and b) the window where the different settings can be entered.**

The main settings for the EBSD scan are the acquisition and calibration settings of the EBSD camera, and the quality of the diffraction patterns can be optimized by changing these. The parameters frame rate, resolution and gain can be adjusted.

The frame rate indicates how many patterns are being recorded each second. A pre-processing technique called binning say something about the resolution of the diffraction patterns. Having a 120x120 resolution corresponds to 4x4 binning; meaning 16 pixels (4x4) is being combined to create one big pixel. The binning technique is simply presented in Figure 2.18. 4x4 binning will also affect the light sensitivity of the CCD digital camera, where the diffraction pattern from the phosphor screen will be imaged, and result in an increase of light sensitivity with a factor 16. The frame rate can be increased with decreasing resolution. The exposure time is automatically set to the highest possible value. If it is low intensity in the pattern, the gain can be increased electronically. This will introduce noise in the pattern; however, the Hugh transformation (explained in section 2.3.3) is not very sensitive regarding noise.

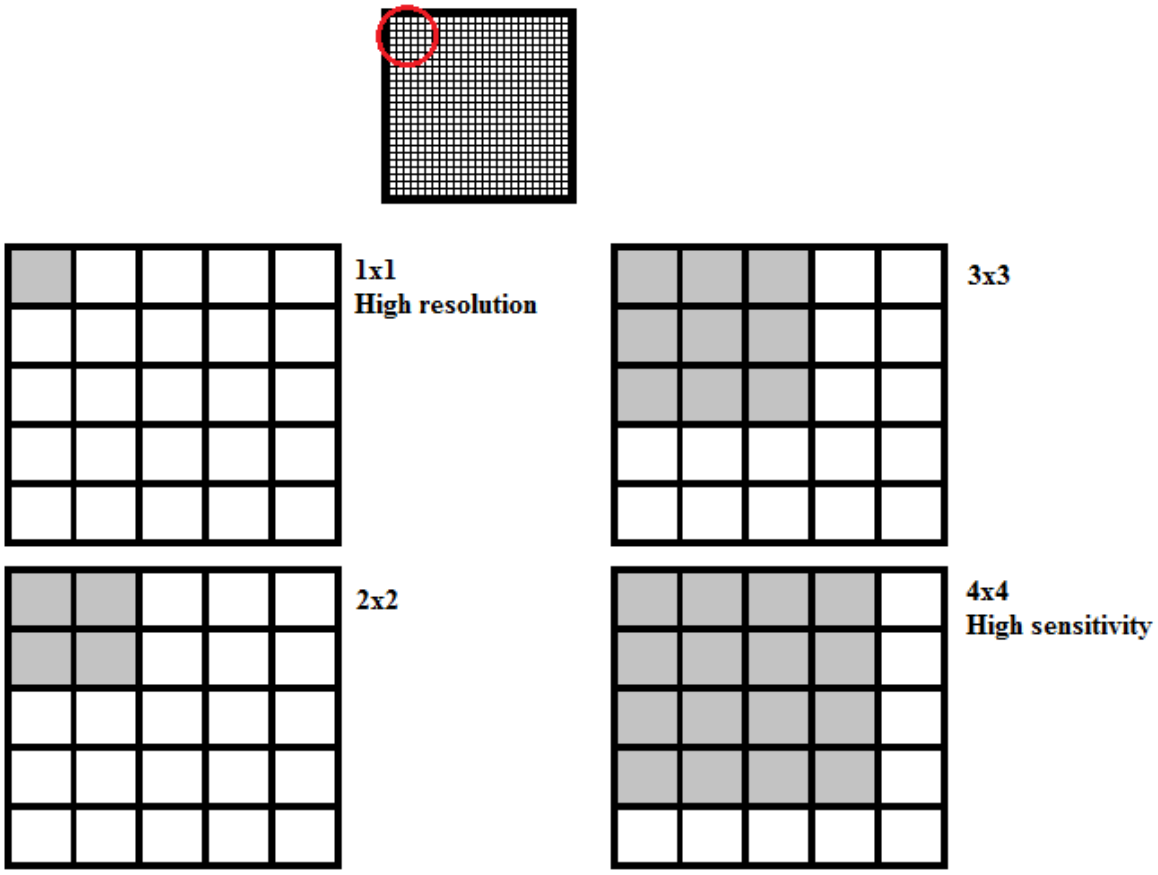


**Figure 2.18: Binning, with the pixels represented by the square grid of the interesting area in the top of the picture. Different kinds of binning are then investigating looking only at the red circle. The gray pixels will, using binning, be combined to one larger pixel. This will then be done to the entire picture.**

The calibration patterns used during indexing need to be of good quality, so these are often taken with high resolution and longer exposure time than the acquisition patterns, which should be obtained with a higher frame rate so the scan is not too slow. One example of a calibration diffraction pattern in presented in the bottom left corner of Figure 2.17a.

Before the patterns of the chosen area are recorded, a background picture is recorded. This is used to remove shadows and illumination gradients in the pattern. The background picture is taken based on more than 100 patterns in the electron image, and the background picture is then subtracted from the diffraction patterns. This is presented in Figure 2.19. Comparing the pattern in Figure 2.19c to the one in Figure 2.17a, the NORDIF program also have the opportunity to use automatic contrast, further highlighting the Kikuchi patterns, as can be seen in the pattern from the NORDIF interface.

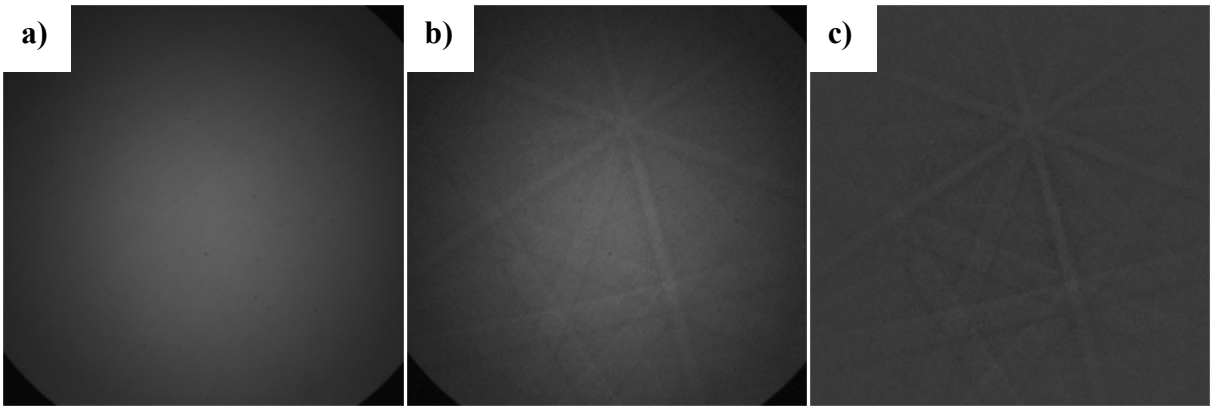


**Figure 2.19: a) Background picture, and diffraction pictures b) without and c) with background correction (from austenite phase during experiments).**

### 2.3.3 Indexing and Analysis

To get information from the diffraction patterns the Kikuchi-lines must be identified. This is done in the TSL OIM DC software by using the Hugh transformation, which transforms the lines into bright peaks. In the Hough transformation the coordinates in the $(x,y)$ plane is transformed to coordinates $(\rho,\theta)$ in the Hugh space, and the transformation is given by

$$\rho = x\cos\theta \cdot y\sin\theta$$

This will give a transformation of the Kikuchi-lines presented in Figure 2.20a to a pattern in the Hugh space, presented in Figure 2.20b. The placing of the bright regions in the Hugh space will be used by the indexing program to find the orientation [22].

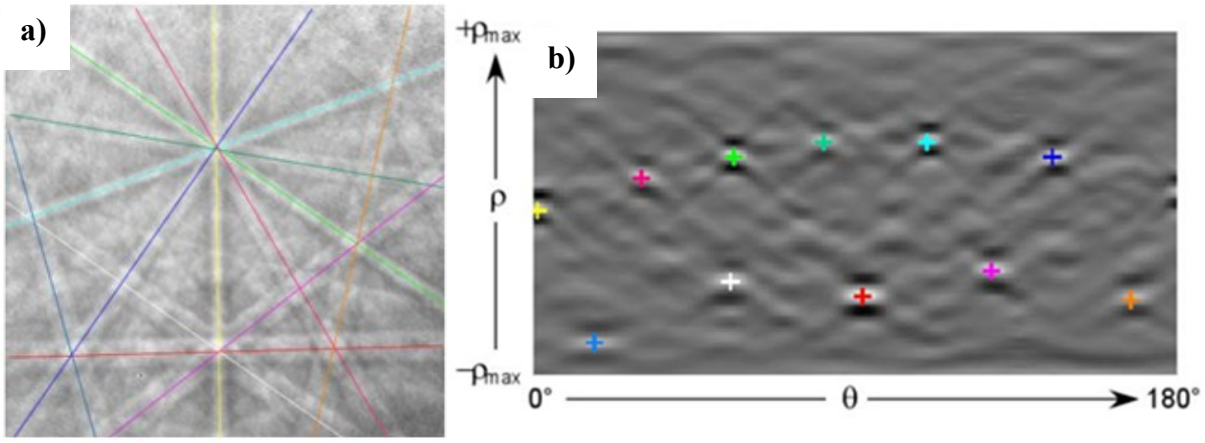


**Figure 2.20: a) The diffraction pattern showing the Kikuchi lines. b) The pattern transformed into Hugh space [22]. The different lines have been given different colors, and the corresponding peak in the Hugh space has the same color. The TSL OIM DC software uses the Hugh peaks to decide the crystallographic orientation the pattern originates from.**

Before the indexing starts the program uses the calibration patterns recorded before the scan to identify the position of the scanned area compared to the phosphor screen. This is done by defining the Pattern Center (PC), consisting of three coordinates defining the beam position on the specimen relative to the screen [22]. This could be seen in Figure 2.15. Also, the sample's phases are defined.

Three important parameters when considering the diffraction patterns during and after indexing are Confidence Index (CI), Fit and Image Quality (IQ).

*Confidence Index* (CI) is a number between 0 and 1, where low values correlates to the program not confident that the pattern is correctly indexed, and high values when it is fairly confident that the pattern is indexed correctly. This means that if a pattern originates from a grain boundary the pattern is most likely a mixture of several patterns, and the resulting CI value is low because the program is not confident that it chose correctly. The same happens when the pattern originates from a boundary between two phases [22].

*Fit* is a value that describes the average angular difference between the detected bands in the diffraction pattern and the corresponding bands reconstructed from the program's orientation solution [27]. A value close to 1 is desired.

*Image Quality* (IQ) describes the quality of the diffraction patterns, and is influenced by factors such as perfection of crystal lattice in the diffraction volume, sample preparation, phases and orientation of the crystal. The IQ is a representation of the detected Hugh-peaks, and will therefore depend strongly on the maximum number of peaks, a value defined by the

user [28]. It is very typical that grain boundaries get a low IQ value, as well as areas with high dislocation density (e.g. areas exposed to large deformations).

After indexing the next step is analysis. Among the things to examine are image quality, phase mapping, inverse pole figure maps and grain boundaries. It is also possible to clean the raw data, but this step is important to do with care as information can easily be lost or misinterpreted.

A much used cleaning operation is *Grain CI Standardization,* before a *CI filter* to remove points with low CI value. Grain CI Standardization changes CI of all points inside one identified grain to the maximal CI value inside that grain. This treatment give points that are most likely indexed correctly but with low CI a higher CI, thus loosing risk that the point is removed during the subsequent filter. This is presented in Figure 2.21. Wrong indexed points with no orientation relation to its neighboring points will keep its low CI value, and most likely be removed using the CI filter [29]. During the Grain CI Standardization the grain tolerance angle is established, e.g. t to 5, meaning neighboring points with can have a misorientation up to 5° and still receive the highest CI value inside the grain. Minimum grain size is also defined, e.g. to 2 (pixels). The CI filter will then remove all points with CI less than 0.050. If the CI value is less than 0.10 it is a large probability that it was not correctly indexed [30], but 0.050 is also much used.

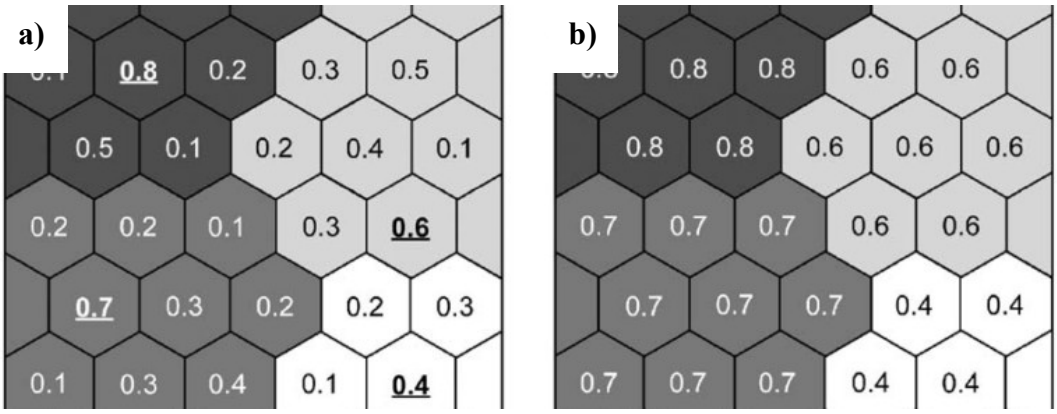


**Figure 2.21: a) Four grains with originally different CI values inside the grain. b) After the Grain CI Standardization all points inside a grain have the highest CI detected inside that particular grain [27].**

## 2.3.4 Presentation of EBSD Results

When presenting the data after the cleaning operations described previously, there are three different maps that are frequently used: Inverse Pole Figure (IPF) map, phase map and Image Quality (IQ) map. The color coding in the IPF maps is presented in Figure 2.22a, where the

color represent the orientation perpendicular to the surface. This gives a partial crystallographic orientation of the crystal because the orientations can be rotated around this perpendicular axis. The phase maps follow the colors in Figure 2.22b, with red as the martensite phase (represented by alpha) and green as the austenite phase. In the IQ map light areas indicate a high IQ value and good quality, and darker points a low IQ value. The points removed by the CI filter are presented as black pixels in all maps; however, this is not present in the examples of the three maps in Figure 2.23.

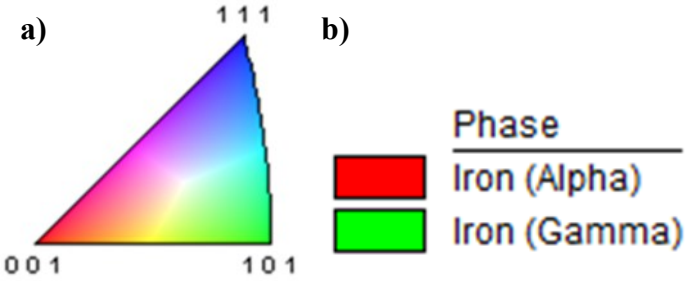


**Figure 2.22: Information regarding a) which orientation is perpendicular to the plane in the inverse pole figure map and b) phase map showing red (martensite or ferrite) and green (austenite).**

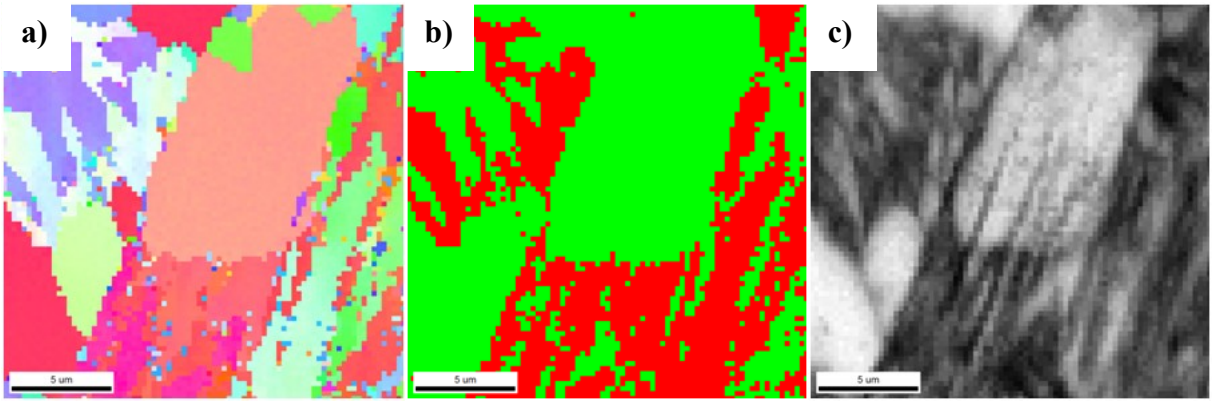


**Figure 2.23: Example of a) IPF map, b) phase map and c) IQ map, without removing bad points from own experiments.**

## 2.3.5 Pole Figures and Orientation Relationships

When a displacive transformation from austenite to martensite occurs, a correlation between the crystallographic orientation in the original and resulting phase can be observed. The closed-packed planes in the two phases are usually parallel, or nearly parallel, to each other. This orientation relationship is called the Kurdjumov-Sachs (KS) relationship [7]. The different variants of martensite will grow from the four closed packed (111)-planes in the austenite, and in six different [110] closed-packed directions, resulting in 24 possibilities of martensite being formed from one austenite orientation [31]. This relationship is presented in

Figure 2.24. If the austenite has a cube orientation the resulting (001) martensite pole figure will look like Figure 2.25 (showing all possible orientations). This can be used when analyzing the experimental results; when investigating the (001) pole figures of the scan the austenite pole figure can be rotated giving it a cube orientation. If the resulting pole figure of the martensite is similar to the KS relationships in Figure 2.25 and specific orientations can be identified, then an orientation relationship has been proved.

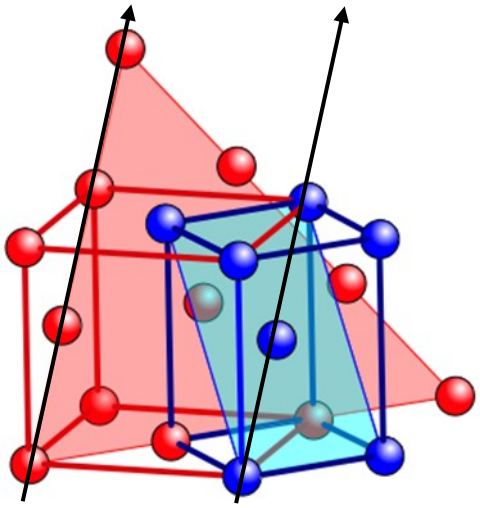

**Figure 2.24: Atomistic presentation of the FCC/BCC(/BCT) element lattice transformation. Here the red $(111)_\gamma$ lattice plane is assumed as parallel to the blue $(101)_\alpha$ plane. Two arrows mark the parallel closed-packed directions. The schematic representation shows that the BCC lattice must be deformed to fulfill the symmetry [32], resulting in a BCT crystal structure.**

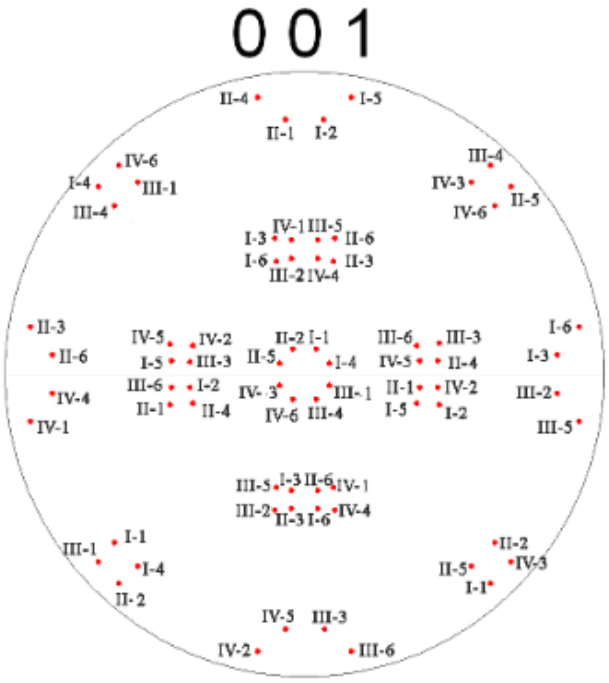


**Figure 2.25: (001)-pole projection figure showing the Kurdjumov-Sachs orientation relationship. There are 24 different orientations possible when one austenite grain transforms to martensite by a displacive transformation [31]. The roman numbering I-IV corresponds to the four closed-packed planes in austenite and the numbering from 1-6 the six closed-packed directions.**

## 2.4 In Situ EBSD Characterization during Heating

When investigating mechanical properties due to a change in microstructure most EBSD investigations are restricted to characterization of the microstructure only in the initial and final state. In situ investigations make it possible to study the change in microstructure directly during changing conditions, and are therefore an important method to help understand how the changes occur. The in situ technique can be used on many different materials, either to investigate deformation mechanisms at different temperatures, or change in microstructure during heating. It is now possible to do several analyses during the in situ experiment because the collection rate of EBSD-data is very high. This makes it easy to follow the changes in the material, as the same area can be investigated after different times at elevated temperatures.

When studying the changes in the microstructure directly using the EBSD-technique it is important that the speed of the EBSD-system is high. Traditionally the diffraction patterns are indexed directly during the collection of patterns, a technique called online-EBSD. The speed of the EBSD-system will then be influenced by both the acquisition process and the indexing process. On the other hand, offline-EBSD saves the diffraction patterns directly on a hard-drive without the indexing process [33], so the acquisition and indexing can be done separately. This increase the speed of the system, as the acquisition time decrease considerably. This technique also makes it possible to index the patterns several times, making it possible to optimize the Hugh-settings. It is not necessary to know all the phases that the material consists of beforehand, as this can be added afterwards. The combination of rapid acquisition of patterns as well as the reliability and flexibility regarding the offline indexing, makes this technique suitable for real-time characterization during in situ experiments.

During the EBSD-scan the sample surface can be contaminated because a layer of hydrocarbons will be deposited on the surface [26]. During in situ EBSD this can be a considerable problem, as the same area of interest is scanned several times. The specimen will then be more contaminated with each scan, and the quality of the diffraction patters will decrease. The effect of repeated scans is presented in Figure 2.26, showing a decrease in both percentage of indexed points and the image quality with increasing number of scans. However, when considering in situ heating this problem is avoided as the high temperature will cause the deposited carbon layer to evaporate.

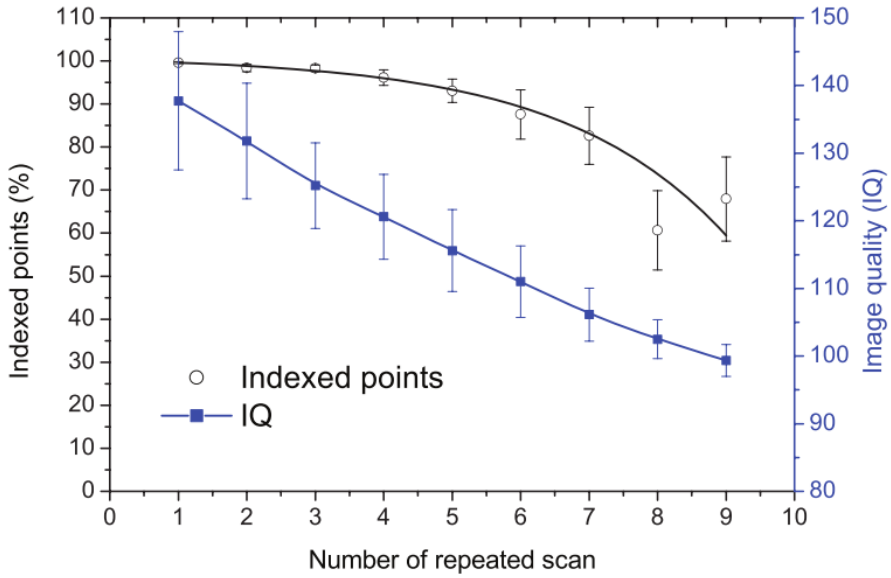


**Figure 2.26: The effect of number of repeated scans on the amount of indexed points and the image quality (IQ) in coarse-grained titanium (probe current 33 nA and frame rate 140 fps) [26].**

Another consideration when using in situ heating together with EBSD is the step size in combination with area of interest and scan time. Figure 2.16 presented the optimum step size given by magnification, indicating that an optimum step size for a magnification of 1000X is 80 nm. When the microstructure is coarse grained, as the case is when investigating the ICCGHAZ, it is important that the area should contain at least one previous coarse grained boundary. Considering that the scan time should be short enough to ensure that the changes during the scan are not too big, this indicates that a larger step size is needed. This will then result in a larger proportion of the patterns being non-indexed or have a low CI. A balance between all these must be considered when doing in situ heating in combination with EBSD.

It has been reported few in situ EBSD investigation during heating of steel. This is because of the high recrystallization temperature, leading to several difficulties. During earlier heating experiments of steel in combination with EBSD it has been developed different types of heating stages to reach the desired temperatures. Nakamichi et al. [34] have performed experiments concerning the recrystallization in an IF-steel (Interstitial Free). It was shown that there was no diminishing of the quality of the diffraction patterns up to 800°C. When comparing the microstructure on the surface and inside the specimen during in situ heating it was established small differences in the recrystallization process for the two locations. However, the texture changes were similar in both places, indicating that the EBSD observations of the surface are representative for the recrystallization in the bulk. The hot stage presented in Figure 2.27 was developed for these experiments.

Lischewski et al. [35] developed a hot stage with the possibility to reach 1000°C, and used it to investigate the α-γ-α phase transformation in steel during in situ heating up to 900°C. A diode infrared laser was used as a heating source, and the hot stage was a SiC sample holder to be heated, with two heating shields. Watanabe et al. [36] also studied the α-γ phase transition using in situ heating in combination with EBSD, and the design of this oven made it possible to heat the sample all the way up to 1500°C.

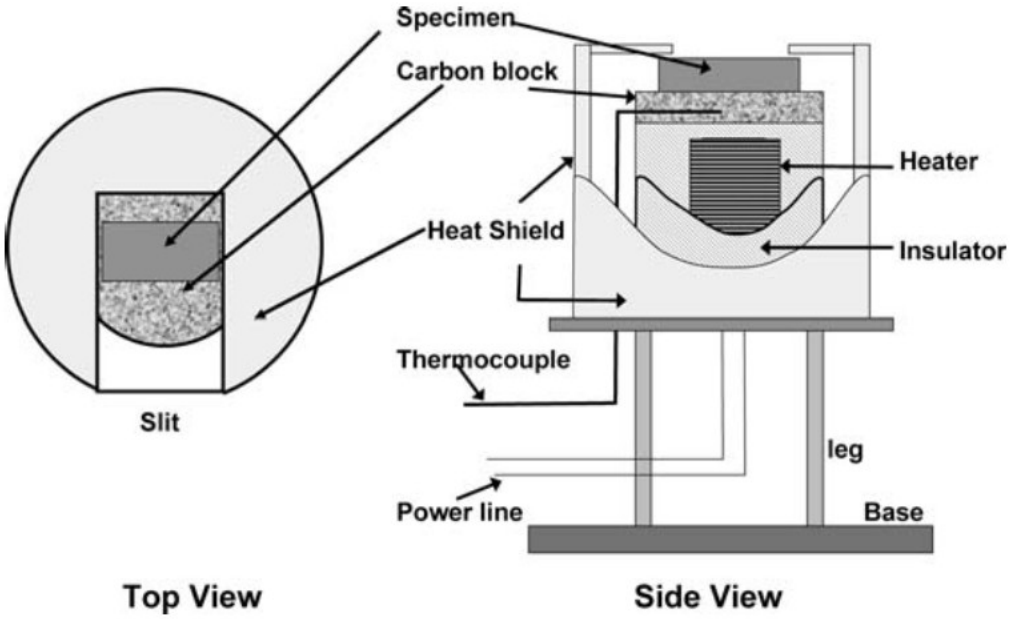


**Figure 2.27: Schematic representation of a hot stage [34]. The specimen is mounted on a carbon disk cemented on top of the heating element, which is coated with alumina for electrical and thermal contact. The heat shield is of stainless steel, with a slit in the top, to make room for the electron beam. The furnace is mounted on aluminum base with titanium legs. The temperature was measured with a thermocouple inserted in the middle of the carbon block.**

At the Department of Materials Science and Engineering at the Norwegian University of Science and Technology, several in situ EBSD-examinations have been executed. Anne-Jorunn Enstad developed an in situ hot stage for heating steel up to 800°C [37, 38]. The thermocouples register the temperature in the furnace and in the middle of the sample. This is the furnace used when investigating the 9% Ni steel in this master's thesis. More details of the hot stage and the in situ EBSD software can be examined in Appendix B and Appendix C.

Earlier hot-stages developed at NTNU have been used to do in situ investigation of aluminum up to 500°C. The present stage has been used to investigate different steels up to 800°C. This stage was further developed to make it possible to investigate the cooling process as well, with e.g. helium as cooling media [39, 40]. However, a stable heating rate higher than 1-2°C/s is difficult with this equipment, limiting investigations to relatively slow heating.

# Chapter 3 Experimental

## 3.1 Material

The material used in the present work is a low carbon 9% nickel steel. This steel is designed for LNG storage at cryogenic temperatures, and has a design temperature of -196°C. For this purpose the steel has production parameters supposed to give it a martensitic structure containing 5-15% retained austenite, in this case the reheat, quench and tempering (RQ-T) process. The precise chemical composition of the steel can be examined in Table 3.1.

**Table 3.1: The chemical composition of the material.**

| Element | C | Mn | P | S | Si | Ni |
|---|---|---|---|---|---|---|
| **weight%** | 0.06 | 0.61 | 0.002 | 0.001 | 0.25 | 9.22 |

## 3.2 Weld Simulation

Prior to the experiments conducted in-situ, five steel rods (dimensions 11x11x100 $mm^3$) were subjected to a single cycle thermal weld simulation with the goal to obtain a coarse grained heat affected zone in HAZ. The rods were subjected to a weld simulation program using an in-house weld simulator unit based on resistance heating principles. Two clamps held the rod in place, and the clamps were water cooled to lead the heat away from the sample. The operational parameters for the simulation are presented in Table 3.2. A dilatometer was used during the weld simulation to experimentally detect the phase transformation temperatures during fast heating ($Ac_1$ and $Ac_3$).

**Table 3.2: The operational parameters for the weld simulation.**

| Parameter | Value |
|---|---|
| Sample type | Thick sample |
| Clamp distance | 21 mm |
| Preheating temperature | 50°C |
| Set peak temperature | 1335°C |
| Upper ΔT | 800°C |
| Lower ΔT | 500°C |
| Set cooling time | 14.9 s |
| Uprate limit | 150°C/s |
| Cooling method | Water cooling |

A typical temperature-time curve for the cycles heating to approximately 1350°C is presented in Figure 3.1.

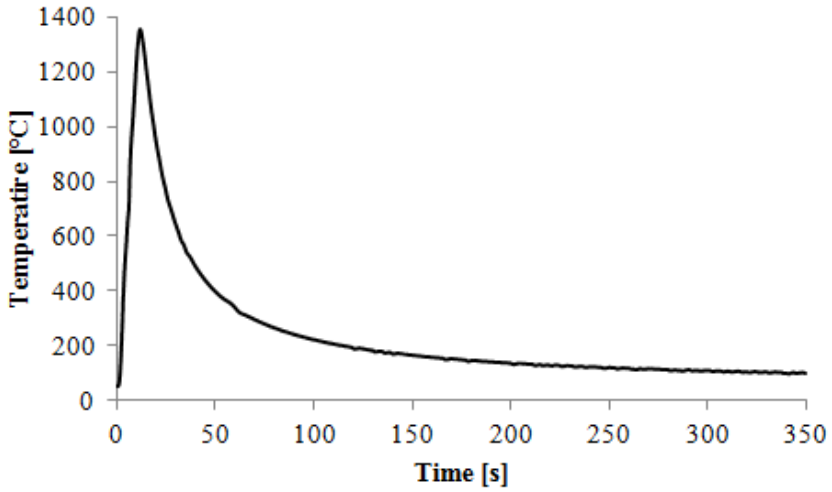


**Figure 3.1: Typical behavior for a weld simulation showing how the temperature changes during the time, with peak temperature almost 1400°C.**

### 3.2.1 Dilatometer Analysis

The dilatometer measures the expansion of the sample during heating and cooling. The temperature where the slope starts to change during heating is the temperature where the phase transformation starts, and where the slope goes back to being linear is where the transformation is complete. This dilatometric result can be used to define the $Ac_1$ and $Ac_3$ temperatures. A typical dilatometric curve is presented in Figure 3.2 corresponding to the weld simulation in Figure 3.1. Further examination of the slope should be done by looking only at the relevant part of the graph to identify the temperatures, e.g. as presented in section 2.2, Figure 2.5.

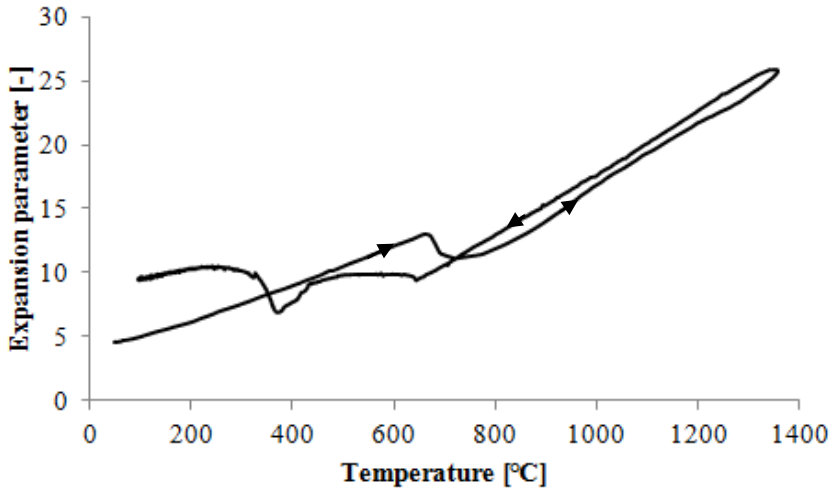


**Figure 3.2: Typical dilatometric curve for the weld simulation in Figure 3.1.**

## 3.3 Sample Geometry

After the weld simulation the final sample geometry was machined out (spark eroded) from the steel rods as presented in Figure 3.3. Three samples (dimensions 11 mm x 12 mm x 2.5-3.5 mm) was machined out from each rod. A hole with diameter 0.55 mm and a depth of 2-3 mm was drilled at the end of the sample as a site for the thermocouple used in the in situ experiment.

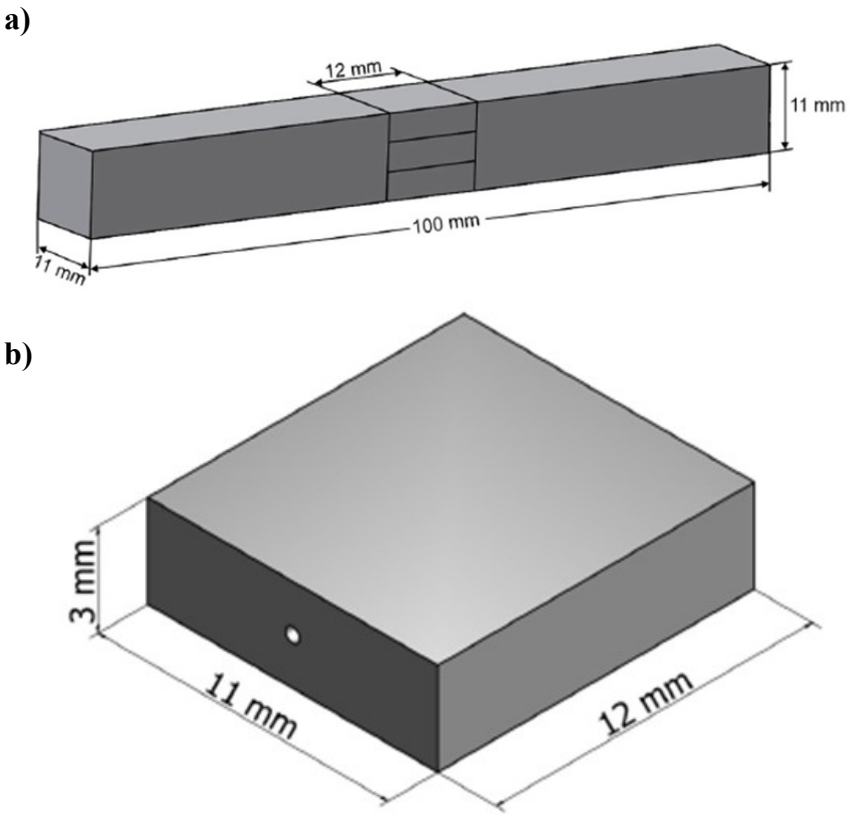


**Figure 3.3: Sample geometry. a) The original steel rod for weld simulation, with the three samples later cut out located in the middle. b) The geometry for the sample to be investigated in situ. The hole is for the thermocouple.**

Five rods, numbered 8-12, were machined out, thus giving 15 samples of the geometry presented in Figure 3.3b. For each rod the three samples were numbered A, B and C, from the top and down as can be seen in Figure 3.4. To achieve the proper height of 2.5-3.5 mm, some of the samples had to be grinded down (one of the three from each rod was usually too thick). In this case the surface not to be investigated with EBSD was grinded. Looking at the samples in Figure 3.4, the top part of A and B was to be investigated, and the bottom of C. This meant grinding A and B at the bottom, and C at the top looking at it from the original sample.

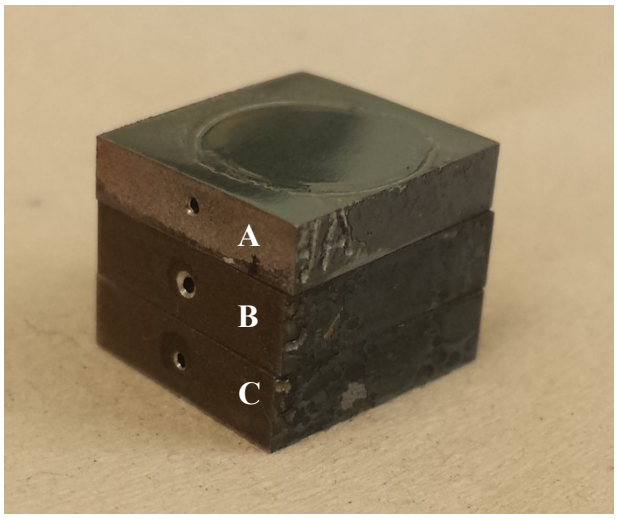


**Figure 3.4: The three samples machined out from one rod. From top to bottom they were marked A, B and C. The heat from the ex situ weld cycle was transferred in the middle of A. Note that A has been prepared with electropolishing.**

## 3.4 Sample Preparation

To obtain good quality diffraction patterns it is very important to prepare the sample properly. As only the uppermost layer of 20-50 nm contributes to the diffraction pattern it is extremely important that this layer is relatively flat, and free of deformations, contaminations and oxide layers [41, 42]. Because the samples were to be placed in a sample holder in the hot stage during EBSD analysis the samples was prepared manually. The samples were prepared for EBSD by the steps below.

1. Grinding with water as lubricant and SiC paper with increasing fineness: 320, 500, 800, 1200 and 2000.
2. Diamond Polish with lubricant (ethanol based): 3 and 1 μm.
3. Electropolish with A3 electrolyte, parameters are given in Table 3.4.
4. Ultrasonic acetone bath 5-10 minutes.
5. Plasma cleaner Fischione Model 1020 for 10 minutes.

Previous experiments have shown that, for the particular 9% nickel steel, the A3 electrolyte exhibit the best results for EBSD preparation when investigating the retained austenite phase [9, 43]. The electropolishing was executed with Struers Lectropol-5 at room temperature. During earlier work done by the author [43], the geometry of the sample, as well as the area to be electropolished, was different than during this thesis. Reducing the sample thickness from 10 to 3 mm and the area from 2 to 0.5 $cm^2$ caused problems with the quality of the electropolishing. Table 3.3 shows the parameters used for the samples to be investigated in

situ, showing three different combinations of flow rate and voltage. The recipe for the A3 electrolyte is presented in Table 3.4.

**Table 3.3: Parameters used for electropolishing, with three combinations with variable voltage and flow rate values.**

| **Sample number** | **8B, 9A, 12B** | **8A, 8C, 9B, 10A, 10B** | **10C, 11A, 11B, 11C, 12A, 12C** |
|---|---|---|---|
| Voltage [*V*] | 31 | 29 | 24 |
| Flow rate | 14 | 14 | 18 |
| Electrolyte | | A3 | |
| Area [$cm^2$] | | 0.5 | |
| Time [*minutes*] | | 1 | |
| Temperature [°*C*] | | 20 | |

**Table 3.4: The recipe for the A3 electrolyte used (provided by Struers).**

| **Chemical substance** | **Amount [*mL*]** |
|---|---|
| Percloric acid | 60 |
| Butyl Cellosolve | 600 |
| Methanol | 360 |

## 3.5 SEM Settings

The electron microscope used was a Zeiss Gemini Supra 55VP, a Low Vacuum (LV) FESEM microscope with the possibility to achieve high current mode without affecting the resolution. Both the electron backscatter diffraction (EBSD) and energy-dispersion spectroscopy (EDS) techniques were employed.

### 3.5.1 EBSD Settings for Characterization

A NORDIF UF-1100 EBSD-detector recorded the diffraction patterns with the program NORDIF 2.0.19. To index the patterns EDAX/TSL OIM Data Collection 7.1.0 was used, and for analysis EDAX/TSL OIM Analysis 7.1.0. The microscope is imaged in Figure 3.5, together with the in situ devices on a separate table.


**Figure 3.5: Zeiss Gemini Supra with in situ devices on the foremost table.**

The parameters in SEM were chosen based on the theory giving the best EBSD results (see section 2.3.1). The parameters used in the experiment are presented in Table 3.5.

**Table 3.5: Settings used in SEM.**

| | |
|---|---|
| Accelerating voltage [$kV$] | 20 |
| Working distance [$mm$] | 18-21 |
| Aperture diameter [$\mu m$] | 300 |
| Tilt angle [°] | 70 |
| Magnification [$X$] | 1000 |
| Beam current [$nA$] | High current |
| Dynamic focus [$\%$] | 3-4 |

Using the theory presented in section 2.3 the settings giving the best diffraction patterns are presented in Table 3.6. The area of interest chosen with this step size will result in each scan taking 6 minutes. During the indexing using OIM Data Collection, using theory presented in

section 2.3.3, there are several parameters that need to be defined. The Hugh settings are presented in Table 3.7; otherwise the phases Iron (alpha) and Iron (gamma) were defined.

**Table 3.6: NORDIF parameter settings.**

| | |
|---|---|
| **Acquisition settings** | |
| Frame rate [*fps*] | 250 |
| Resolution [*px*] | 120x120 |
| Exposure time [$\mu s$] | 3950 |
| Gain | 3 |
| **Calibration settings** | |
| Frame rate [*fps*] | 100 |
| Resolution [*px*] | 240x240 |
| Exposure time [$\mu s$] | 9950 |
| Gain | 5 |
| **Area of interest** | |
| Length [$\mu m$] | 75 |
| Width [$\mu m$] | 75 |
| Step size [$\mu m$] | 0.25 |

**Table 3.7: Hough settings.**

| | |
|---|---|
| Hough type | Classic |
| Hough resolution | Low |
| Convolution mask | 9x9 |
| Min peak magnitude | 5 |
| Min peak distance | 15 |
| Peak symmetry | 0.5 |
| Vertical bias [%] | 0 |
| Binned pattern size | 120 |
| Theta step size [°] | 1 |
| Rho fraction [%] | 80 |
| Max peak count | 7 |
| Min peak count | 3 |

### 3.5.2 EDS

To examine if the chemical composition varied between the coarse grains in the weld simulated microstructure EDS spot analysis was carried out with 15 kV accelerating voltage, 120 μm aperture and 10 mm working distance. Based on the original chemical composition of the steel (Table 3.1), the elements Si, Mn, Fe and Ni were defined (not C).

The quantitative analysis is not precise, but by using "Smart Quant eZAF analysis" the amounts can be approximately decided.

## 3.6 In Situ Heating Experiments

The heating was done with the in situ heating equipment developed by Rémi Chiron at the CNRF research center [44] and further developed by Anne-Jorunn Enstad at NTNU [37, 38]. The system consists of a furnace placed inside a hot stage, and a computer able to detect the sample and furnace temperatures and control the heat power supply. The furnace has a maximum temperature of 800°C. The hot stage is imaged in Figure 3.6, and the computer and controller system in Figure 3.9. The work done in situ can be divided into two parts; one part concerning the refinement and use of the hot stage and the other on the actual in situ heating experiments.

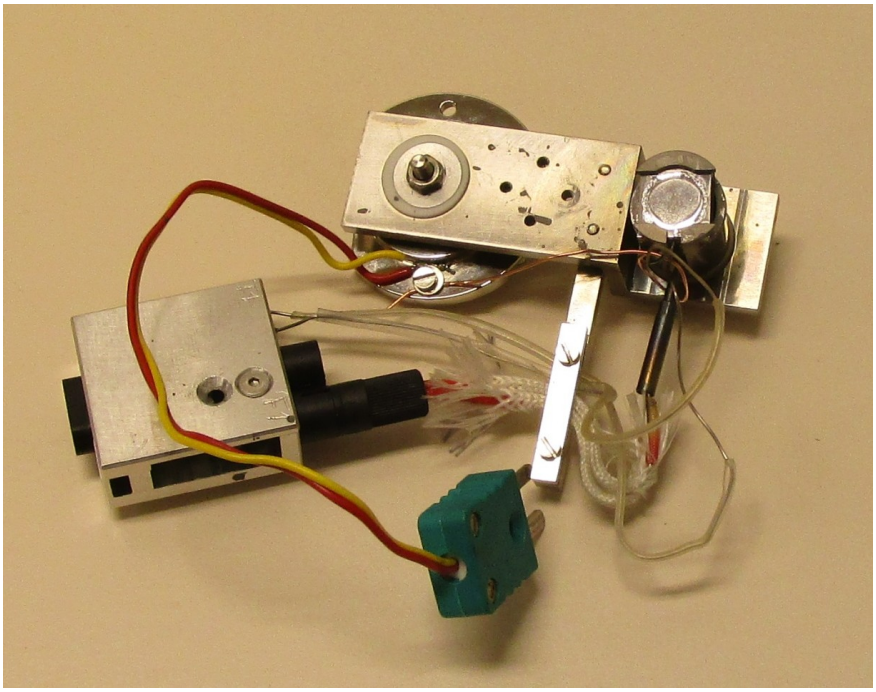

**Figure 3.6: The in situ hot stage with all connections ready to mount in the sample chamber.**

### 3.6.1 In Situ Hot Stage - Refinement and Use

The stage developed by Enstad was used during the experiments [37, 38]. However, a few minor changes were done to improve the design and use of the original stage. Part of the master's thesis was therefore to revise and change the original manuals from Enstad. The complete, new manual for the in situ hot stage can be examined in Appendix B.

When assembling the hot stage it was first discovered that the chord anchorage, installed to hold both the furnace and thermocouples in place, was not as effective as is could be. The chord anchorage consist of two screws, a flat short beam and a longer beam connected to the rest of the stage as seen in Figure 3.7 from two different angles. After fastening the screws the chord anchorage was supposed to hold the thermocouples and the furnace firmly in place, but because of difficulties doing this further examinations revealed a design flaw. There were internal screw threads in the holes for both the top and bottom beam, and trying to faster these two together will not be advantageous. By removing the screw threads in the top beam the chord anchorage could be fastened to a much larger extent, and both furnace and especially the thermocouples were more secure during the experiments.

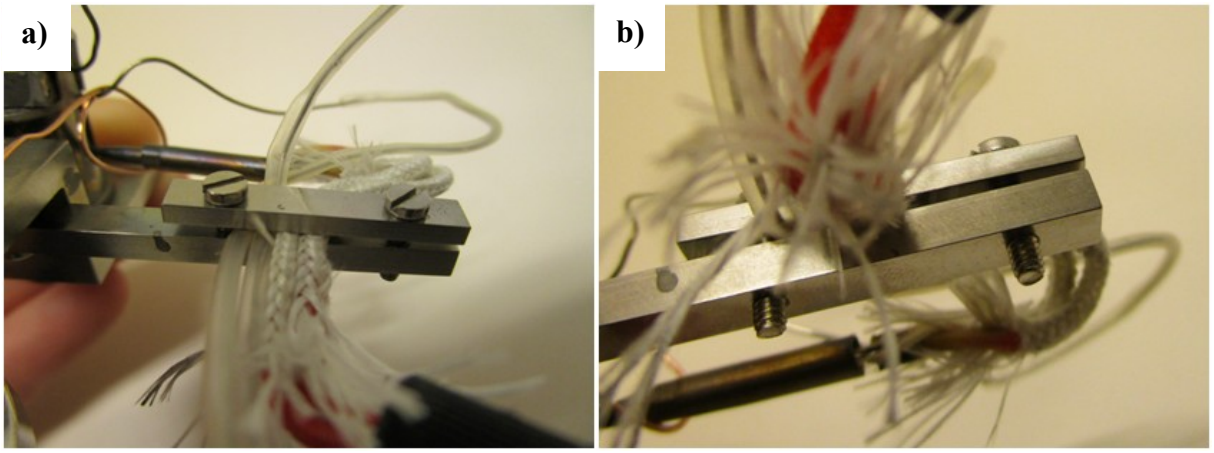


**Figure 3.7: The chord anchorage seen from the a) top and b) bottom. The long beam is connected to the rest of the stage.**

Enstad also discovered that to use a vacuum compatible platinum paint (SPI CHEM platinum paint) to reduce the temperature difference between the furnace and the sample could make it possible for the sample to almost reach the maximum furnace temperature of 800°C. The interface between the sample and the furnace should be wetted by the paint to achieve a better thermal contact. However, after many times use the paint was only placed on a lot of older paint, and was thus absorbed before the sample could be mounted. For the paint to have any effect it was placed on the back side of the sample before mounting. Also, the furnace was wetted with solvent to try to remove some of the old paint, and also gently scraped. However,

as the temperature of the sample did not need to reach 800°C in the experiments because of the low transformation temperatures during slow heating, the effect of the paint was not as important as it would have been on higher temperatures.

When the hot stage and sample was first mounted inside the SEM, the secondary electron picture visibly moved downwards, and this large drift in the image is an indication of charging. Further examination revealed that both furnace, furnace holder, and thus the sample itself, were completely isolated. This resulted in charging because the electrons were not diverted from the sample. To avoid this a copper wire was placed as presented in Figure 3.8, going from the furnace and/or thermocouple to the hot stage, which also was grounded.

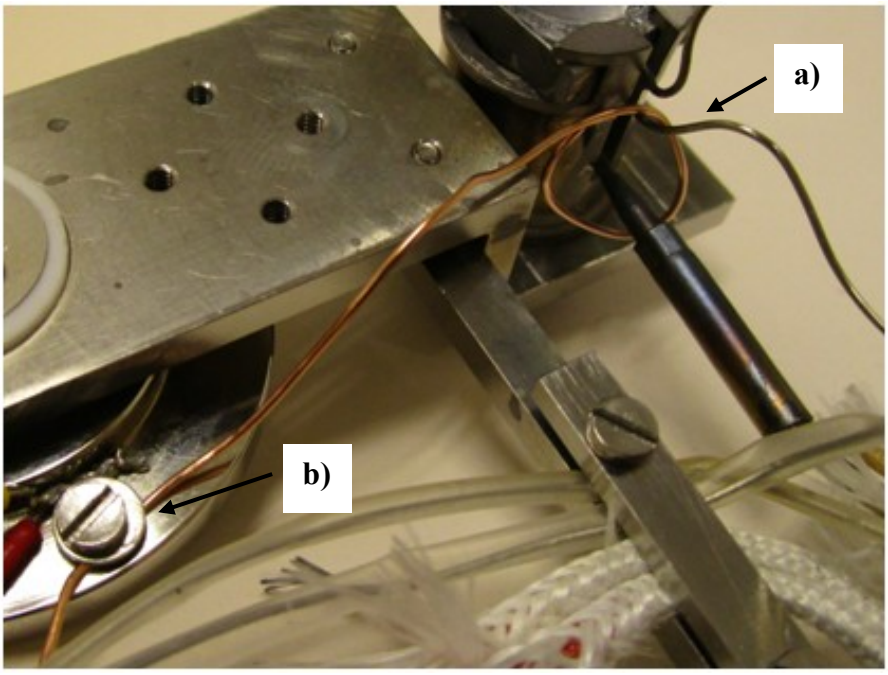


**Figure 3.8: Close-up of hot stage with copper wire touching a) the transition cable and the thermocouple from the furnace, leading electrons to the hot stage by b) fastening the wire beneath the screw. This is to avoid charging of the sample.**

The in situ hot stage, with these small refinements, was otherwise assembled and installed as described in the now updated manual in Appendix B. Some further development suggestions are also described at the end of this appendix.

### 3.6.2 In Situ EBSD

The improved user manual for the in situ software is presented in Appendix C, although it is not many differences from the original manual (which can be examined in Enstad's work [38]). The interface of the program is presented in Figure 3.10.

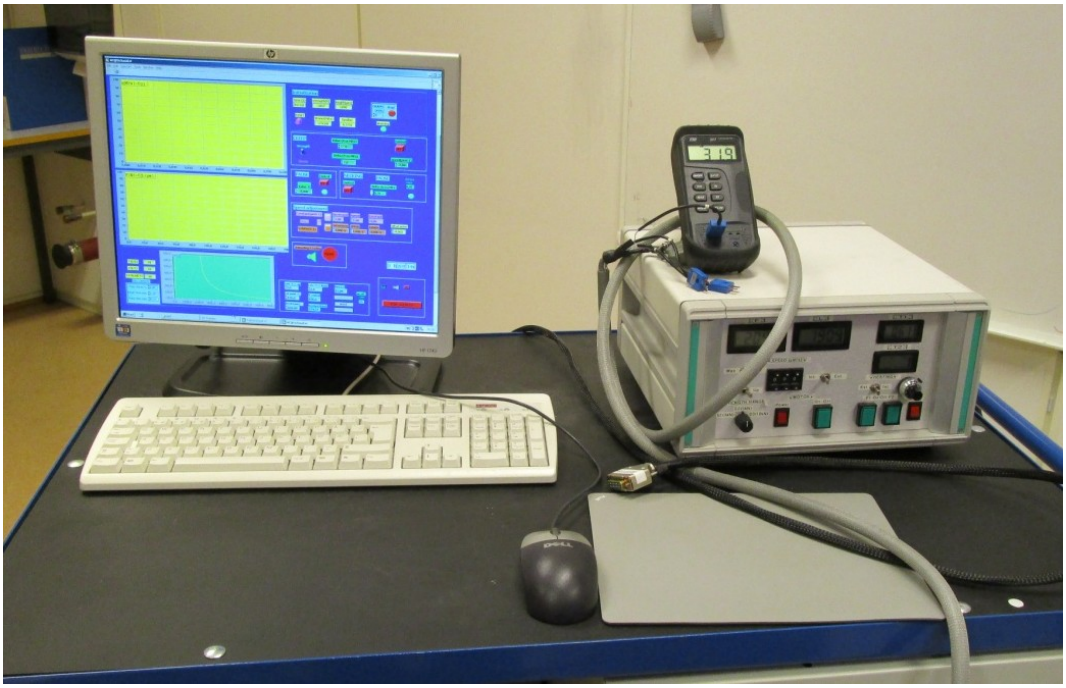

**Figure 3.9: To the left is the computer with the software opened, and to the right the stage controller with an extra temperature logger for overlooking the hot stage temperature placed on top.**


**Figure 3.10: The interface of the software, with three marked temperatures in two red rectangles.**

The actual temperature of the furnace was recorded by the thermocouple marked *T1* in the program and the temperature of the sample was recorded as *T2*. The *set point °C* temperature

gave what the furnace temperature heat up to, and afterwards be stable at. During the in situ experiments the temperature of the sample did not quite reach the temperature of the furnace. This, in combination with the fact that the previous user manual stated that the controller was calibrated, for the furnace, 85-90°C too high, made it difficult to choose a set temperature for the furnace and at the same time knowing what temperature the sample would reach. The amount of SPI paint together with how much old paint it was possible to remove affected the heat transfer between the furnace and the sample, and thus the temperature control.

Based on the minimum temperature difference of the set temperature and the sample temperature achieved during the first experiments (36°C) the set point of the following experiments was set only 30°C higher than the actual wanted temperature (to avoid overheating) in the beginning of the experiment. After the sample had reached a stable temperature, or when the actual heating rate slowed considerably down, the set temperature of the furnace was increased carefully until the desired temperature of the sample was achieved. This did not take much extra time; however, the heating rate at the highest temperatures was thus not stable.

For an overview of the sample settings please look in Table 3.8. A scan was taken before start, and then 10 minutes after the T2 temperature was stable to avoid drift in the EBSD-scan. The sample reached a stable temperature around 3 minutes after the furnace (T1) was stable at the set temperature. Each scan, with the NORDIF settings presented in Table 3.6, lasted 6 minutes. The next scan was then started as quickly as possible, making the time difference between starting two scans 8-9 minutes. The temperature of the stage was carefully watched, as more scans could be taken if this did not reach the critical temperature of 47°C (this temperature is set to prevent damage on the microscope). One scan was also recorded after the sample had cooled down. The EBSD detector was retracted 5 mm from the original position during the in situ experiments to protect the phosphor screen.

**Table 3.8: In situ heating settings with notes about the experiments.**

| Sample | Set temperature [°*C*] | Heating rate [°*C/s*] | Time at stable temperature [*minutes*] | Notes |
|---|---|---|---|---|
| 8A | 730 | 1 | 34 | - |
| 8C | 680 | 1 | 42 | - |
| 9A | 710 | 1 | 41 | - |
| 9B* | 715 | 1 | 32 | Heated twice to the same T2 temperature. |
| 10A* | 670 | 1 | 31 | - |
| 10B* | 680 | 1 | 32 | - |
| 10C | 770 | 1 | 33 | The two thermocouples were swapped, making the actual temperature of the sample the T1 temperature. |
| 11A* | 720 | 1 | 35 | First heated to 350°C (T2) for 15 minutes. |
| 11B* | 486 | 1 | 32 | The thermocouple in the furnace had almost fallen out, so it did not show the temperature inside the furnace, but rather at the surface. Was stopped based on T2 temperature. |
| 11C* | 733 | 1 | 31 | - |
| 12A* | 696 | 5 | 31 | The furnace tried to heat faster, at this rate, but the sample heating rate was slower. |
| 12C* | 650 | 1 | 41 | First heated to 500°C (T2) for 15 minutes. |

* Better resolution during the first scan (at room temperature), thus the acquisition time was longer than during the in situ scans.

One sample (12B) was investigated with a different approach; the temperature increased stepwise. One scan was recorded for each temperature during the heating, and at the maximum temperature of 605°C only two scans were recorded due to the temperature of the stage reaching the critical temperature of 47°C. These scans also followed the NORDIF settings in Table 3.6. The steps were as presented in Figure 3.11: 100 - 200 - 300 - 400 - 500 - 550 - 605°C.

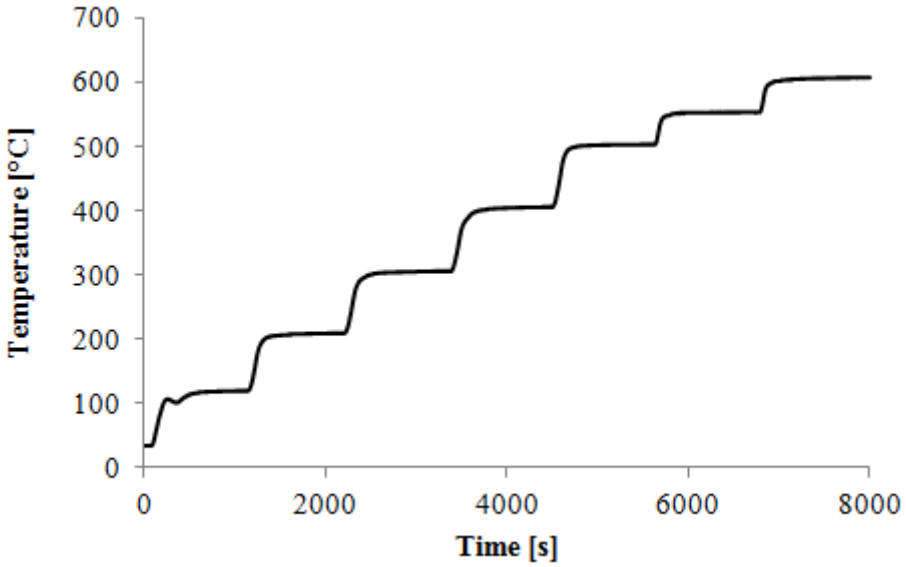


**Figure 3.11: The heating curve for the stepwise heating. One scan was recorded on each step, and on the maximum temperature of 605°C two scans was recorded before cooling (not presented in the figure).**

## 3.7 Light Optical Microscopy

All the samples were examined with a Leica MEF4M light microscope with software ProgRes Capture Pro 2.8.8. The samples were prepared for light microscope by the steps:

1. Grinding with water as lubricant and SiC paper with increasing fineness: 320, 500, 800, 1200 and 2000.
2. Diamond Polish with lubricant (ethanol based): 3 and 1 μm.
3. Etching with Marble etch (based on $CuSO_4$, hydrochloric acid and water) for 7 seconds.
4. Cleaning with acetone.

Two samples, one after the ex situ weld simulation and the sample heated in situ to 590°C (12C) was investigated with light optical microscopy.

# Chapter 4 Results

## 4.1 Weld Simulation and Dilatometer Results

During the weld simulation of the five original rods the temperature reached a peak temperature of 1357±1°C and had sufficiently large cooling rate in the relevant area to obtain a coarse grained martensitic microstructure. When defining $Ac_1$ and $Ac_3$ as the temperatures where the expansion slopes with regards to the temperature start to change and get stable again, these temperatures can be located at approximately 660°C and 780°C. This is presented in Figure 4.1, where only the relevant part of the dilatometic curve is investigated. The heating rate was 110°C/s.

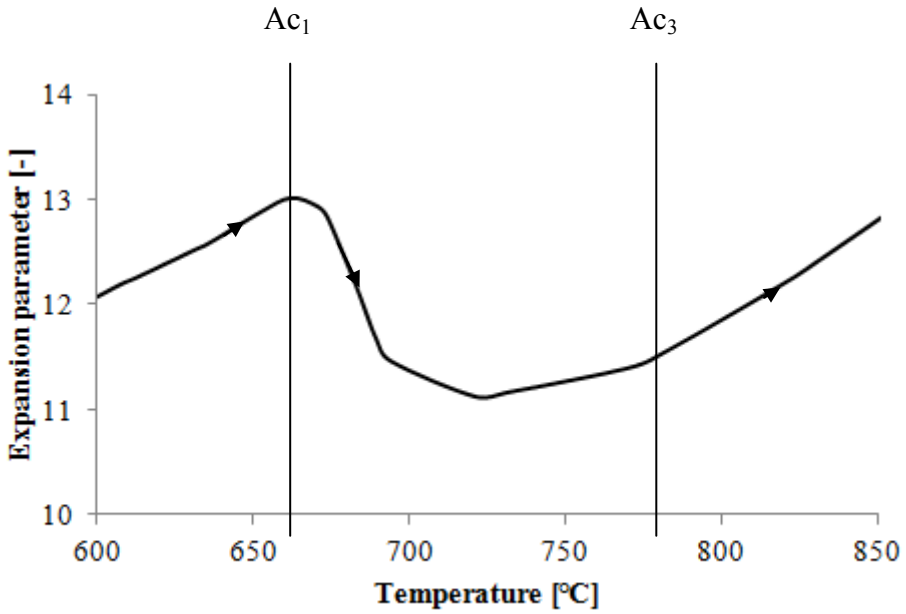


**Figure 4.1: The relevant area of the dilatometric curve during the weld simulation (110°C/s), with marked transformation temperatures $Ac_1$ and $Ac_3$ at 660°C and 780°C respectively.**

## 4.2 Temperature Investigations

During the in situ heating experiment the temperatures of the sample and furnace temperature were logged and could be evaluated based on the input data. It is observed an irregular temperature difference between the furnace and sample temperature. The heating rates were also investigated based on the raw data from the controller. It could also be observed a temperature dependence on the secondary electron image and the quality of the patterns.

### 4.2.1 Difference in Furnace and Sample Temperature

Presuming that the temperatures recorded by the software is correct, the sample temperature was always 35-85°C lower than the furnace temperature at the stable maximum temperature. This is presented in Table 4.1 for all samples but two; during the experiment with 11B the furnace thermocouple did not record the temperature inside the furnace but the surface of the furnace instead, and 12B which was heated in steps. The furnace temperature can be observed to be higher than the sample temperature at all times during the experiment presented in Figure 4.2, and the furnace stabilizes 43°C above the sample temperature of 635°C.

**Table 4.1: The difference of the sample and the furnace temperature as recorded by the software at the stable maximum temperature.**

| Temperature measured in sample [°C] | Sample | Temperature difference sample and furnace [°C] |
|---|---|---|
| 590 | 12C | 60 |
| 605 | 8C | 75 |
| 615 | 11B | - |
| 625 | 9A | 85 |
| 635 | 10B | 43 |
| 635 | 12A | 61 |
| 640 | 10A | 35 |
| 645 | 9B | 75 |
| 645 | 9B (second heating) | 70 |
| 670 | 11C | 63 |
| 670 | 11A | 50 |
| 690 | 8A | 38 |
| 770 | 10C | 36* |

* The thermocouples for the furnace and sample were interchanged.

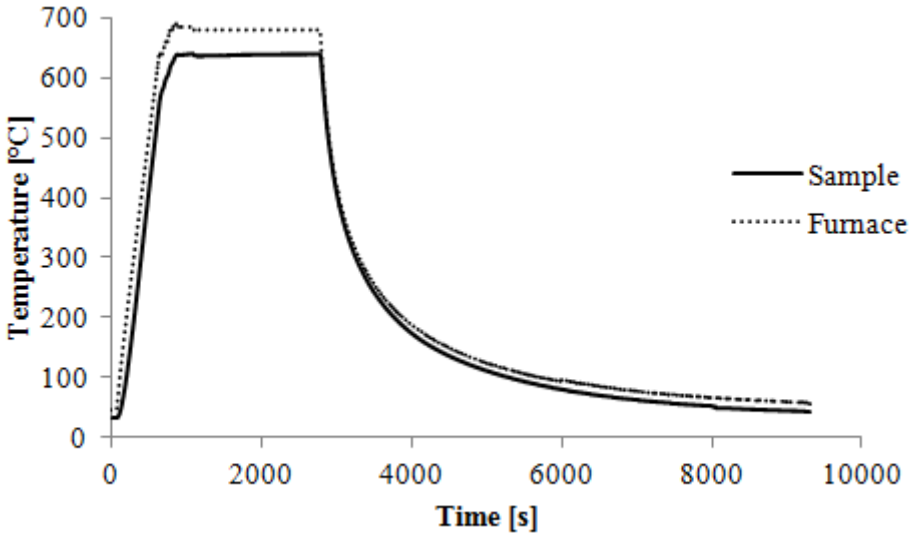


**Figure 4.2: An example of a temperature curve during the in situ heating experiment of sample 10B heated to 635°C. During heating the furnace temperature is higher than the sample temperature, and at the stable holding temperature the temperature difference is 43°C.**

### 4.2.2 Temperature and Heating Rate Investigations

The experiments without an intermediate holding temperature (step) during heating exhibited a temperature development of the sample temperature as the black graph in Figure 4.3. The heating rate development was dependent on the settings presented in Table 3.8. A heating rate setting of 1°C/s resulted in an actual heating rate of 1.1-1.2°C/s for a period of time, as seen in the grey graph in Figure 4.3. When the heating rate was faster, e.g. 5°C/s the heating rate was not stable at any point during the heating, with a fast increase to 6°C/s before a fast decrease to 0. Other examples of temperatures and heating rates are presented in Appendix D.

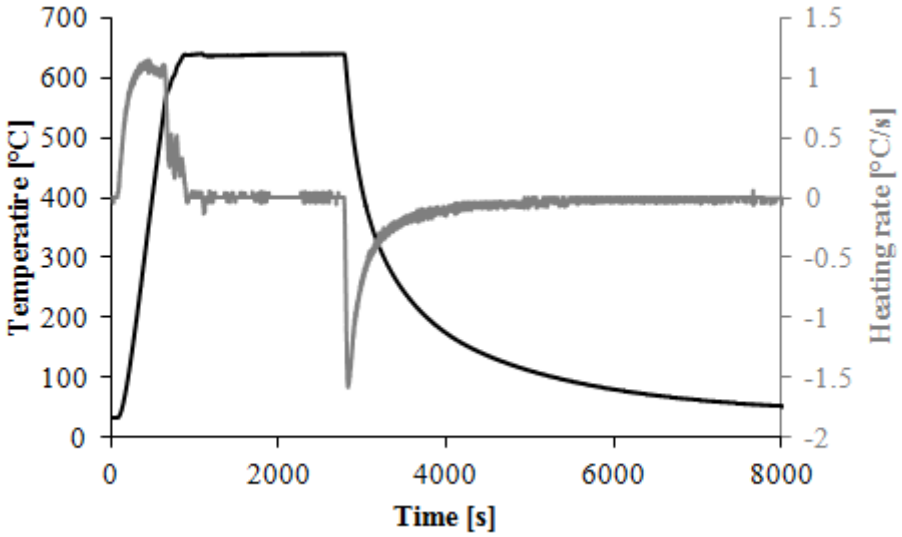


**Figure 4.3: The temperature development (black graph) and the heating rate (grey graph) during the in situ heating experiment of sample 10B to 635°C. Most of the samples had a similar development as this experiment.**

### 4.2.3 Glowing and Temperature Effect on Image and Patterns

During the experiments a very sudden brightness change was detected in the secondary electron image when the sample reached 570°C. By tuning brightness and contrast the secondary electron image was much clearer than at lower temperatures, and investigating the stage and sample revealed that the sample was glowing. This is observed in Figure 4.4a, where the sample temperature was 590°C. The glowing resulted in much better patterns and image, and contamination from both preparation and previous scans disappeared. The effect on the secondary electron image recorded in NORDIF for the sample heated stepwise is presented in Figure 4.6, with a large difference can be observed after the sample has reached the glowing temperature. The effect on the patterns is better to observe using the NORDIF built-in function of automatic contrast; however, it can still be identified on the acquisition patterns before and after glowing in Figure 4.5. The improved quality of the patterns was usually maintained after cooling.

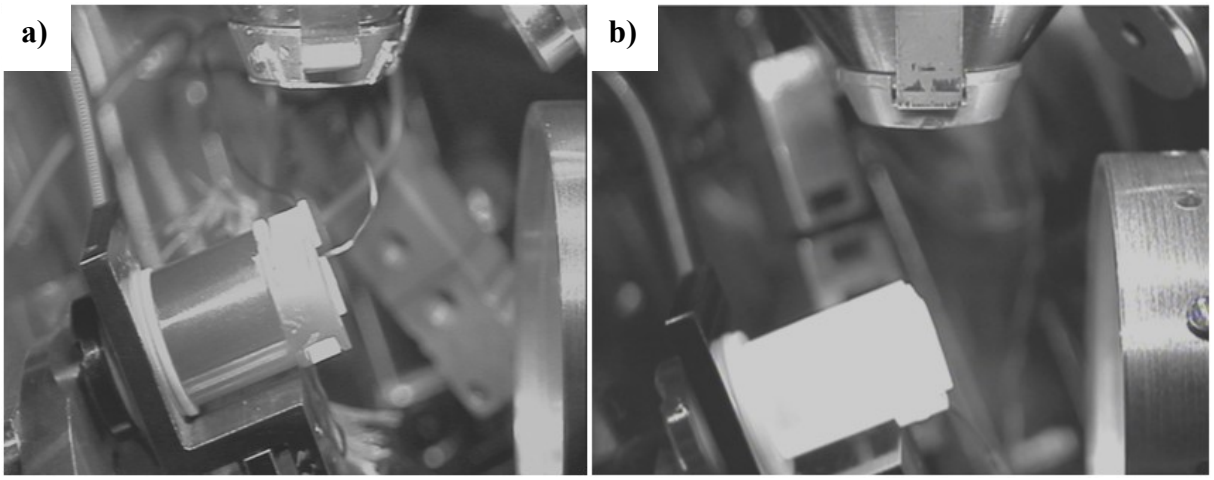


**Figure 4.4: Glowing at a) 590°C with only the sample glowing and b) at approximately 760°C from previous experiments [38] where both sample holder and sample is glowing.**

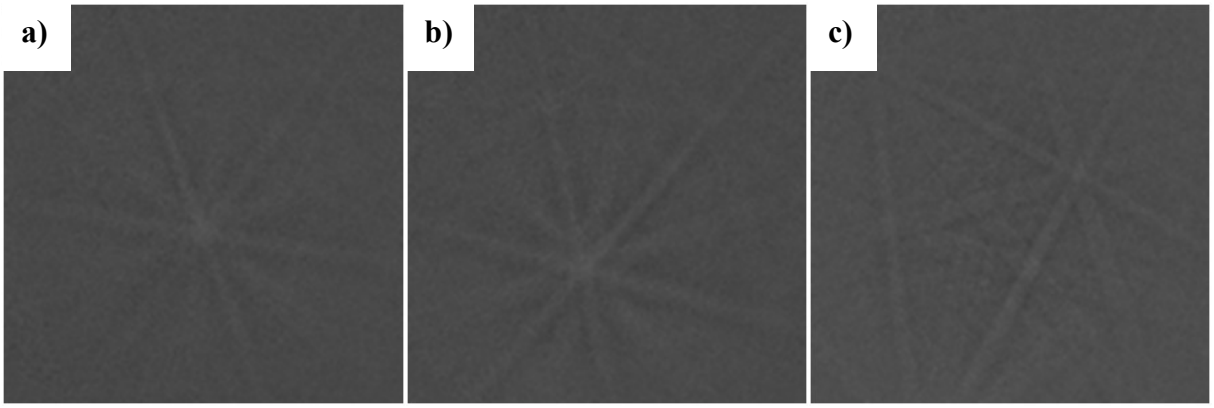


**Figure 4.5: Appearance of acquisition patterns a) before glowing (550°C) and b) just after glowing starts (600°C) and c) example of acquisition pattern after recrystallization (770°C). The effect of glowing on the patterns is even easier to see using automatic contrast in the NORDIF software as well.**

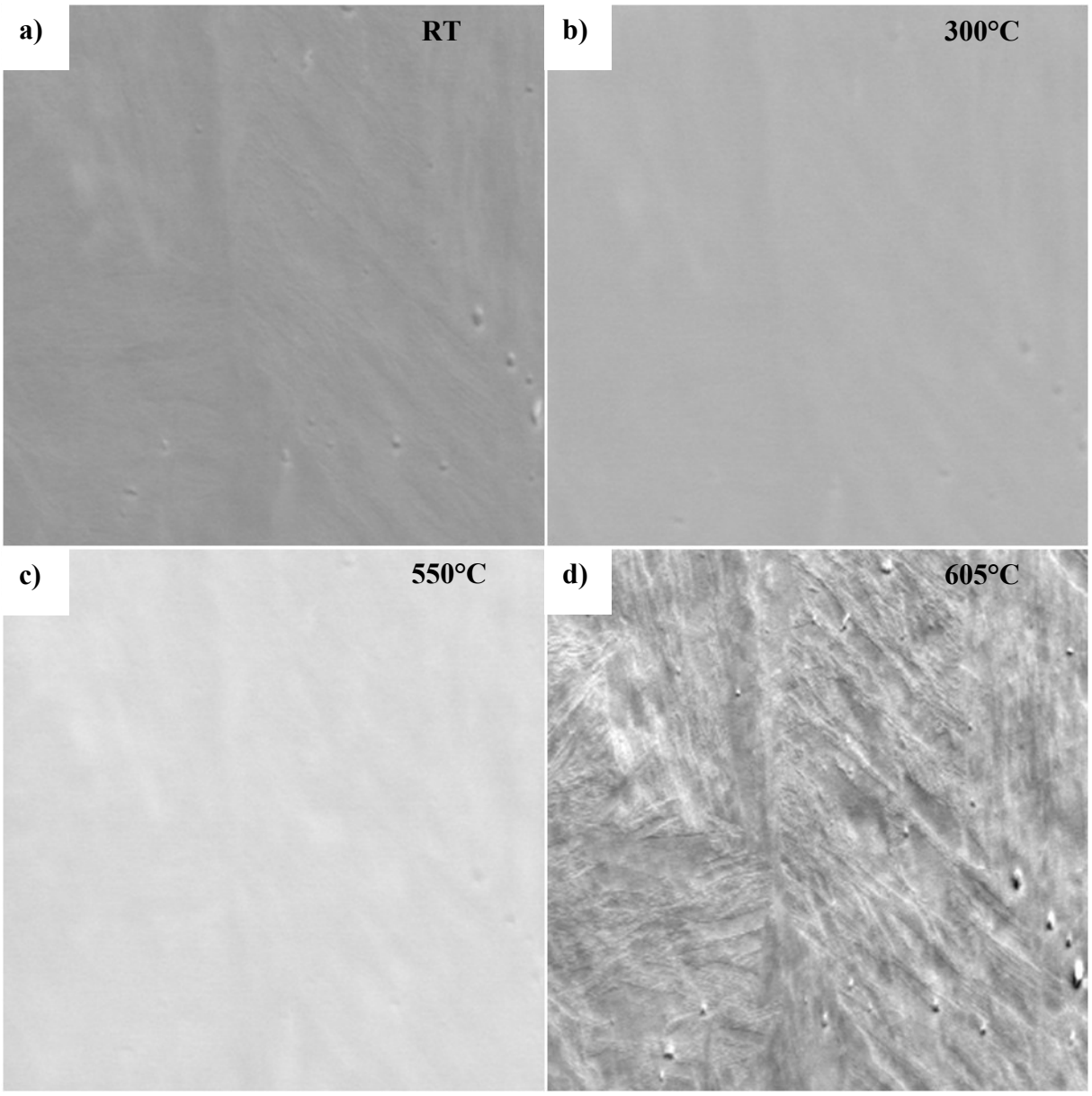


**Figure 4.6: The secondary electron image recorded by NORDIF of the stepwise heating experiment of sample 12B at different temperatures. There is a pronounced difference after the sample begins to glow at approximately 570°C. a) Before heating, b) 300°C, c) 550°C and d) 605°C.**

## 4.3 Microstructure and Grain Size After First Weld Simulation

The coarse grains obtained at the peak temperature during the ex situ weld cycle have many different sizes, and the previous grains are easy to observe in Figure 4.7 (scan cleaned with grain dilation, an iterative cleaning method to include all pixels in grains). Several of the coarse grains are larger than the scale bar of 100 μm, thus obtaining 75x75 $\mu m^2$ scans during the in situ experiments might result in an area with a clear previous grain boundary, as presented in Figure 4.8a, or in the middle of a grain which can be observed in Figure 4.8b. Because of the fast cooling in the intercritical temperature region and the low carbon content the resulting microstructure is lath martensite, also observable in the following figures.

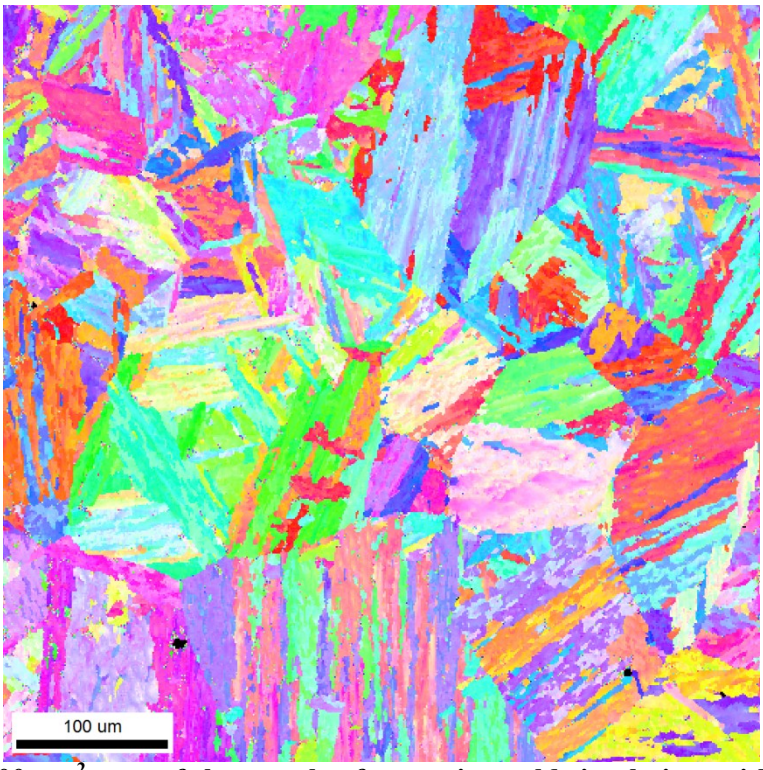


**Figure 4.7: 500x500 µm$^2$ scan of the sample after ex situ weld simulation, with clean-up chosen to best display the size of the coarse grains.**

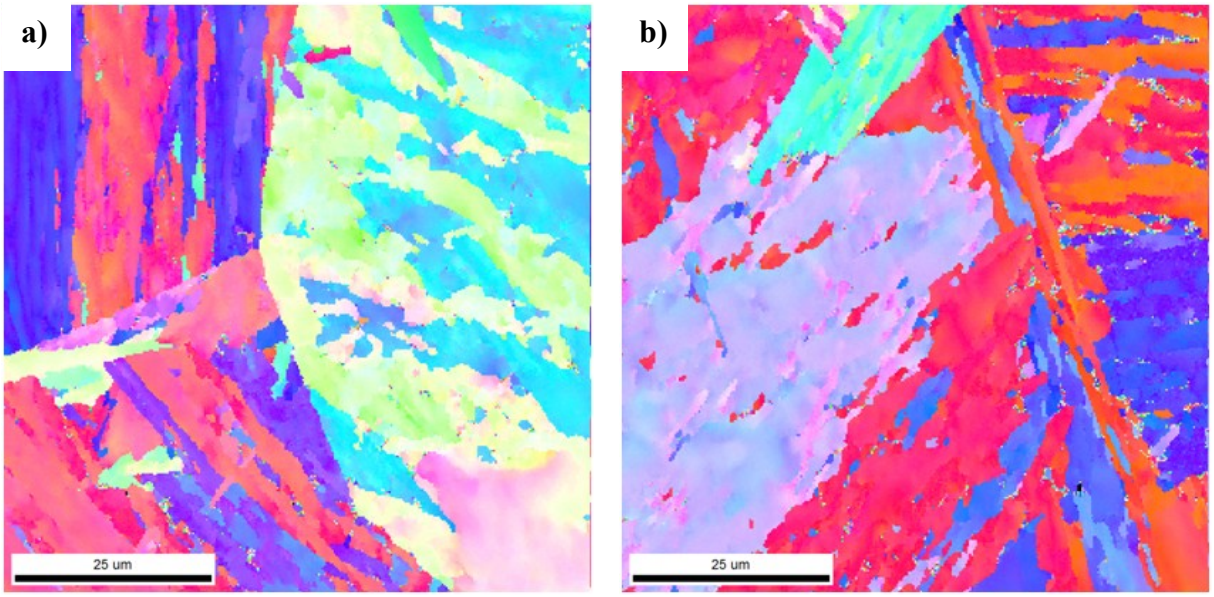


**Figure 4.8: Two examples of 75x75 µm$^2$ scans after clean-up, a) with three clear grains and a triple junction, and b) in the middle of a coarse grain.**

The austenite amount detected in the EBSD scans is between 0.8 and 1.5% after the ex situ weld simulation of the reference sample (weld simulated to obtain a coarse grained microstructure).

## 4.4 Austenite Evolution during and after In Situ Heating

The austenite evolution during and after in situ heating was investigated using EBSD. Table 4.2 presents the quantification data for each of the samples except three (8A, 10C and 12B). The exact times for each scan are elaborated further for each of the samples presented in the different subsections or with the rest of the results presented in Appendix E. The quantification in Table 4.2 show several important trends concerning the quantification of austenite during in situ heating and the stability of the formed austenite. For the sample heated to 590°C all the austenite formed is stable after cooling. Approximately identical austenite development is observed for all the samples heated in the temperature interval 605-635°C, but there is a difference concerning the stability after cooling occurring at 620°C. In this temperature region the stability was lower than for the sample heated to 590°C. For the samples heated above 640°C the amount austenite increased further and very little is stable at room temperature. The EBSD results reveal that partial recrystallization occurred in this temperature interval. The two samples heated to 700°C and higher transformed completely to austenite at the maximum temperature, and is not presented in Table 4.2.

**Table 4.2: The amount of austenite for the samples heated in the temperature interval 590-670°C during the stable holding temperature. The time indicates how long after the maximum temperature was reached the scan started.**

| | | Time interval for start of scan [*minutes*] | | | | | |
|---|---|---|---|---|---|---|---|
| | | **Before heating** | **10** | **17-20** | **25-29** | **35-36** | **After cooling*** |
| **T [°C]** | **Sample** | **Amount austenite [%]** | | | | | |
| 590 | 12C | 1.3 | 3.6 | 6.2 | 7.9 | 10.5 | 11.5 |
| 605 | 8C | 3.0 | 9.9 | 15.7 | 19.0 | 22.5 | 11.7 |
| 615 | 11B | 1.7 | 9.3 | 15.3 | 19.6 | | 11.0 |
| 625 | 9A | 4.5 | 8.6 | 16.4 | 20.0 | 22.6 | 4.9 |
| 635 | 10B | 1.4 | 8.5 | 13.3 | 17.5 | | 3.0 |
| 635 | 12A | 1.0 | 13.0 | 19.7 | 23.9 | | 2.8 |
| 640 | 10A | 1.2 | 25.5 | 32.0 | 36.8 | | 2.9 |
| 645 | 9B | 2.0 | 48.6 | 56.2 | 62.8 | | 2.2 |
| 670 | 11C | 0.9 | 69.4 | 77.0 | 81.1 | | 3.5 |
| 670 | 11A | 1.1 | 57.3 | 63.4 | 68.7 | | 0.8 |

* Recorded at approximately 50°C.

Drift can be observed in the EBSD-scans caused by the thermal expansion at the higher temperatures, although it gets more stable after a longer time. This should be taken in consideration when evaluating the results in Table 4.2.

The fractions presented in Table 4.2 are not from the original 75x75 $\mu m^2$ scans, because they were cropped to 60x60 $\mu m^2$ to remove bad points caused by reference points in the corner of the original scan (e.g. some dirt or dust to navigate around). The amount of austenite varied with ±1% from the original scan to the cropped scan in the areas where there was a uniform distribution of austenite. The variation was higher in the cases with recrystallization and non-uniform distribution of austenite. The EBSD results originating from the in situ experiments are all from the cropped area, but the areas evaluated after storage are 75x75 $\mu m^2$ unless specified otherwise.

### 4.4.1 590°C

Sample 12C was heated in situ to 590°C and quantification of austenite was done during in situ heating and after storage at room temperature. The extensive investigations done at room temperature made it possible to observe a variation of quantity caused by the original coarse-grained microstructure, and whether this variation was affected by grain size. How the step size affected the quantification was also investigated.

#### 4.4.1.1 Quantification of Austenite during In Situ Heating

Four consecutive scans were recorded during the time on the holding temperature, imaged in the IPF maps in Figure 4.9 and the phase maps in Figure 4.10. Note that the figures do not contain the data based on the third scan recorded at elevated temperature. The temperature varied with ±1°C at the maximum temperature. Further examination of the austenite phase formed during the in situ heating can be done by looking at the plotted inverse pole figure of the austenite phase. Based on the IPF in Figure 4.9f only one orientation of austenite is formed in this area (white). Because the austenite content does not decrease after cooling, the (001) pole figures during heating and after cooling are almost identical, as can be investigated in Figure 4.11. The quality of the scan, explored in Appendix F, indicates that the amount austenite before heating is negligible. The quality of the scan increased noticeably during and after heating.

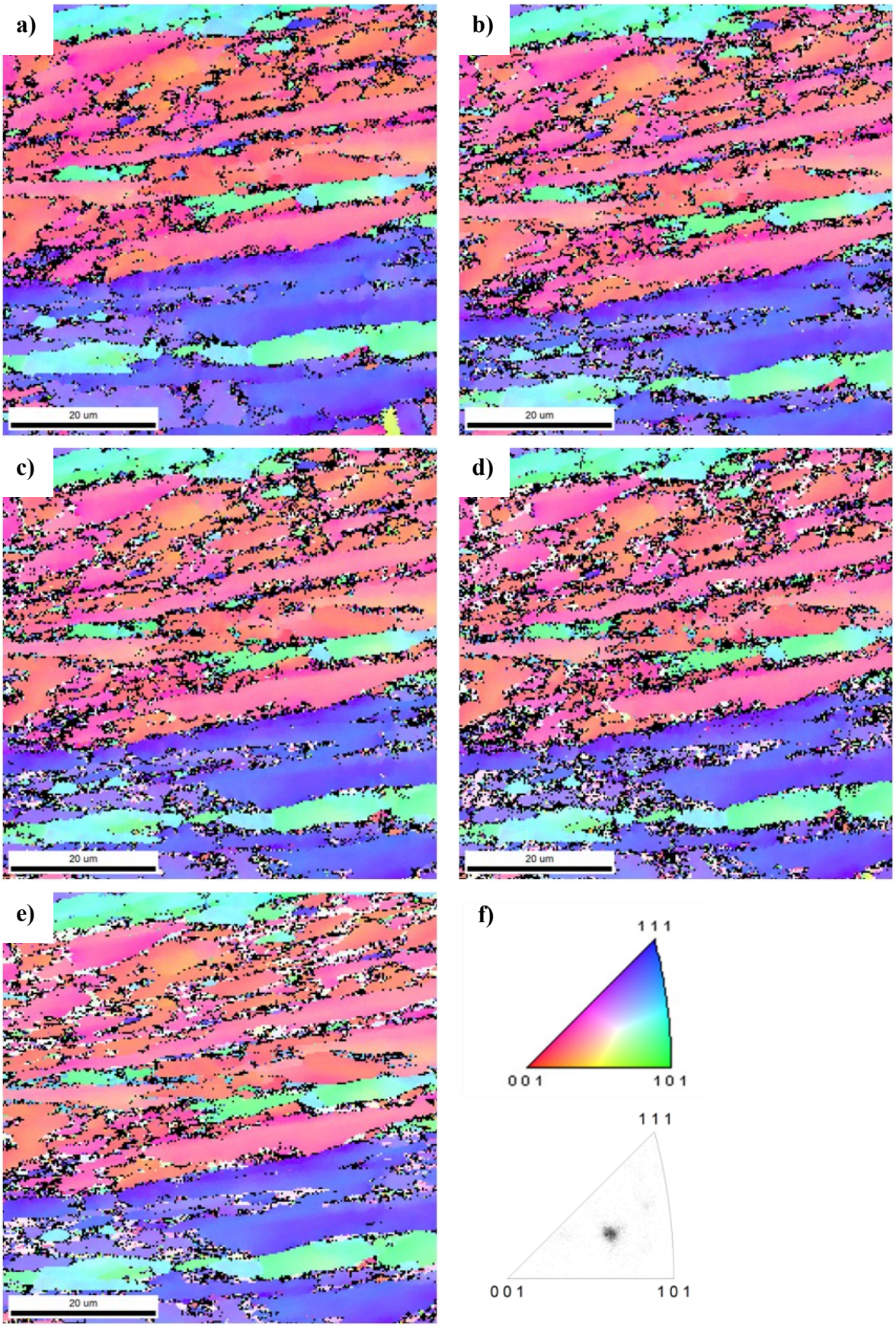


**Figure 4.9: IPF maps of the sample heated in situ with a heating rate of 1°C/s to 590°C a) before heating, after b) 10, c) 18 and d) 35 minutes, and e) after relatively slow cooling. f) The IPF for the austenite phase after 35 minutes.**

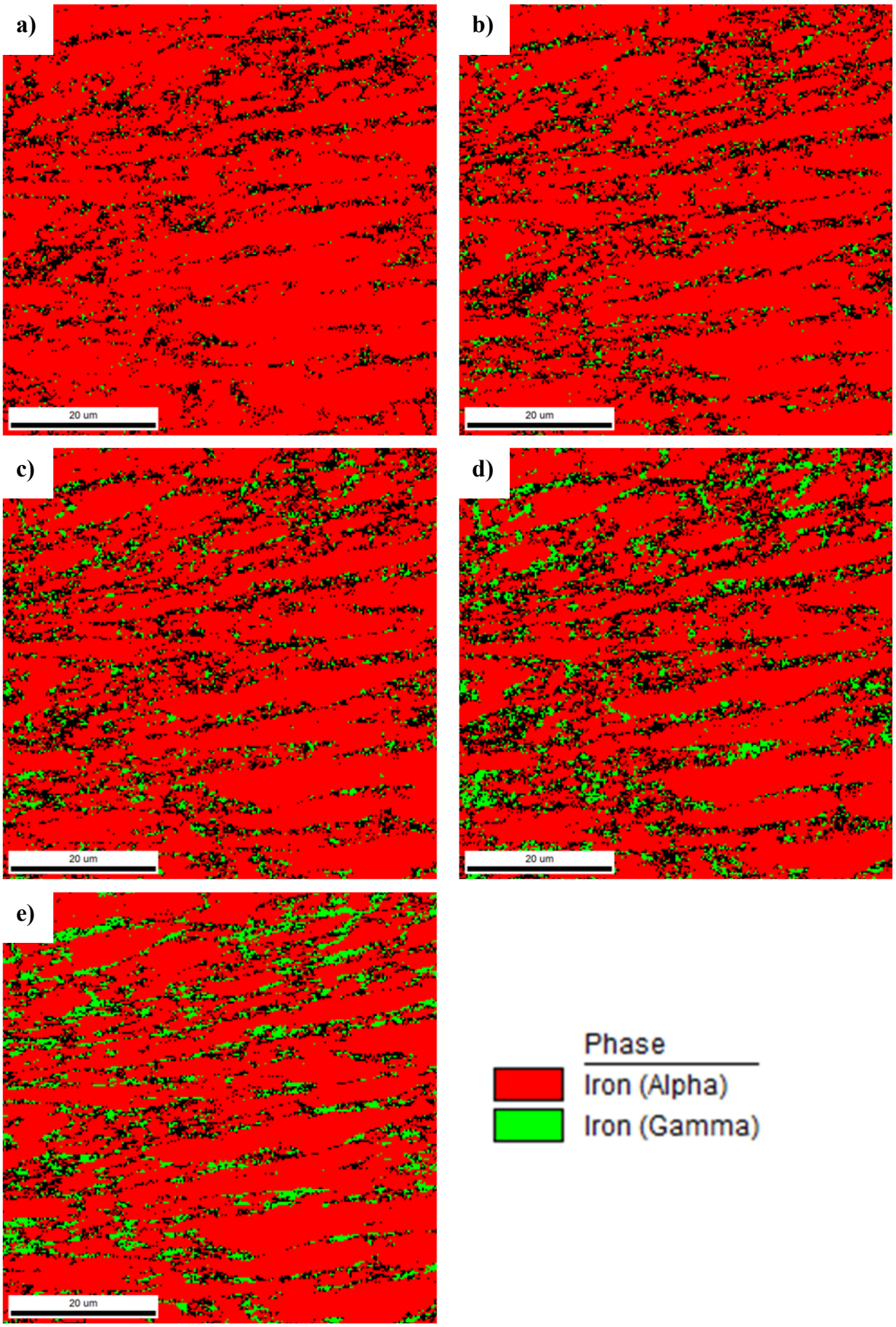


**Figure 4.10: Phase maps of the sample heated in situ with a heating rate of 1°C/s to 590°C a) before heating, after b) 10, c) 18 and d) 35 minutes, and e) after relatively slow cooling.**

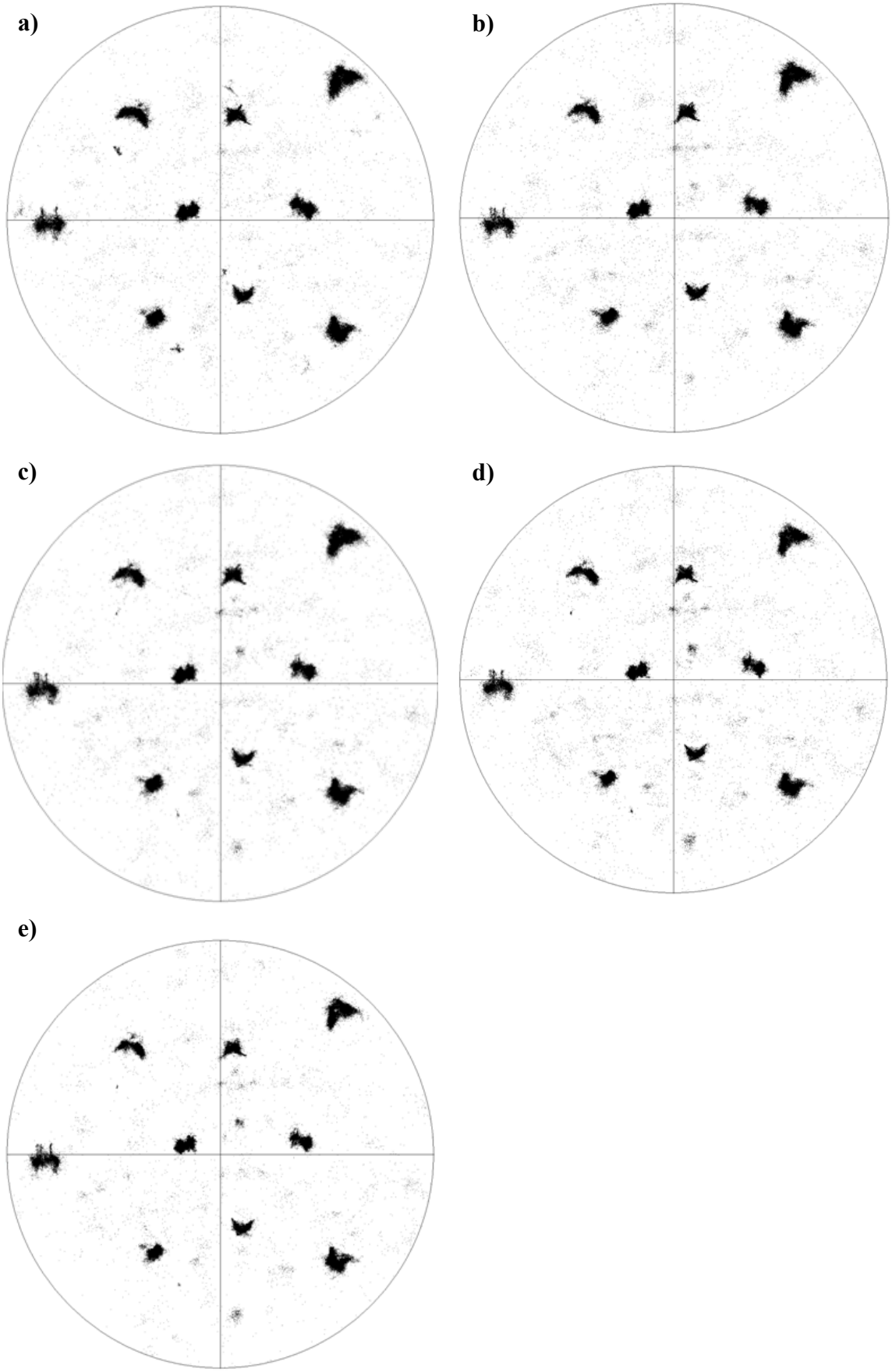


**Figure 4.11: (001) pole figures for the martensite phase of the sample heated in situ with a heating rate of 1°C/s to 590°C a) before heating, after b) 10, c) 18 and d) 35 minutes, and e) after relatively slow cooling**

#### 4.4.1.2 Quantification of Retained Austenite at Room Temperature

The sample was investigated further after storage at room temperature for several days. Numerous areas in the sample were investigated, revealing many local differences in austenite amount. Figure 4.12 presents two different areas with 3.6 and 13.7% retained austenite respectively (same step size as during the in situ experiments). The orientations of the austenite phase in these two figures can be observed to be very similar in the IPFs in Figure 4.13. Investigating other areas of the same size and magnification revealed austenite contents varying between the two amounts presented in Figure 4.12 (4-14%), with a variety of orientations depending on the area investigated.

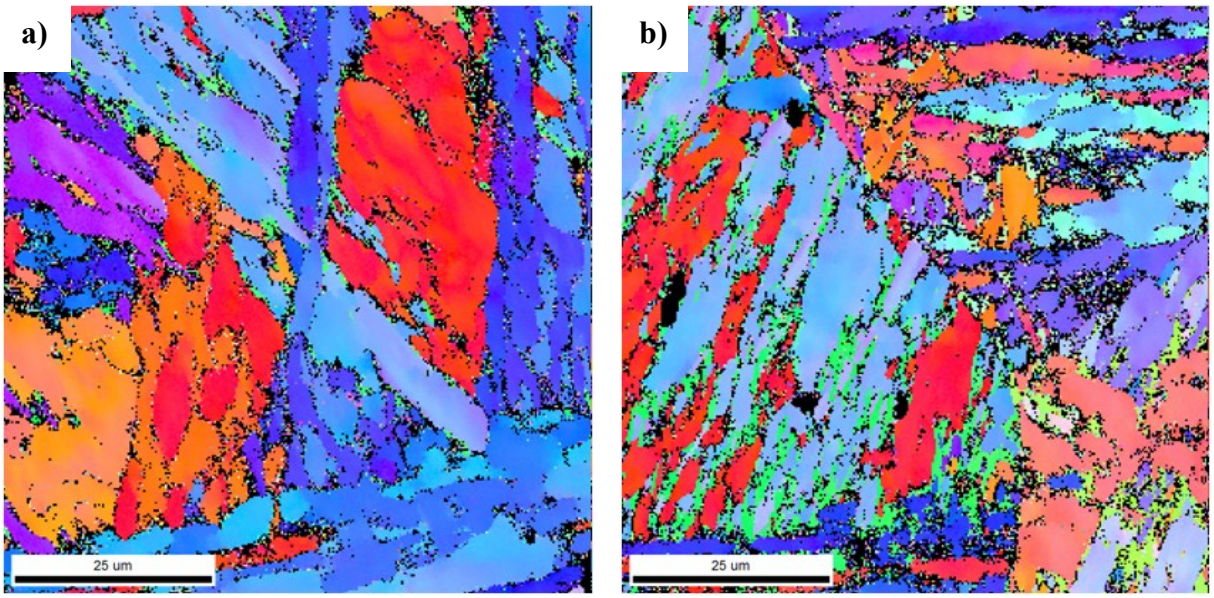


**Figure 4.12: Two IPF maps of different places in the sample heated in situ to 590°C after storage at room temperature. There is a large difference in the austenite amount, with a) 3.6% and b) 13.7%. The austenite looks to have approximately the same orientations.**

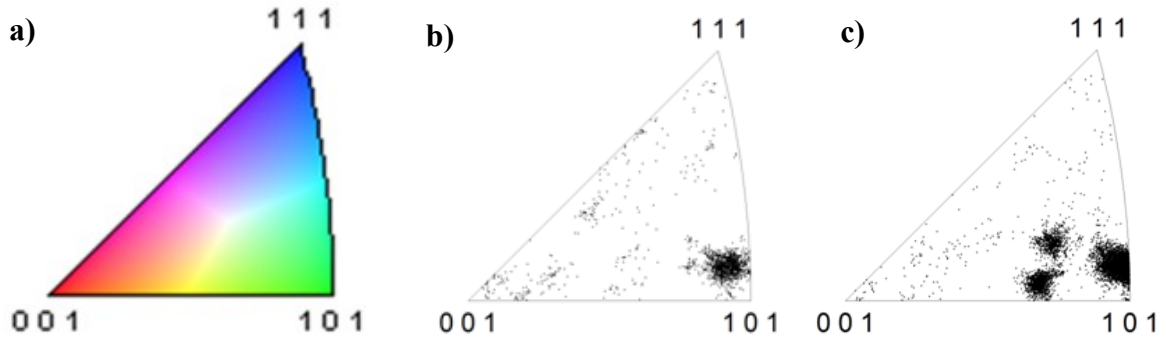


**Figure 4.13: The IPFs of the austenite in the two scans presented in Figure 4.12. a) The IPF colors, and the resulting IPFs of the sample with b) mostly one austenite orientation (Figure 4.12a), and c) several austenite orientations (Figure 4.12b).**

One example of a very interesting scan obtained with a smaller step size (0.15µm) is presented in Figure 4.14 (11.5% austenite). Figure 4.14c is an additional IPF map of only the austenite, to easier observe the grains and the colors matching the IPF. It seems like the orientation of the austenite depend on the prior austenite grains, which are easy to identify in this scan. The austenite present in the individual prior austenite grains, represented in Figure 4.14c with numbers 1-5 indicating the orientation of the austenite, is evaluated based on amount austenite in Table 4.3. Grain 2 contains the highest amount austenite.

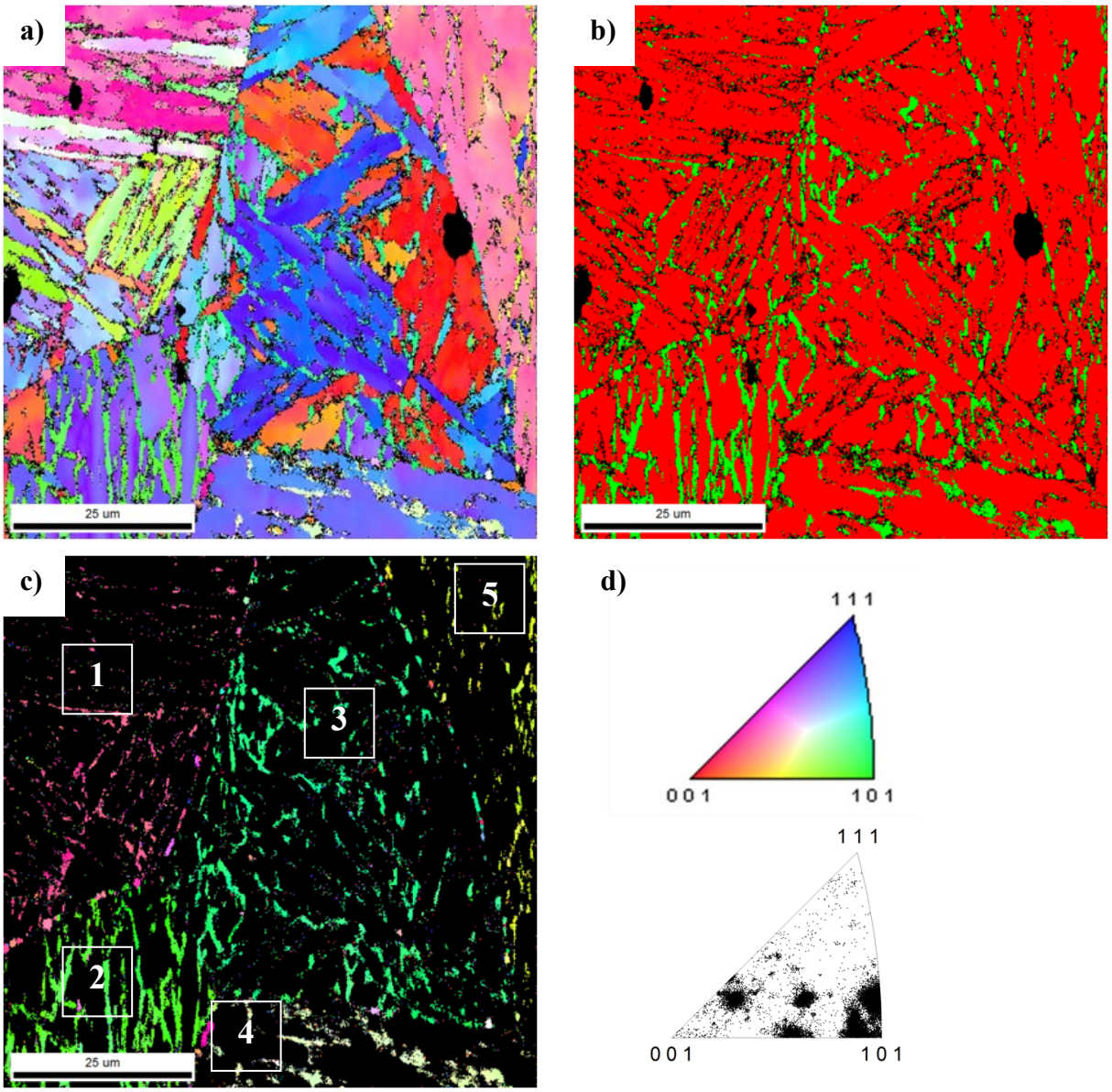


**Figure 4.14: a) IPF map of total area, b) phase map of total area, c) IPF map of only austenite, where the black is other phases (martensite), and d) the IPF for the austenite phase (11.5% austenite in total).**

**Table 4.3: Evaluation of the five austenite orientations present in the five different grains marked in Figure 4.14c. Note that the austenite present on the grain boundaries is not included.**

| Grain | Amount austenite [%] |
|---|---|
| 1 | 5.1 |
| 2 | 24.9 |
| 3 | 10.7 |
| 4 | 13.6 |
| 5 | 6.5 |

Inside one grain near all Kurdujmov-Sachs orientaition relationships can be observed in the experimental (001) pole figure in Figure 4.15 (obtained after rotation). The data originates from the pink oriented austenite in grain 1 in Figure 4.14.

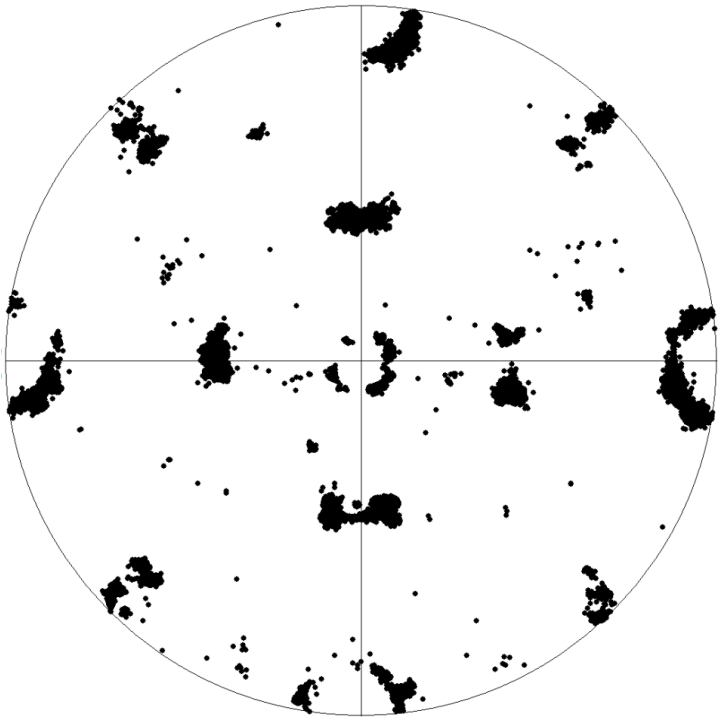

**Figure 4.15: The experimental (001) pole figure is very similar to the theoretical pole figure presented in Figure 2.25. It looks like all Kurdujmov-Sachs orientation relationships is present for one austenite orientation.**

#### 4.4.1.3 Effect of Prior Grain Size and Step Size

Whether or not the size of the original austenite grain have an effect on the amount retained austenite can be studied in Figure 4.16. This scan is of 250x250 $\mu m^2$ magnitude and obtained with a step size of 0.5 μm. Grain 1 is of unknown size and contains 1.7% retained austenite. Grain 2 looks almost complete, and with its two orientations (blue and pink) it contains 10.5%

retained austenite. The much larger grain 3 with turquoise oriented austenite contains 13.2% retained austenite.

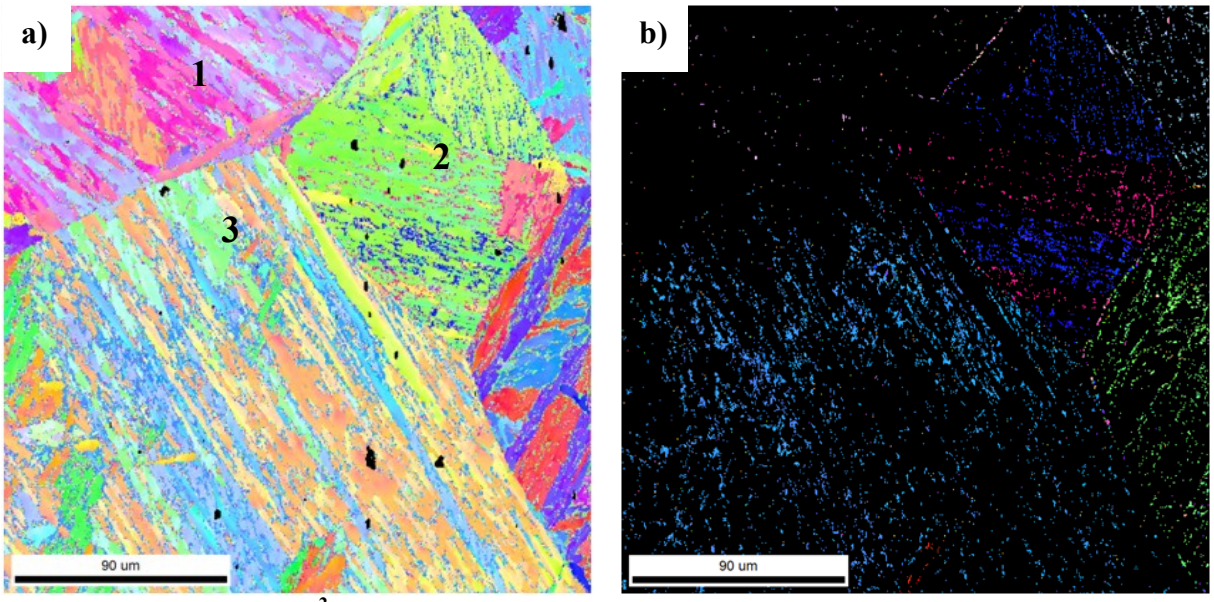


**Figure 4.16: 250x205 µm$^2$ IPF map in the sample heated in situ to 590°C after storage at room temperature. a) The whole area with no removed points and three marked grains, and b) only the austenite phase.**

One area was investigated with both step size 0.08 and 0.25 µm for a magnification of 1000X. This is presented in Figure 4.17. The amount austenite increased from 15.7 to 17.4% with the smaller step size. This scan is in the middle of a coarse grain which contains a lot of austenite. The amount indexed points with CI≥0.050 increased from 78.8 to 85.6% with the smaller step size.

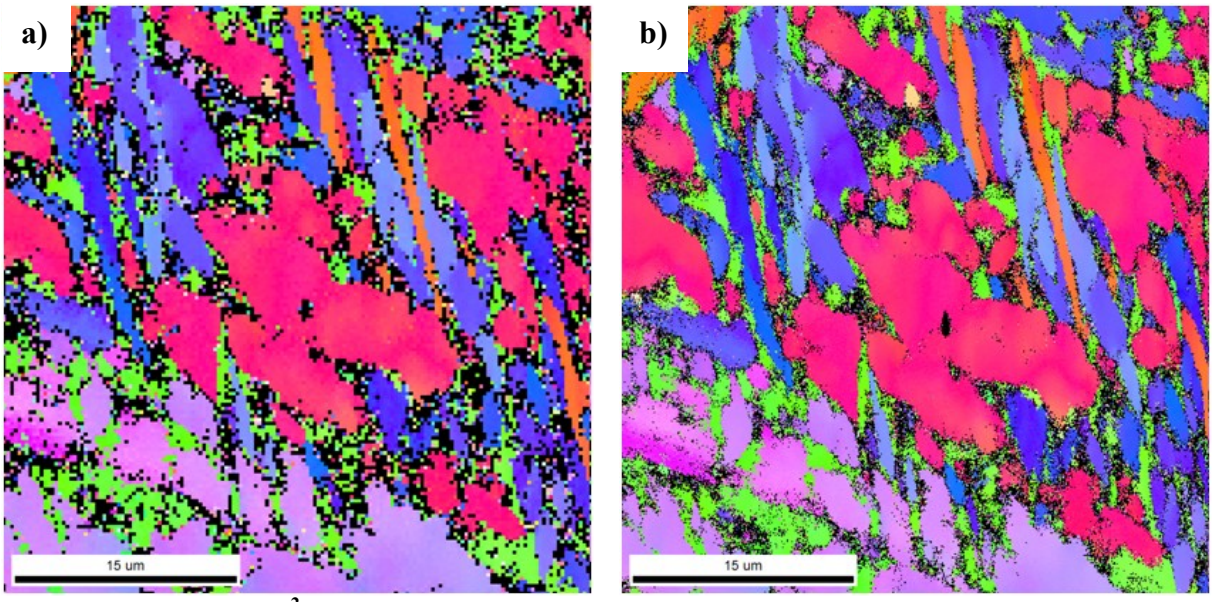


**Figure 4.17: 40x40 µm$^2$ area investigated with step size a) 0.25 µm and b) 0.08 µm. The larger step size give 15.7% austenite and the smaller 17.4%. Many of the points with low CI in a) are correctly indexed with the smaller step size.**

### 4.4.2 605-635°C

The austenite amounts presented in Table 4.2 indicate that the samples heated in the temperature interval 605-635°C all experienced approximately the same with regard to austenite formation during the in situ heating. A graphical representation of this is presented in Figure 4.18. Note that the fraction austenite during heating is almost identical for all but one of the samples, and that the amounts after cooling can be split in two depending on the holding temperature.

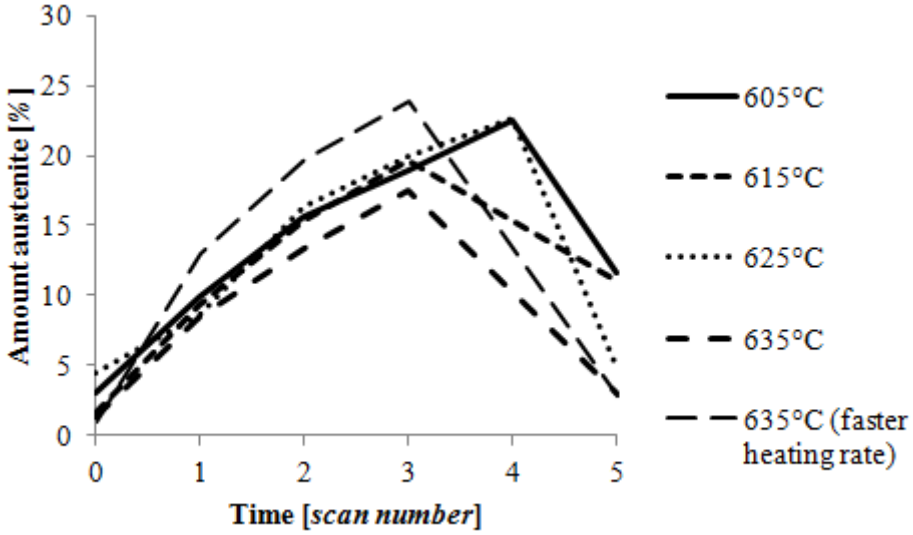


**Figure 4.18: The amount of austenite detected in each scan for the samples held at 605-635°C. There is a similar development in all experiments during heating, and at scan number 5 (after cooling) the amount is either 11% (for the lowest temperatures) or around 3% (for the highest temperatures). Note that only two of the scans have a value at scan 4, because one more scan was recorded during these experiments comparing to the other three.**

The sample heated to 605°C is presented in the following section as an example of the in situ experiments in this temperature interval. Because this scan contains two grains the difference between orientations can be examined during the in situ experiment, and nucleation at both prior austenite grain boundaries and lath boundaries can be investigated. The rest of the in situ scans can be examined in Appendix E, with the quality of the scans in Appendix F. The samples heated to 605, 625 and 635°C were also investigated for retained austenite after storage at room temperature, with a scan from 605°C presented as an example. Some interesting observations for the sample heated stepwise to 605° are presented at the end of this subsection.

#### 4.4.2.1 Quantification of Austenite during In Situ Heating

Sample 8C was heated in situ to 605°C and four consecutive scans were recorded during the time on this maximum temperature, where the temperature varied with ±1°C. The IPF maps

are presented in Figure 4.19, and the phase maps in Figure 4.20. Note that the scan taken before heating is not great, with many removed points and a higher amount of austenite than expected before heating (Table 4.2). The following figures do not contain the data based on the third can recorded at elevated temperature. Figure 4.19b has two marked areas which is investigated in section 4.4.2.2. Based on the IPF in Figure 4.19f the austenite forms with two orientations, green and white, corresponding to which of the original coarse grained austenite (achieved during the ex situ weld simulation) it formed in. Further investigations of the individual grains in Table 4.4 reveal that there is formed more austenite with the green than the white orientation during heating, but relatively speaking the white austenite grows faster and is more stable after cooling. The pole figures of the martensite presented in Figure 4.21 show that there is formed no new martensite orientations after cooling. The quality data considered in Appendix F indicate that the austenite is correctly indexed during and after heating based on the high average CI-values.

**Table 4.4: The austenite development in the two grains observed in the scan investigated in situ, with two austenite orientations.**

| Time [*minutes*] | Before heating | 10 | 19 | 28 | 36 | After cooling |
|---|---|---|---|---|---|---|
| Austenite amount in left grain (green γ) [*%*] | 3.3 | 14.3 | 22.7 | 27.1 | 31.3 | 14.2 |
| Austenite amount in right grain (white γ) [*%*] | 2.7 | 6.4 | 10.6 | 13.3 | 16.8 | 10.3 |

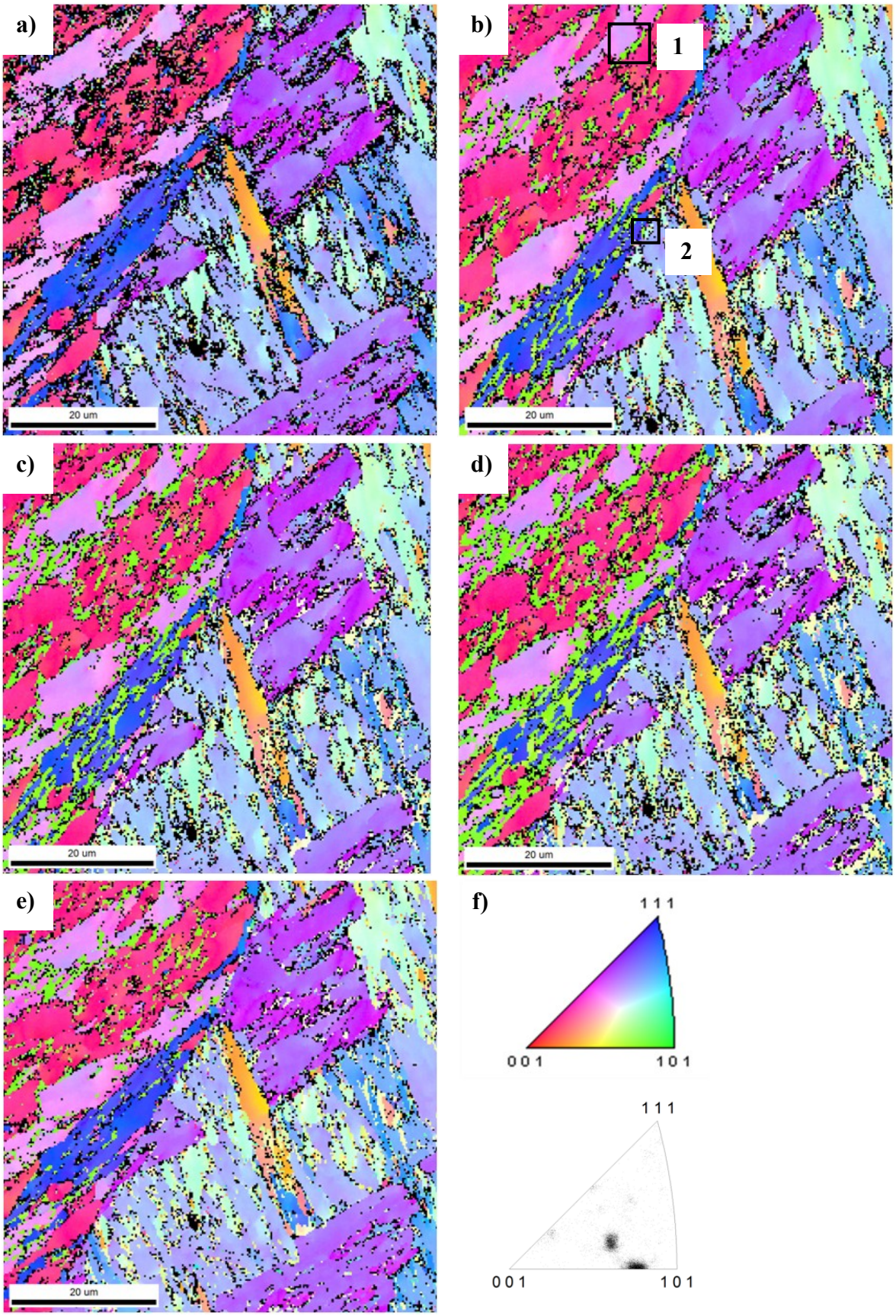


**Figure 4.19: IPF maps of the sample heated in situ with a heating rate of 1°C/s to 605°C a) before heating, after b) 10, c) 19 and d) 36 minutes, and e) after relatively slow cooling. f) The IPF for the austenite phase after 36 minutes. The areas marked in b) is for further investigations.**

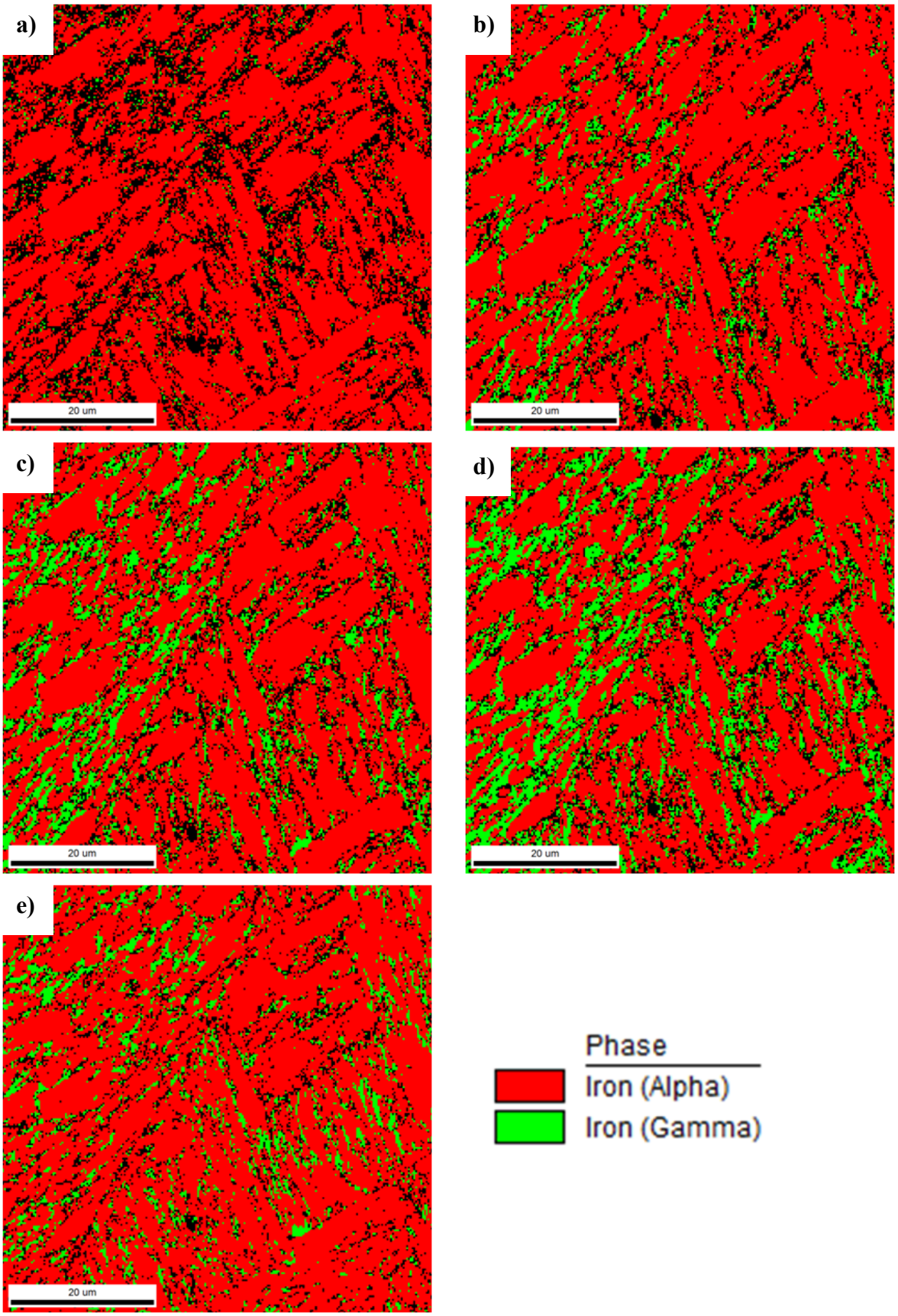


**Figure 4.20: Phase maps of the sample heated in situ with a heating rate of 1°C/s to 605°C a) before heating, after b) 10, c) 19 and d) 36 minutes, and e) after relatively slow cooling.**

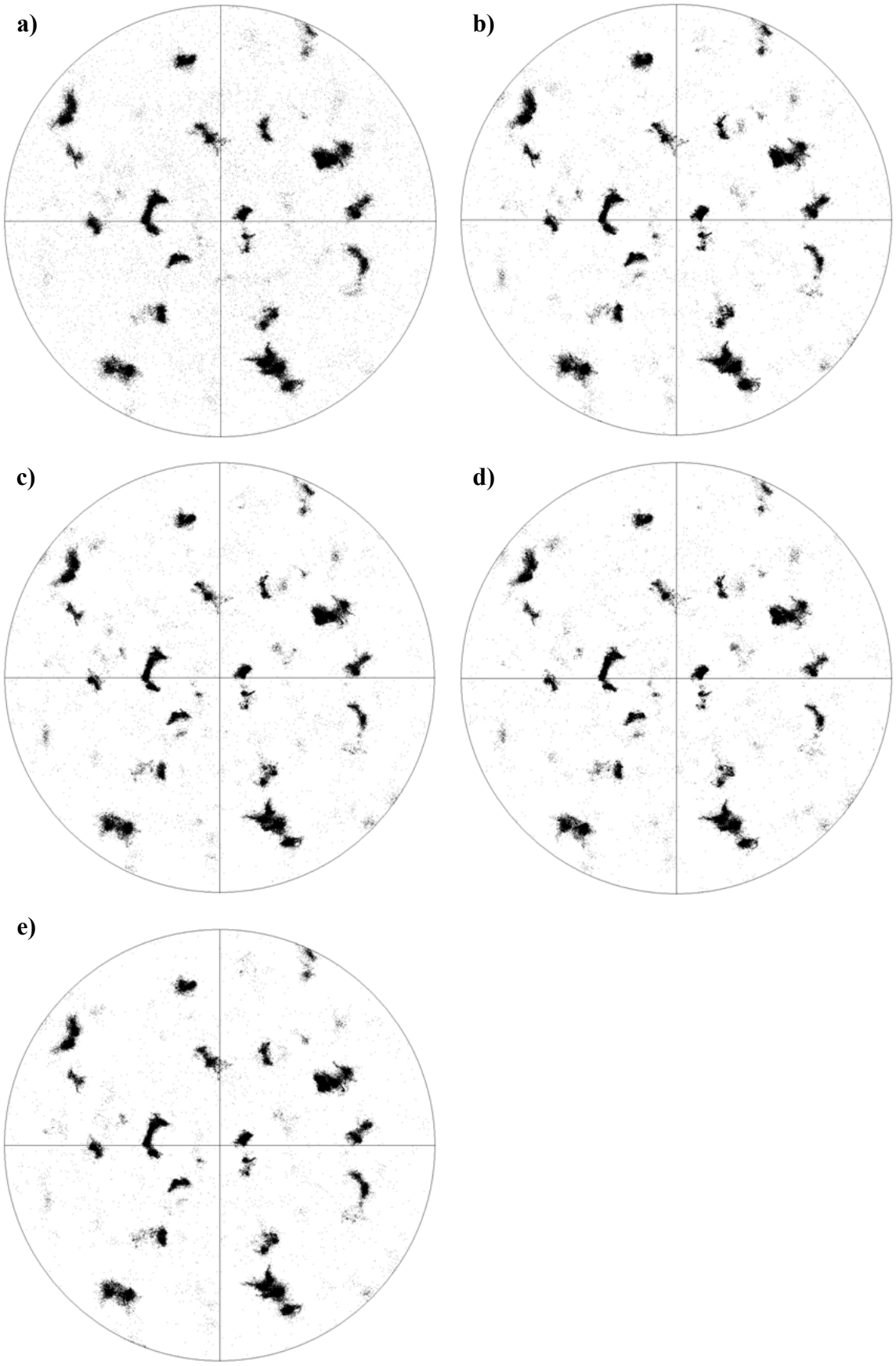


**Figure 4.21: (001) pole figures for the martensite phase of the sample heated in situ with a heating rate of 1°C/s to 605°C a) before heating, after b) 10, c) 19 and d) 36 minutes, and e) after relatively slow cooling.**

#### 4.4.2.2 Formation and Growth of Austenite

Austenite forms on both prior austenite grain boundaries and at martensite lath boundaries during the heating of the steel, and the two marked areas in Figure 4.19b can be further investigated. Both areas have the same austenite orientation (green). The austenite formed on lath boundaries, area 1, is presented in Figure 4.22 and seems to grow quite a lot at the holding time at 605°C. The relative increase from the first to the last scan is 162%, and the austenite phase appears to grow into both laths. However, the austenite growing on the prior austenite boundary, area 2, grows only on behalf of the martensite in the dark blue grain presented in IPF maps Figure 4.24. It does not look like it grows as much as the austenite between the laths, and the relative growth from the first to the last scan is 61%.

These two areas were also investigated based on the Kurdujmov-Sachs (KS) orientation relationship in the scan taken after 36 minutes. The austenite formed on the lath boundary, presented in Figure 4.23, has a KS orientation relationship with both martensite laths. The blue can be either I-1 or I-4 (or both), and the red I-2 and I-5. For the austenite at the prior austenite grain boundary presented in Figure 4.25 there is a clear orientation relationship between the austenite and only one of the neighboring grains. This is the grain it originates from, and is a I-3 and/or IV-1 KS orientation relationship. The martensite in the other grain, in the figures highlighted with red, have no orientation relationship with the austenite on the boundary. All identified orientation relationships are based on the same closed-packed plane, indicated by the roman number I.

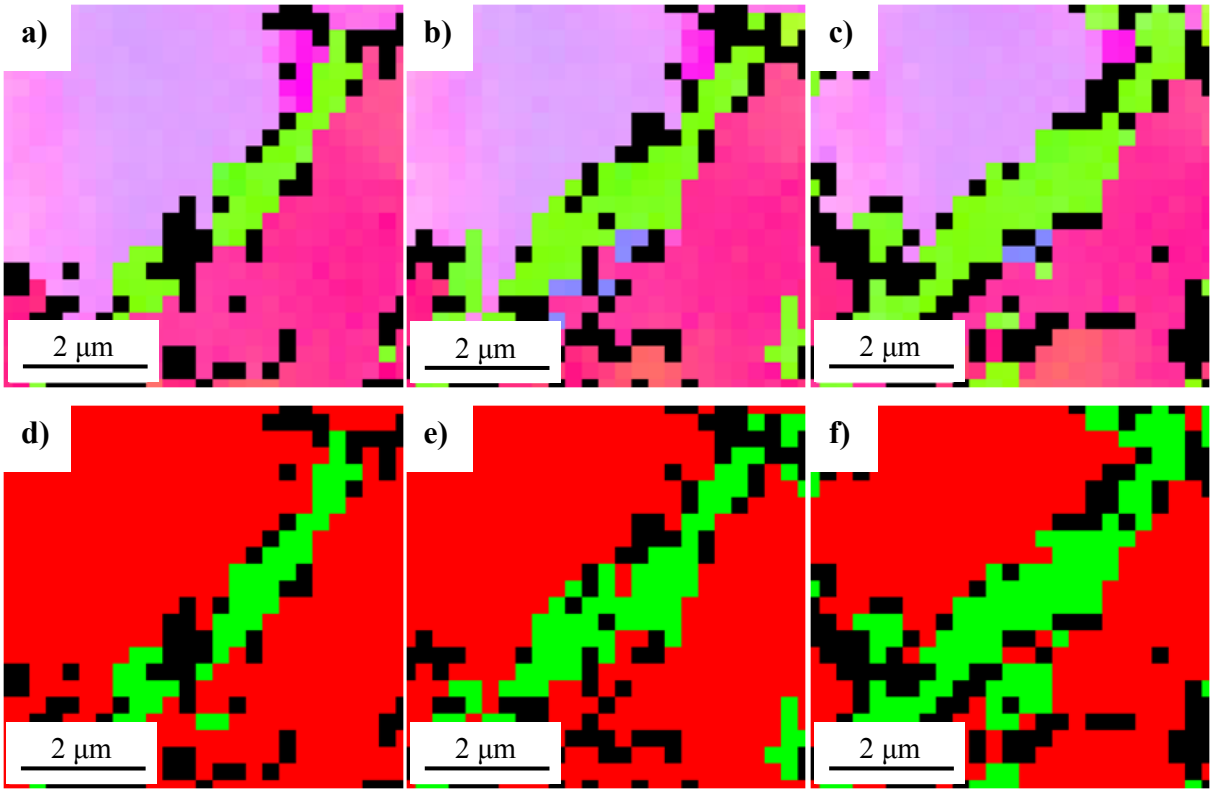


**Figure 4.22: The development of austenite with green orientation during heating, which grows on a martensite lath boundary (area 1 from Figure 4.19b). Times from left to right are 10, 19 and 36 minutes, with a-c) IPF maps and d-f) phase maps.**

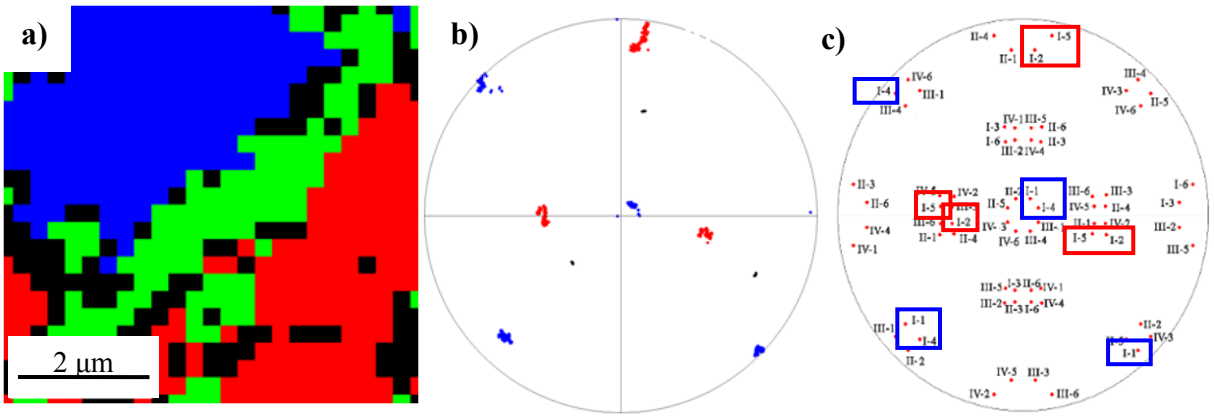


**Figure 4.23: Austenite formed lath martensite boundary after a holding time of 36 minutes at 605°C. a) Highlighted phase map with blue and red corresponding to the colors in the b) experimental and c) theoretical (001) pole figure.**

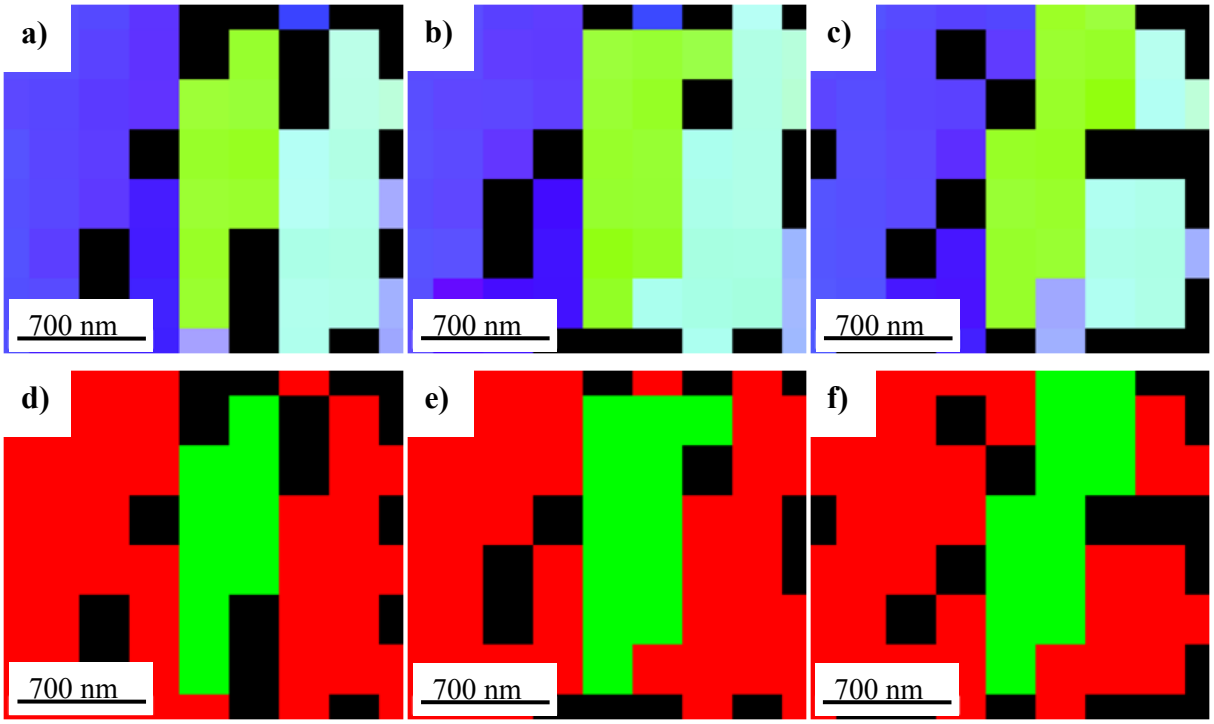


**Figure 4.24: The development of austenite with green orientation during heating, which grows on a grain boundary (area 2 in Figure 4.19b). Times from left to right are 10, 19 and 36 minutes, with a-c) IPF maps and d-f) phase maps.**

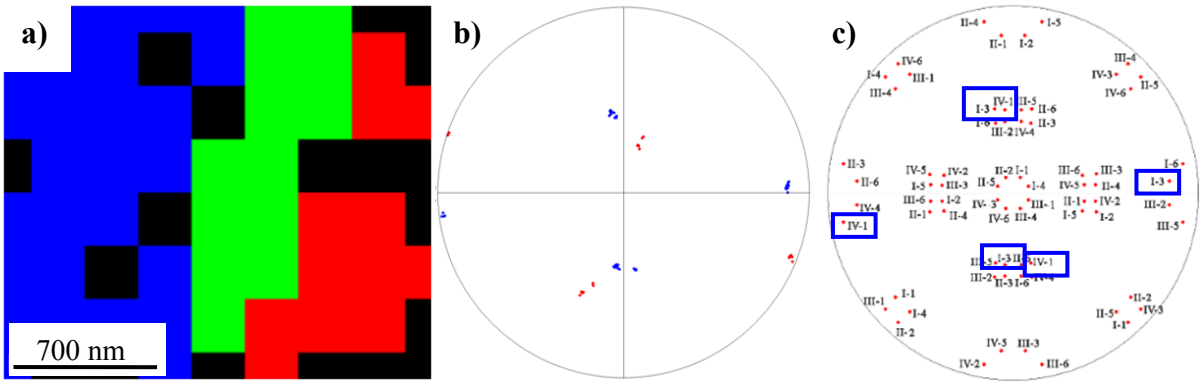


**Figure 4.25: Austenite formed on former austenite grain boundary after a holding time of 36 minutes at 605°C. a) IPF map, b) highlighted phase map with blue and red corresponding to the colors in the c) experimental and theoretical (001) pole figure.**

#### 4.4.2.3 Quantification of Retained Austenite at Room Temperature

The amount austenite after cooling was investigated in the sample heated to 605°C, as well as the sample heated to 625°C and both to 635°C. The amount is very dependent on the area investigated, seen by the variations in Table 4.5.

**Table 4.5: Amount austenite detected after the in situ experiment to different maximum temperatures, where the temperature after cooling is approximately 50°C, and the retained austenite in four scans in each of the samples investigated after storage at room temperature.**

| Temperature [°C] | Sample | Retained austenite after cooling [%] | Retained austenite after storage [%] |
|---|---|---|---|
| 605 | 8C | 11.7 | 3.7 - 3.5 - 2.7 - 1.4 |
| 625 | 9A | 4.9 | 1.8 - 1.5 - 1.5 - 1.3 |
| 635 | 10B | 3.0 - 16.2* | 4.2 - 2.5 - 2.3 - 2.2 |
| 635 | 12A | 2.8 | 2.4 - 2.3 - 2.1 - 1.8 |

* One additional scan was obtained after this experiment directly after the area investigated in situ.

The sample heated to 605°C included one area with 3.5% retained austenite, and further investigations showed that this was not evenly distributed in the scan. One grain contained almost all the austenite, and this grain is examined in Figure 4.26. When only evaluating this grain the fraction austenite increased to 6.2%. It can be observed that there are two orientations of the austenite appearing in this grain, purple and turquoise. Whether or not both of these orientations have a KS orientation relationship with the surrounding microstructure is investigated in Figure 4.27. The pole figures indicate that both austenite orientations have a KS orientation relationship with the surrounding martensite, the turquoise (highlighted with blue) an II-2 or II-5, and the purple (highlighted with green) an I-1 or I-4 orientation relationship. A relationship between the two austenite orientations can also be observed based on the orientations after rotation. Rotating the turquoise austenite to a red (001) orientation in the IPF gives the purple grain a turquoise orientation, and vice versa. The pole figures also seem to mirror each other. The misorientation between the two orientations is 60°, and twinning is detected by the software indicated by the thick red line in Figure 4.27a.

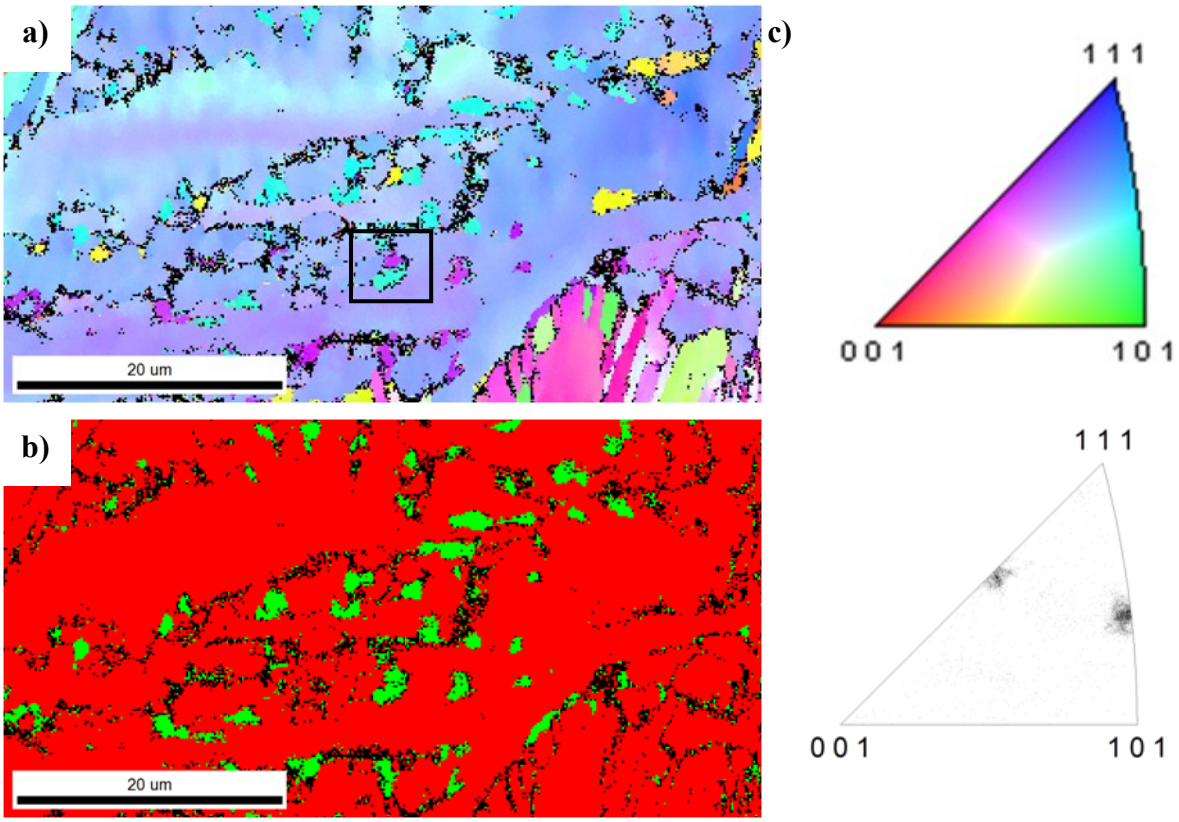


**Figure 4.26: An extract of the area containing the highest amount austenite of the samples after storage at room temperature. a) IPF map, b) phase map and c) IPF of austenite phase.**

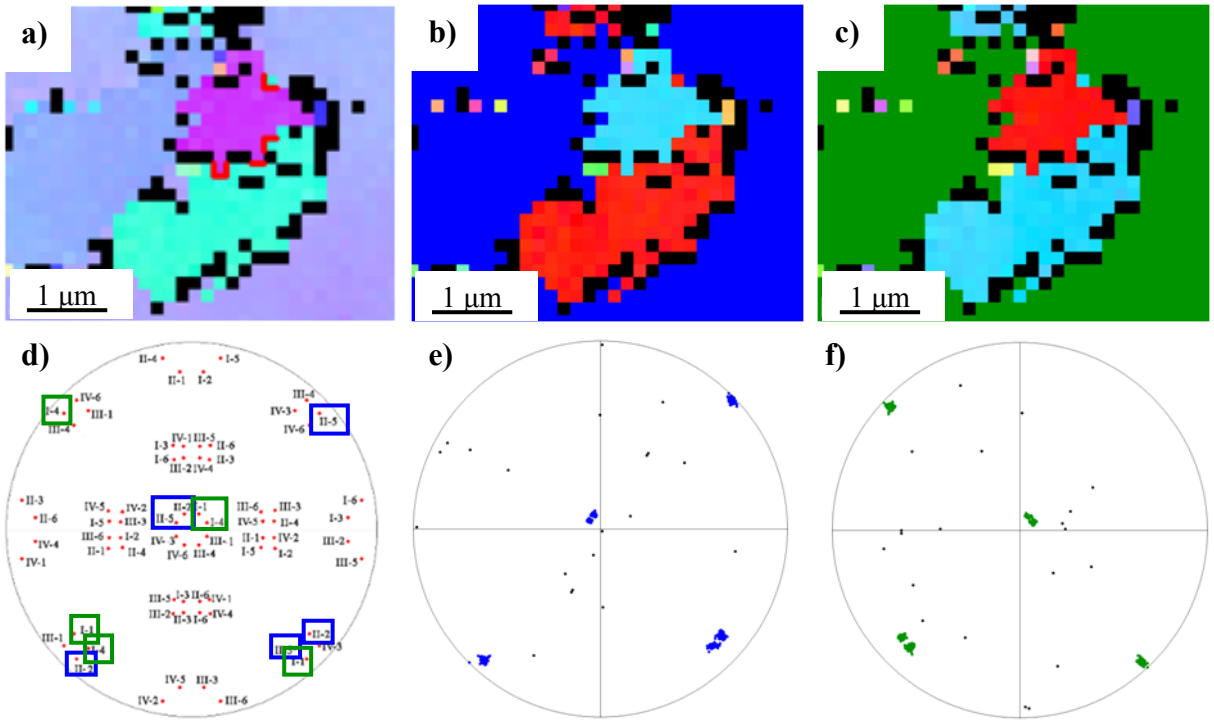


**Figure 4.27: Investigation of two austenite orientations inside the same grain. The IPF maps with austenite in a) original orientation, b) rotated to red (001) orientation based on turquoise grain and c) rotated to red (001) orientation based on purple grain. The highlighted colors in b) and c) correspond to the colors in the d) theoretical and e) and f) experimental pole figures.**

#### 4.4.2.4 Observations during Stepwise Heating to 605°C

The scans obtained during the stepwise heating decreased in quality for each step before the glowing temperature of approximately 570°C (effect presented in section 4.2.3). The scans taken at 500 and 550°C were better than the previous ones, as is presented with the development in Figure 4.28, but comparing to how it appear at 605°C, which is presented in Figure 4.29a, the scan obtained at 550°C is still not of the wanted quality. The amount indexed points with CI≥0.05 decrease from 75.0 to 62.8% after the first scan, is stable around 60% up to 500°C, where the fraction increase to 77.1%, then to 84.5% at 550°C and at the holding temperature of 605°C it is over 90%. In this experiment the resolution was the same in all scans.

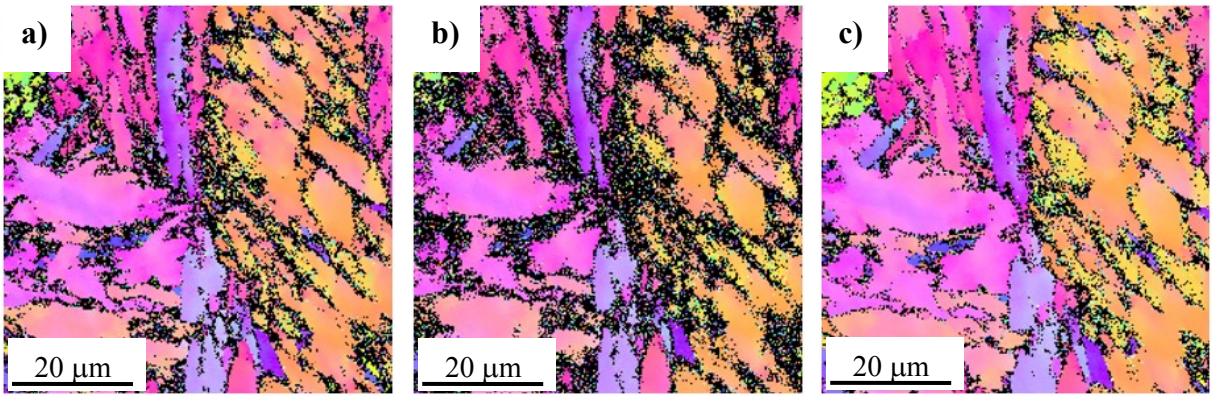


**Figure 4.28: The IPF maps a) before start, at b) 100°C and c) 550°C.**

During the stepwise heating of sample 12B no austenite was detected before the holding temperature of 605°C. The data presented in Figure 4.29 clearly shows that the amount austenite is also here dependent on the grain, with the left grain containing much more austenite. Table 4.6 also shows that the austenite formed in the left grain is more stable after cooling to approximately 50°C.

**Table 4.6: The austenite development in the two grains observed in the scan investigated in situ, with two austenite orientations.**

| Time [*minutes*] | At 550°C | 6 | 14 | After cooling |
|---|---|---|---|---|
| Austenite amount in total scan [*%*] | 2.9 | 10.7 | 16.5 | 10.6 |
| Austenite amount in left grain (white γ) [*%*] | 2.3 | 13.7 | 20.7 | 14.8 |
| Austenite amount in right grain (light pink γ) [*%*] | 3.6 | 6.0 | 9.8 | 5.1 |

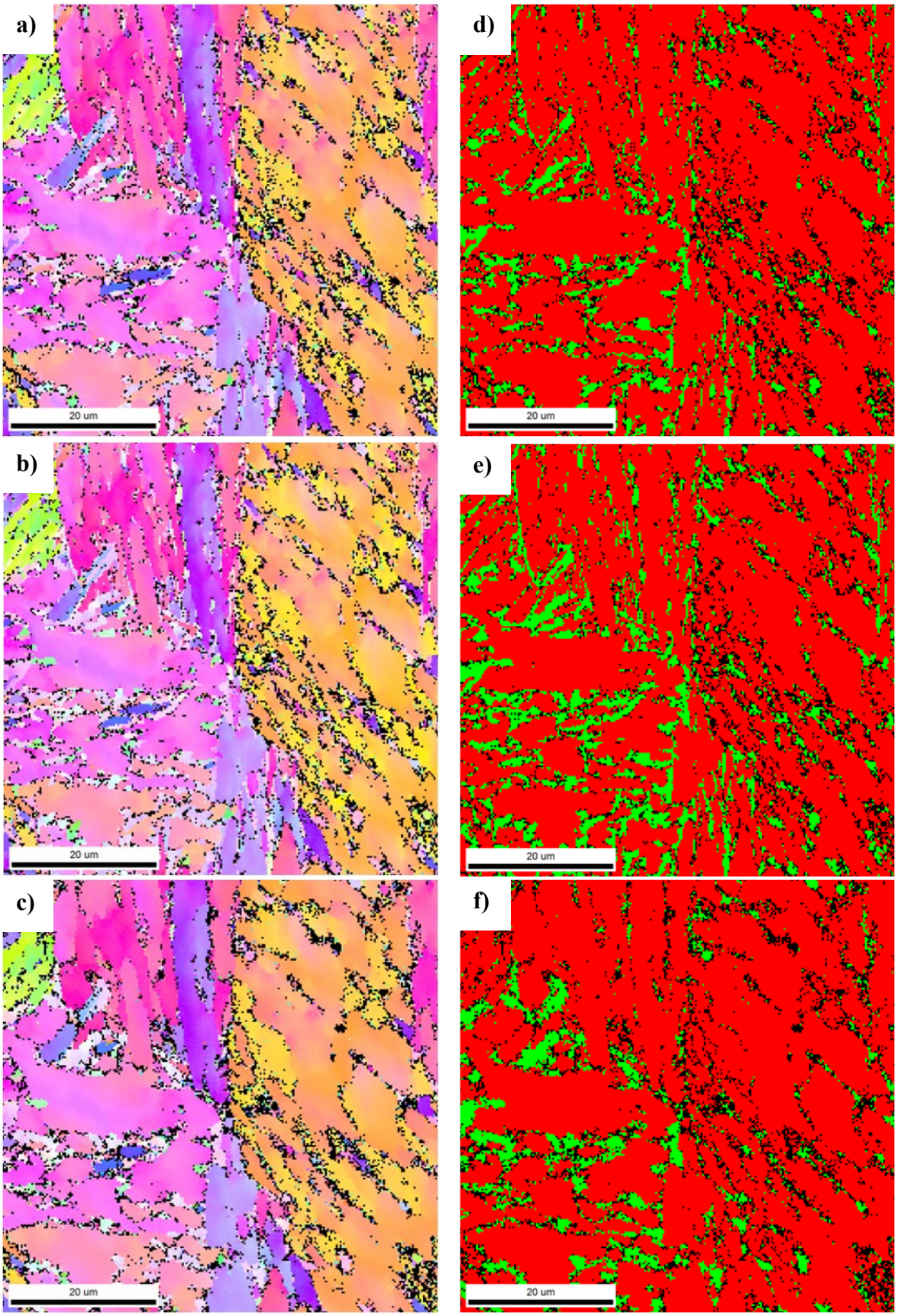


**Figure 4.29: The a)-c) IPF maps and d)-f) phase maps of the sample heated stepwise to 605°C on the maximal holding temperature, after, from top to bottom, 6 minutes, 14 minutes and after cooling.**

### 4.4.3 640-670°C

After the temperature reached 640°C as its maximal temperature, partial recrystallization was observed in this an all samples heated above this temperature. The temperature was thus higher than the $Ac_3$ temperature. The sample heated twice to 645°C, presented in Appendix E, has clear areas where recrystallization occurs during the first cycle, but this is not observed during the second cycle (with much higher heating rate). The sample heated to 700°C reached a fully austenitic state with complete recrystallization. Parts of the results from the two experiments heated to 670°C are presented below because of different observations concerning the transformation from recrystallized grains to the final microstructure after cooling.

The IPFs for the two scans at 670°C are presented in Figure 4.30 with many small, intense points as an indication of recrystallization. Figure 4.31 shows the IPF maps, with only the last scan obtained at the holding temperature presented. Recrystallization can be observed in both examples at the maximum temperature. The recrystallized areas usually transform to many small grains with high deformation and tension as can be observed in the middle belt for the sample heated directly to 670°C in Figure 4.31c. However, in the sample heated to the same apparent temperature, only with a holding time of 15 minutes at 350°C before continued heating to 670°C something else can be observed concerning the recrystallized grains. The austenite transforms back to the orientations it had before heating, or adapts the orientation of some of the other neighboring areas, e.g. expanding the yellow area in the marked areas 1 and 2 presented in Figure 4.31d-f.

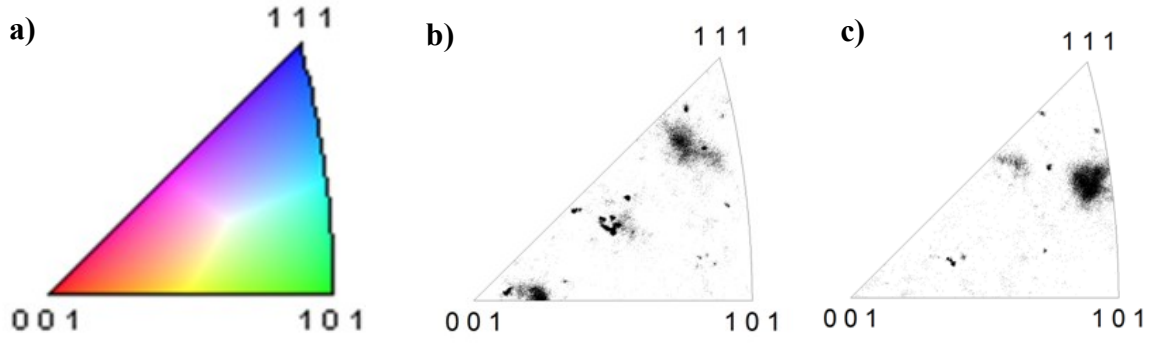


**Figure 4.30: The IPFs of the austenite phase formed in Figure 4.31. a) The IPF colors, and the resulting IPFs of the sample with b) much recrystallization and b) less recrystallization.**

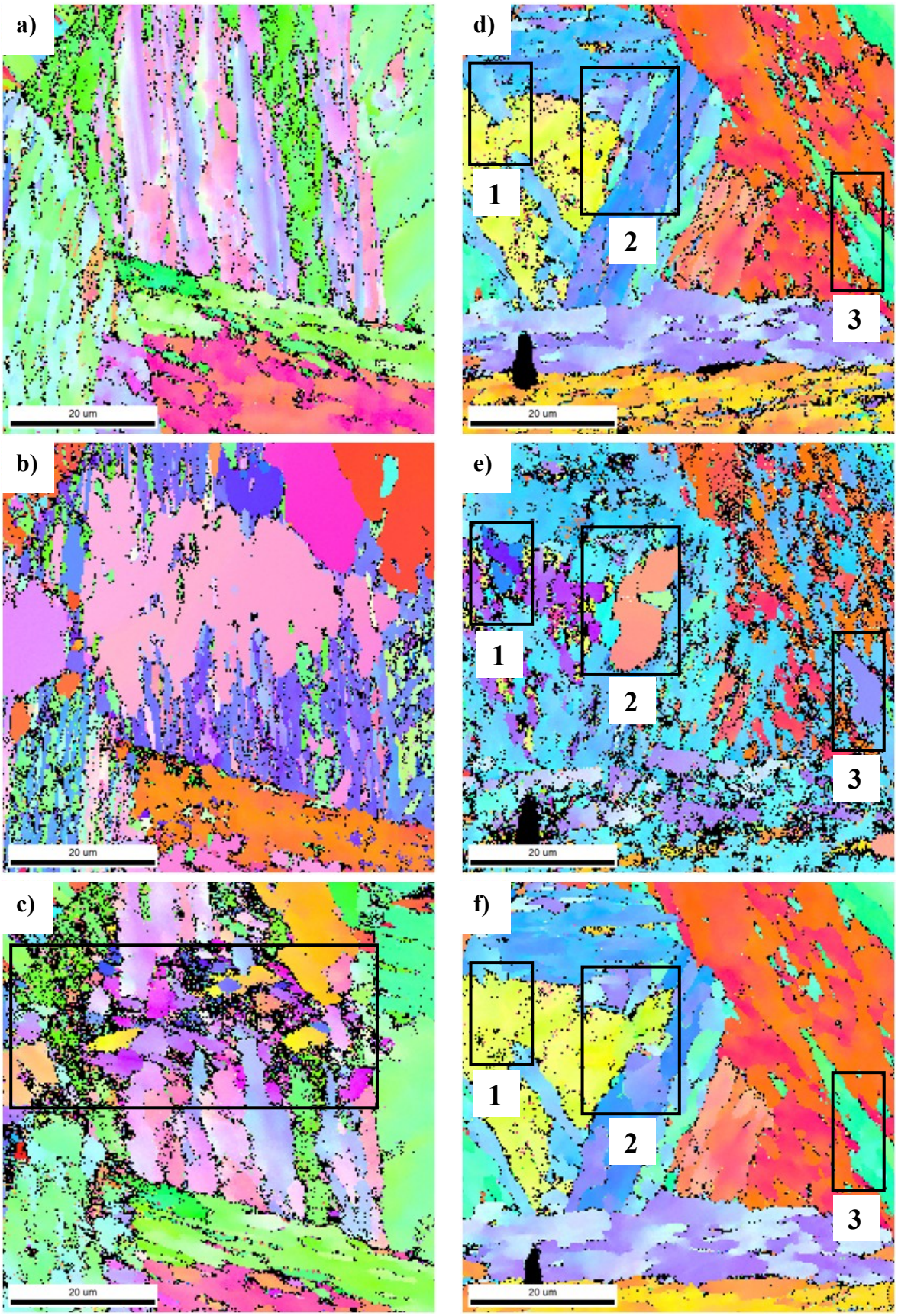


**Figure 4.31: IPF maps of the two samples heated to 670°C. a)-c) with small grains after recrystallization and d)-f) where the areas transform back to original microstructure. a) and d) before heating, b and e) after 25 and 29 minutes respectively, and c) and f) after relatively slow cooling.**

## 4.5 EDS

Because the EBSD analyses of the samples revealed a pronounced difference in amount of austenite (see examples in section 4.4.1), EDS with a simple ZAF quantitative analysis was used to investigate if the chemical composition, especially the Ni content, varied between the coarse grains.

Four different areas of sample 8B, weld simulated to achieve a coarse grained HAZ, were investigated. One area is presented in Figure 4.32, with the X-ray spectrum belonging to spot 2 presented in Figure 4.33. The weight% of each element (Fe, Ni, Mg and Si) calculated in the ZAF-analyses based on the Kα X-rays are presented in Table 4.7 (for all three spots). The values for Z (effect of atom number), A (effect of X-ray absorption) and F (effect of X-ray fluorescence) for each of the interesting elements are presented in Appendix G together with the complete analysis for all three spots.

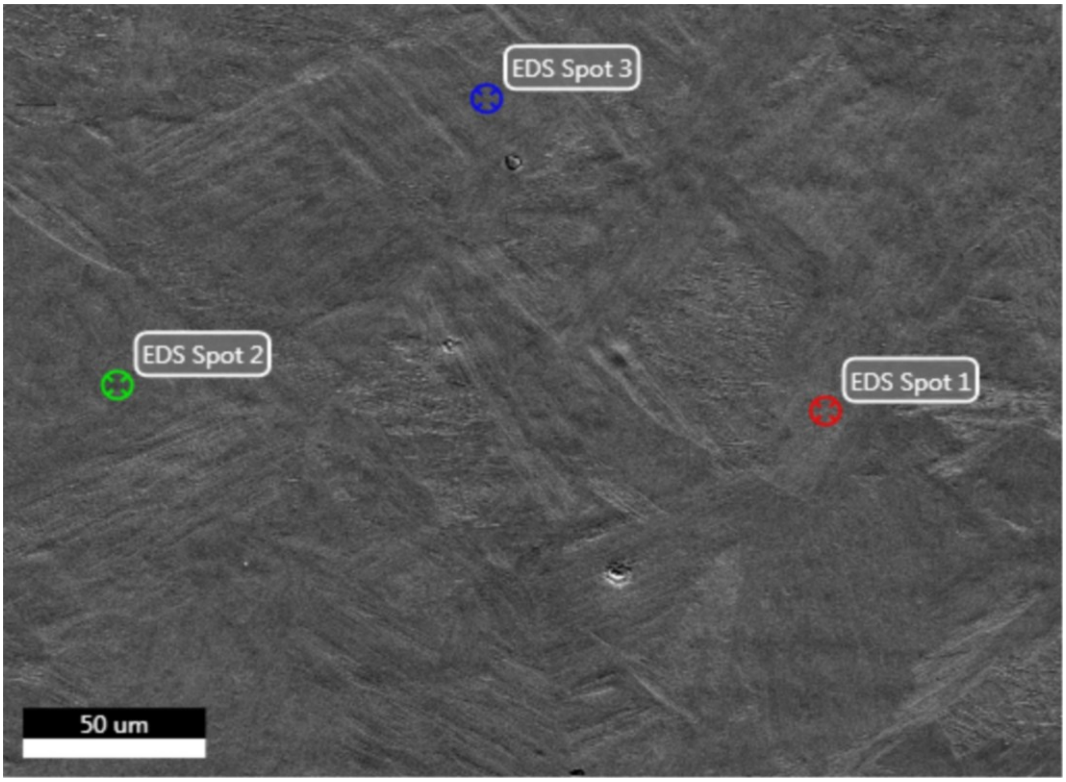


**Figure 4.32: Secondary electron image of one of the areas investigated with EDS. Point analysis were completed in three marked spots.**

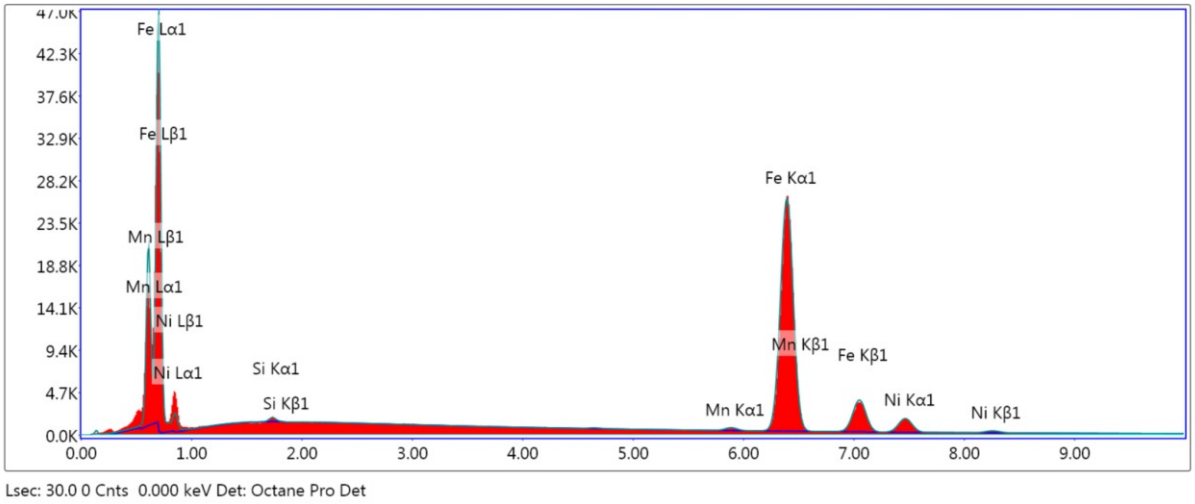


**Figure 4.33: The EDS spectrum of spot 2 in Figure 4.32.**

**Table 4.7: The resulting weight% of the EDS analysis of the three spots presented in Figure 4.32. Carbon is emitted from the analyses. The complete analyses can be investigated in Appendix G.**

| Element | Spot 1 | Spot 2 | Spot 3 |
|---|---|---|---|
| **Si** | 0.10 | 0.21 | 0.18 |
| **Mn** | 0.62 | 0.79 | 0.74 |
| **Fe** | 91.20 | 89.60 | 90.34 |
| ***Ni*** | *8.08* | *9.40* | *8.75* |

Table 4.7 reveals that the Ni-content varies from approximately 8% to 9.5%. Investigations of three more areas in the sample resulted in Ni-contents in this range as well. In one of these scans two spots was chosen with close proximity of each other, inside the same grain, and the amounts were 9.30% and 9.24%. The error of the calculated nickel content was approximately 5%.

## 4.6 Light Optical Microscopy

Optical micrographs of the original coarse grained microstructure and the structure after heating to 590°C are presented in Figure 4.34. The austenite amount is so high in the second sample that it is possible to discern this phase along the prior grain boundaries.

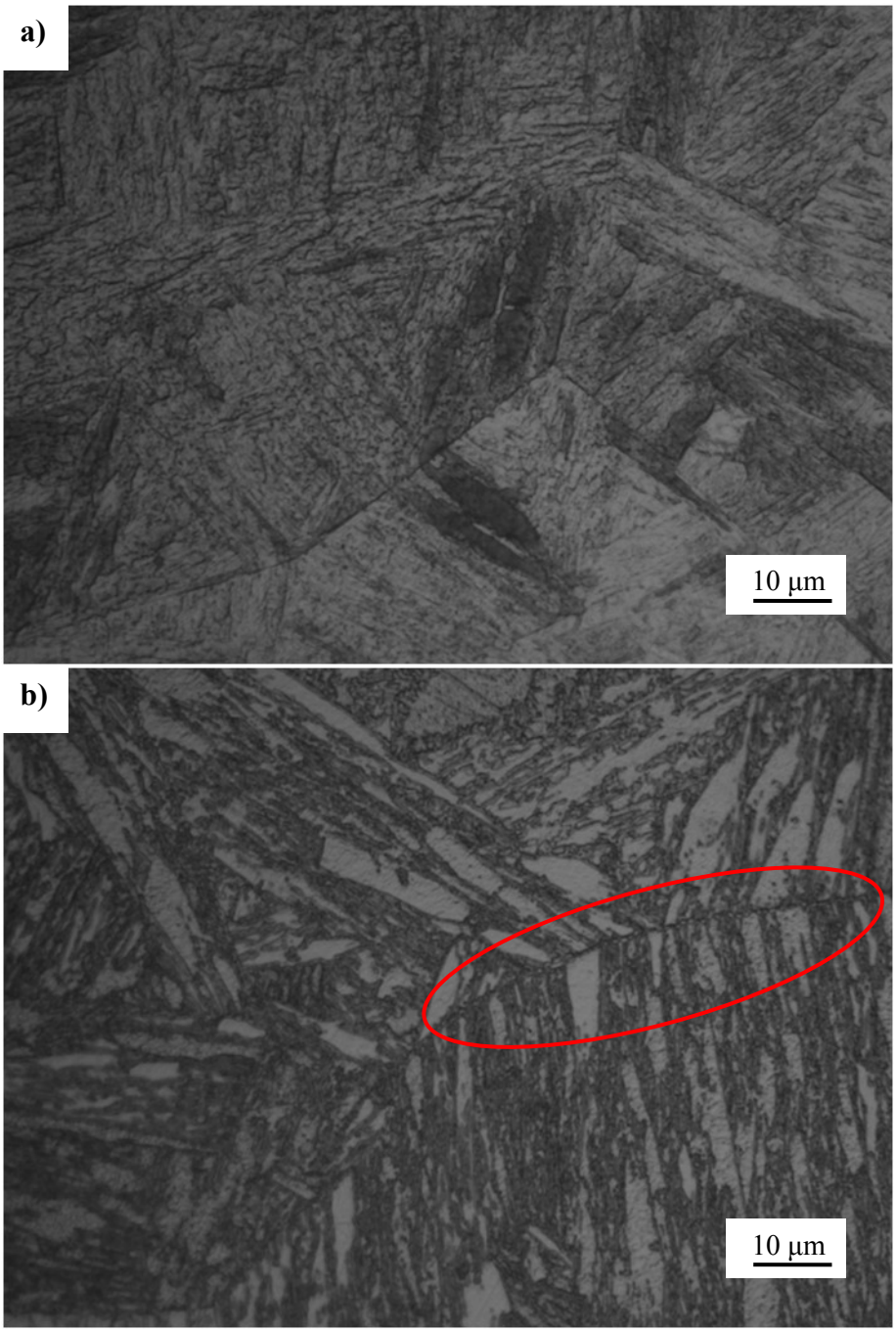


**Figure 4.34: Optical micrographs of a) weld simulated material and b) sample reheated in situ to 590°C. Retained austenite is possible to detect in the second micrograph along the grain boundary, marked with the red oval.**

# Chapter 5 Discussion

## 5.1 EBSD Characterization

The in situ heating experiments represent the second cycle of a two cycle weld simulation, but because of slow heating and cooling times as well as the long holding time on the maximum temperature it was not optimal considering actual welding conditions. The long holding time was necessary to avoid drift in the picture caused by thermal expansion, and made it impossible to observe the first changes occurring in the microstructure. During actual welding the sample is only at the maximum temperature for a very short period of time, thus the really interesting microstructural changes are not possible to examine using this in situ technique. The slow cooling rate will also result in no formation of MA-phases after quenching from the intercritial region of the phase diagram, and with lack of MA-phases in the microstructure the true low temperature properties of the ICCGHAZ can not be evaluated. What is more prominent to evaluate is where in the microstructure the austenite forms, as well as compare the quantity and stability of the austenite formed at different temperatures. The EBSD results on both elevated temperatures and at room temperature show that the austenite orientations and stability clearly depend on the original coarse austenite grain, with austenite of the same orientation being formed inside the same grain.

The first weld cycle prior to the in situ heating experiments resulted in a coarse grained martensitic microstructure after cooling to ambient temperature. The EBSD scans of this material revealed no austenite present in the microstructure. The amounts austenite was very small (0-2%) before heating, and further investigating the data this is mostly single pixels indexed as austenite, and not continuous areas. The CI values are, even after clean up, below 0.1 for the austenite, which indicates that there is a large probability that many of the pixels are incorrectly indexed [30]. The amount austenite is, hence, negligible after the first welding cycle.

The size of the coarse grained austenite formed during the weld simulation to 1350°C varied largely, as observed Figure 4.7. Some prior austenite grains were larger than the scale bar of 100 μm and others much smaller. However, during the in situ experiments it was clear that the chosen area of 75x75 $\mu m^2$ (later cropped to 60x60 $\mu m^2$) might not be representative of an interesting area considering the location of austenite formation. Fukino and Tsurekawa's results [45] found that formation of austenite preferably occurs on α/α low angle boundaries

(lath boundaries) and previous austenite boundaries, including triple junctions. This indicates that the most interesting areas are located at such places, and if the investigated area during EBSD is in the interior of a prior austenite grain some of these areas will be unobservable.

### 5.1.1 Quality of Data

Regarding the quality of the scans both the amount of indexed points with a CI≥0.050 together with the average CI, Fit and IQ values must be considered. These values are presented in Appendix F for all scans. It seems like the fraction of indexed points was between 80 and 90% during the scans recorded at the holding temperature. This fraction is approximately constant during the holding time, observable in the EBSD scans, with small variations caused by drift in the scan and the amount of interface boundaries. This value is much lower than during earlier work done by the author [43], indicating that the optimal settings might not have been chosen during acquisition, or that the preparation method is not optimal.

The most obvious mistake based on the theory presented earlier is the step size of 0.25 μm. Investigations done by Chen et al. [26] indicate that the optimal step size at the chosen magnification is 0.08 μm. The step size value was chosen based on the need of investigating a large area because of the large and uneven prior austenite grains, to increase the probability that areas with austenite formation were found within the area of interest. The fact that the EBSD detector was retracted, as presented in Figure 2.15, resulting in a smaller solid angle, might also have affected the quality of the patterns. This parameter was inspected in the reference sample (8B), with 0.25 μm step size. The fraction of indexed points with CI≥0.050 was over 90% in all cases with the detector as close to the sample as possible, and not close to 80% as it was in the quality data presented in Appendix F (with retracted detector and the same step size). This indicates that the retraction of the detector could have an impact on the quality of the scan. This was pointed out by Wright et al. [46] as they state that the contrast of the diffraction patterns are much lower with a detector positioned further from the sample. Lower contrast of the diffraction patterns can result in more difficulties during indexing. The low fraction of points with CI≥0.050 compared to the earlier work could also have been caused by the electropolishing parameters. However, because of the clear mistakes obtained at grain and interphase boundaries the step size is most likely to blame for the relatively high amount of removed points from interesting areas. Based on the scan obtained at room temperature presented in Figure 4.17, the increase in correctly indexed points by the use of smaller step size also lead to an increase in austenite detected. This indicates that the austenite

present at boundaries, in this case lath boundaries, is very affected by the step size. It is also a possibility that the phases close to the boundaries are more distorted compared to the ideal crystal lattice, so that e.g. the martensite is not possible to detect (the martensite is indexed as alpha phase in the software). This could come from very high saturation of e.g. nickel in the martensite phase.

When evaluating the quality data of the EBSD results in Appendix F in combination with the EBSD scans it is evident that at the higher temperatures gives a much better quality of the scans than before heating. To reduce the fraction of bad indexed points a solution would be to start by investigating the area chosen thoroughly before heating, and thus be sure that a relevant area is being investigated. This can be observed if the EBSD scan is evaluated before heating, and then choose a different area if it does not contain interesting areas (e.g. prior austenite boundaries). With this technique a smaller area can be chosen as well, and because of shorter scanning time this will reduce drift in the image. However, if longer scanning time (in this thesis 6 minutes was used) is acceptable it is possible to choose a smaller step size and most likely increase the fraction correctly indexed patterns in combination with the previously mentioned smaller area. Because of the increase in IQ and the very clear diffraction patterns observed at higher temperatures in Figure 4.5, the frame rate during acquisition could have been increased to (at least) 300 fps, thus reducing the time for each scan. A reduction in scan time will give the same options concerning step size and reducing drift as reducing the area of interest. Sætran [40] compared IQ values before, during and after heating with different acquisition rates and discovered that it was still possible to have good quality of all scans while varying the frame rate. Thus there is no need to use the same settings for all scans. A solution executed during several of the in situ experiments during this thesis was to do the first scan with a better resolution, as the time each scan takes is not relevant at this temperature. Most likely a acquisition rate higher than 250 fps could have been chosen at the elevated temperatures without it compromising the quantification results.

During the preparation of the steel only the A3 electrolyte was used. Previous experiments done by the developer of the stage [38] revealed that, with the HSLA steel in question, the amount austenite varied largely when heating to the same temperature depending on the electrolyte (from 5.4% to 43.6% after 10 minutes holding time). Whether or not this large difference originated from variations in the grains, the temperature of the sample not being identical because of faulty measurements (discussed later) or the two different electrolytes were not evaluated, but based on the in situ results of the 9% Ni-steel (in this thesis) it was

most likely a combination of all three. Previous experiments done with the 9% Ni-steel [9] concerning the bulk material also revealed that using A2 and A3 Struers electrolyte resulted in different amounts of austenite detected. Because the original austenite amount is so low in the base material, confirmed in the same investigations using the X-ray diffraction (XRD)-technique, the difference in quantity caused by electrolyte might be accidental. However, the electrolyte and the electropolishing parameters are still variables concerning the amount austenite detected one should reflect on.

The quality evaluations indicate that better solutions could have been chosen regarding the EBSD settings during in situ heating. Although the amounts of austenite detected are not as exact as they could have been because of many removed points, the trends observed at different temperatures are still correct concerning growth, recrystallization, stability and orientation relationships.

### 5.1.2 590°C

The sample heated to 590°C is the only one of the samples investigated where all austenite formed during the in situ heat treatment is retained after cooling to 50°C. The austenite amount increases slowly between the scans in Figure 4.9 and Figure 4.10, and the quantity data reveals that the amount retained austenite after cooling is actually higher than during the heating. This difference is only 1% and the scan is more stable at lower temperatures. The difference may be caused by thermal expansion at higher temperatures and drift in the image, so it is difficult to say for certain if the fraction has increased or not. However, the EBSD results clearly indicate that austenite formed in this experiment at this temperature is very stable with regards to the cooling rate, since most of the austenite is still present in the scan obtained after cooling. In the IPF and IPF maps in Figure 4.10 it is observed that only one austenite orientation is formed at the elevated temperature, in this case between the martensite laths. This indicates that the area investigated is inside one prior austenite grain. Because all the formed austenite is stable after cooling it is not possible to say something about the orientation correlation before and after cooling for this sample. The small differences in the pole figures in Figure 4.11 probably originate from the increase in quality during and after heating and the drift observed in the image. It does not appear as any of the martensite orientations are more likely to form austenite than others.

#### 5.1.2.1 Stability of Retained Austenite and Local Differences

After in situ heating the sample was only cooled down to 50°C, and at this temperature the EBSD scan revealed that all austenite formed during the experiment was still stable. When investigating an excerpt of the samples after storage at room temperature, the sample heated to 590°C is the one exhibiting most retained austenite compared to the ones heated to higher temperatures. These high amounts also indicate that the austenite formed at 590°C is very stable after the relatively slow cooling to room temperature. This sample was thoroughly investigated after storage at room temperature. The fraction retained austenite is in this sample so large that it is possible to discern the phase using light optical microscopy, as seen in Figure 4.34b. It is easy to observe small particles on the prior austenite boundary which is not possible to observe after the first ex situ heat treatment.

The results presented in section 4.4.1.2 indicate that the orientation of the original coarse austenite grain is most likely very influential concerning the amount retained austenite present after the in situ experiment. It appears that inside one prior austenite grain only one austenite orientation is formed during the in situ heating. Near all Kurdujmov-Sachs orientation relationships are present inside one grain as presented in the experimental pole figure in Figure 4.15, and comparing this to the theoretical pole figure in Figure 2.25 it looks almost identical. It will require very detailed work to determine if any of the 24 possible orientation relationships are more stable than others, and whether or not this will affect the stability of the retained austenite.

The results presented in Figure 4.14 and Table 4.3 make it possible to compare the different austenite orientations appearing for the retained austenite with respect to the prior austenite grains. Variations for the total scans varied from 4 to 14% retained austenite, but investigating the individual grains larger differences were observed. The scan in Figure 4.14 was obtained with 0.15 μm step size (and not retracted EBSD detector), and the prior austenite grain boundaries are presented as a combination of austenite phase, removed points or actual good points where the orientation change between the grains is obvious. The austenite present at the grain boundaries have an orientation relationship with only the original γ grain that it originates from. This relationship was evaluated during in situ heating for the sample heated to 605°C (section 4.4.2.2), and using the same technique for the austenite left on prior grain boundaries in this sample the same thing could be observed. The area fraction, and thus also the volume fraction, retained austenite in each grain varies from 5.1% in grain 1 to 24.9% austenite in grain 2. The austenite is mostly present as continuous long islands at lath

boundaries, most noticeable in grain 2. The size of the original grains are not the same, so the difference between the grains might be less or more because the grain containing most austenite is approximately half the size of the one containing the lowest austenite amount, and the whole grain is not imaged.

With a lower magnification in Figure 4.16 it can be observed that in the largest prior austenite grain (grain 3) more austenite is present in some regions of the grain compared to others, indicating local differences also inside each grain. This figure was also used to investigate if the original grain size had an influence on the amount retained austenite, and the difference in area fraction of austenite between the smallest and largest grain was found to be less than 3%. The total size of grain 1 is unknown, but it is most likely larger than the smallest grain (grain 2), and contains a much smaller amount of retained austenite. The observations concerning grain size indicate that the size of the prior austenite grain has little influence on the fraction retained austenite.

In the scan with five grains in Figure 4.14 there was a factor of 5 in difference concerning the fraction retained austenite when comparing the different grains. This is most likely not a bad number based on the results observed in other samples as well, although from the three grains investigated in Figure 4.16 the difference was closer to a factor of 8. The austenite orientation of the grains formed during the first ex situ weld simulation will most likely be the main decider of the amount retained austenite detected.

#### 5.1.2.2 Comparison to Production Parameters

Based on the investigations, the sample heated to 590°C is the one containing the highest amount of retained austenite. It is also the sample with a microstructure most similar to the 9% Ni-steel used for LNG storage. There are many similarities with the heat treatment done during the in situ experiment and the production parameters of the original steel explaining the high austenite fraction detected in this sample. The major difference between the two is the prior austenite grain size, which is much coarser in the weld simulated and in situ heated material than after the regular production process. If tempering is performed in the two phase region above the lower critical temperature, in some cases defined to be 580°C, the high nickel content will stabilize the austenite, and the 5-15% austenite formed at this temperature will be retained at room temperature after relatively slow cooling [47-49]. The sample investigated in situ was heated just above this critical temperature, and the austenite formed seemed very stable. The actual tempering process is further described to occur at temperatures

between 565 and 605°C (610°C in some productions) for no less than 15 minutes (also dependent on the thickness of the sample), indicating that this temperature region is where the formed austenite is stable after cooling to ambient temperature. These evaluations might also explain why there is less retained austenite present in the samples heated to 605°C (and higher) after the in situ experiments.

The varying amounts of austenite detected at different places in the microstructure might also be explained by comparing the in situ experiment to the production parameters; before the tempering in the production process the sample is homogenized at either 790±15°C or in the 800-925°C temperature interval before quenching [14, 48]. This is to obtain a uniform microstructure of small-grained austenite before quenching during the production process. During welding, and in weld simulation to a peak temperature of 1350°C, the short time on the maximum temperature will most likely result in non-uniform distribution in the coarse grained (CG) HAZ compared to what occurs during a homogenization process. The nickel helps stabilize the austenite phase during tempering, and if the nickel content is non-uniform in the CGHAZ it is likely that this may influence the fraction of austenite formed during subsequent heating, as well as the fraction of retained austenite observed after the sample is cooled down. Whether there was a considerably large difference in nickel content in the different prior austenite grains was investigated with EDS spot analysis with regard to the coarse grained weld simulated material. The results are close to each other and resulted in no definite answer. The two measurements done close to each other in the same grain resulted in very similar nickel content, but because of the error this could be a coincidence. The EDS analysis was not a precise enough method to be certain of the non-uniformity of the nickel content, and is best used to qualify, not quantify, different elements.

Kim and Schwarts [47] investigated the effect of intercritical tempering on different properties on a 9% Ni-steel and concluded that during tempering the austenite grew, what they described, as a continuous interlath precipitate of austenite. The continuous austenite phase can be observed to be formed in the in situ experiments, and looking at the scans during and after heating in Figure 4.9 and Figure 4.10 the phase is now dividing many of the laths from each other (stable austenite between the laths). The continuous austenite phase is easiest to observe in grain 2 in Figure 4.14 when investigating the retained austenite. The in situ heating of the sample heated to 590°C thus show many similarities with the tempering process.

### 5.1.3 605-635°C

Investigating the data concerning the samples heated in the temperature interval of 605 to 635°C, approximately the same development concerning austenite quantity could be observed during the in situ heating. This was easy to observe in the graphical representation in Figure 4.18. After 10 minutes on the holding temperature the area fraction austenite was between 9 and 13%, and after 25-28 minutes the amount had increase to 18-24%. However, the stability of the formed austenite can be divided into two groups, whether the maximum temperature was higher or lower than 620°C. The samples heated to the lowest temperatures (605 and 615°C) lost approximately half of its austenite upon cooling and ended up with 11% retained austenite. This is the same amount as the area investigated in situ to 590°C, but in that case all formed austenite was stable after cooling (much less was formed during the experiment). For the samples heated to higher temperatures than 620°C the fraction austenite detected at 50°C was reduced to 3-5%. It appears that this temperature was too high to make the austenite stable after cooling.

The pole figures of the martensite phase of the sample heated to 605°C after heating did not seem to contain any new orientations which were not present before heating, only small differences concerning the intensity of the dots occur during heating. The much better quality of the data during and after heating will result in more defined points, and some scattering is reduced when comparing the pole figures with each other. The disappearance of some martensite orientations and less intensity of some points is caused by austenite formation, as well as drift in the image. There are no pronounced new martensite orientations after cooling, an indication of a memory orientation effect. When the austenite formed at high temperature is transformed back to martensite it remembers its exact "old" orientation. The memory effect is easier to observe in the IPF maps for the sample heated to 625°C (in Appendix E), because it forms more austenite during the heating and more transforms back to martensite and its original orientations after cooling than in the scan from 605°C.

#### 5.1.3.1 Growth of Austenite

Austenite forms on both lath boundaries and prior austenite grain boundaries during in situ heating. Comparing austenite formed on lath boundaries in Figure 4.22 with austenite formed on a previous grain boundary in Figure 4.24, it can be observed that the austenite formed on laths grew much faster than the one on a previous grain boundary. The relative increase of the areal fraction of austenite was 162% vs. 61% when comparing the outtake after 10 minutes with the one after 36 minutes. Further, investigating the Kurdujmov-Sachs orientation

relationship in Figure 4.25 reveals that the austenite formed on previous grain boundaries only has a KS relationship with one of the grains, and it looks like it only grows into this specific grain. This retards the growth. However, how much the phase investigated actually grows is hard to determine because of the step size and low CI at the grain boundary, so the relative growth of 61% is questionable. In the case of growth on lath boundary this austenite has a KS relationship with both laths, observed in the pole figure in Figure 4.23, and grows into both of the laths. The formation of the previously described continuous interlath austenite is easier to observe in the scans of the whole area in Figure 4.19 or Figure 4.20 than in the outtake in Figure 4.22. Comparing either IPF or phase maps obtained after 10 minutes with the one obtained after 36 minutes it can be observed that the austenite formed at earlier times grows together to form a continuous system.

The area investigated for the sample heated to 605°C contained two grains with two different orientations during the in situ experiments (Figure 4.19). The results in Table 4.4 can be evaluated based on growth speed and stability after cooling, and it indicates an obvious difference for the two orientations. The left grain (green austenite) contains almost twice as much austenite than in the right grain (white austenite) after 36 minutes (comparing 31.3% with 16.8%). At the same time, the growth of the austenite phase was both slower between each of the scans and less of the austenite formed at the elevated temperature was stable after cooling in the left grain compared to the right grain. This is based on the decrease from 31.3% to 14.2% is larger (relatively) than from 16.8% to 10.2%, as well as the relative increase between each of the scans. Overall the left grain still contains more austenite after cooling than the right grain after 42 minutes at 605°C (the total time after the last scan finished). This indicates that austenite could have started to form at an earlier point during the heating in this grain compared to the other, and that the austenite formed at a later time during the experiment is not as stable in the left grain as the right grain. Comparing these evaluations with the two grains investigated during the stepwise heating to 605°C (Figure 4.29) the opposite was observed. The grain with highest increase during the holding time (which was much shorter in this experiment) also had the highest decrease in quantity after cooling. This observation could be affected by the previous heating steps, or that the stability of the white oriented austenite (which is present in both experiments) is actually very high after both experiments regardless of the growth rate in the different grains. There are no other comparable scans because the bulk of the experiments do not contain several grains. In the

experiment heated fast to 635°C (12A) the two orientations grow with the same rate and almost 90% of the austenite formed during heating was not stable down to 50°C.

The two samples heated to 635°C had two different heating rates. The quantification during the in situ investigations indicates that the faster heating rate resulted in more austenite at the holding temperature, and less retained austenite after cooling. This is also evident when looking at the samples after storage at room temperature, but it could be a coincidence depending on the grain and area investigated. This is further questioned when comparing the amount of austenite in the slowly heated sample (10B) directly after cooling with a scan obtained 100-200 μm beside the in situ area, the second scan obtained only minutes after the first scan had finished. The area investigated during and after the in situ experiment contained 3.0% retained austenite at 50°C; however, the other scan contained a much higher quantity (16.2%). A variation of a factor larger than 5 concerning the retained austenite is thus observed at the two scans obtained at 50°C. The differences in the austenite quantification observed for the two different heating rates could therefore be coincidental.

#### 5.1.3.2 Retained Austenite after Storage

Of the five samples heated in the temperature region 605 to 635°C all but the one with holding temperature of 615°C was investigated after storage at room temperature. The results concerning retained austenite in these scans were presented in Table 4.5. The variation between grains was observable in these scans as well, for example in the outtake presented in Figure 4.26. The austenite fractions presented in Table 4.5 should therefore be considered with these local variations in mind. The results varied from approximately 1 to 5% retained austenite, thus still a variation with a factor 5 (which also was observed for the retained austenite in the sample heated to 590°C). The difference observed at 620°C considering the stability of the austenite formed during the in situ heating is not obvious, indicating that the difference of austenite stability observed at 50°C might only be coincidental for the area investigated.

Such great differences in austenite amount observed after cooling in this temperature interval might indicate that the differences are also evident at elevated temperatures. This might explain the seemingly similar austenite growth and stability in the temperature interval of 605-635°C, because it might actually be coincidental depending on the area investigated.

The observed twinning in Figure 4.26 and Figure 4.27 indicates that the two orientations originates from two twin grains obtained during the first cycle of the ex situ weld simulation.

This has not been observed during the in situ heating experiments so there is no indication if any of the austenite occurring in any of the two twin grains grows faster or is more stable than the other, but the orientation relationship between them is quite clear. It is most likely twinning which is observed in grain 2 in Figure 4.16 as well (retained austenite after heating to 590°C), because it looks like the orientations switch between blue and pink several times through the grain. The same investigations were performed as in Figure 4.27, and the results indicate that the KS relationship mirrors each other across the boundary between the two orientations in a similar fashion, indicating that this is also caused by twinning.

As mentioned before, the tempering temperature during production of this steel does not usually exceed 605°C. This is consistent with the results obtained during the in situ experiments; there is formed quite a lot of austenite but it is not stable after cooling. The 605-635°C temperature interval must then be in the higher part of the two phase region, and stable austenite is formed in the lower part of the two phase region.

### 5.1.4 Observations Above 640°C

It was observed partial recrystallization in the investigated area for the sample that reached 640°C. This observation indicates that the sample reached a temperature above the two phase region, and instead reached the pure γ-region. Thus the sample heated above the $Ac_3$ temperature is no longer relevant when considering true ICCGHAZ microstructure, but some other observations are interesting. The orientation memory effect is obvious for areas not recrystallized, most noticeably in Figure 4.31d-f. The samples heated to and above 700°C were completely transformed to austenite upon heating, with one example in Appendix E.

The recrystallized areas transform to a very fine grained structure after cooling, as could be observed in the EBSD scan of the sample heated to 670°C in Figure 4.31a-c. Further investigating the IQ values in Appendix F, the sample with high amount of recrystallization got a large decrease in IQ after cooling when comparing to the values at elevated temperatures, but the ones where memory effect was dominant the IQ value increased instead. This indicates that there might be much dislocations and high tension in the new fine-grained microstructure after recrystallization. The effect is also affected by the step size, as there are a large number of grain boundaries in this area. Higher IQ after cooling indicates that the high temperature removed dislocations and that there is less tension in the microstructure, and this is preserved after transforming back to its original microstructure in areas without

recrystallization. Higher IQ after heating is also observed at the temperatures where no recrystallization and only memory effect was observed, as can be investigated in Appendix F.

Something new was observed for the sample heated to 670°C after a holding time of 15 minutes at 350°C. Partial recrystallization can be observed in the IPF map in Figure 4.31e, but after cooling there are no new small grains with new orientations as could be observed e.g. in Figure 4.31a-c. In Figure 4.31d-f recrystallized austenite transformed back to its original orientation, or the neighboring orientation thus expanding the areas with one orientation. The first was observed in area 3 in Figure 4.31d-f, and an expansion of the yellow grain can be observed in areas 1 and 2 in the same figure. Why this occurs in this sample is unknown to the author; however, it is possible that there are very favorable orientation relationships between the phases, which will cause the large grain in area 2 at the elevated temperature to grow very much and only appearing to recrystallize. It was discovered a KS relationship between this austenite and the yellow martensite, so it is possible that during cooling the apparent recrystallized area transformed back to a structure which was more favorable than after the weld simulation. Verifying this will require a much more comprehensive study and is just speculations.

## 5.2 Evaluation of Investigated Temperatures and Heating Rates

It was discovered during the dilatometer analysis done during the ex situ weld simulation that the lower and upper transformation temperatures at a heating rate of 110°C/s was approximately 660°C and 780°C (section 4.1, Figure 4.1). Earlier investigations done by the author revealed the same temperatures, only with the $Ac_3$ (the upper transformation temperature) closer to 750°C (section 2.2, Figure 2.5). In this graph it could also be noticed that, for the two heating rates (110 and 65°C/s respectively), the transformation temperatures increased marginally with higher heat input, in agreement with previously presented theory. Comparing the measured $Ac_1$ and $Ac_3$ temperatures to the ones discovered by Nippes [5], 618 and 666°C measured with a much higher heating rate (350°C/s), it does question the reliability of the dilatometer measurements during the weld simulation. The temperatures should have decreased compared to Nippes results because of the lower heat input (350°C/s vs. 110°C/s). The steel presented in the CCT-diagram in Figure 2.2 [11] have not defined the heating rate, but $Ac_1$ and $Ac_3$ are 602 and 705°C respectively. These variations make it difficult to compare the measured values with theoretical values, as the heating rate and chemical composition seem to be very influential on the transformation temperatures.

During the in situ heating experiments the heating rate fluctuated, in most cases, between 0 and 2°C/s (not stable). Thus we have a much lower heating rate and energy input than the former cases, and the $Ac_1$ and $Ac_3$ temperatures should decrease compared to the temperatures identified based on the dilatometer measurements. Austenite formation can be detected at the lowest temperature examined, at 590°C, thus it can be presumed that the $Ac_1$ temperature is lower than this value. This is lower than all temperatures discussed earlier. As the $Ac_1$ temperature is not as dependent on heating rate as the $Ac_3$ temperature [15] this questions the experimental value because the lower transformation temperature decreased with at least 70°C when comparing to the dilatometer analysis. Earlier investigations done by Hansen [39] comparing two very different heating rates, approximately 0.1°C/s vs. 100°C/s, showed that with the lower heating rate the $Ac_1$ temperature only decreased with 20°C, and in the in situ experiments the heat input does not decrease as much. The $Ac_3$ temperature decreased in Hansen's experiment with 160°C. Recrystallization started to occur at 640°C during the in situ experiments in this thesis, an indication that the pure γ-region of the phase diagram is reached. This is over 100°C decrease from the dilatometer results, and in correlation with Hansen's investigations. Thus the heating rate is shown to have a much larger effect on the $Ac_3$ temperature than the $Ac_1$ temperature. Because of the logical $Ac_3$ results this questions the reliability of the temperature measurements during the in situ equipment rather than the dilatometer measurements. The dilatometric results are most likely correct.

## 5.3 Glowing and Topography

Glowing of the sample started at approximately 570°C. This resulted in better EBSD patterns and a much better quality of the EBSD scans (CI, IQ). Most likely this is because the evaporation of hydrocarbons on the surface is very effective after the sample itself begins to glow. This evaporation also leads to a much better secondary image after glowing; however, this can simply be because of not optimal contrast and light intensity settings at the lower temperatures. The glowing results in higher brightness from the sample itself, as could be observed in Figure 4.4, leading to large adjustments of the contrast and brightness settings for the secondary electron image. With the sample glowing this tuning appeared to be simpler, although it could be a coincidence (even if it happened in all experiments). Successive scans did not leave any trace of hydrocarbons on the surface, thus contamination at elevated temperatures are irrelevant. Contamination was not evident during the stepwise scans either, indicating that hydrocarbons left on the surface during the scan will evaporate at only 100°C.

The secondary electron image at 590°C in Figure 4.6d shows what appears to be topography in the image. This was observed during several of the experiments at elevated temperatures but not always before and after cooling. It is not easy to say anything about formation of topography because, especially with low contrast, topography might not be visible. If information about topography is desired a 3D image of the surface can be constructed by taking secondary electron images of the surface at different angles before processing them together [50, 51].

## 5.4 Temperature Investigations

During the in situ experiments it was very important to control the sample temperature so the temperature reached the two phase area of the phase diagram. This was problematic because the difference between the furnace and sample temperature varied between 35 and 85°C. This variation made it difficult to predict what temperature the sample would reach based on the software settings. Because the deviation between T1 (furnace) and T2 (sample) is so large, this implies that there are several parameters affecting the measured temperatures, most of them difficult to control. Whether or not the temperature measured by the sample thermocouple is actually correct can also be questioned, and an error in the temperature controller for the furnace has been pointed out from the developer of the stage. It was discovered that there was an error in the controller, not 85-90°C as Enstad described (at both room temperature and above 700°C), but 20°C at room temperature for the furnace thermocouple. If this error does not increase noticeably at elevated temperatures, this indicates that the temperature difference of the sample and furnace instead is 15-65°C during the in situ experiments.

Deviations between the actual furnace temperature and the actual sample temperature are due to environmental heat loss and poor heat transfer between furnace and sample. This is dependent on the amount of SPI platinum paint used. The deviation of the true furnace temperature with the measured value is dependent on poor heat transition between the thermocouple and the furnace. This is also important considering the sample measurements, but another important parameter is the penetration tightness and depth of the thermocouple. Earlier investigations [39] using the same equipment showed that a small hole with the same diameter as the thermocouple resulted in shallow and tight penetration, and the temperature measured by the controller was 50-100°C lower than the actual temperature of the sample. This was affirmed by a spot welded thermocouple to the top of the sample during a reference experiment. This difference was reduced with a larger hole, where the controller logged a

temperature only 20°C lower than the spot welded thermocouple. The deeper penetration resulted in a more correct measurement of sample temperature and thus gave more control to the experiment.

The mistakenly logged temperature of the sample caused by bad thermal contact between thermocouple and sample, in combination with the error in the controller, indicate that the heat transfer from the furnace to the sample is actually very good. With the evaluations concerning the controller the smallest temperature difference between the furnace and the sample is measured to be only 15°C. The SPI paint works well in several of the experiments. However, the precise sample temperature is hard to determine because no experiments with spot welding have been completed with this exact hole diameter (0.55 mm). It is questionable if the large measured temperature differences (between T1 and T2) in some of the experiments originate from bad heat transfer from furnace to sample, or if it is because the thermocouple does not measure high enough temperature. This makes it hard to compare experiments heated to the same temperature, or when looking at samples with small differences in holding temperature, because of uncontrollable factors. The sample heated to 590°C had a measured temperature difference between sample and furnace of 60°C, but with the recent evaluations it can be assumed that the temperature actually could have been closer to, or above, 600°C, thus the $Ac_1$ temperature could have been higher than previously discussed. This also indicates that the seemingly similar observations in the different temperature intervals, e.g. 605-635°C, are not only affected by the grain investigated, but also that the temperature might be more alike than first assumed.

# Chapter 6 Conclusions

In this master's thesis in situ heating has successfully been used in combination with EBSD measurements. The goal was to use this technique to observe the microstructure evolution throughout the heating experiment, with focus on the emergence of austenite when heating to the $\alpha + \gamma$ region of the phase diagram, and the stabilization of the formed austenite after cooling.

- The combined in situ heating and EBSD technique was well suited for these investigations. The results may, however not be comparable to what appears during actual welding properties because of the low heating and cooling rate, and the long holding time at the maximum temperature.
- Growth rate, stabilization of austenite after cooling and total quantity of austenite during and after the in situ experiment were found to be dependent on the prior coarse grained austenite formed at the peak temperature of 1350°C during the weld simulation.
    - Variance with a factor 5 was established concerning the retained austenite at room temperature.
    - The prior austenite size did not affect the retained austenite amount.
    - Whether the local differences were caused by a variation of nickel content in the grains or not could not be affirmed.
    - When several orientations was observed inside one apparent grain this originates from twin grains in the original austenite microstructure.
- The austenite formed in the lower part of the two phase region is formed slowly and is very stable after cooling slowly down to room temperature.
    - Further investigations of the sample after storage reflected this, with a variation of 5 to 25% retained austenite depending on the original coarse grained austenite formed during the ex situ weld simulation.
    - The experiment conducted at 590°C had parameters closest to the tempering process for the production of the steel, where theory indicates that 5-15% austenite is stable.

- Austenite formed in the temperature range 605-635°C exhibited approximately the same development during the in situ heating for all the experiments, and the austenite formed at this temperature was not stable after cooling.
    - The in situ investigations indicated that the austenite formed at the lowest temperatures in this region might be more stable, but because of uncertain temperature measurements this was not confirmed.
    - Orientation memory effect was observed after cooling, where the austenite reformed to its original orientation.
    - The amount retained austenite varied from 1 to 5% after storage
- Examinations showed that the orientation relationship between newly formed austenite and the surrounding martensite fulfilled the Kurdujmov-Sachs (KS) orientation relationship, and suggest that the austenite was correctly indexed and not an artifact.
- Austenite formed more quickly on lath boundaries than on previous grain boundaries.
    - The austenite on lath boundaries grew at expense of both laths and it had an KS orientation relationship between both grains.
    - The austenite at grain boundaries only had a KS orientation relationship with one grain, and grew at expense of this grain.
- When heating above 640°C partial recrystallization was observed, and upon cooling these grains usually transformed to many small grains.
- The transformation temperatures $Ac_1$ and $Ac_3$ are strongly dependent on the heating rates.
    - The dilatometric measurements during weld simulation gave the upper and lower transformation temperatures to be 780 and 660°C with a heating rate of 110°C/s.
    - The austenite detected at 590°C indicates a lower transformation temperature lower than this when the heating rate is 1°C/s.
    - The recrystallization of austenite appearing at 640°C indicated an upper transformation temperature very much lower than the one obtained after weld simulation, thus the $Ac_3$ temperature is more affected by the heating rate than the $Ac_1$ temperature.

# Chapter 7 Further Work

To get a better understanding of the microstructural changes in the HAZ during welding of this steel the following work should be performed:

- Measurements of the sample temperature during the in situ experiments need to be improved.
    - The best parameters concerning mounting of the thermocouples should be thoroughly investigated e.g. the hole diameter and the depth of the hole for the thermocouple.
    - For better improvement the thermocouples needs to be replaced by infrared detectors inside the SEM.
- More investigations concerning the acquisition settings during the in situ experiment should be evaluated, including the need of a retracted detector.
- Investigating the effect of using SPI paint is necessary concerning this particular steel because of the low transformation temperatures.
- The effect of holding time on the retained austenite content in the temperature region 605-635°C can be investigated.
- Formation of MA-phases can be investigated by the use of a quenching system based on helium.
- Further investigations of the chemistry variations in the steel, from grain to grain and across grain boundaries would be interesting to examine. This could be done by e.g. transmission electron microscopy (TEM) investigations.

Propositions about further development and refinement of the in situ equipment is presented in Appendix B, including more permanent solutions to some of the refinements done during the in situ work.

# Reference List


1. Gautier, D.L., Bird, K.J., Charpentier, R.R., Grantz, A., Houseknecht, D.W., Klett, T.R., Moore, T.E., Pitman, J.K., Schenk, C.J., Schuenemeyer, J.H., Sørensen, K., Tennyson, M.E., Valin, Z.C., and Wandrey, C.J., *Assessment of Undiscovered Oil and Gas in the Arctic.* Science, 2009. **324**(5931): p. 1175-1179.
2. Solberg, J.K., *Teknologiske Metaller og Legeringer*. 2013, NTNU: Institutt for Materialteknologi.
3. Thaulow, C., Ødegård, J., and Østby, E., *Arctic Steels. Criteria for safe materials utilisation*, in *Internasjonal konferanse*. 2006: St Petersburg.
4. ArcelorMittal USA, *Plate- 9% Nickel Steel: For use at cryogenic temperatures*, ArcelorMittal USA, Editor. 2010.
5. Nippes, E.F. and Balaguer, J.P., *A study of the weld heat-affected zone toughness of 9% nickel steel.* Weld. Res. (Miami), 1986(Sept.): p. 237S-243S.
6. Syn, C.K., Fultz, B., and Morris, J.W., Jr., *Mechanical stability of retained austenite in tempered 9Ni steel.* Metall. Trans., A, 1978. **9A**(11): p. 1635-40.
7. Bhadeshia, H.K.D.H. and Honeycombe, R.W.K., *Steels: microstructure and properties*. 2006, Amsterdam: Elsevier. XI, 344 s. : ill.
8. Larsen, K., *Mikrostrukturkarakterisering av et 9%Ni stål ved hjelp av EBSD*, in *Institutt for Materialteknologi*. 2011, Norges teknisk- naturvitenskapelige universitet: Trondheim.
9. Wenn, M., *9 % Nikkel stål: Karakterisering av mikrostruktur ved hjelp av SEM og EBSD*, in *Institutt for Materialteknologi*. 2013, Norges teknisk- naturvitenskapelige universitet: Trondheim.
10. Swartzendruber, L.J., Itkin, V.P., and Alcock, C.B., *The Fe-Ni (iron-nickel) system.* Journal of Phase Equilibria, 1991. **12**(3): p. 288-312.
11. International Institute of Welding, *Guide to the Welding and Weldability of Cryogenic Steels, Document IIS/IIW-844-87, Sub-commission IXG of Commission IX of the International Institute of Welding*. 1987.
12. Pense, A.W. and Stout, R.D., *Fracture Toughness And Related Characteristics Of The Cryogenic Nickel Steels.* Welding Research Council Bulletin, 1975: p. 43.
13. JFE Steel, *9% Ni Steel with High Brittle Crack Arrestability*, in *JFE Technical Report*. 2008. p. 29-31.
14. ASTM International, *Standard Specification for Pressure Vessel Plates, Alloy Steel, Double-Normalized and Tempered 9 % Nickel*. 2009.
15. Andrews, K.W., *Empirical formulas for the calculation of some transformation temperatures.* J. Iron Steel Inst., London, 1965. **203**(7): p. 721-7.
16. Davis, C.L. and King, J.E., *Cleavage initiation in the intercritically reheated coarse-grained heat-affected zone: Part I. Fractographic evidence.* Metallurgical and Materials Transactions A, 1994. **25**(3): p. 563-573.
17. Easterling, K.E., *Introduction to the physical metallurgy of welding*. 1992, Oxford: Butterworth-Heinemann. 270 s. : ill.
18. Tipler, P.A. and Mosca, G., *Physics for Scientists and Engineers, Volume 1*. 6th ed. 2008, New York: NY: Worth Publishers.
19. Ikawa, H., Oshige, H., and Tanoue, T., *Effect of Martensite-Austenite Constituent on HAZ Toughness of a High Strength Steel.* Transactions of the Japan Welding Society, 1980. **11**(2): p. 87-96.

20. Morris, J.W., Kinney, C., Pytlewski, K., and Adachi, Y., *Microstructure and cleavage in lath martensitic steels.* Science and Technology of Advanced Materials, 2013. **14**(1).
21. Schwarzer, R.A., Field, D.P., Adams, B.L., Kumar, M., and Schwartz, A.J., *Present State of Electron Backscatter Diffraction and Prospective Developments*, in *Electron Backscatter Diffraction in Materials Science*. 2009. p. 1-20.
22. Hjelen, J., *EBSD*. 2013, NTNU: Trondheim.
23. Hjelen, J., *Scanning elektron-mikroskopi*. 1986, Trondheim: Metallurgisk Institutt, NTH.
24. Field, D.P., *Improving the Spatial Resolution of EBSD.* Microscopy and Microanalysis, 2005. **11**(SupplementS02): p. 52-53.
25. Humphreys, F.J., *Review - Grain and subgrain characterisation by electron backscatter diffraction.* Journal of Materials Science, 2001. **36**(16): p. 3833-3854.
26. Chen, Y., Hjelen, J., Gireesh, S.S., and Roven, H.J., *Optimization of EBSD parameters for ultra-fast characterization.* J. Microsc. (Oxford, U. K.), 2011. **245**(2): p. 111-118.
27. Nowell, M.M. and Wright, S.I., *Orientation effects on indexing of electron backscatter diffraction patterns.* Ultramicroscopy, 2005. **103**(1): p. 41-58.
28. Wright, S.I. and Nowell, M.M., *EBSD image quality mapping.* Microsc. Microanal., 2006. **12**(1): p. 72-84.
29. *OIM Analysis 5.3 Manual.*
30. Field, D.P., *Recent advances in the application of orientation imaging.* Ultramicroscopy, 1997. **67**(1-4): p. 1-9.
31. Karlsen, M., Hjelen, J., Grong, O., Rorvik, G., Chiron, R., Schubert, U., and Nilsen, E., *SEM/EBSD based in situ studies of deformation induced phase transformations in supermartensitic stainless steels.* Materials Science and Technology, 2008. **24**(1): p. 64-72.
32. Nolze, G., *Characterization of the fcc/bcc orientation relationship by EBSD using pole figures and variants.* Z. Metallkd., 2004. **95**(9): p. 744-755.
33. Schwarzer, R.A. and Hjelen, J., *High-speed orientation microscopy with offline solving sequences of EBSD patterns.* Diffus. Defect Data, Pt. B, 2010. **160**(Texture and Anisotropy of Polycrystals III): p. 295-300.
34. Nakamichi, H., Humphreys, F.J., and Brough, I., *Recrystallization phenomena in an IF steel observed by in situ EBSD experiments.* Journal of Microscopy, 2008. **230**(3): p. 464-471.
35. Lischewski, I., Kirch, D.M., Ziemons, A., and Gottstein, G., *Investigation of the α−γ−α Phase Transformation in Steel: High-Temperature In Situ EBSD Measurements.* Texture, Stress, and Microstructure, 2008. **2008**.
36. Watanabe, T., Obara, K., and Tsurekawa, S., *In-situ observations on interphase boundary migration and grain growth during α/γ phase transformation in iron alloys.* Mater. Sci. Forum, 2004. **467-470**(Pt. 2, Recrystallization and Grain Growth): p. 819-824.
37. Enstad, A.-J., *Utvikling og utprøving av varmebord for in situ EBSD-karakterisering av stål i SEM*. 2010: Norwegian University of Science and Technology, Department of Materials Science and Engineering.
38. Enstad, A.-J., *EBSD characterization of a HSLA steel during in situ heating*. 2011: Norwegian University of Science and Technology, Department of Materials Science and Engineering. p. 132.
39. Hansen, K.W., *Phase Transformation Study of Arctic Steel by EBSD during in Situ Heating and Quenching*. 2012: Norwegian University of Science and Technology, Department of Materials Science and Engineering.

40. Sætran, T.G., *Utvikling av metode for bråkjøling i SEM og in situ EBSD-karakterisering av fasetransformasjoner i F 70 stål.* 2012: Norwegian University of Science and Technology, Department of Materials Science and Engineering.
41. TSL/EDAX, *Specimen Preparation for Electron Backscatter Diffraction (EBSD) Analysis*.
42. Wynick, G.L. and Boehlert, C.J., *Use of electropolishing for enhanced metallic specimen preparation for electron backscatter diffraction analysis.* Materials Characterization, 2005. **55**(3): p. 190-202.
43. Jahrsengene, G., *EBSD microstructure characterization of weld simulated 9% nickel steel*. 2014: Norwegian University of Science and Technology, Department of Materials Science and Engineering.
44. Chiron, R., Fryet, J., and De Lesegno, P.V., *DEVICE FOR SEM AND EBSP IN SITU TENSILE TESTS UP TO 800°C*, in *Local Strain and Temperature Measurement*, J. Ziebs, et al., Editors. 1999, Woodhead Publishing. p. 149-158.
45. Fukino, T. and Tsurekawa, S., *In-situ SEM/EBSD observation of α/γ phase transformation in Fe-Ni alloy.* Mater. Trans., 2008. **49**(12): p. 2770-2775.
46. Wright, S.I., Nowell, M.M., de Kloe, R., Camus, P., and Rampton, T., *Electron imaging with an EBSD detector.* Ultramicroscopy, 2015. **148**(0): p. 132-145.
47. Kim, K.J. and Schwartz, L.H., *On the effects of intercritical tempering on the impact energy of Fe・9Ni・0.1C.* Materials Science and Engineering, 1978. **33**(1): p. 5-20.
48. Strife, J.R. and Passoja, D.E., *The effect of heat treatment on microstructure and cryogenic fracture properties in 5Ni and 9Ni steel.* Metall. Trans., A, 1980. **11A**(8): p. 1341-50.
49. Syn, C.K., Morris, J.W., and Jin, S., *Cryogenic fracture toughness of 9Ni steel enhanced through grain refinement.* Metallurgical Transactions A, 1976. **7**(12): p. 1827-1832.
50. Beil, W. and Carlsen, I.C., *Surface reconstruction from stereoscopy and "shape from shading" in SEM images.* Machine Vision and Applications, 1991. **4**(4): p. 271-285.
51. Podsiadlo, P. and Stachowiak, G.W., *Characterization of surface topography of wear particles by SEM stereoscopy.* Wear, 1997. **206**(1–2): p. 39-52.

# Appendix A ISOPE Conference Paper

## EBSD Quantification of Retained Austenite in 9% Ni Steel Related to Thermal Treatments

*G. Jahrsengene[1], M. Wenn[1], M. Karlsen[1,2], I. Westermann[1], O.M. Akselsen[1,3], J. Hjelen[1]*
[1]Norwegian University of Science and Technology(NTNU), [2]Statoil ASA, [3]SINTEF
Trondheim, Norway

ABSTRACT

The present work involves quantification of retained austenite in a low carbon 9% nickel steel designed for storage of liquefied natural gases (LNG) at cryogenic temperatures. Investigations were carried out in a high resolution field emission scanning electron microscope (FESEM) using Electron Backscatter Diffraction (EBSD) measurements. Weld simulated steel was examined by this technique to determine which combination of heating cycles gave the highest amount of austenite in the resulting steel, the retained austenite being a very important parameter considering low temperature use. The as-received material was also investigated with respect to austenite content.

KEY WORDS: Arctic steel; 9% nickel steel; retained austenite; EBSD; XRD; weld simulation

INTRODUCTION

Oil and gas production in arctic environments has become an interesting target for oil companies worldwide in recent years. United States Geological Survey assessed the area north of the Arctic Circle, and concluded that approximately 30% of the remaining gas reserves and 13% of oil reserves may be found in this region of the world (Gautier et al., 2009). Knowledge about the microstructure that forms during heat treatments of steel is of uttermost importance, because the combination of low temperature and unwanted phases formed during welding increase the probability of brittle fracture.

The good low temperature toughness of the 9% Ni steel is believed to come from stable retained austenite phases in an otherwise tempered martensitic matrix. 9% nickel steel has, depending on precise production parameters, 5-15 volume% retained austenite (Syn et al., 1978; Nippes and Balauger, 1986; ArcleorMittal USA, 2010). It is well known how the mechanical properties are affected by changes in the microstructure during welding of the material (Nippes and Balauger, 1986; Bhadeshia and Honeycombe, 2006), and this might influence the good low temperature properties. Earlier investigations have shown that thermal cycling to different peak temperatures significantly decreases the retained austenite content, and this will reduce the impact toughness at cryogenic temperatures (Nippes and Balauger, 1986).

In the present work the microstructure is examined after weld simulations. The main objective is to find out how the low temperature properties change with respect to future use in arctic environments, with focus on the quantity of retained austenite. The welding cycles are completed ex situ before examination. The characterization and quantification is done using the EBSD technique.

The EBSD technique is based on the signal received from the backscattered electrons that meet Bragg's law of diffraction. This signal, the electron backscattered diffraction pattern (EBSP), is unique depending on both crystal structure (e.g. austenite and ferrite in steels) and crystal orientation (e.g. different grains in a polycrystal). The sample is tilted 70° inside the SEM, and the diffraction patterns are captured on a phosphor screen originating from a thin top layer of approximately 50 nm. The modern EBSD system enables the user to predefine an area to be scanned, and use of offline indexing to be carried out on the saved patterns gives a very high scanning speed (Schwarzer and Hjelen, 2010; Chen et al., 2011). The EBSD technique can be used to obtain a large variety of information about the microstructure of the material, which again can be used to draw conclusions about the mechanical properties of the material.

When a phase transition from austenite to martensite during a displacive transformation occurs, there can be a correspondence between the close-packed planes in the original and resulting phase. These planes are usually parallel, or nearly parallel, to each other (Bhadeshia and Honeycombe, 2006). This orientation relationship is called the Kurdjumov-Sachs (KS) relationship. There are 24 different possibilities for the orientation of the resulting martensite from one austenite orientation. While analyzing the (001)-pole figures of the scan the austenite pole figure can be rotated giving it a cube orientation, and the experimental pole figure obtained from the EBSD results of the martensite directly in contact with this austenite phase can be compared to the theoretical KS-orientations.

The aim of the study is to investigate the initial and final stage of different welding cycles of the 9% Ni steel by use of weld simulation, with the aim to determine the quantity of the austenite phase using EBSD. A determination of the intercritical temperature range during fast heating will also be conducted, by investigating the volume change during the heating using a dilatometer, as well as hardness measurements of the resulting microstructure. The as-received steel is investigated by use of both the X-ray diffraction technique as well as EBSD to examine the microstructure prior to heat treatment.

EXPERIMENTAL

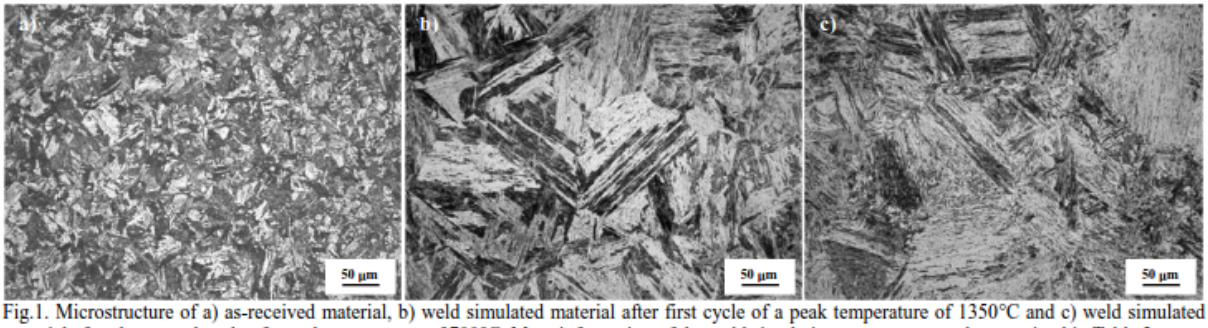


Fig.1. Microstructure of a) as-received material, b) weld simulated material after first cycle of a peak temperature of 1350°C and c) weld simulated material after the second cycle of a peak temperature of 700°C. More information of the weld simulation parameters can be examined in Table 3.

**The Material**

The material used in the present study is a low carbon 9 % nickel steel designed for storage of LNG at cryogenic temperatures. The steel used for this purpose has a design temperature of -196°C. The as-received material has been subjected to heat treatment giving it a tempered martensitic structure with 5-15% stable retained austenite, in this case reheat, quenched and tempered (RQ-T) process. The microstructure of the as-received material can be examined in Fig. 1a.

**Sample Preparation**

The sample surface was prepared for SEM and EBSD by standard metallographic preparation technique, including mechanical grinding and polishing, followed by electropolishing at room temperature. The parameters electrolyte and polishing time was varied when investigating the as-received material. The relevant parameters are presented in Table 1. The electropolishing was done with a Struers Lectopol-5.

Table 1. The parameters for the electropolishing. The variable parameters are the electrolyte and the polishing time.

| | |
|---|---|
| Electrolyte | Struers A2 and A3 |
| Voltage | 24 V |
| Time | 1, 2, 5, 10 minutes |
| Flow rate | 14 |
| Temperature | 20°C |
| Area | 2 $cm^2$ |

Based on the results the A3 electrolyte and shortest time was chosen when preparing the weld simulated steel. Prior to EBSD investigation the samples were cleaned in an ultrasonic bath of acetone for approximately 5 minutes before plasma cleaning for 5-10 minutes.

One as-received sample was investigated with X-ray diffraction (XRD) analysis technique. The preparation for this investigation was similar to the one used for EBSD preparation. The A3 electrolyte was used, and a higher voltage because of a larger area was to be prepared. Plasma cleaning was not necessary for this technique.

The optical micrographs presented in Fig. 1 were taken with a Leica MEF4M light microscope with software ProgRes Capture Pro 2.8.8. After mechanical grinding and polishing the surface was etched with Marble's Reagent for 6 seconds.

**X-ray Diffraction Analysis**

For the XRD analysis the as-received sample was investigated with a D8 DaVinci machine, $K_\alpha$ from Cu in the area $35° \leq 2\theta \leq 105°$ with steps of 0.02°. The data was analyzed with software Diffracplus Topas 4.2. The method, quantitative Rietveld analysis, compares experimental values with theory. This technique gives a larger penetration depth (3 µm) than the EBSD technique (50 nm) (Wege and Wendrock). Table 2 gives the structural parameters used for the Rietveld analysis.

Table 2. Structural parameters for use of Rietveld analysis.

| | |
|---|---|
| Unit cell profile, austenite | Fm-3m |
| Unit cell length, austenite | 3.59 Å |
| Unit cell profile, martensite | I4/mmm |
| Unit cell length, martensite | 2.86 Å |

**Welding Simulation**

When investigating the steel with respect to welding properties all samples were subjected to a single or double cycle weld simulation program using an inhouse weld simulator unit based on resistance heating principles. The first cycle had a maximum peak temperature of 1350°C with subsequent cooling time between 800 and 500°C, $\Delta t_{8/5}$, of 15 seconds. The cooling time $\Delta t_{x/y}$ for the second cycle differs in each of the samples, as the peak temperature is different. The samples subjected to double cycles had a second peak temperature as presented in Table 3 together with relevant cooling times. The cooling times were chosen to correspond to the time spent in the relevant temperature interval during the first cycle. A dilatometer was used during the experiments, to detect the transformation temperature during fast heating.

Table 3. The data for the second cycle during the weld simulation, with the measured peak temperatures ($T_p$). The cooling time $\Delta t_{x/y}$, i.e. from 600 to 400°C, $\Delta t_{6/4}$, depends on the peak temperature and temperature interval.

| Sample Number | Measured peak temperature $T_p$ | Cooling time $\Delta t_{x/y}$ |
|---|---|---|
| 1* | - | - |
| 2 | 793°C | $\Delta t_{6/4}$=17s |
| 3 | 696°C | $\Delta t_{6/4}$=18s |
| 4 | 597°C | $\Delta t_{5/3}$=31s |
| 5 | 496°C | $\Delta t_{4/2}$=65s |
| 6 | 399°C | $\Delta t_{3/2}$=48s |

*Sample 1 only exhibited a single welding cycle, for reference.

The microstructure of sample 1 and 3, i.e. after one and two weld simulation cycles, respectively, are shown in the optical micrographs in Fig.1b and c.

### EBSD Observations

The EBSD measurements were carried out in a Zeiss 55 Ultra FESEM attached with a NORDIF detector for high speed EBSD data collection and offline EBSD indexing. Post processing of the diffraction patterns was carried out using TSL OIM software. The EBSD investigations were conducted using an accelerating voltage of 20 kV, a tilt angle of 70°, an aperture size of 300 µm in high current mode. The working distance was between 19 and 22 mm. All six weld simulated samples, as well as several of the as-received specimen, was investigated with the technique.

The investigated area of the weld simulated sample was 80x80 µm$^2$ with a step size of 0.2 µm. This gave an acquisition time for the EBSD mapping of about 8 minutes. The cleaning operations used on the raw data is *Grain CI Standardization* and a *CI filter* removing data with CI<0.05. The data is represented by inverse pole figure (IPF) maps showing a color representing the direction that is perpendicular to the surface, giving a partial crystallographic orientation of the grain. The austenite content is investigated using phase maps, where green color indicates FCC structure and austenite, and red color BCC structure and ferrite (in our case the BCT martensite). The average Confidence Index (CI) and Fit-values of the phase could help indicate if the patterns were correctly indexed. CI-values are between 0 and 1, with a high CI the program is fairly confident that the pattern is indexed correctly. The Fit-value describes the average angular difference between the detected bands in the diffraction pattern, and the corresponding bands reconstructed from the program's orientation solution. A value close to 1 is good (Nowel and Wrigth, 2005). The quality of the remaining austenite could be investigated by looking at the rotated pole figure of the two phases of a confined area using Kurdujmov-Sachs orientation relationship.

### Microhardness

Hardness tests were done using a Matsuzawa model LVK-1S, with 5 kg loading, 15 seconds loading time and a loading speed of 100 µm/s. The measurements were taken across the middle of the weld where the temperature was the highest during the simulation, and one millimeter at each side. A millimetric screw was used to get measurements with equal distance. At each indentation three readings were done to get the uncertainty of each point.

## RESULTS

### As-Received Material

The received material is proposed to have a martensitic structure with 5-15% stable retained austenite. The austenite contents after the cleaning operations are 0.5-2.0% in the different scans. The IPF map in Fig. 2a indicates a martensitic structure, and the phase map in Fig. 2b a very low austenite content of 0.5%.

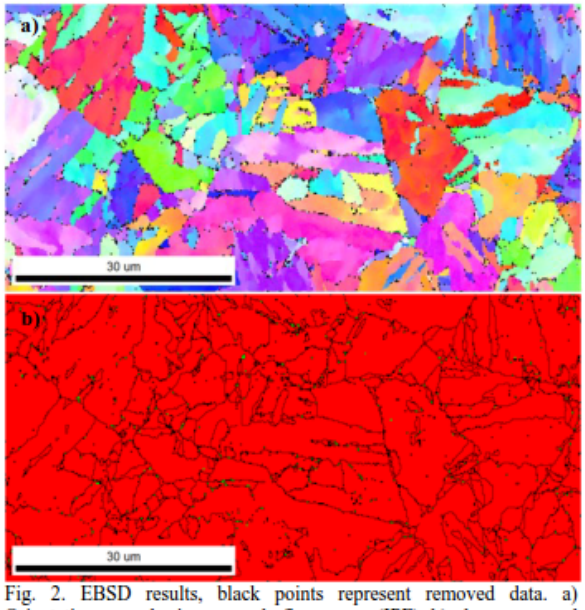


Fig. 2. EBSD results, black points represent removed data. a) Orientation maps by inverse pole figure map (IPF), b) phase map; red ferrite (martensite) and green austenite.

The X-ray diffraction analysis gave an austenite fraction of 1.6% in the as-received material.

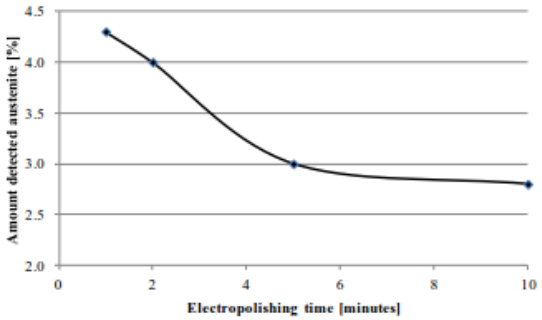


Fig. 3. The amount of austenite plotted with respect to polishing time with the Struers A3 electrolyte.

The A2 electrolyte did not give good enough preparation with 2 and 10 minutes polishing, so the amount of retained austenite was not determined in these experiments. A2 gave smaller amount of indexed

points than A3 in all experiments, as well as lower average quality of the scan. Comparing the austenite content using A2 and A3, the A2 electrolyte gave varying results with not clear trends, while the amount of retained austenite detected when using A3 decreased with increasing polishing time. This is presented in Fig. 3 (note: raw data without cleaning operations).

**Weld Simulated Material**

The two phase region of the phase diagram could be observed to be very narrow by looking at the dilatometric analysis, approximately 660 to 750°C. The dilatometric results are presented in Fig. 4, with $Ac_1$ as the transition temperature for fast heating from ferrite to austenite, and $Ac_3$ from austenite to ferrite, also during rapid heating. The temperature lines representing these transition temperatures in Fig. 4 is placed in association with the slowest heating rate, and is when the slope goes from being constant ($Ac_1$) and to being constant again after the intercritical region ($Ac_3$).

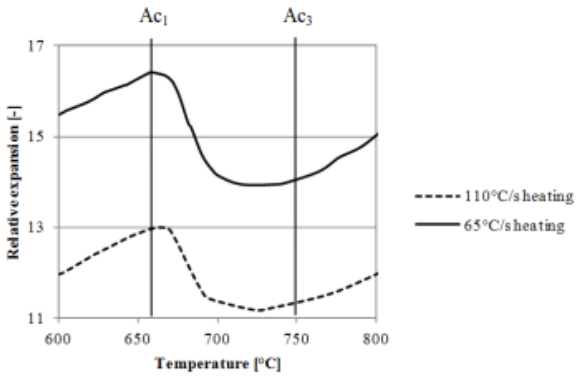


Fig. 4. Dilatometric analysis for two different heating rates. The intercritical temperature range is approximately between 660 and 750°C. Note that the expansion values are relative, giving non-comparable values on this axis.

The average of all hardness measurements across the weld has been plotted against the temperature of the second welding cycle in Fig. 5.

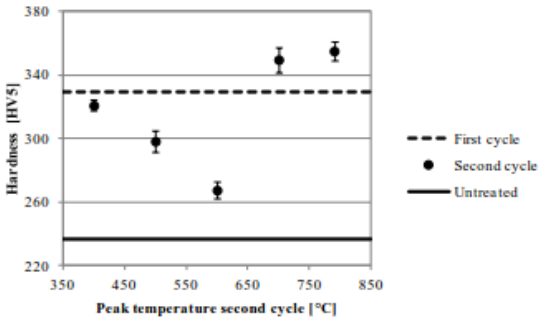


Fig. 5. The hardness of the samples with respect to the peak temperature of the second welding cycle. The hardness of the untreated material and the hardness after the first welding cycle can be used as references.

The microstructure and phase distribution of sample 1, heated to 1350°C, is presented in Fig. 6. Large grains with different forms of lath martensite inside each of the grains can be observed. The same is seen in the representation of sample 4, heat treated with a successive second weld cycle of 600°C, in Fig. 7. The austenite content is almost negligible in both cases, below 0.5%. However, there are few more pronounced austenite islands in the right side of Fig. 7b.

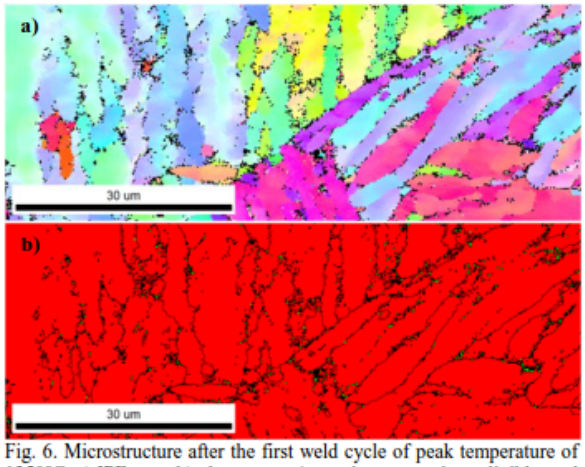


Fig. 6. Microstructure after the first weld cycle of peak temperature of 1350°C, a) IPF map, b) phase map. Austenite content is negligible, and the martensite phase is coarse grained with pronounced laths.

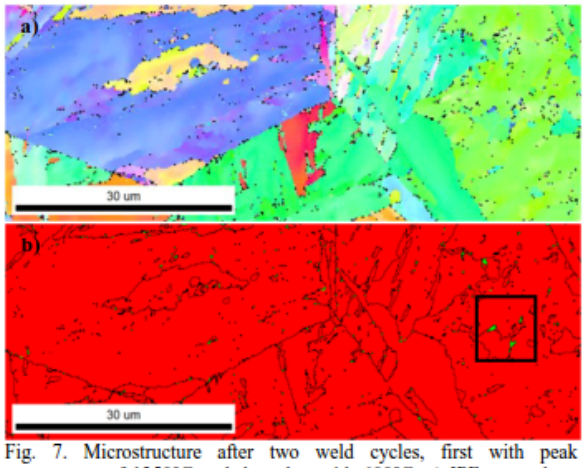


Fig. 7. Microstructure after two weld cycles, first with peak temperature of 1350°C and the other with 600°C. a) IPF map where coarse grains with martensite laths are observed, b) phase map. Austenite content is almost negligible, with some pronounced green islands in the right side of the phase map (square).

Investigation of sample 3 (heated to 700°C, Fig. 9) give small grains in the IPF map in combination with pronounced, large islands of austenite near high angle grain boundaries in the phase map. The austenite content is 1.5%, and is present in association with grain boundaries.

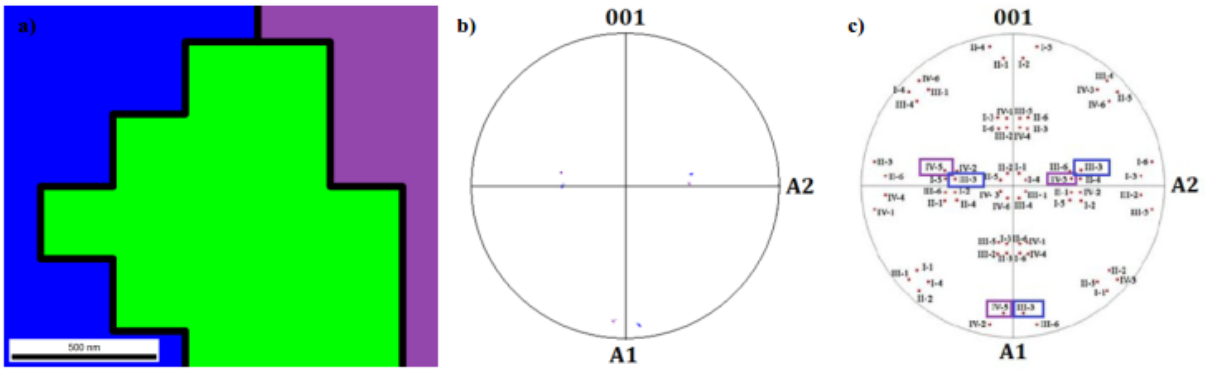


Fig. 8. The quality of the a) chosen austenite island is represented by the b) experimental rotated pole figure showing two orientations, and c) the standard pole projections with the 24 possible K-S martensite variants (Karlsen et. al., 2008), from a single austenite orientation (the experimental values are marked).

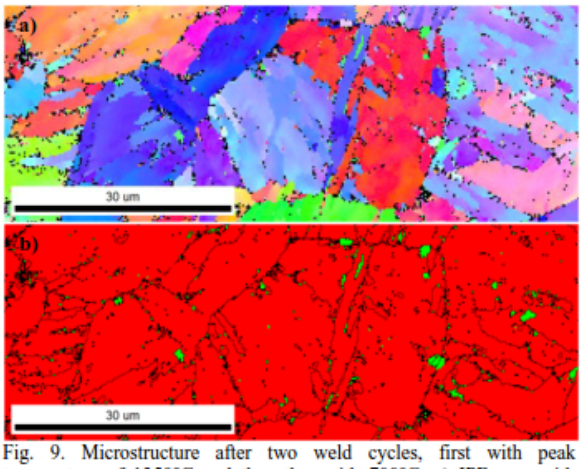


Fig. 9. Microstructure after two weld cycles, first with peak temperature of 1350°C and the other with 700°C. a) IPF map with smaller grains and some martensite laths are observed, b) phase map where the green austenite is quite pronounced.

The quality of the austenite was investigated by looking at the pole figures of the martensite and austenite phase around a specific island, as seen in Fig. 8. The experimental results match the theory quite well, with the III-3 marked blue and the IV-5 orientation marked purple.

Further investigation of the quality of the retained austenite was accomplished by looking at the quality data of some of the larger austenite areas. Investigating the average Confidence Index (CI) and Fit values for the areas in Fig. 10, both of these are near the ideal values of 1. CI is 0.79 in both cases, and the Fit is 1.09 and 1.28, respectively.

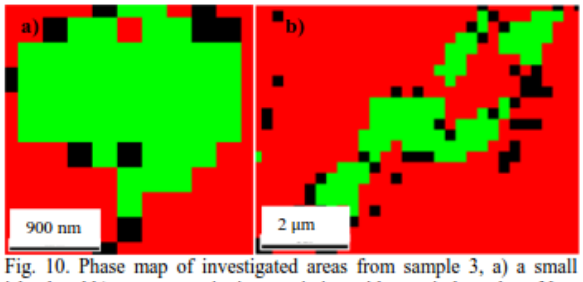


Fig. 10. Phase map of investigated areas from sample 3, a) a small island and b) more austenite in association with a grain boundary. Note the different magnifications.

## DISCUSSION

The low amount of austenite detected in the results of the as-received material in both EBSD and using XRD rise some confusion about the preparation method for all experiments. The electrochemical polishing is a "try and fail" method for finding the appropriate parameters, and the parameters might not be optimized for this particular steel. According to the graph in Fig. 3, the quantity of detected austenite is also dependent on the polishing time, as well as different electrolytes giving different result. Previous work (Enstad, 2011) using the same machine (Struers Lectopol-5) have shown similar results, with the only changing parameter being the electrolyte, and the quantity austenite of the relevant steel being different with a factor 8. Why this is the case has not been discovered.

However, the good quality of the main bulk of the detected EBSPs rise questions about the original amount of austenite in the as-received steel, and the stability of this austenite. It is possible that the material was not subjected to the tempering process giving it 5-15% retained austenite, but at the same time it has been processed giving it a relatively small grained microstructure as seen in Fig. 1a (optical microscopy) and Fig. 2a (IPF map). The production parameters from the producer are not precise, and a possibility is that the temperature of the reheating might not have been ideal to form stable austenite before the quenching. To be sure about this, more investigations concerning the original production parameters and retained austenite content would have to be performed on the as-received material, i.e. investigating the grain size distribution by high resolution SEM or TEM. If it turns out

that the average size or the retained austenite is very small, i.e. 0.4 µm or less, the chosen step size of 0.2 µm will not be fine enough to ensure good detection of the phase in question.

Another possibility is the presence of a deformation layer that has not been properly removed during preparation, which can affect the EBSD patterns. Also, if the austenite is not stable it can be subjected to deformation induced martensite transformation (Lecroisey and Pineau, 1972), giving a lower amount of austenite. A deeper penetration depth for the XRD technique should avoid this problem, and the amount of austenite do increase from 0.5% detected with the EBSD technique to 1.6% detected with XRD. This might indicate that the step size in EBSD do not give precise enough patterns, but the XRD-result is still much lower than the predicted amount of 5-15%. The results still point to the preparation method not being ideal or the production parameters are not optimized to form the stable austenite.

The low amount of austenite observed in the weld simulated material can be explained by the original production procedure of the as-received material: the steel is tempered in the lower part of the two phase region of the phase diagram. The austenite formed during this process is enriched with austenite stabilizers (e.g. Ni and C), making it stable at room temperature. During high temperature welding the austenite phase will most likely lose its stability, as the whole microstructure changes to austenite before rapid cooling resulting in a martensitic structure without much retained austenite. This is well known (Nippes and Balauger, 1986). The high temperature gives coarse grains, as seen when comparing the as-received material in Fig. 2a with the microstructure after the first welding cycle in Fig. 6a. When the second peak temperature is 600°C and below, the dilatometric results in Fig. 4 states that the transformation temperature to form austenite has not been achieved. This heat treatment will only give a tempering of the coarse grained structure, as the EBSD result in Fig. 7a shows.

The hardness data in Fig. 5 indicate this as well, as the hardness decrease with increasing temperature on the second cycle in the temperature interval 400-600°C. The hard martensitic microstructure achieved after the first weld cycle is only tempered when being treated to these temperatures on the second cycle, as both EBSD results and hardness results clearly states. After a second peak temperature of 700°C the hardness increases with increasing temperature. This obviously comes from a change in microstructure, as the dilatometer analysis show that 700°C is in the middle of the intercritical interval. This means that some of the coarse grained martensite obtained after the first cycle will transform to austenite at the highest temperature, before rapid cooling transforms it back to martensite. This will give a microstructure with partially smaller grains, and smaller grains will give a harder microstructure than the reference after the first cycle as it only had large, coarse grains. The rod heated to the highest temperature of 790°C most likely reached a completely austenitic microstructure before fast cooling. As the temperature just exceed the $Ac_3$ temperature the austenite will be very fine grained, and after fast cooling a hard martensitic structure from small grains will have formed. Small grains and a martensitic structure will have a high hardness compared to the tempered, as-received material with low hardness, as well as the coarse martensite grains obtained after the first cycle.

The sample heated to 700°C, as presented in Fig. 9, seems to be in the middle of the intercritical temperature interval according to the dilatometric curve in Fig. 4. This second welding cycle is the one -most similar to the original production parameters. The austenite formed during the second cycle will be more stable, just as during production, and thus more austenite is detected in this phase after fast cooling. This is also evident when looking at the hardness results in Fig. 5, as the smaller grains formed in the intercritical temperature interval will give a higher hardness than the larger grains obtained after the first cycle. Besides the more obvious austenite islands present in the phase map in Fig. 9b, when comparing the IPF maps in Fig. 2a and 9a, the size of the grains seems more similar here than in the other cases. The microstructure in sample 3 can be categorized as intercritically reheated coarse grained heat affected zone (ICCGHAZ) (Davis and King, 1994; Bhadeshia and Honeycombe, 2006).

Looking at the results from sample 3 in Fig. 8, 9 and 10, the change in microstructure and austenite content comparing to the previous results can easily be observed. The smaller grains come from the recrystallization that occurs when the austenite forms in the intercritical temperature interval. The phase map clearly shows several areas with retained austenite. The austenite has formed in association with grain boundaries, and further investigation of the data from the austenite in Fig. 10 gives good CI and Fit-values. It seems that the EBSD-technique managed to detect the correct phase. Knowing about the Kurdujmov-Sachs orientation relationship between the original austenite and the resulting martensite can also help qualify that the detected austenite indeed is austenite and not wrong indexed martensite. Fig. 8 clearly shows that two martensite orientations are produced by the chosen austenite phase, as all three areas needed in the theoretical pole figure are also present in the experimental figure. This means that the martensite is formed during a displacive transformation (Karlsen et. al., 2008). The austenite content after this heat treatment is still low, but comparing the phase map in Fig. 9a with the others it seems like the small amounts detected in the other scans (including the as-produced) are likely to be either wrong indexed martensite or negligible.

## CONCLUSIONS

Based on the present investigations some conclusions can be drawn:

The low carbon 9% Ni steel has mainly a martensitic microstructure, both before and after weld simulation.

- The quantity of austenite is negligible when investigating the as-received material using the EBSD technique. This is not according to theory (5-15% retained austenite).
- Further quantity analysis using XRD on the as-received steel still gave a low austenite quantity of 1.6%, although this was as increase from the amount detected with EBSD (after cleaning).
- The preparation methods might not be ideal for the EBSD investigations, as the austenite is not easily indexed.
- The size of the retained austenite phase, especially in the as-received material, might be too small to be detected with the chosen step size of 0.2 µm in EBSD.
- The intercritical temperature interval for this steel during rapid heating is between 660 and 750°C based on the dilatometric results.
- The microhardness results also gave a phase transformation between 600 and 700°C.
- The steel weld simulated to achieve ICCGHAZ, with the second weld cycle of 700°C, is the only specimen with a non negligible amount of austenite, of 1.5% (after cleaning).
- The quality of the austenite phase is confirmed using Kurdujmov-Sachs orientation relationship and looking at average CI and Fit-values.

ACKNOWLEDGEMENTS

The authors wish to thank the Research Council of Norway for funding through the Petromaks 2 Programme, Contract No.228513/E30. The financial support from ENI, Statoil, Lundin, Total, Scana Steel Stavanger, JFE Steel Corporation, Posco, Kobe Steel, SSAB, Bredero Shaw, Borealis, Trelleborg, Nexans, Aker Solutions, Marine Aluminium, FMC Kongsberg Subsea, Hydro and Sapa are also acknowledged.

REFERENCES

ArcleorMittal USA (2010). "Plate- 9% Nickel Steel: For use at cryogenic temperatures", *ArcleorMittal*, Editor

Bhadeshia, HKDH and Honeycombe, RWK (2010). "Steels: Microstructure and Properties", Amsterdam: Elsevier. XI, 344 s. : ill

Chen, Y et al., (2011). "Optimization of EBSD parameters for ultra-fast characterization." *J. Microsc.* (Oxford, U. K.). 245(2): p. 111-118.

Davis, CL, King, JE (1994). "Cleavage initiation in the intercritically reheated coarse-grained heat-affected zone: Part I. Fractographic evidence." *Metallurgical and Materials Transactions A*, **25**(3): p. 563-573.

Enstad, A-J (2011). "*EBSD characterization of a HSLA steel during in situ heating*", NTNU

Gautier, DL, Bird, KJ, Charpentier, RR, Grantz, A, Houseknecht, DW, Klett, TR, Moore, TE, Pitman, JK, Schenk, CJ, Schuenemeyer, JH, Sorensen, K, Tennyson, ME, Valin, ZC and Wandrey, JC (2009). "Assessment of Undiscovered Oil and Gas in the Arctic", *Science*, 324(5931): p. 1175-1179.

Karlsen, M, Hjelen, J, Grong, Ø, Rørvik, G, Chiron, R, Schubert, U, Nilsen, E (2008). "SEM/EBSD based in situ studies of deformation induced phase transformations in supermartensitic stainless steels." *Materials Science and Technology*, 24(1): p. 64-72.

Lecroisey, F, Pineau, A (1972). "Martensitic Transformations Induced by Plastic Deformation in the Fe-Ni-Cr-C System", *Metallurgical Transactions*, 1972, pp. 391-400

Nippes, EF and Balaguer, JP (1986). "A study of the weld heat-affected zone toughness of 9% nickel steel", *Weld. Res.* (Miami), p. 237S-243S.

Nowell, MM, and Wright, SI (2005). "Orientation effects on indexing of electron backscatter diffraction patterns." *Ultramicroscopy*, **103**(1): p. 41-58.

Schwarzer, RA and Hjelen, J (2010). "High-Speed Orientation Microscopy with Offline Solving Sequences of EBSD Patterns", *Solid State Phenomena*, Vol. 160, p. 295-300

Syn, C.K., Fultz, B and Morris Jr., JW (1978). "Mechanical stability of retained austenite in tempered 9Ni steel", *Metall. Trans., A*, 9A(11): p. 1635-40.

Thaulow, C, Ødegård, J and Østby, E (2006). "Arctic Steels. Criteria for safe materials utilisation" *The 7th International Conference "High technologies in advanced metal science and engineering"*, St. Petersburg, Russia.

Wege, S, Wendrock, H. *"Comparison between EBSD and X-Ray texture Measurement of high textured thin Al layers"*, IFW Dresden

# Appendix B  Assembly Manual for the In Situ Hot Stage

This manual is a guideline for the hardware installation of the in situ hot stage. Use gloves during the whole installation. If you are inexperienced in working with the equipment or feel uncomfortable with assembling the in situ stage, you should ask an experienced user for help.

## B.1  Required Tools

1 x 3,0 mm Allen wrench

1 x 2,5 mm Allen wrench

1 x 1,5 mm Allen wrench

1 x 0,9 mm Allen wrench

1 x Phillips screwdriver

A picture of the required tools is shown in Figure B.1.

**Figure B.1: Required tools for installation of hot stage.**

## B.2  Bill of Materials

Ensure that all of the items listed in the tables below are found. Be sure to take note of which part are listed as fragile and handle them with care as they easily break.

**Table B.1: In situ hot stage.**

| Item | Quantity | Notes |
|---|---|---|
| Hot stage | 1 | |
| Ceramic disk | 2 | Fragile |
| Stainless steel disk | 2 | |

The hot stage and the disks are shown in Figure B.2.

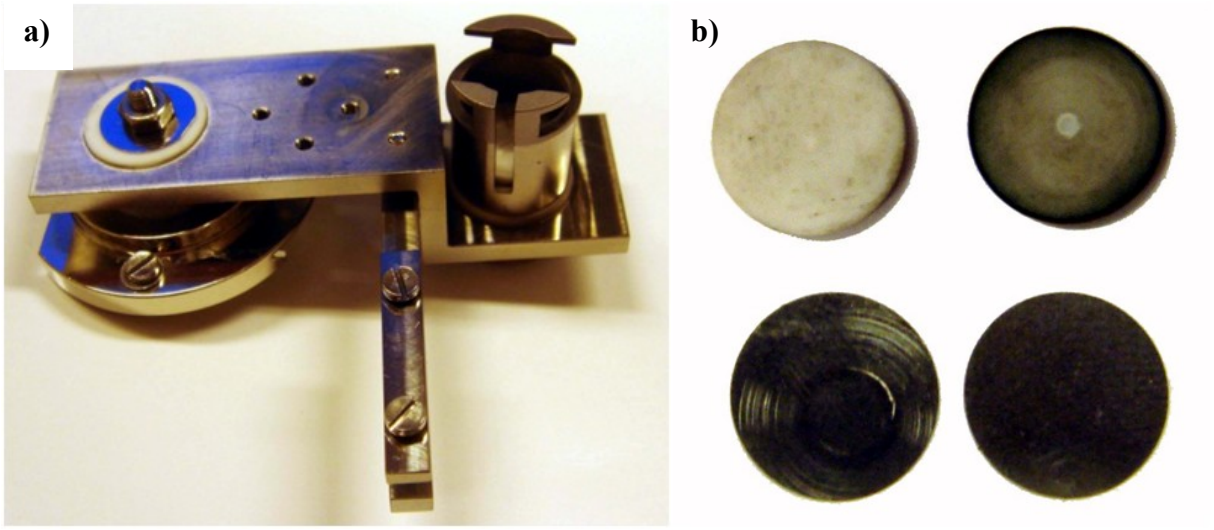


**Figure B.2: a) Hot stage and b) ceramic and stainless steel disks.**

The dimensions of the sample are given in Figure B.3. The width of the sample is not critical and can be larger than 11 mm. The height can vary between 2.5-3.5 mm. The hole should have a diameter of 0.55 mm and be about 2-3 mm deep (for a placing a thermocouple deep enough).

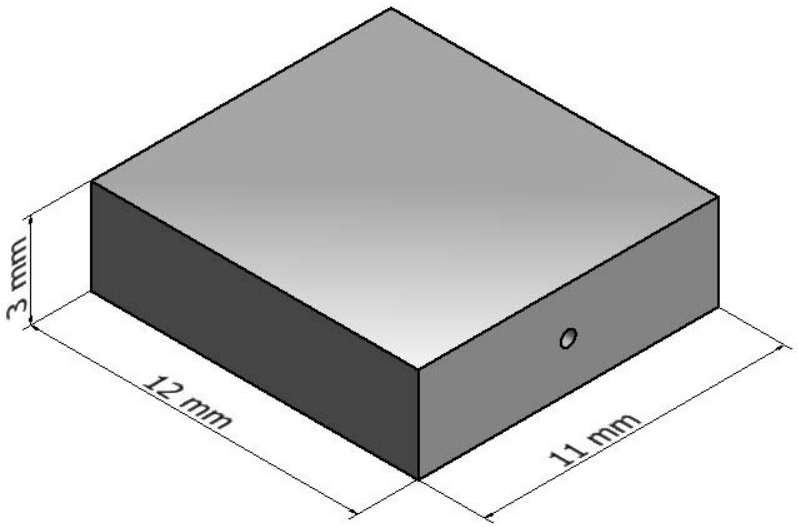


**Figure B.3: Sample dimensions.**

The different components the hot stage consists of is shown in Table B.2, and an overview of the hot stage with the components are marked in Figure B.4.

**Table B.2: The different components of the hot stage, with the item number corresponding to the same number in Figure B.4.**

| Item | Part | Quantity | Description | Material |
|---|---|---|---|---|
| 1 | Bracket | 1 | | Titanium |
| 2 | Holder | 1 | | Titanium |
| 3 | Screw | 1 | M6 x 9mm | Titanium |
| 4 | Fastener to the SEM | 1 | | Nickel plated brass |
| 5 | Screw | 1 | M3 x 15mm | Titanium |
| 6 | Disk | 2 | D=11mm | MACOR |
| 7 | Disk | 2 | D=11mm | Stainless steel |
| 8 | Washer | 4 | OD=15mm, ID=6mm | MACOR |
| 9 | Set screw | 1 | M2 x 4mm | Stainless steel |
| 10 | Hexagon nut | 1 | M3 | Stainless steel |
| 11 | Washer | 1 | M3 | Stainless steel |
| 12 | Washer | 6 | OD=14mm, ID=4mm | MACOR |
| 13 | Screw | 1 | M2 x 3mm | Stainless steel |
| 14 | Washer | 2 | M2 | Stainless steel |

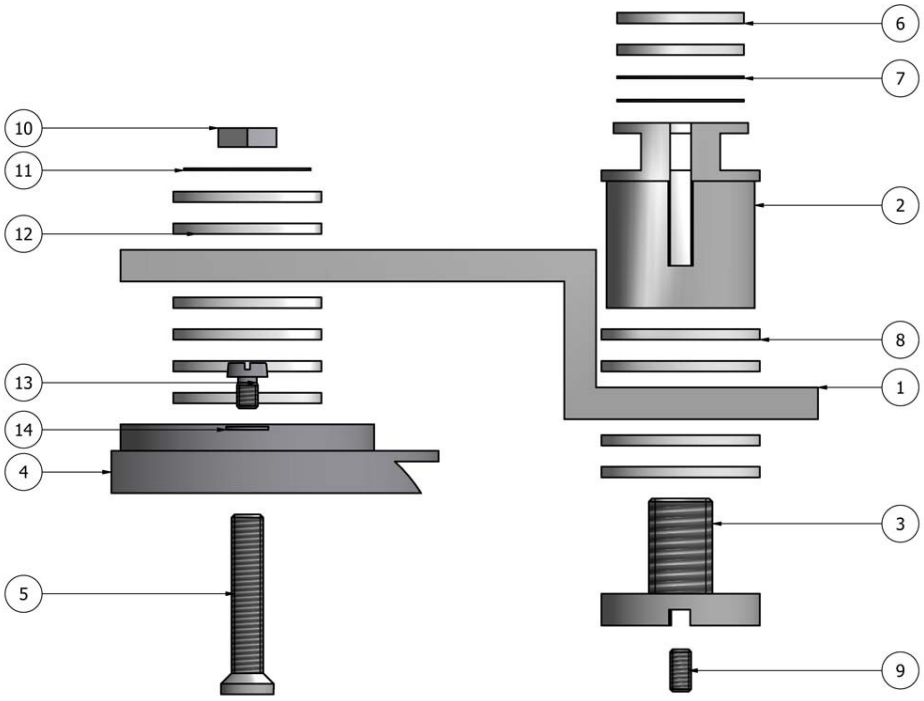


**Figure B.4: The different components the hot stage consist of, corresponding to numbering in Table B.2.**

The small furnace and the thermocouples for the furnace, sample and hot stage are listed in Table B.3, and shown in Figure B.5.

**Table B.3: Furnace and thermocouples for the furnace, sample and hot stage.**

| Item | Quantity | Notes |
|---|---|---|
| Furnace | 1 | |
| Thermocouples | 1 | For hot stage |
| Thermocouples | 1 | For furnace and sample. Fragile |

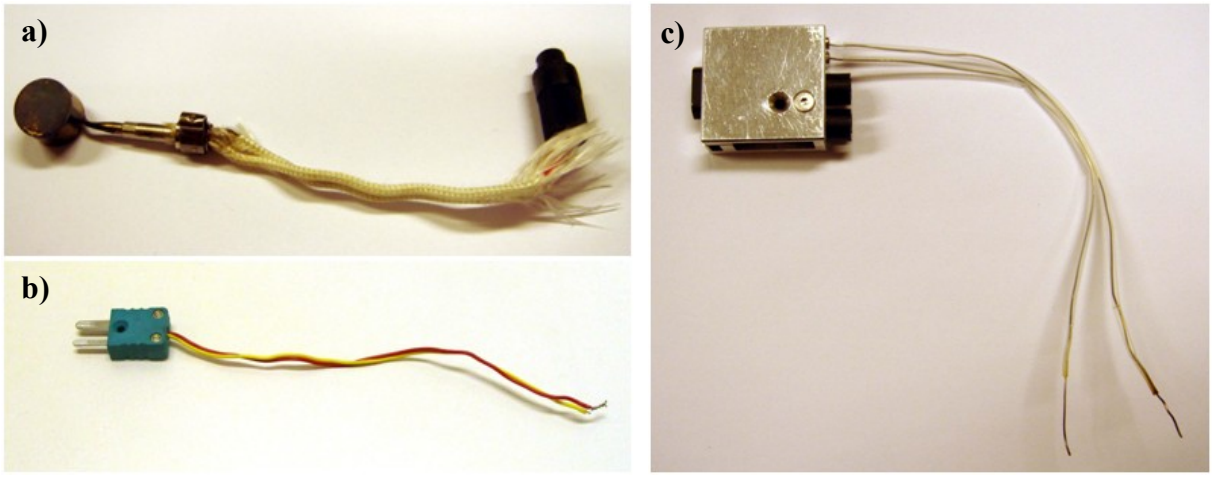


**Figure B.5: a) Furnace with plug, b) thermocouple to connect on hot stage and c) thermocouples for furnace and sample.**

The cables and connectors needed to get signals from the stage, inside the specimen chamber, to the loggers outside the SEM, are listed in Table B.4 and shown in Figure B.6.

**Table B.4: List of cables and connectors.**

| Item | Quantity | Notes |
|---|---|---|
| Heating cable | 1 | Fragile. Inside SEM |
| Thermocouple for hot stage | 1 | Inside SEM, sends signal through connector. |
| Connector for hot stage controller | 1 | |
| Cable to hot stage controller | 1 | Outside SEM |
| Cable to temperature logger | 1 | Outside SEM |

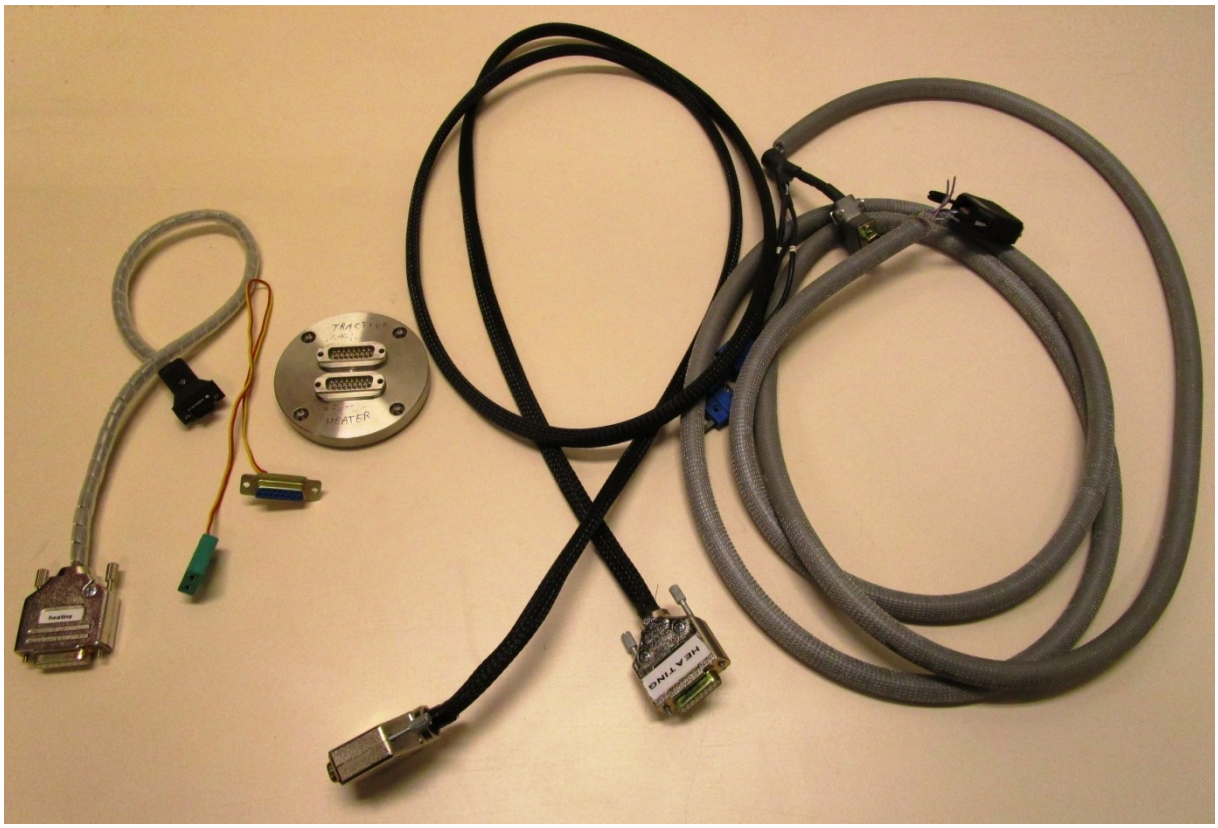


**Figure B.6: Cables and connectors needed for the in situ experiment. From left to right: heating cable, thermocouple able to send signal through the connector, the connector, cable to hot stage controller (black) and cable to temperature logger (grey).**

## B.3 Assembling the In Situ Hot Stage

Place the two stainless steel disks inside the holder for the furnace and the sample. Afterwards, place the two ceramic disks on top of these as shown in Figure B.7a. Note that if the stainless steel disks are very deformed after use, thus are not completely flat, only one ceramic disk is enough. Place the furnace on top of the ceramic disks as shown in Figure B.7b.

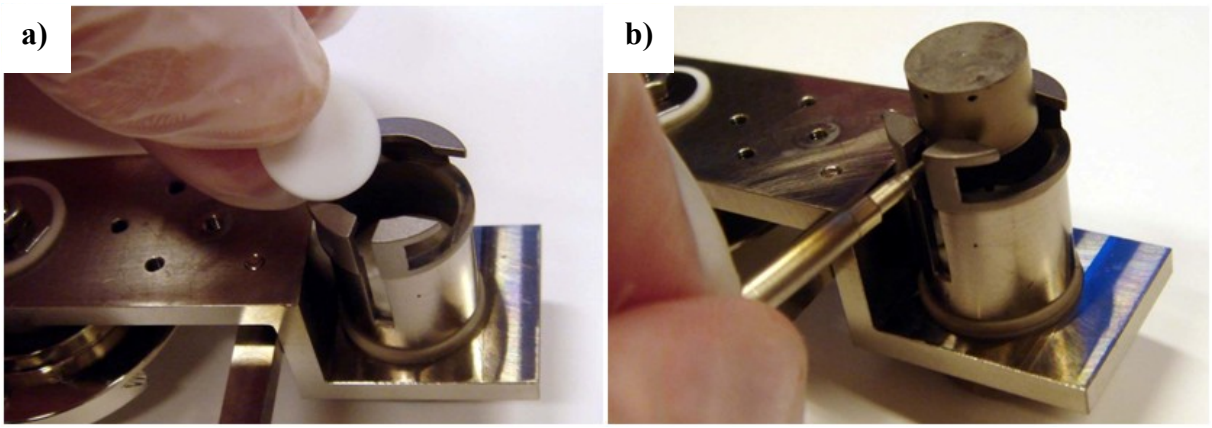


**Figure B.7: Placement of a) disks and b) furnace.**

Mount the sample on top of the furnace as shown in Figure B.8a. Screw the furnace up in contact with the sample by using the screw in the bottom of the hot stage as shown in Figure B.8b. Do not screw too tight, as the ceramic disk might break. This will move the furnace up to the sample. It is important that the furnace and sample are in full contact with each other.

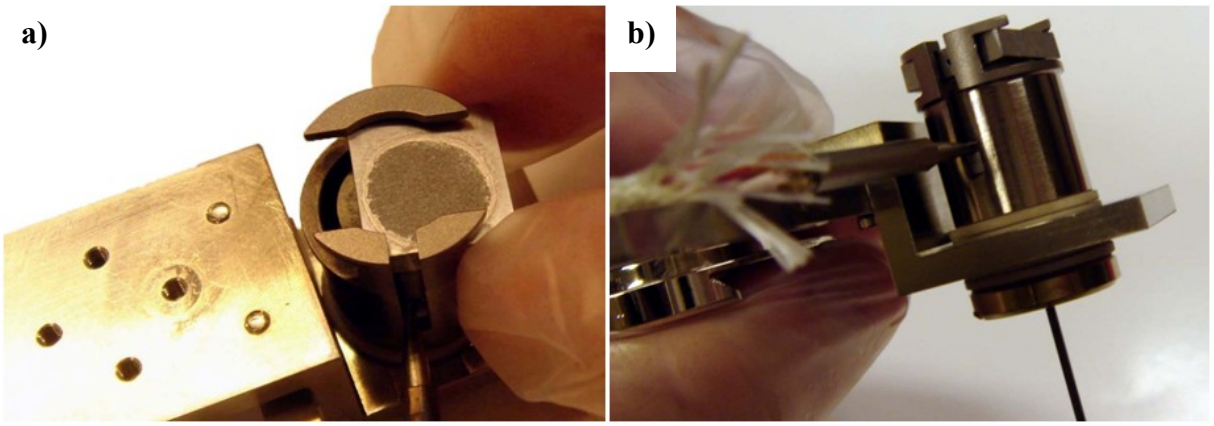


**Figure B.8: Mounting of sample a) over the furnace and b) screwing the furnace up to the sample.**

If it is wanted to reach a sample temperature above 700 °C, it is necessary to use SPI platinum paint between the sample and the furnace. Apply the paint on the furnace before you mount the sample. If the paint is absorbed instantly, this means that there is old paint on the furnace, and this should be removed. Another possibility is to apply the paint on the sample before mounting the sample. Only one drop of the paint should be sufficient. After application, the paint must be left to dry a minimum of three hours before heating, but if the stage is placed in a vacuum chamber it will dry much quicker (20 minutes should be sufficient). The paint and thinner (solvent) is presented in Figure B.9.


**Figure B.9: The left bottle contains the SPI platinum paint and the right one a thinner that can be used to remove the paint already on the furnace.**

Connect the furnace to the plug marked as F1 as shown in Figure B.10a. Place the thermocouples in the furnace and sample as shown in Figure B.10b. The thermocouple marked as T1, the one closest to the edge in Figure B.10a should be placed in the furnace, and the other one in the sample. Make sure that the thermocouples get pressure pressing it into the sample and furnace, otherwise it will pop out.

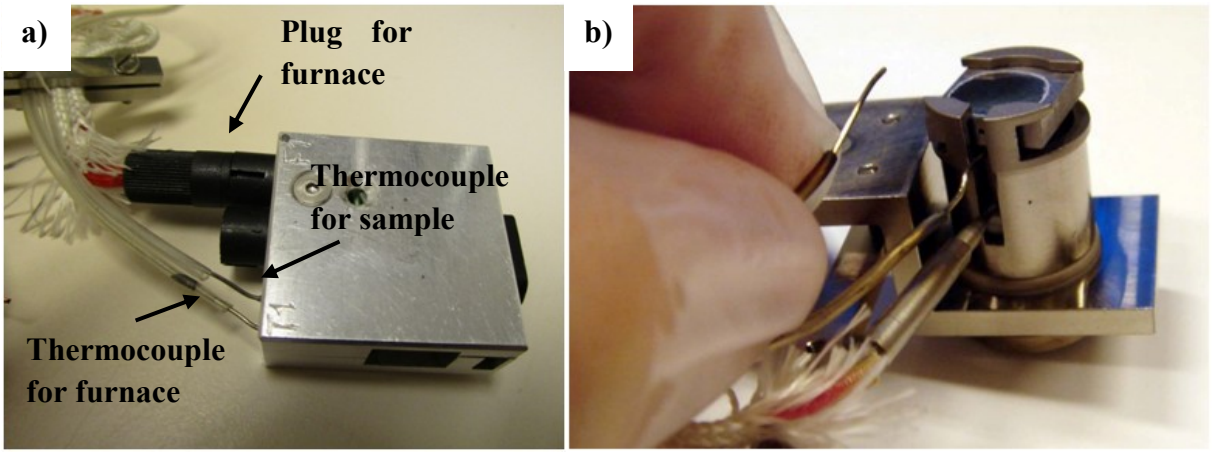


**Figure B.10: a) Where to plug in the furnace, and which thermocouples belong to which, and b) placing the thermocouples in the furnace and sample.**

Fasten the chord anchorage on both the furnace and the thermocouples as shown in Figure B.11a. To avoid the sample being charged during the experiment, a connection between the furnace and the stage must be present. This can be done by installing a copper wire touching both installments, e.g. one part touching the wire from the furnace (and/or the thermocouple), and the other fastened by a screw to the hot stage. Fasten the thermocouple to the hot stage beneath the same screw as the copper wire, and below the washer. This is presented in Figure B.11b.

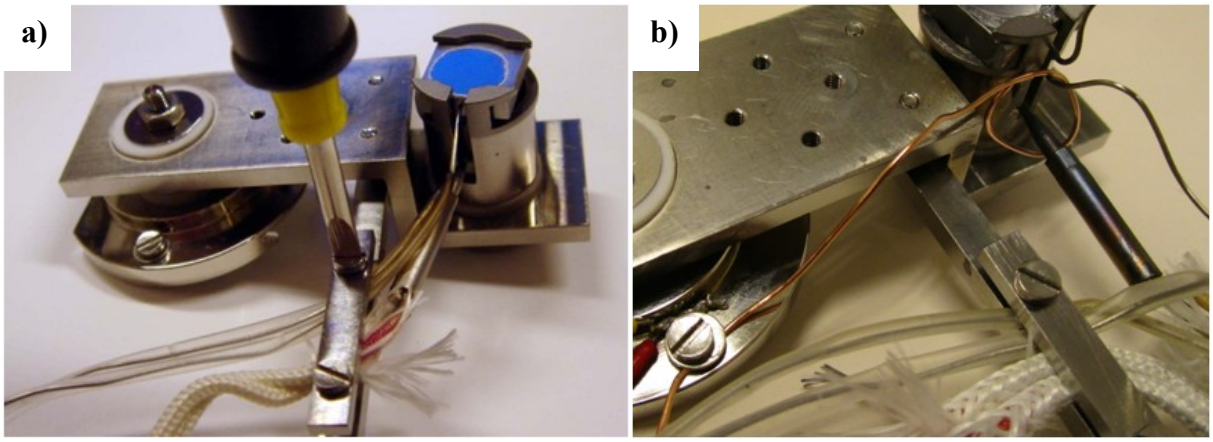


**Figure B.11: Fastening the a) chord anchorage on the furnace and the thermocouples and b) fastening of thermocouples to the hot stage.**

Figure B.12 shows how the hot stage should look when everything has been correctly connected to it.

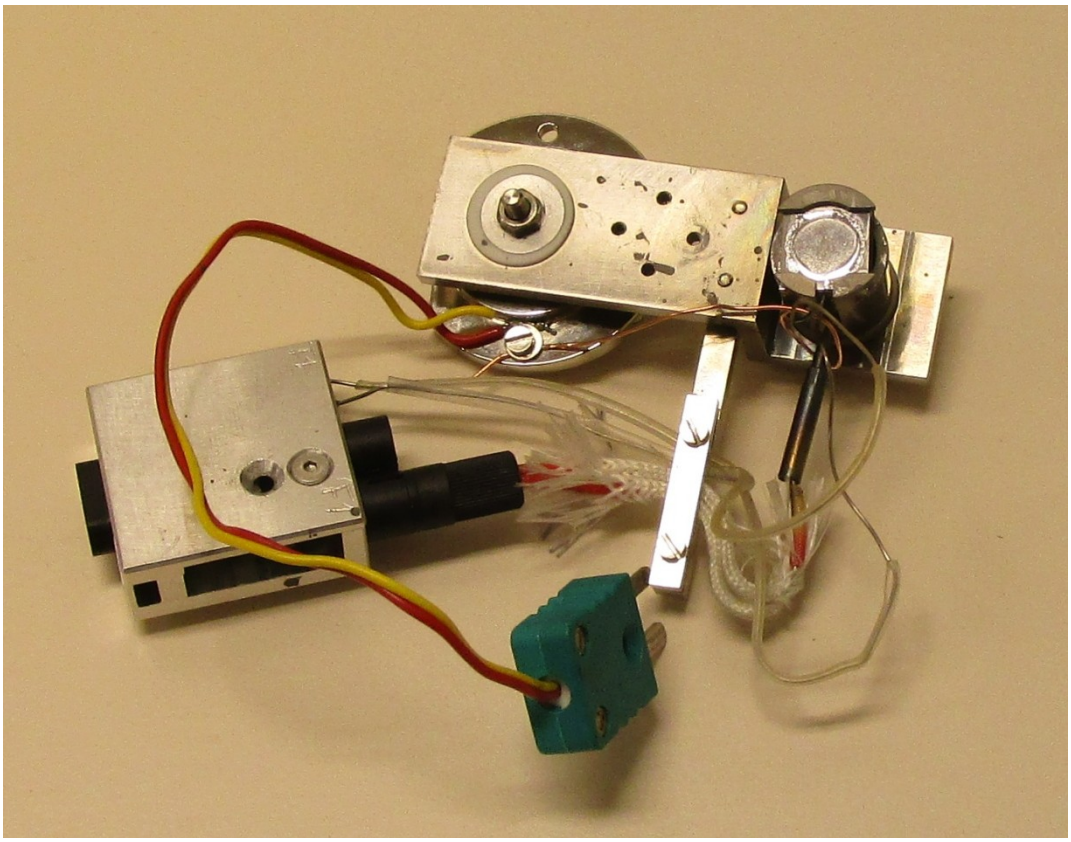

**Figure B.12: Hot stage with everything connected, including furnace, sample, thermocouples and copper wire.**

Mount the heating cable and thermocouples to the connector as shown in Figure B.13.

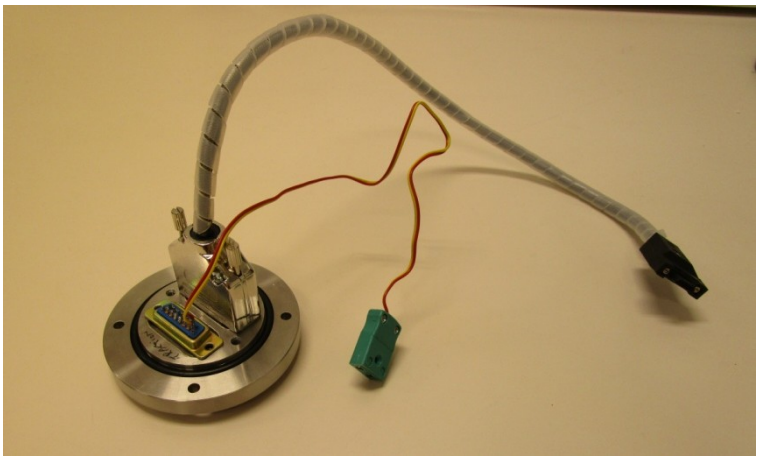

**Figure B.13: The heating cable and thermocouple mounted on the connector.**

Remove the upper door panel by unfastening the four hexagonal cap screws as shown in Figure B.14a. Place the round panel in a plastic bag. Gently enter the heating cable and thermocouples through the upper port as shown in Figure B.14b. The screws for the panel

should be used to mount the heating cable connector as shown in Figure B.14c. Make sure the connector is clean before exchanging it with the panel.

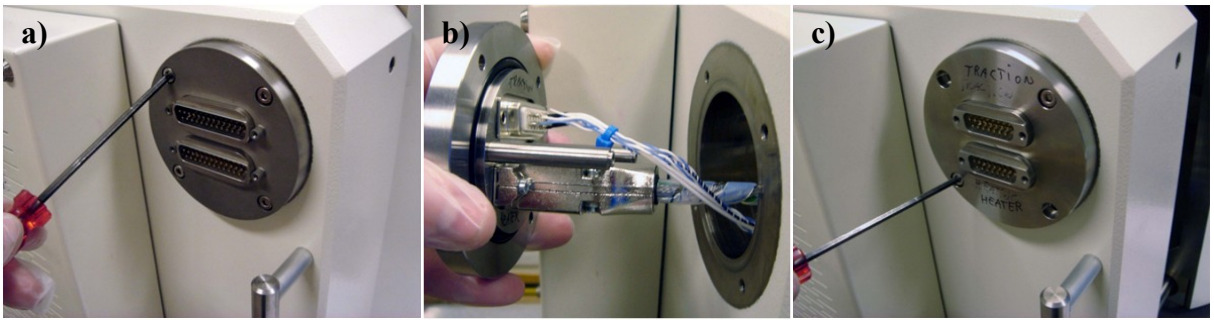


**Figure B.14: a) Removal of upper door panel, b) gently enter the heating cables and thermocouples through the port, and c) mount the cable connector.**

To prevent that the alarm "Stage is touching" goes off during heating, the pin for the ground cable has to be disconnected. In Figure B.15 it is in connected position. The simplest solution is to remove it all together, and put it into a plastic bag. Remember to connect the pin again after the heating experiment is finished!

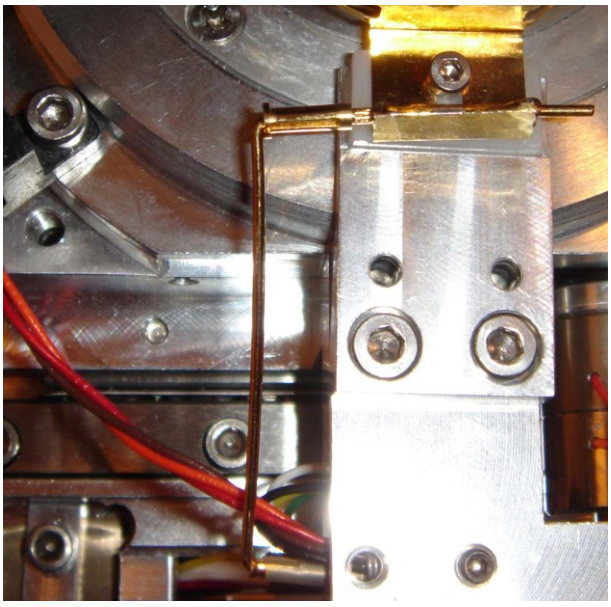

**Figure B.15: The pin for the ground cable in connected position.**

This pin prevents the sample for charging since the stage is isolated from the rest of the microscope. Since the pin is now disconnected it is necessary to form a conductive connection between the stage and the microscope. This can be done by using aluminum foil fastened beneath the screw on the microscope and the stage, as seen in Figure B.16. When loosing screws inside the microscope it is very important not to lose any of them, and that it disappears beneath the gap of the specimen chamber. A protective strip of foam rubber can be placed in front of the gap, as seen in Figure B.17.

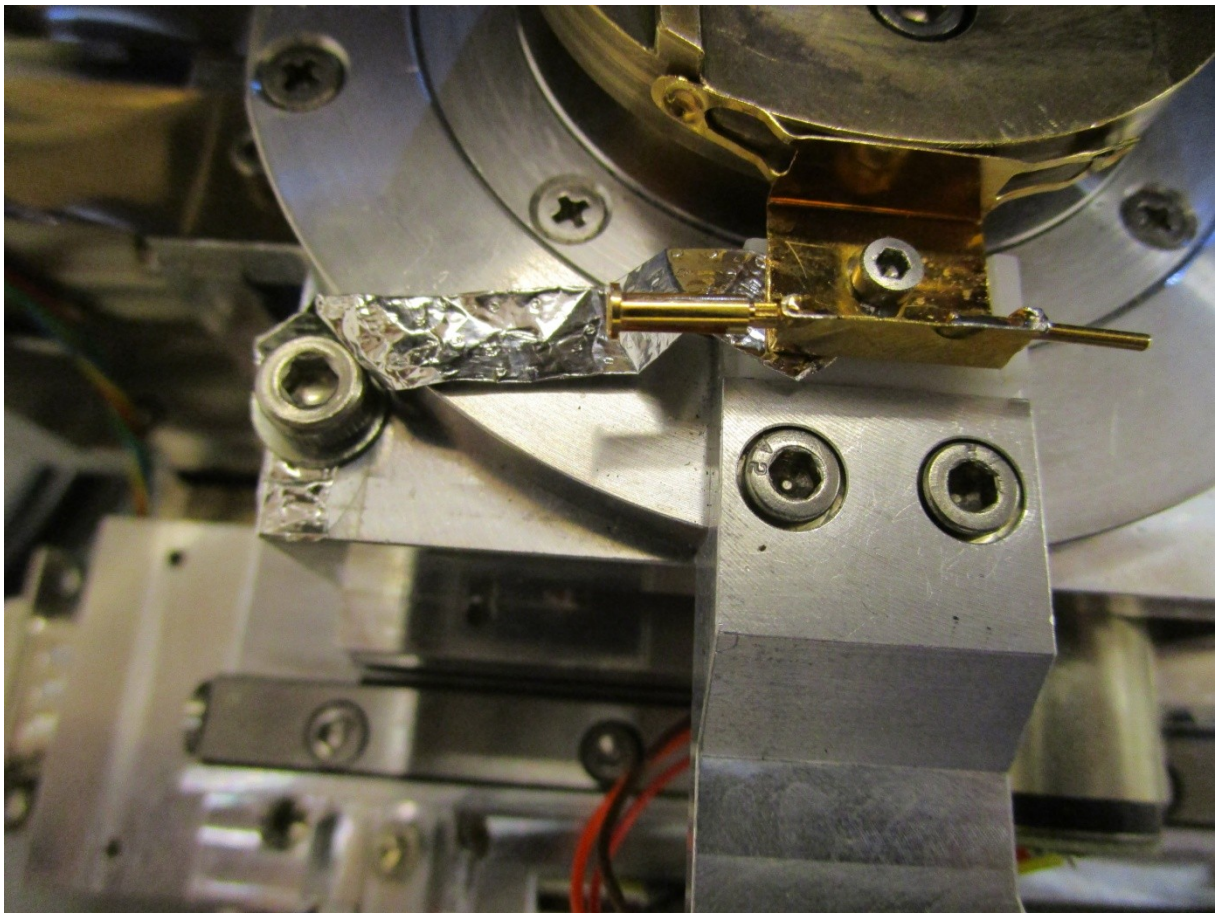

**Figure B.16: How aluminum foil can be fastened beneath the screw in the microscope and beneath the stage. Make sure to fasten the screws.**

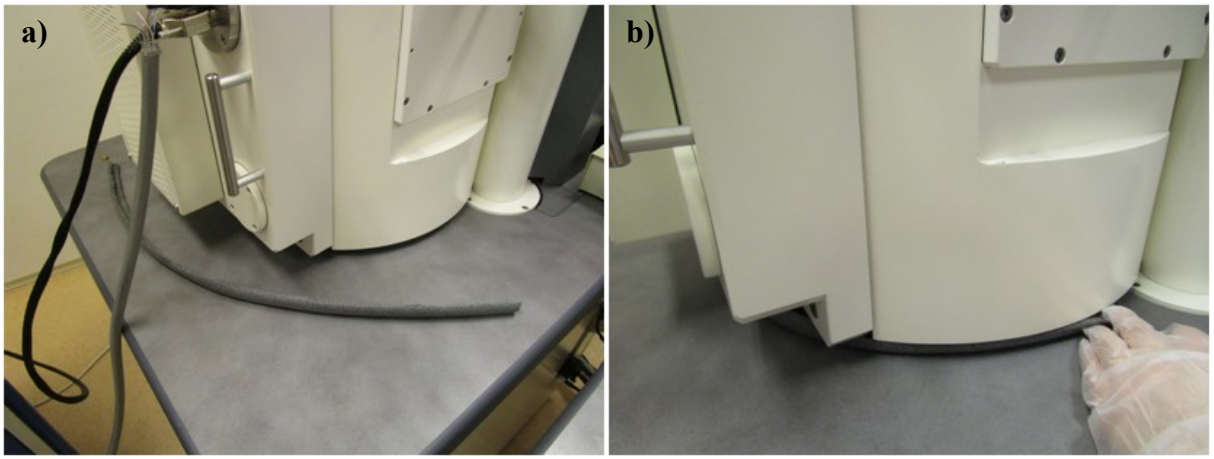


**Figure B.17: Foam rubber to prevent loose part from disappearing in the gap.**

Mount the in situ hot stage in the SEM. Connect the heating cable and the thermocouples to the hot stage as shown in Figure B.18.

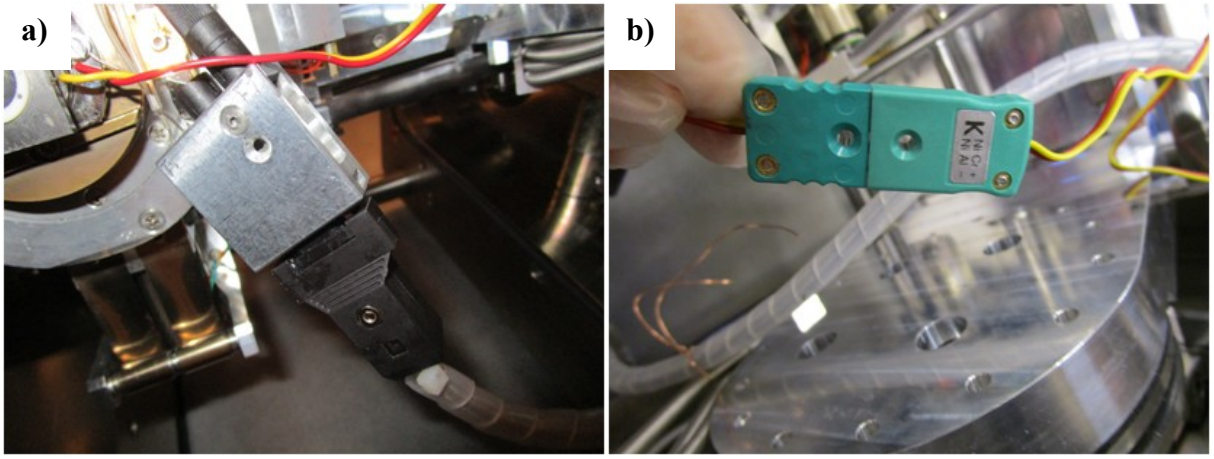


**Figure B.18: Connect the a) heating cable and b) thermocouples to the hot stage.**

Finally the cable from the hot stage controller and the temperature logger should be connected to the SEM as shown in Figure B.19. The black cable is connected to the temperature controller, as seen as the large box in Figure B.20, while the grey cable have three thermocouples at its end, the one marked 3 can be connected to a temperature logger, which then can be used to control the temperature of the hot stage itself.

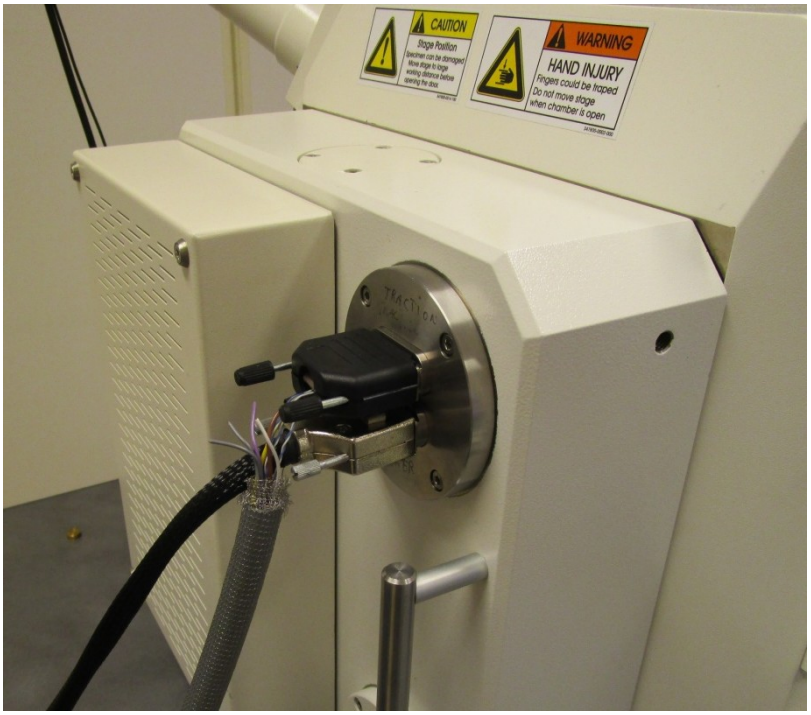


**Figure B.19: Cables from hot stage controller and temperature logger connected to the SEM.**

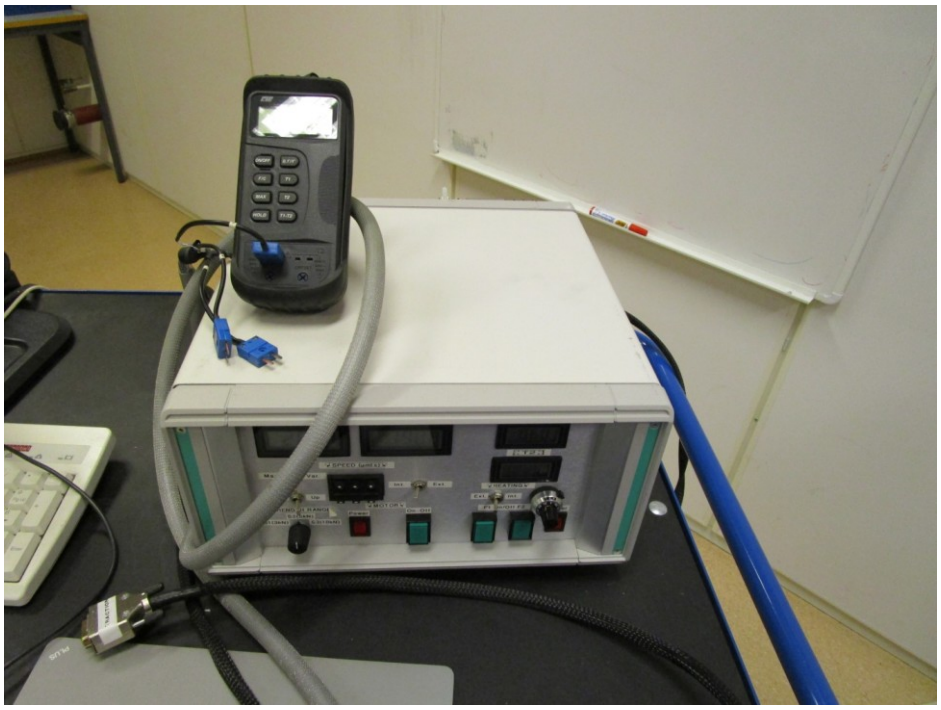

**Figure B.20: Temperature controller, with a simple temperature logger on top to watch the temperature of the hot stage.**

When tilting the hot stage the SEM door should be open to make sure that none of the cables move out of place during tilting. The cable from the hot stage controller can be fastened to some cables on the rotating device, with e.g. a copper wire as seen in Figure B.21. This way it will rotate with the stage and not be in the way.

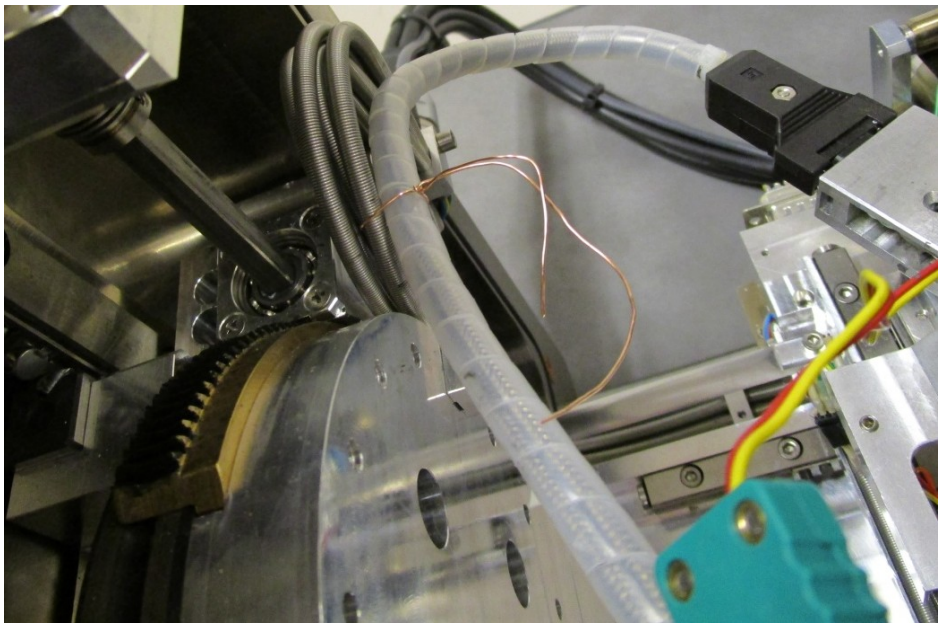

**Figure B.21: Fastening of the heating cable to some cables, which also rotates.**

The hot stage should now be correctly installed. The result should look like Figure B.22.

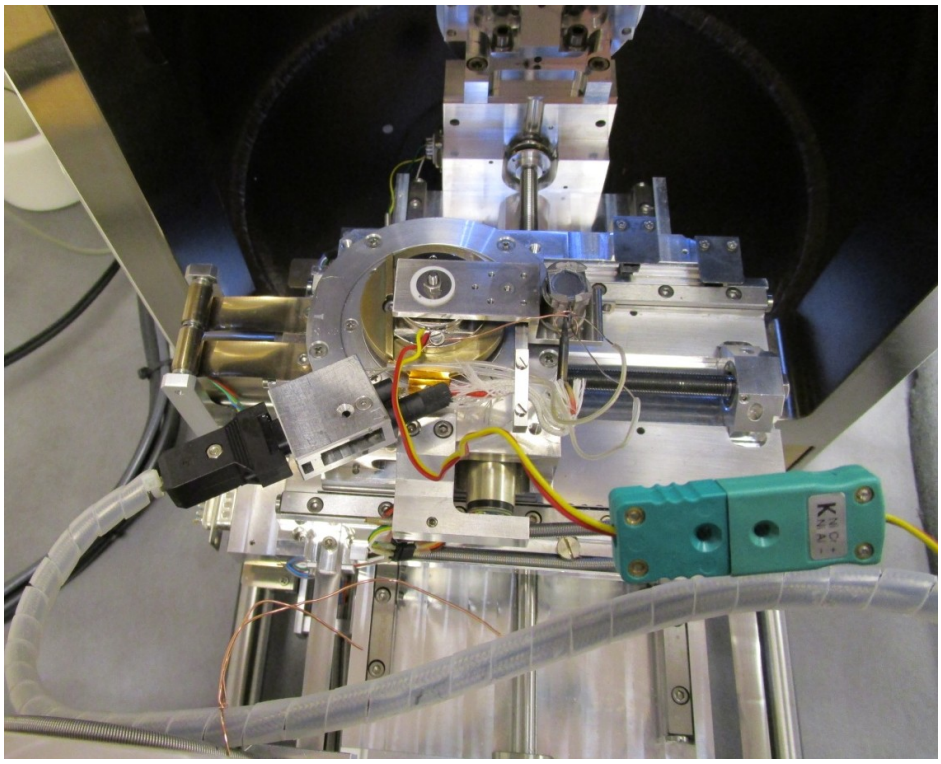

**Figure B.22: Hot stage mounted in SEM.**

Tilt the stage to 70° while the door to the microscope is still open. Afterwards, close the door and press "Exchange". It is important that the "Z move on vent" is unchecked as shown in Figure B.23. If this is not possible doing in the regular guest-user in SmartSEM ask any of the senior engineers or an experienced user. Remember to check this again when you are finished.

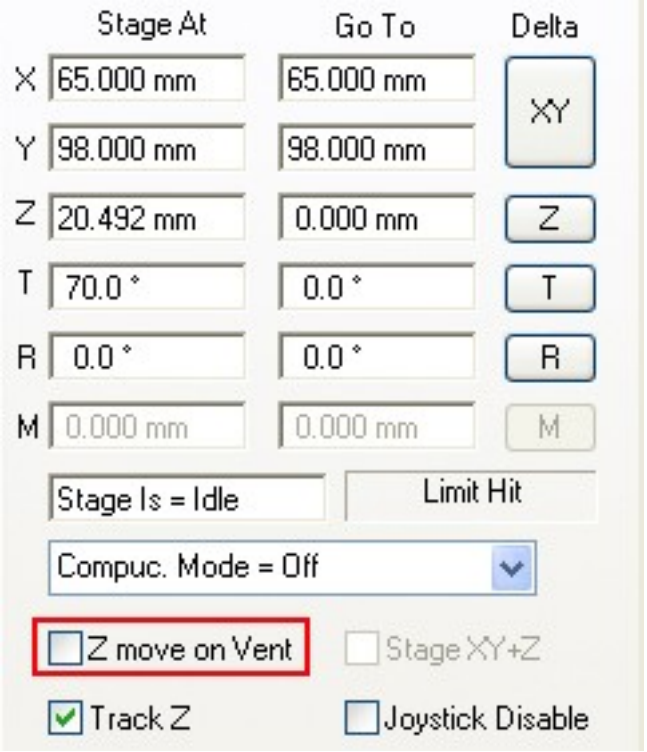


**Figure B.23: Uncheck "Z move on Vent"**

To protect the EBSD-detector from the heat from the furnace it can be smart to retract it a couple of millimeters from the original position. This can be done by placing a small object between the detector and the stopper, as seen in Figure B.24.

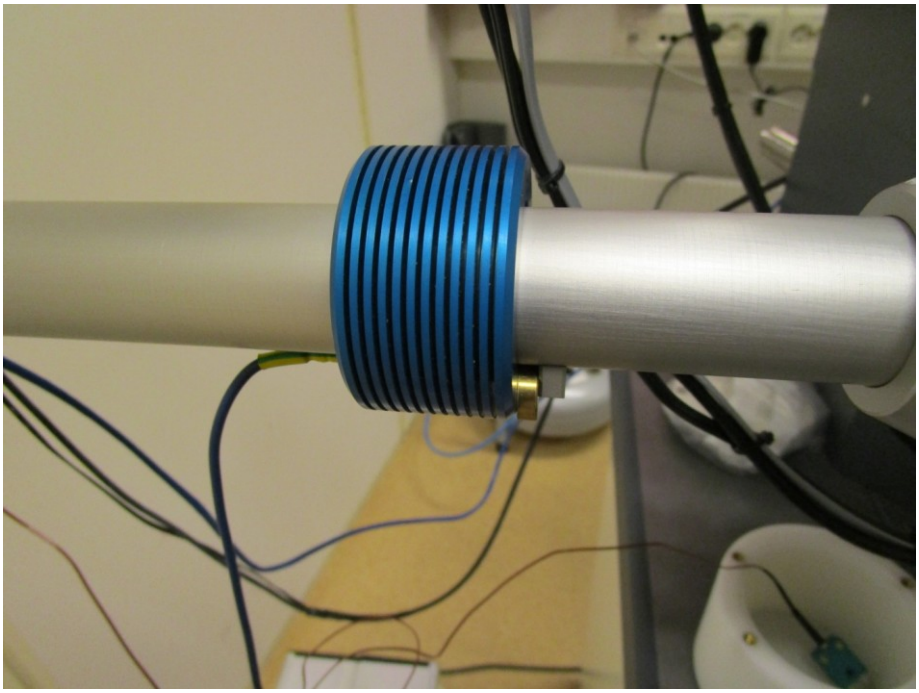

**Figure B.24: Placement of small object to protect the EBSD-detector from the furnace.**

The current for the temperature controller and the computer should be taken from an outlet in the SEM. This can be done with a special cable marked AUX DVI, in Figure B.25a, and placed in the outlet in the back of the SEM marked AUX 1, pictured in Figure B.25b.

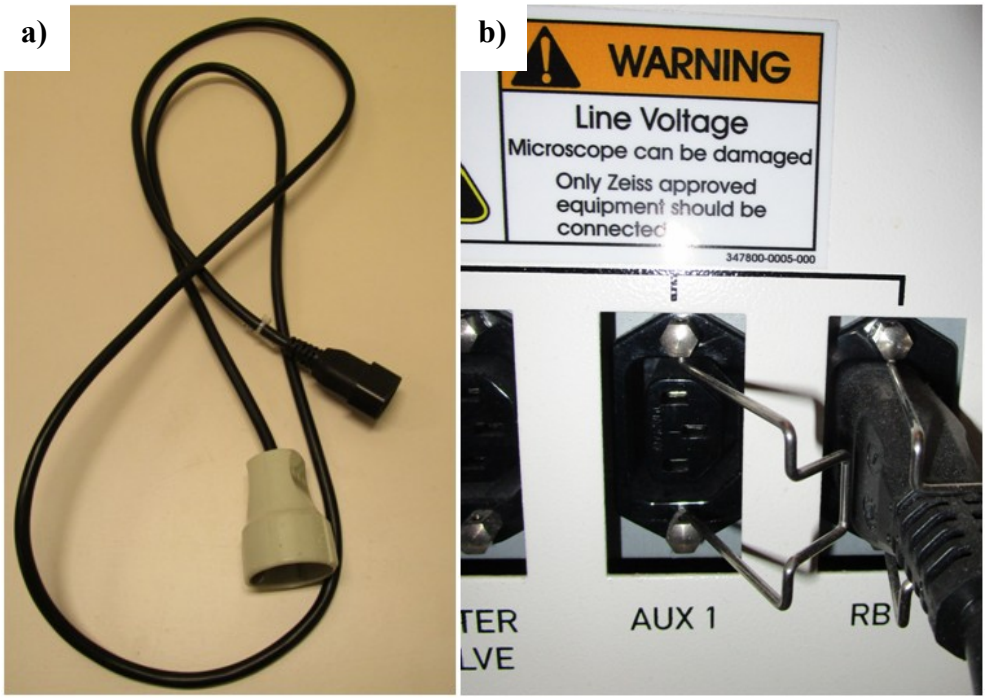


**Figure B.25: a) The AUX DVI cable and b) where to plug it in the SEM (AUX 1).**

## B.4 Proposals for Development

After the experiments were conducted a few more suggestions for further development can be noted. A more permanent solution to the grounding problem should be investigated as the copper wire was a fast and simple solution. If this solution is retained it should be noted that the fastening of the wire beneath the same screw and washer as the thermocouple for the hot stage, marked b) in Figure B.26 could become problematic. If these were fastened beneath two different screws it could simplify the installment work considerably, as it is less chance for it to loosen during mounting and preparation of sample.

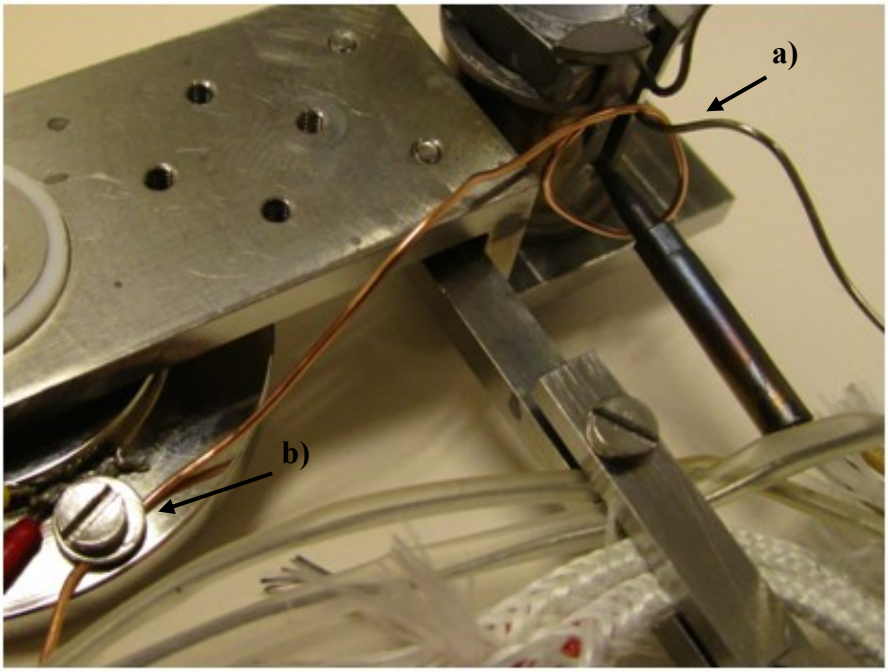


**Figure B.26: Close-up of hot stage with copper wire touching a) the transition cable and the thermocouple from the furnace, leading electrons to the hot stage by b) fastening the wire and thermocouple under the same screw.**

The hot stage itself is also a bit loose. The design makes it possible to rotate the whole stage around the screw marked in Figure B.27 if the screw is not fastened thigh enough. Ideally, when fastening this screw the rest of the stage should be in place and not possible to move, but especially after tilting the stage inside the SEM it was evident that it did not work as well as it should be. It was always possible to rotate no matter how hard the screw was fastened. This should be further investigated so this problem is avoided during later experiments. One solution is to simply have an additional screw installed, thus making it impossible to rotate as it is not one origin point.

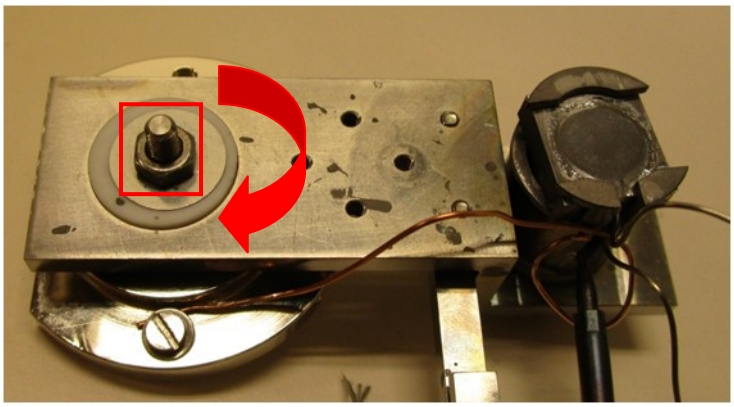

**Figure B.27: The hot stage with marked screw which is the point of origin of rotation. Another screw can fix this problem.**

A minor change concerning the electronics and the cables to get the signal from the hot stage thermocouple to the outside temperature logger was conducted. The old, grey cable is from a previous temperature controller, and based on Figure B.28a it is starting to fall apart at the head connecting it to the SEM. A new cable with better reinforcement should be made. Today this cable has three thermocouples at the other end, marked in Figure B.28b, but only one is needed. However, it is important that the signal is still readable through the connector, and a new cable must have wiring matching the cable inside the SEM. The inside thermocouple wiring in Figure B.28c is today matched to the thermocouple marked 3 at the end of the gray cable. Whether the wiring is correct is easy to investigate without connecting up the SEM.

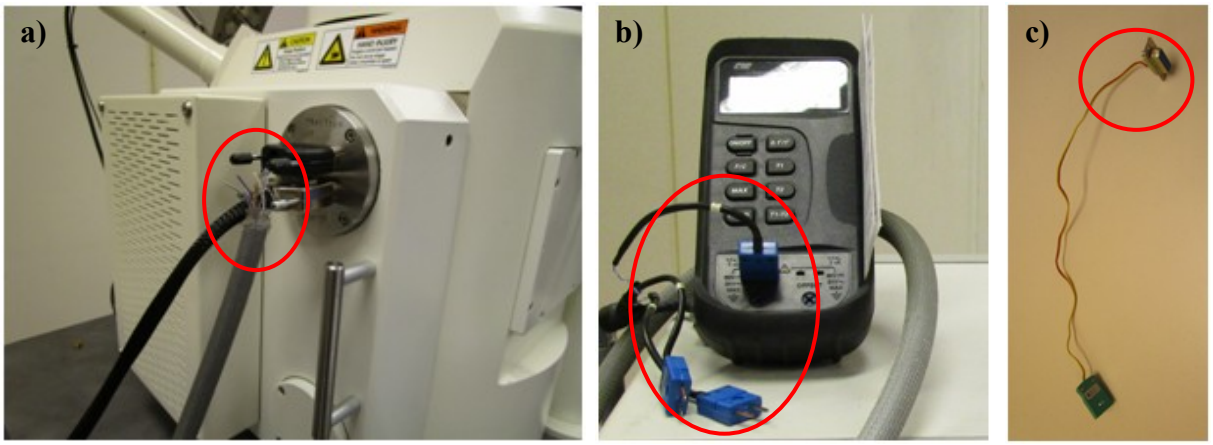


**Figure B.28: a) The outside cables with the gray cable head loosing much of its wiring. b) The three thermocouples on the other side of the grey cable, with the one marked 3 in the temperature logger. c) The inside thermocouple wiring which match the thermocouple marked 3 at the end of the grey cable.**

Further investigations of how to best remove the SPI paint from the furnace should also be completed. Further investigating the best parameters concerning the hole for the thermocouple in the sample is also advised.

# Appendix C User Manual for the In Situ Hot Stage Software

Turn on the PC and in situ stage controller shown in Figure C.1. Note that the controller does not need to be placed in this exact location. The on-switch for the controller is on the back, as seen and marked with a red rectangle in Figure C.2. The username for the computer is Semlab (no password). The switch on the stage controller should be on External as shown with the red rectangle in Figure C.1b.

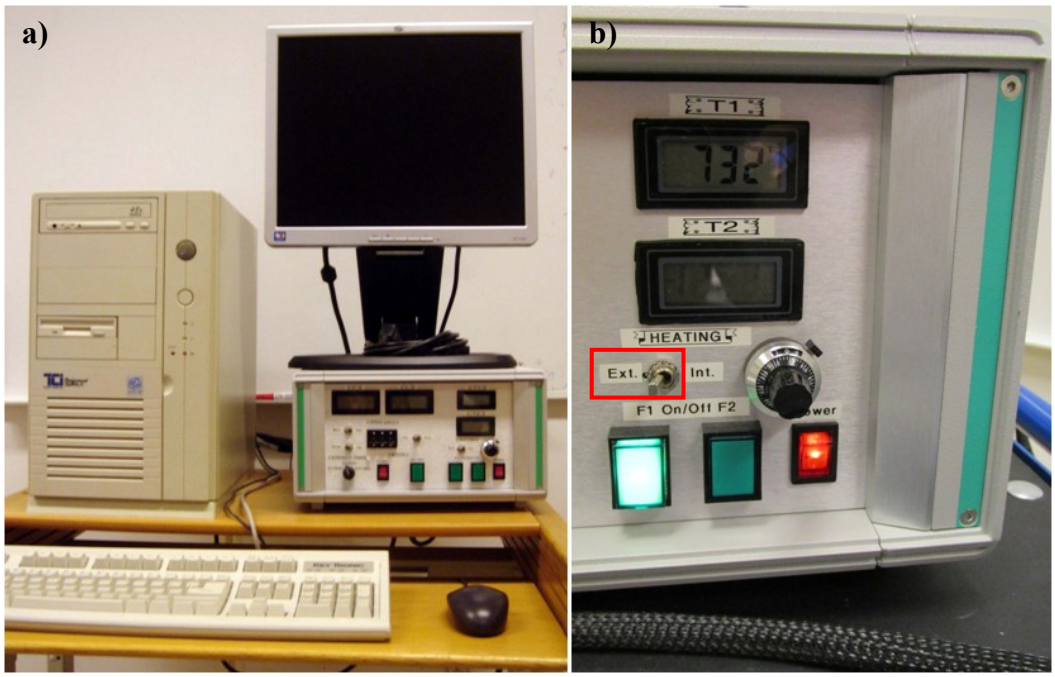


**Figure C.1: The a) PC with the controller placed below the screen, and b) close-up of the stage controller (turned on during experiment) highlighting the External switch. The lamps on F1 and Power are on, indicating that the controller is being used.**

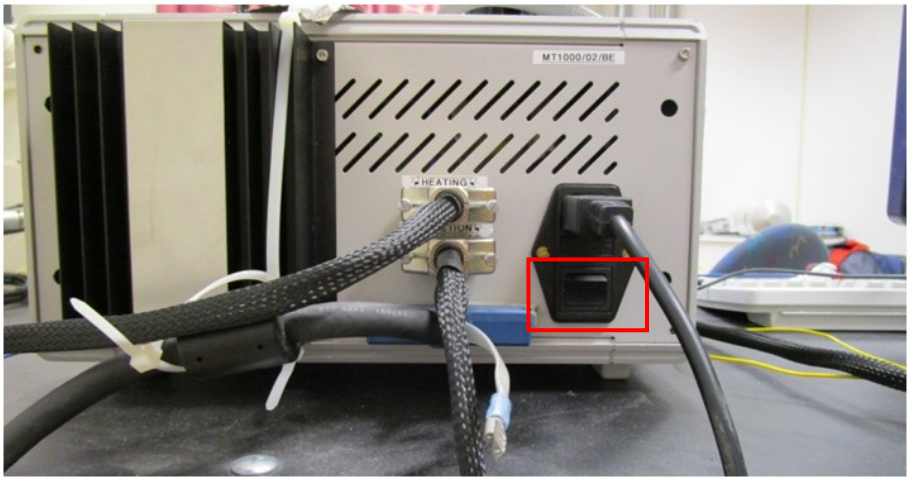

**Figure C.2: Back side of controller, highlighting with a red rectangle the on-off switch and the cable (both heating and traction cables are fastened in the picture).**

Choose the program HT-Traction on the desktop of the PC. The interface of the program is shown in Figure C.3. Type in 18 and 14 under L1 and H1 respectively. These parts are marked with a red square in the Figure C.3. Choose S2 (4500N) under Strength Range. The message No Error will then appear. Be aware that there is a temperature error in the controller. The temperature difference between the furnace (T1) and sample (T2) at room temperature (before the experiment) should be approximately the same, but the furnace is observed to measure approximately 20°C higher than the sample temperature. Previous experiments experienced a temperature difference of 85-90°C. It is important to be aware of this error, as the temperature difference experienced during the experiment should be subtracted from the furnace data. Choose the location of the file under User String. Finally press Start Acquisitions.

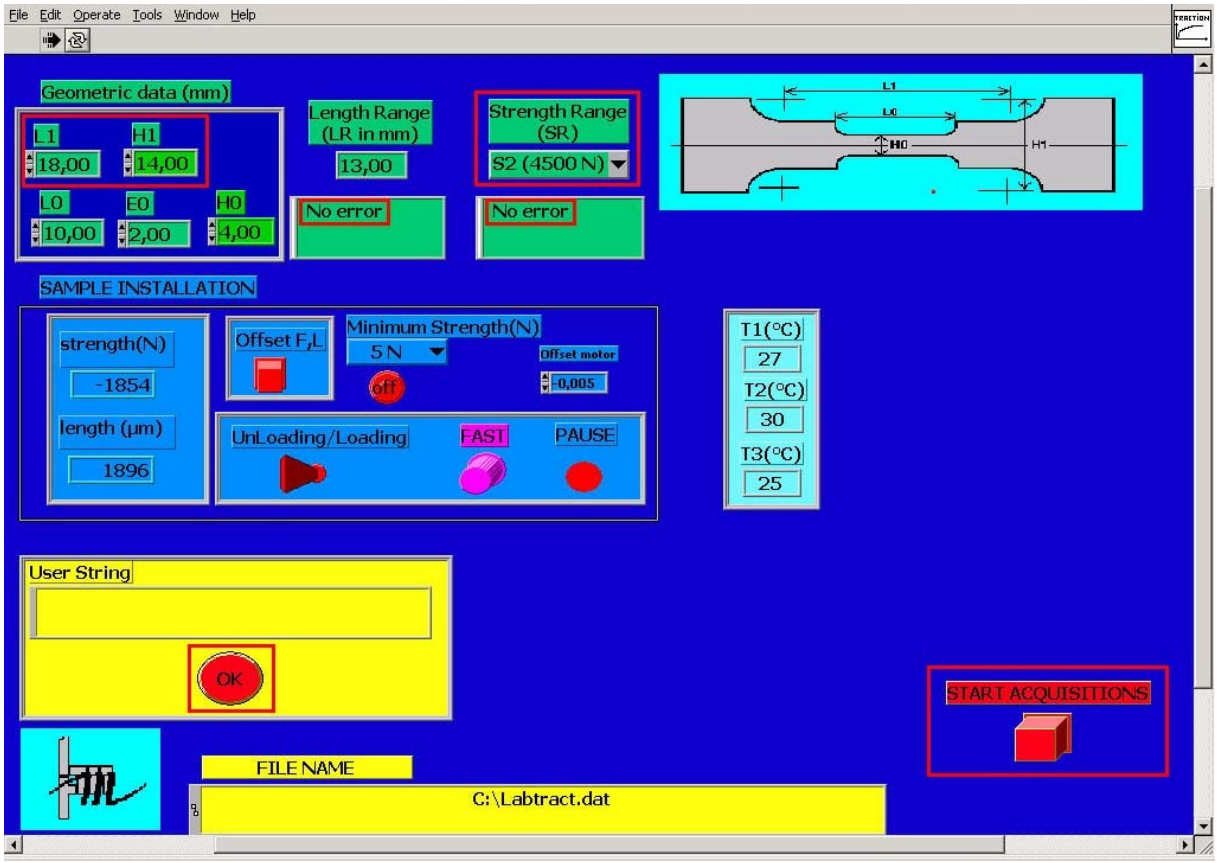


**Figure C.3: Software for the in situ heating stage, with red highlighting showing where to fill in fixed settings, and where to change user string before moving on to the next interface.**

The next interface is shown in Figure C.4. T1 gives the temperature in the furnace, while T2 gives the sample temperature. Set the wanted heating rate, set point for the furnace and level:t. Be aware that because of the temperature difference between T1 and T2 it is necessary to add this temperature difference to the wanted set point. An indication of the error is the difference between the T1 and T2 at room temperature. The level:t should have a greater value than the

set point. The maximum temperature in the furnace is 800°C. If the error message NaN appears under T Control when opening the program, as shown in Figure C.5, the software needs to be restarted.

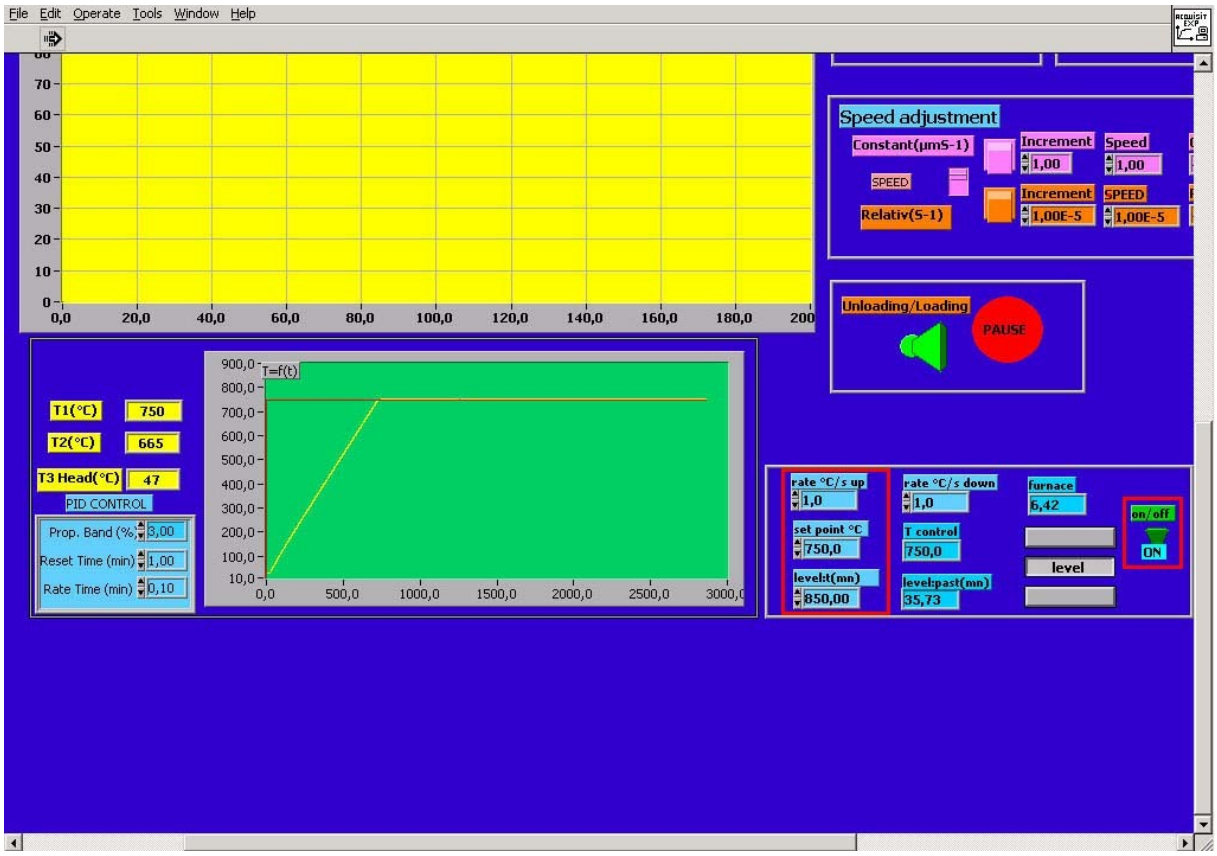


**Figure C.4: Software for the in situ heating stage, with red highlighting showing where to fill in the settings and what to switch on when the heating is to start (in this example turned on).**

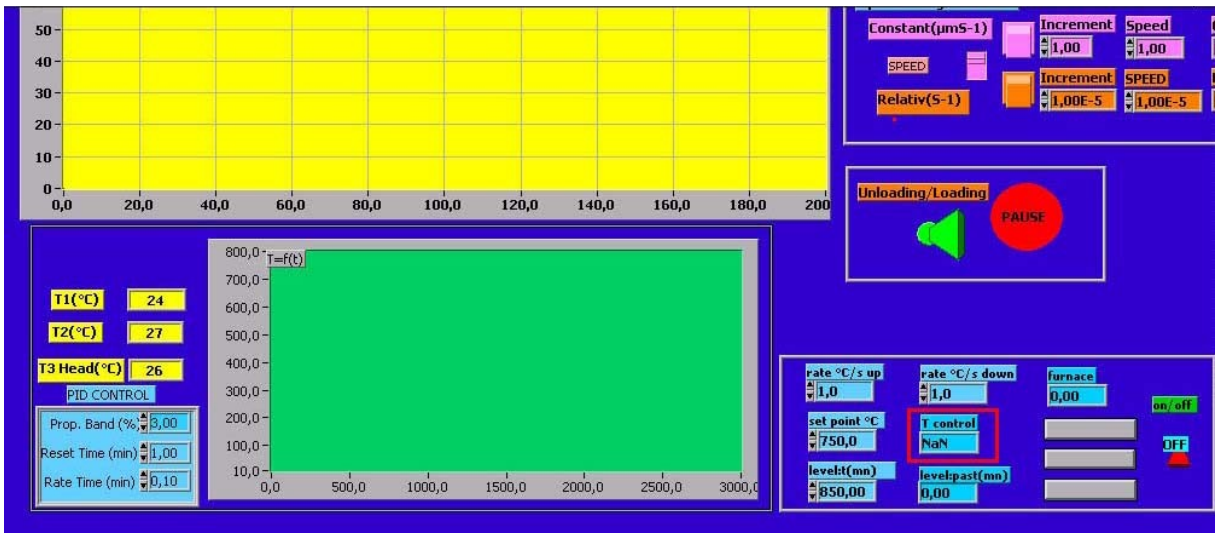


**Figure C.5: Error message highlighted, with T control showing NaN.**

When the wanted values are entered, press the on button, also marked in the interface presented in Figure C.4. Then press the F1 and Power buttons on the in situ stage controller as shown with the lamps being on in Figure C.1b. The furnace is now heating.

When the temperature is set to reach a high temperature, typically above 700°C, the furnace will reach maximum effect. The furnace will then turn itself on and off and will fluctuate between 0 and 10 as shown with a red rectangle in Figure C.6. This will interfere with the electron beam in the SEM. It is therefore necessary to adjust the Prop. band to a higher value until the effect of the furnace is stable as shown in Figure C.6.

Please make sure to keep an eye on the temperature logger of the hot stage during the experiment. The furnace must be turned off when the temperature on the stage reaches 47°C. This is to prevent damage on the microscope.

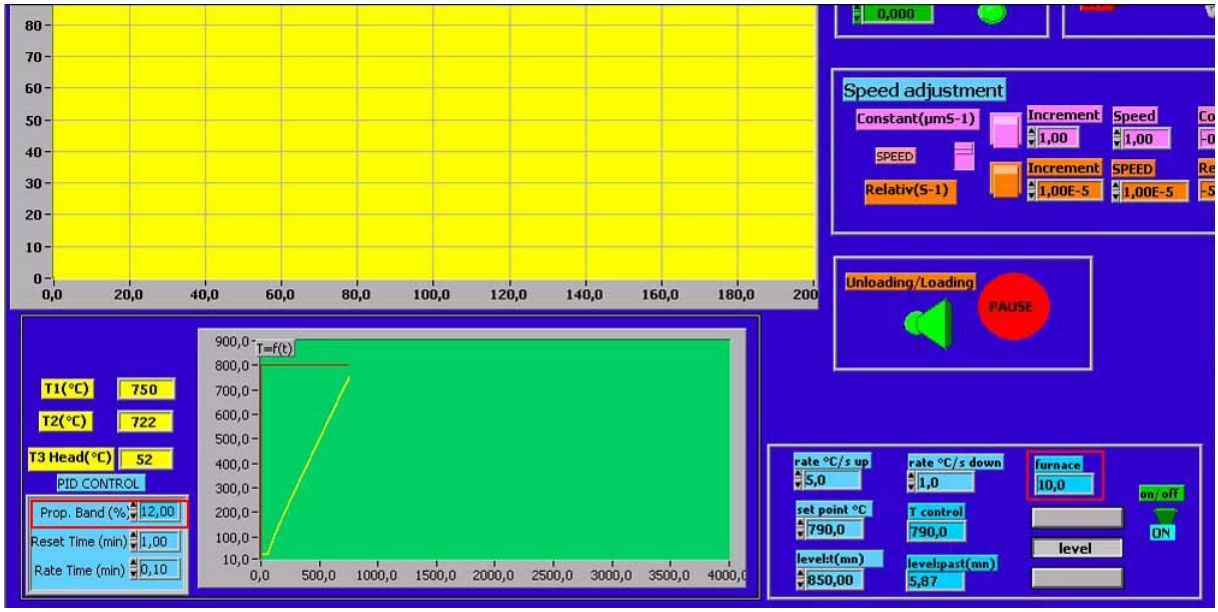


**Figure C.6: Where to adjust Prop. band if the furnace fluctuates.**

# Appendix D  Temperature and Heating Rate Investigations

Other examples of temperature graphs and heating rates achieved during the experiments are presented in this appendix.

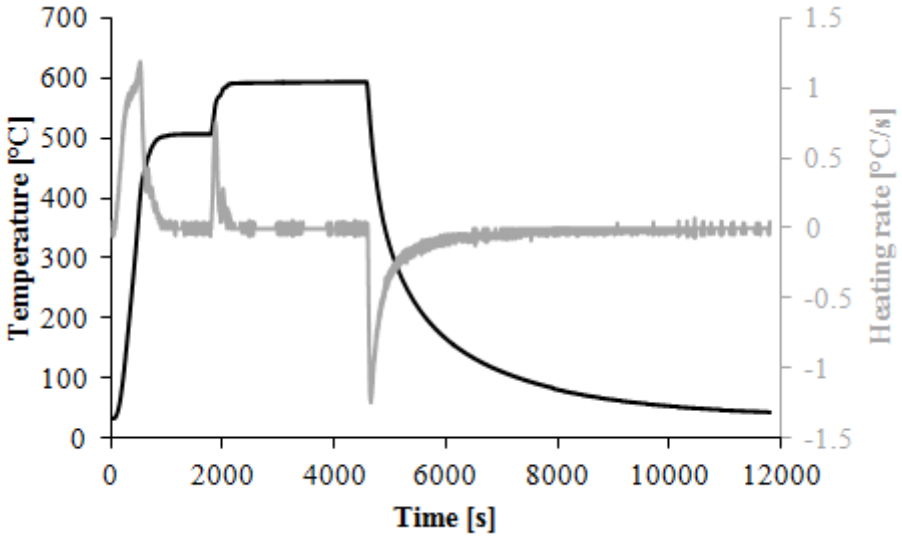


**Figure D.1: The temperature development (black graph) and the heating rate (grey graph) during the in situ heating experiment of sample 12C to 590°C with an intermediate step at 500°C. The heating rate was set to 1°C/s. During the heating from 500 to 590°C the heating rate did not quite reach 1°C/s, and at no point during the heating did it have a stable heating rate.**

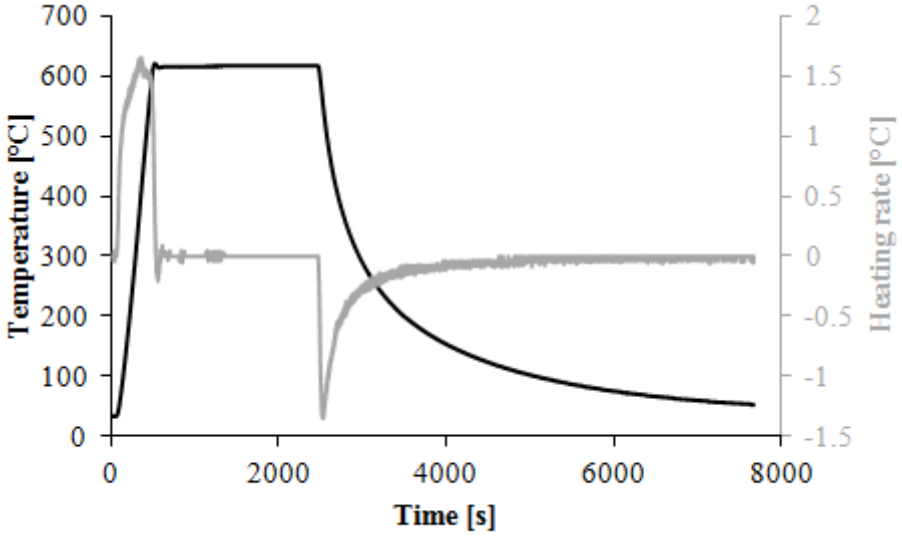


**Figure D.2: The temperature development (black graph) and the heating rate (grey graph) during the in situ heating experiment of sample 11B to 615°C. The heating rate was set to 1°C/s, but reached 1.6°C/s at its maximum.**

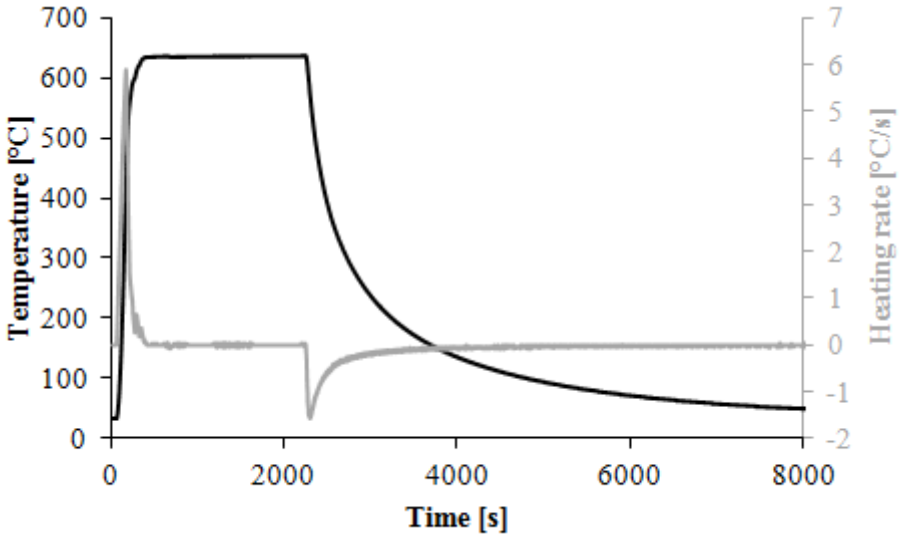


**Figure D.3: The temperature development (black graph) and the heating rate (grey graph) during the in situ heating experiment of sample 12A to 635°C. The heating rate was set to 5°C/s. For the sample this resulted in a heating rate increasing to 6°C/s a short time before the maximum temperature was reached.**

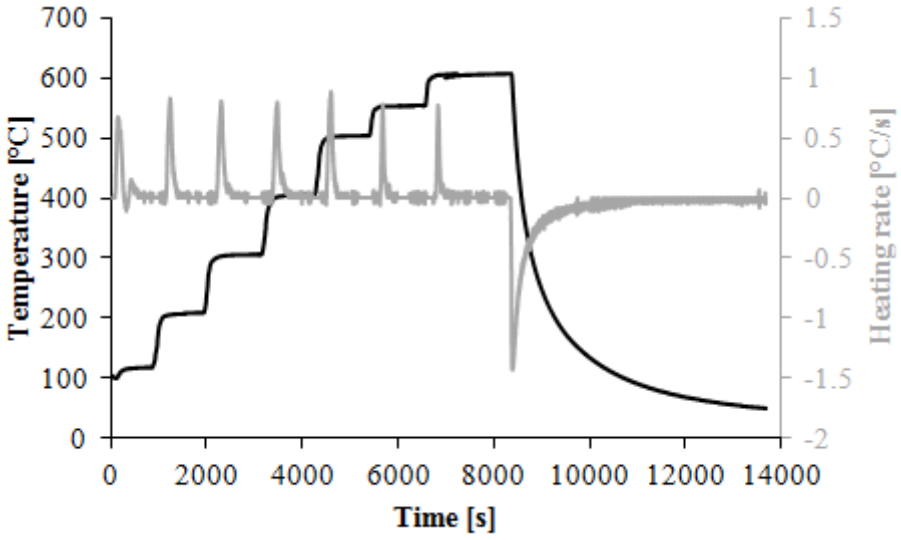


**Figure D.4: The temperature development (black graph) and the heating rate (grey graph) of the stepwise in situ experiment of sample 12B. The heating rate increase to approximately 1°C/s in all steps, a bit below on the two last steps where the change in temperature was 50°C. The maximal temperature was 600°C.**

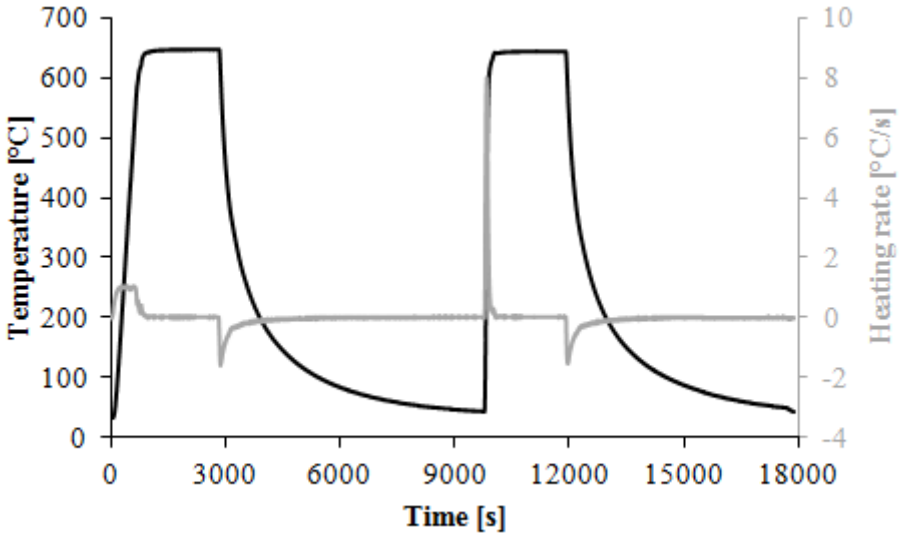


**Figure D.5: The temperature development (black graph) and the heating rate (grey graph) during the in situ heating experiment of sample 9B to 645°C.The first heating is similar to the graph in Figure D.2, but during the second heating the heating rate was much higher, 8°C/s. The temperature reached maximum at a very fast pace.**

# Appendix E EBSD: In Situ Scans

In this Appendix the IPF and phase maps of the sample not presented in the results is presented. Table E.1 gives the austenite amounts for the different scans presented below.

**Table E.1: The amount of austenite for the samples heated in the temperature interval 615-670°C during the stable holding temperature. The time indicates how long after the maximum temperature was reached the scan started, and is further elaborated for each of the series.**

| | | Time interval for start of scan [*minutes*] | | | | | |
|---|---|---|---|---|---|---|---|
| | | **Before heating** | **10** | **17-20** | **25-29** | **35-36** | **After cooling** |
| **T [°C]** | **Sample** | **Amount austenite [%]** | | | | | |
| 615 | 11B | 1.7 | 9.3 | 15.3 | 19.6 | | 11.0 |
| 625 | 9A | 4.5 | 8.6 | 16.4 | 20.0 | 22.6 | 4.9 |
| 635 | 10B | 1.4 | 8.5 | 13.3 | 17.5 | | 3.0 |
| 635 | 12A | 1.0 | 13.0 | 19.7 | 23.9 | | 2.8 |
| 640 | 10A | 1.2 | 25.5 | 32.0 | 36.8 | | 2.9 |
| 645 | 9B | 2.0 | 48.6 | 56.2 | 62.8 | | 2.2 |
| 670 | 11C | 0.9 | 69.4 | 77.0 | 81.1 | | 3.5 |
| 670 | 11A | 1.1 | 57.3 | 63.4 | 68.7 | | 0.8 |

# Sample Heated to 615°C (11B)

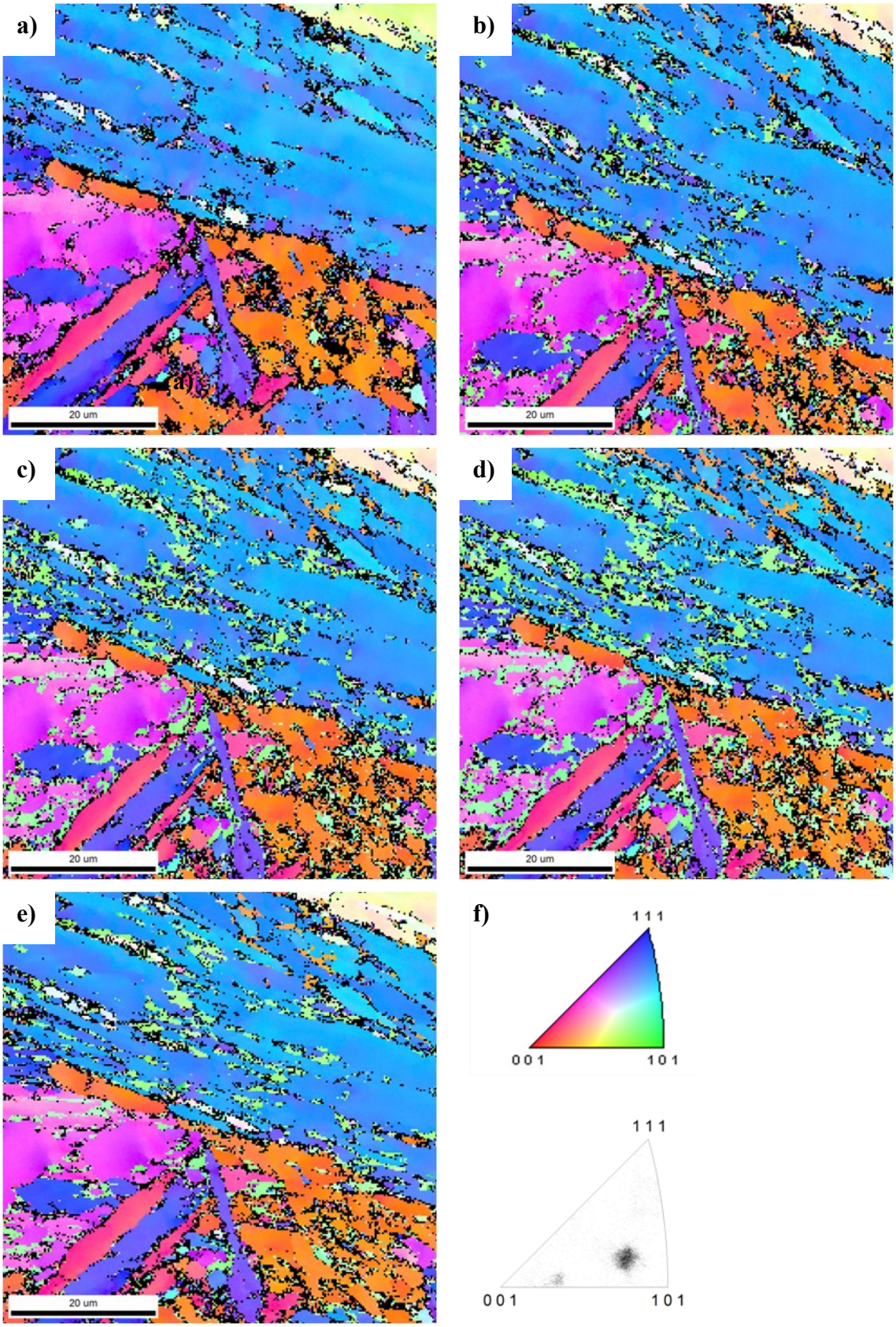


**Figure E.1: IPF maps of the sample heated in situ with a heating rate of 1°C/s to 615°C a) before heating, after b) 9, c) 17 and d) 26 minutes, and e) after relatively slow cooling. f) The IPF of the austenite phase after 26 minutes.**

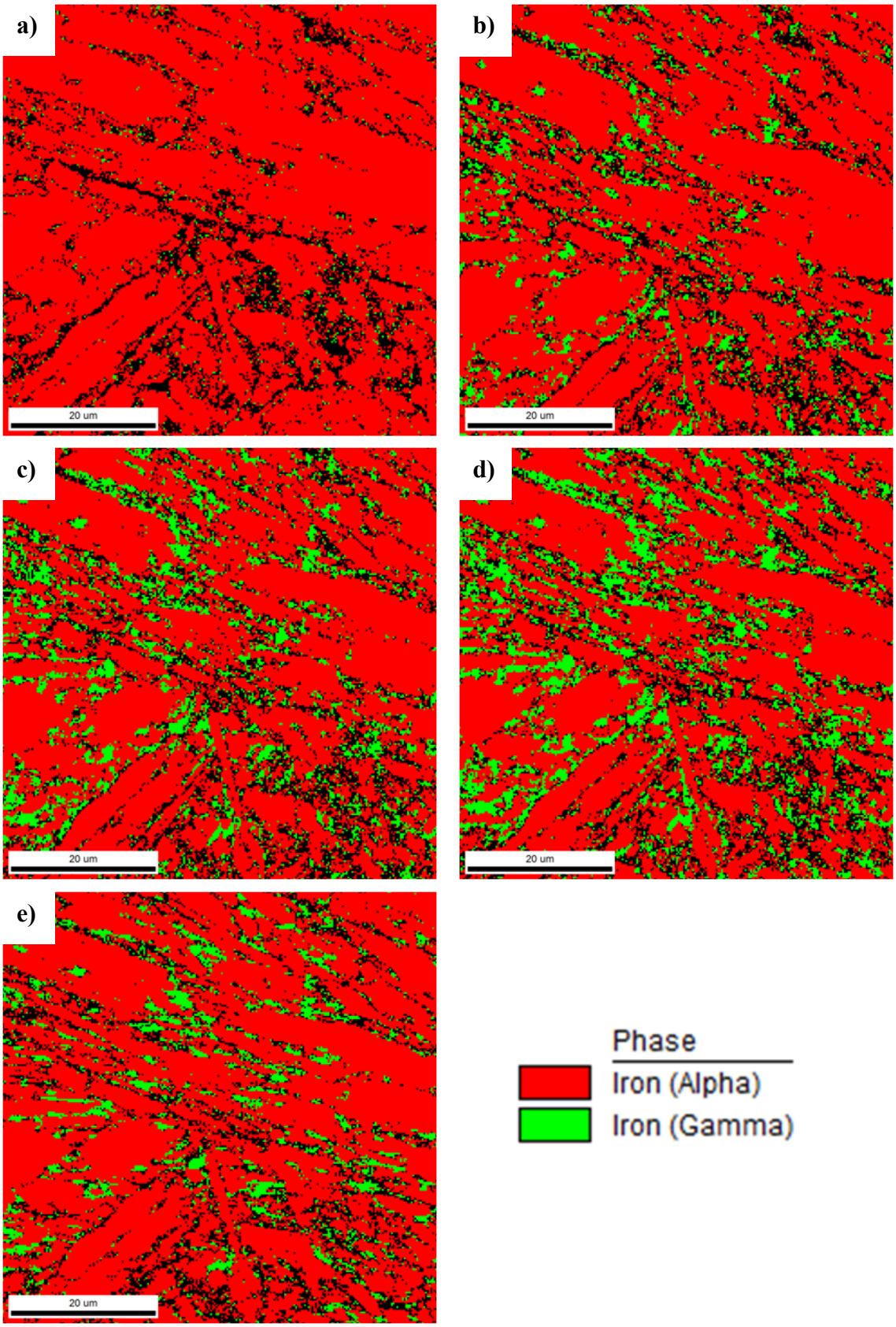


**Figure E.2: Phase maps of the sample heated in situ with a heating rate of 1°C/s to 615°C a) before heating, after b) 9, c) 17 and d) 26 minutes, and e) after relatively slow cooling.**

# Sample Heated to 625°C (9A)

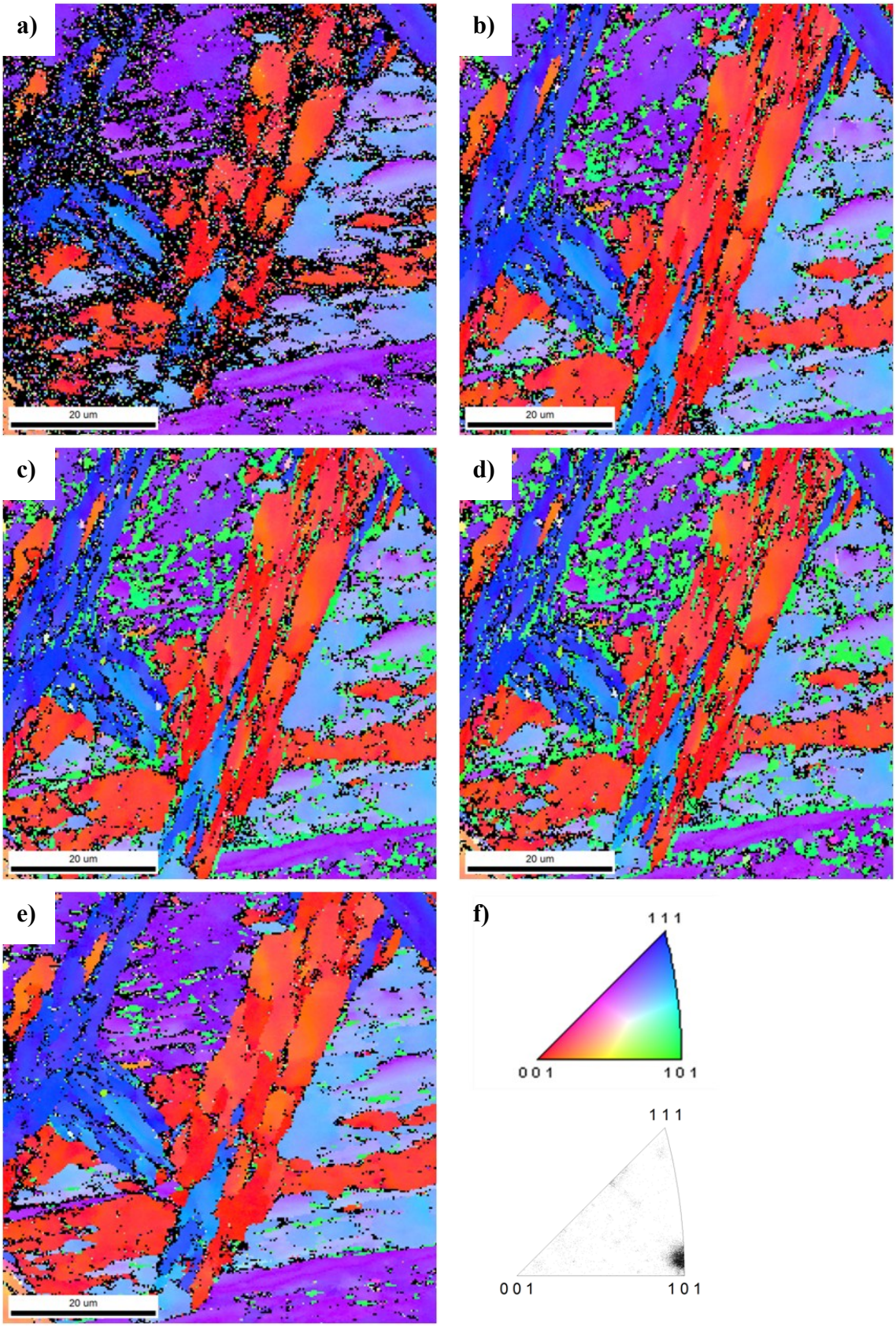


**Figure E.3: IPF maps of the sample heated in situ with a heating rate of 1°C/s to 625°C a) before heating, after b) 10, c) 19 and d) 35 minutes, and e) after relatively slow cooling. f) The IPF of the austenite phase after 35 minutes.**

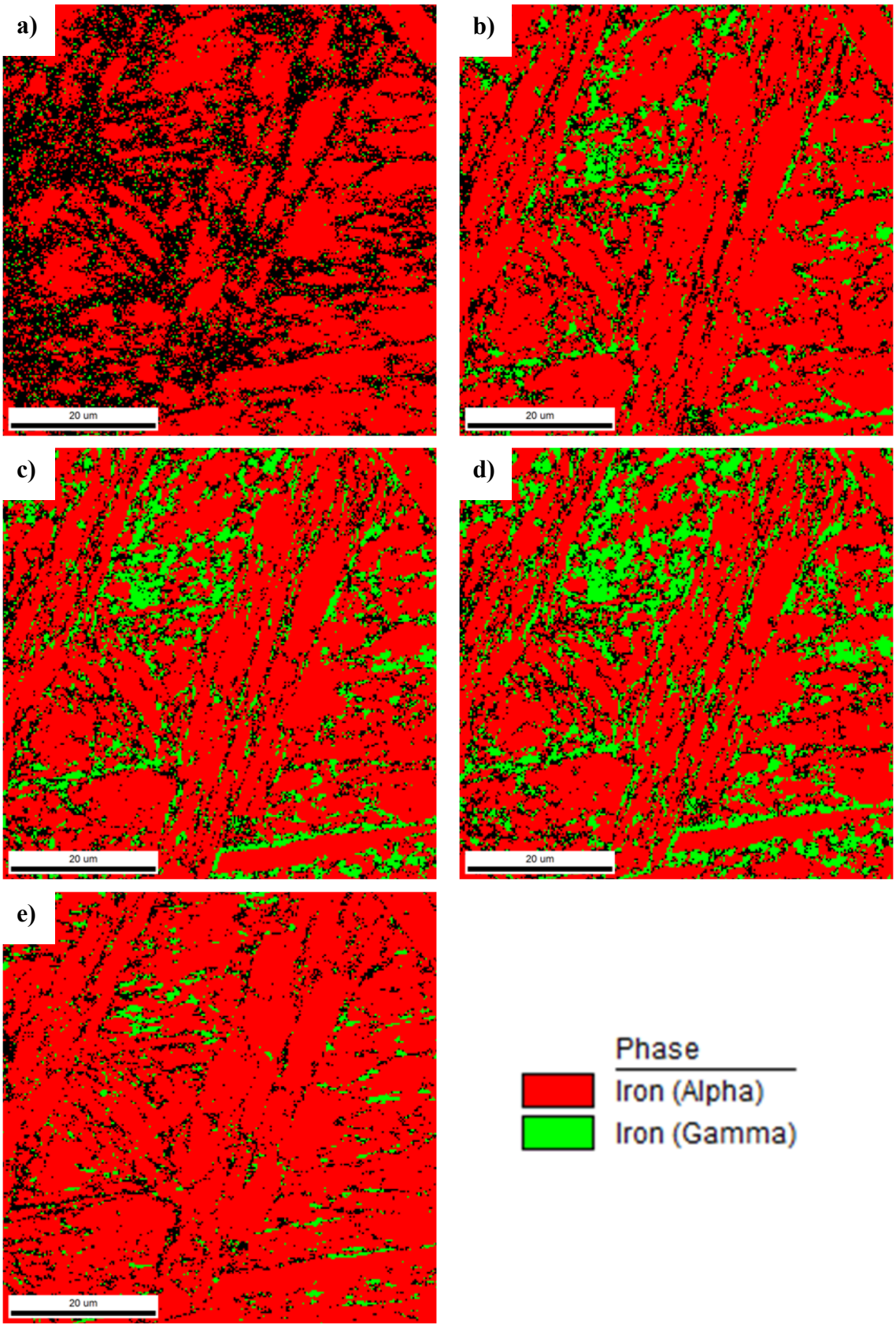


**Figure E.4: Phase maps of the sample heated in situ with a heating rate of 1°C/s to 625°C a) before heating, after b) 10, c) 19 and d) 35 minutes, and e) after relatively slow cooling.**

# Sample Heated to 635°C (10B)

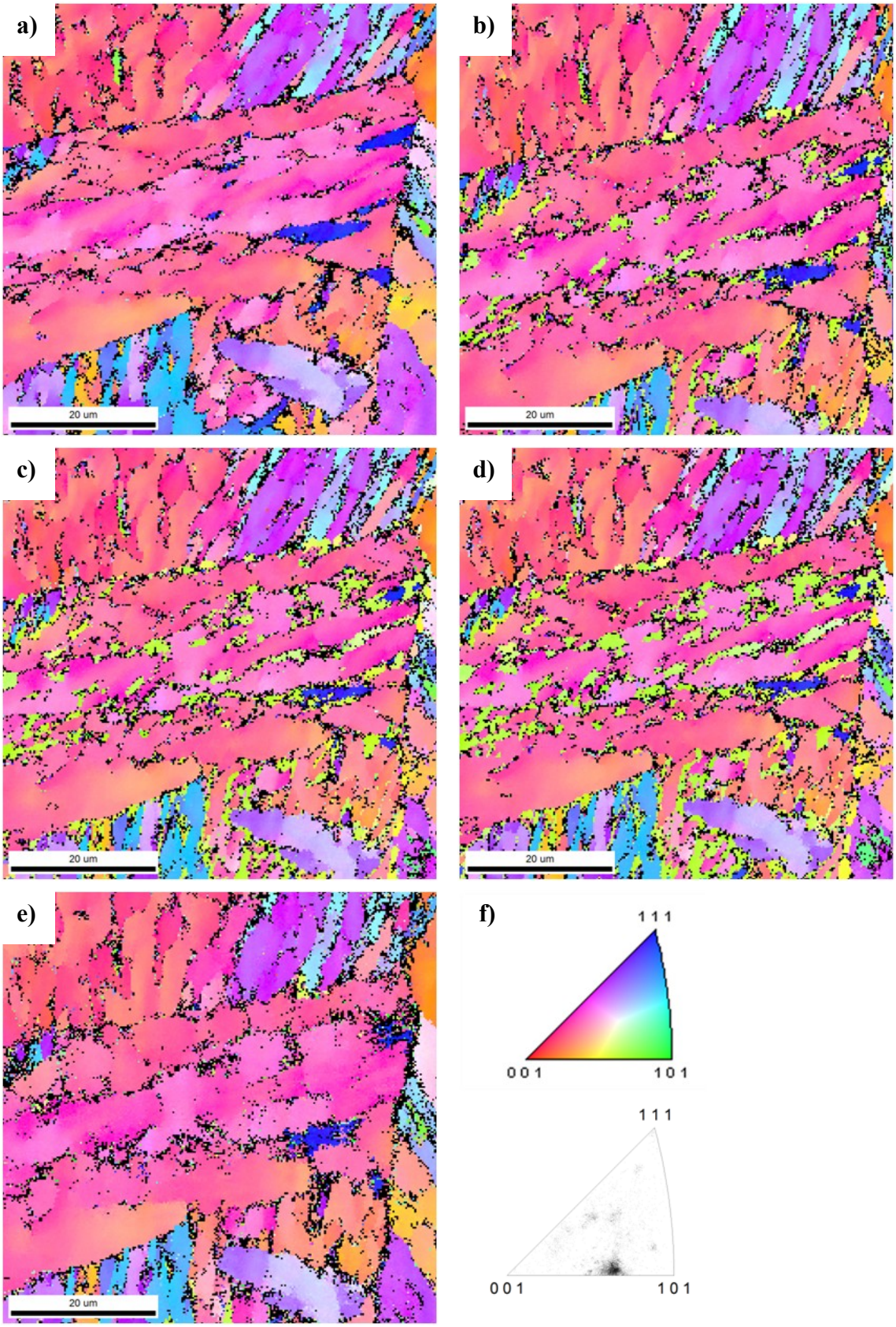


**Figure E.5: IPF maps of the sample heated in situ with a heating rate of 1°C/s to 635°C a) before heating, after b) 10, c) 18 and d) 26 minutes, and e) after relatively slow cooling. f) The IPF austenite phase after 26 minutes.**

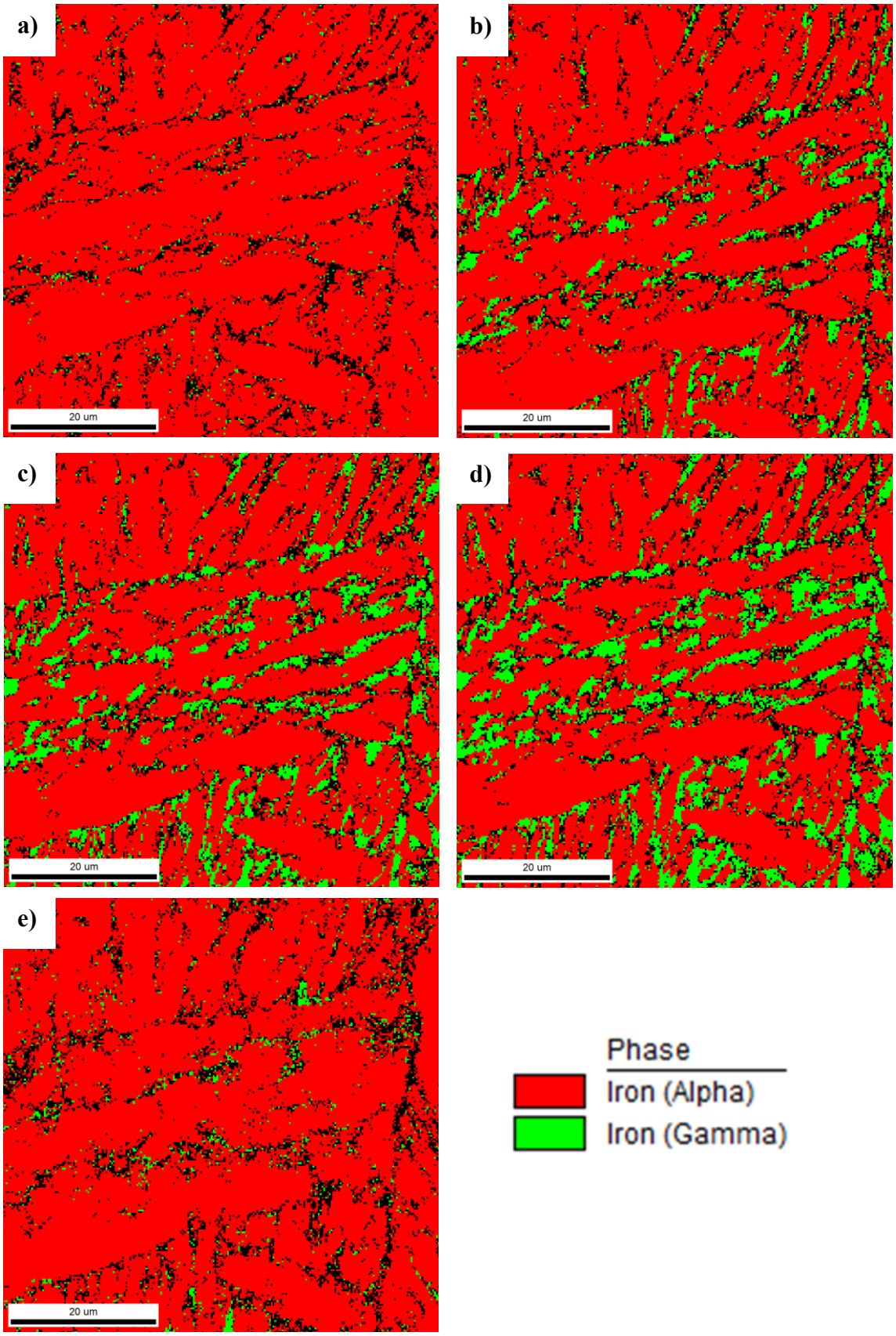


**Figure E.6: Phase maps of the sample heated in situ with a heating rate of 1°C/s to 635°C a) before heating, after b) 10, c) 18 and d) 26 minutes, and e) after relatively slow cooling.**

# Sample Heated Fast to 635°C (12A)

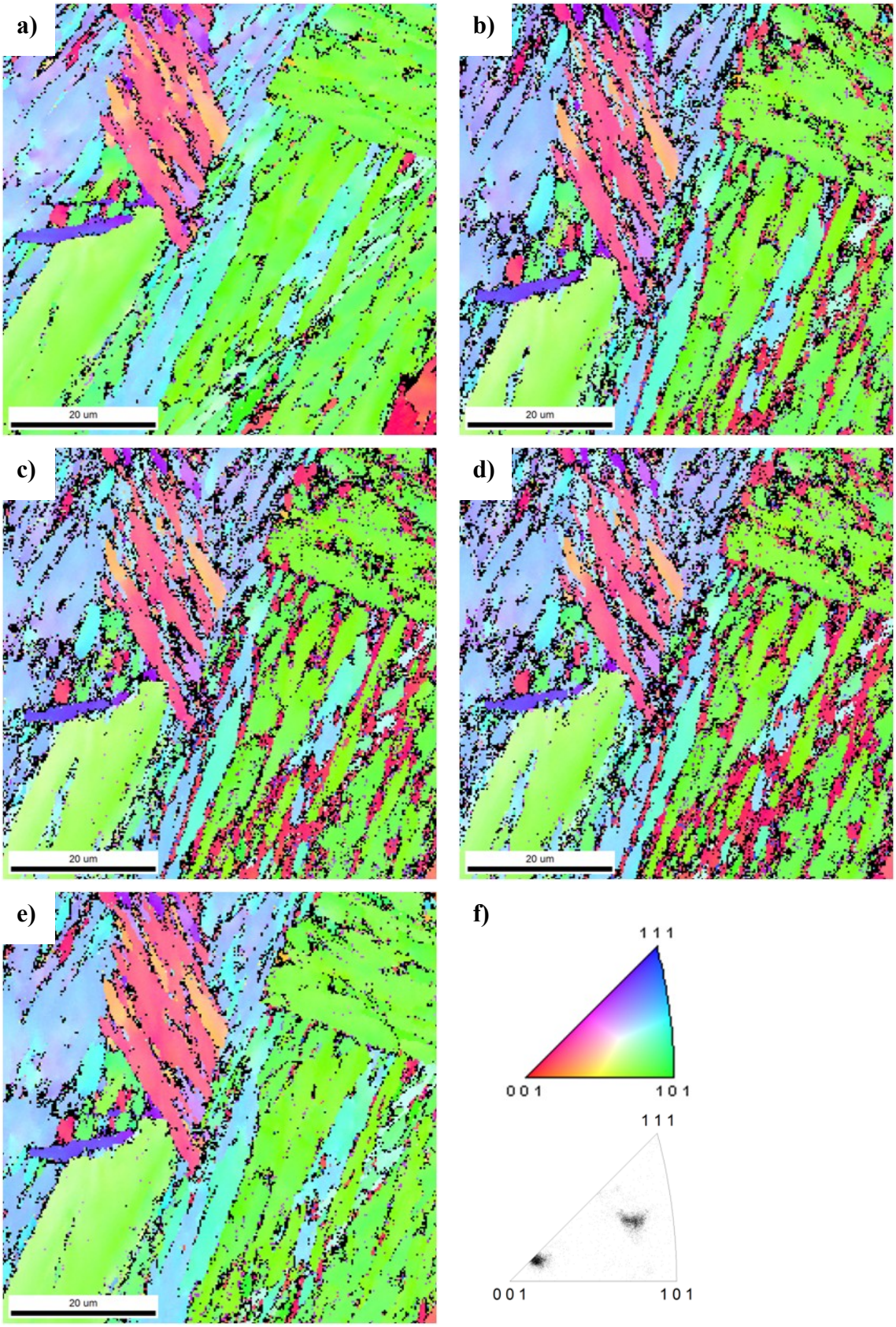


**Figure E.7: IPF maps of the sample heated in situ with a heating rate of 5°C/s to 635°C a) before heating, after b) 10, c) 18 and d) 25 minutes, and e) after relatively slow cooling. f) The IPF for the austenite phase after 25 minutes.**

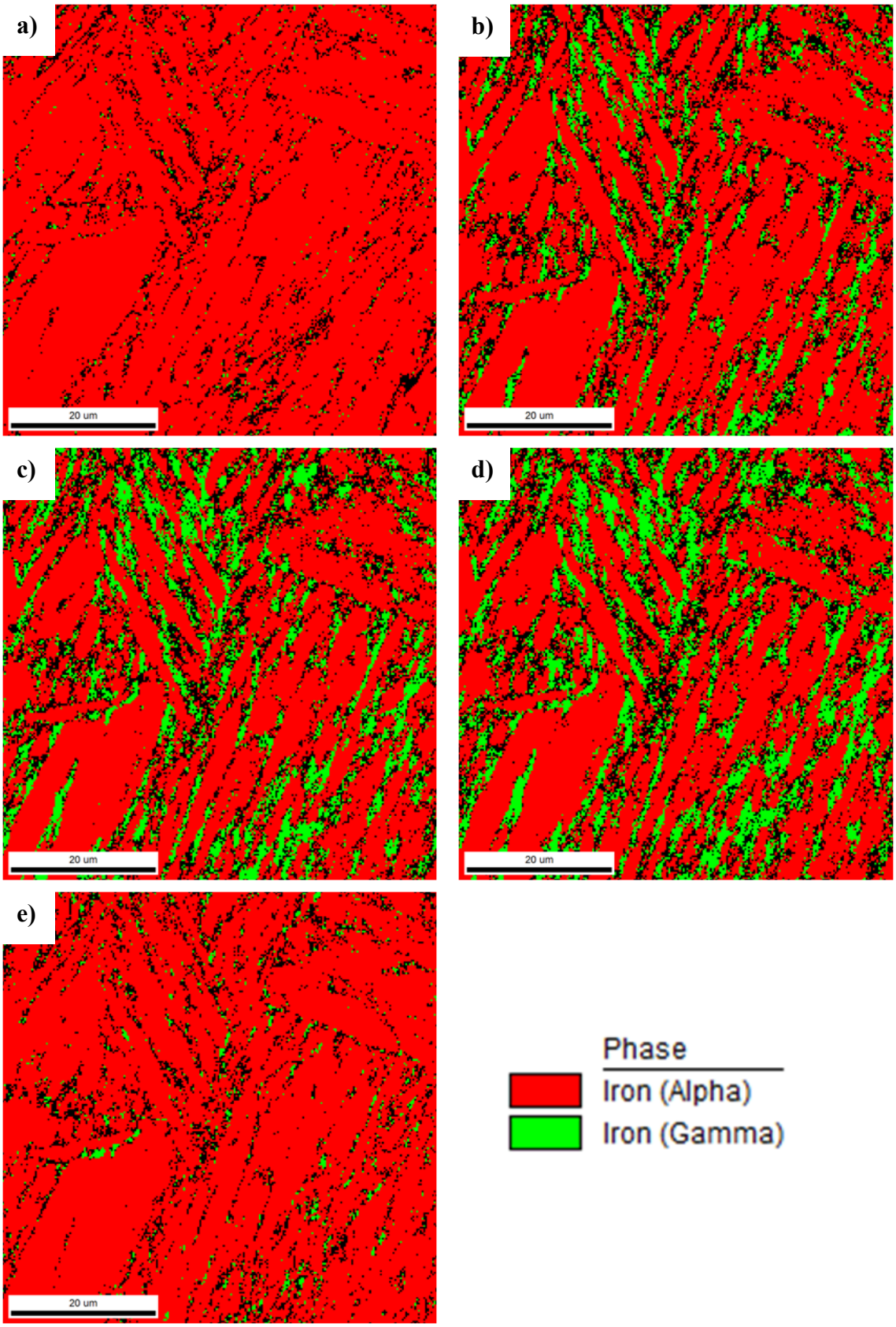


**Figure E.8: Phase maps of the sample heated in situ with a heating rate of 5°C/s to 635°C a) before heating, after b) 10, c) 18 and d) 25 minutes, and e) after relatively slow cooling.**

# Sample Heated to 640°C (10A)

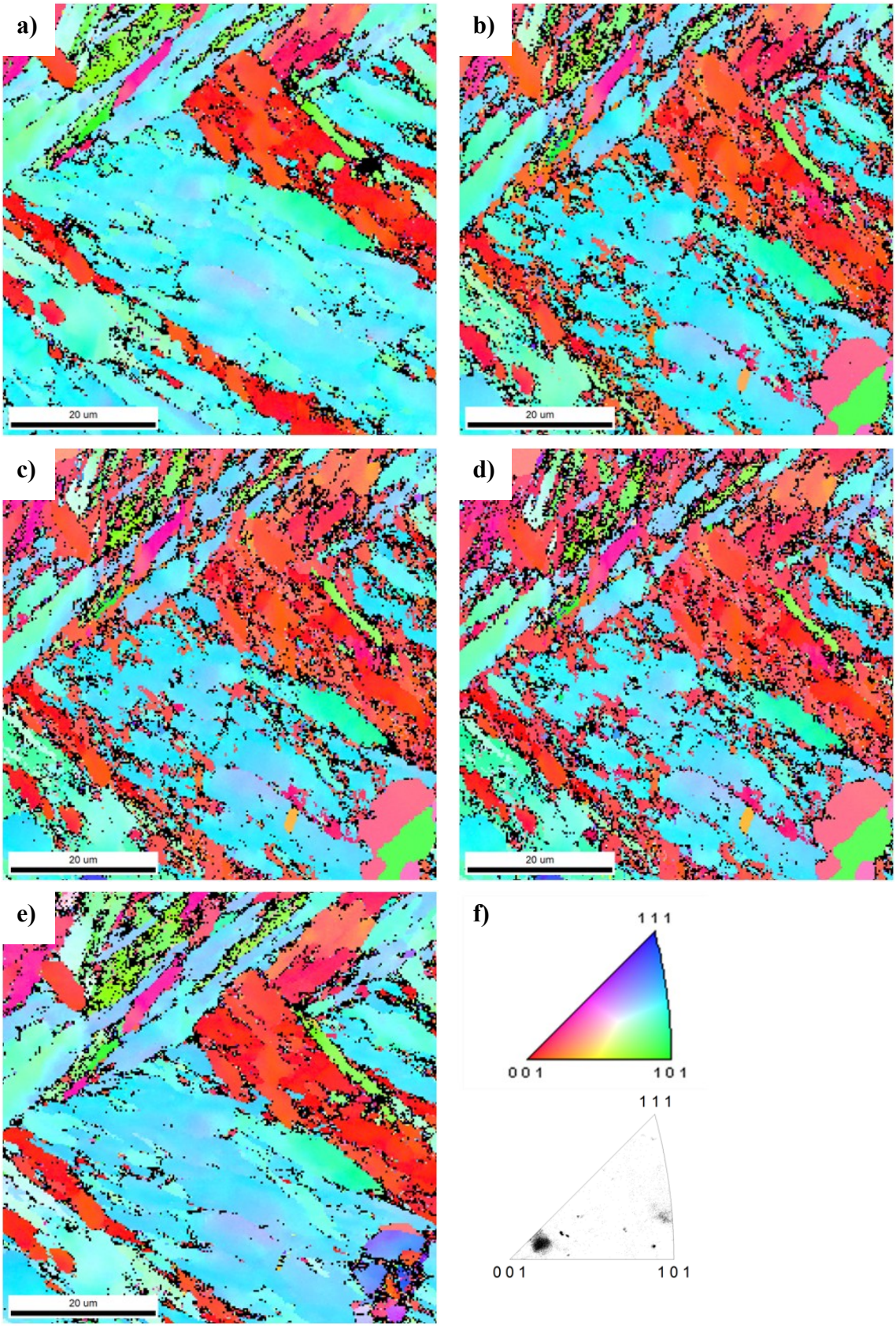


**Figure E.9: IPF maps of the sample heated in situ with a heating rate of 1°C/s to 635°C a) before heating, after b) 9, c) 17 and d) 25 minutes, and e) after relatively slow cooling. f) The IPF of the austenite phase after 25 minutes.**

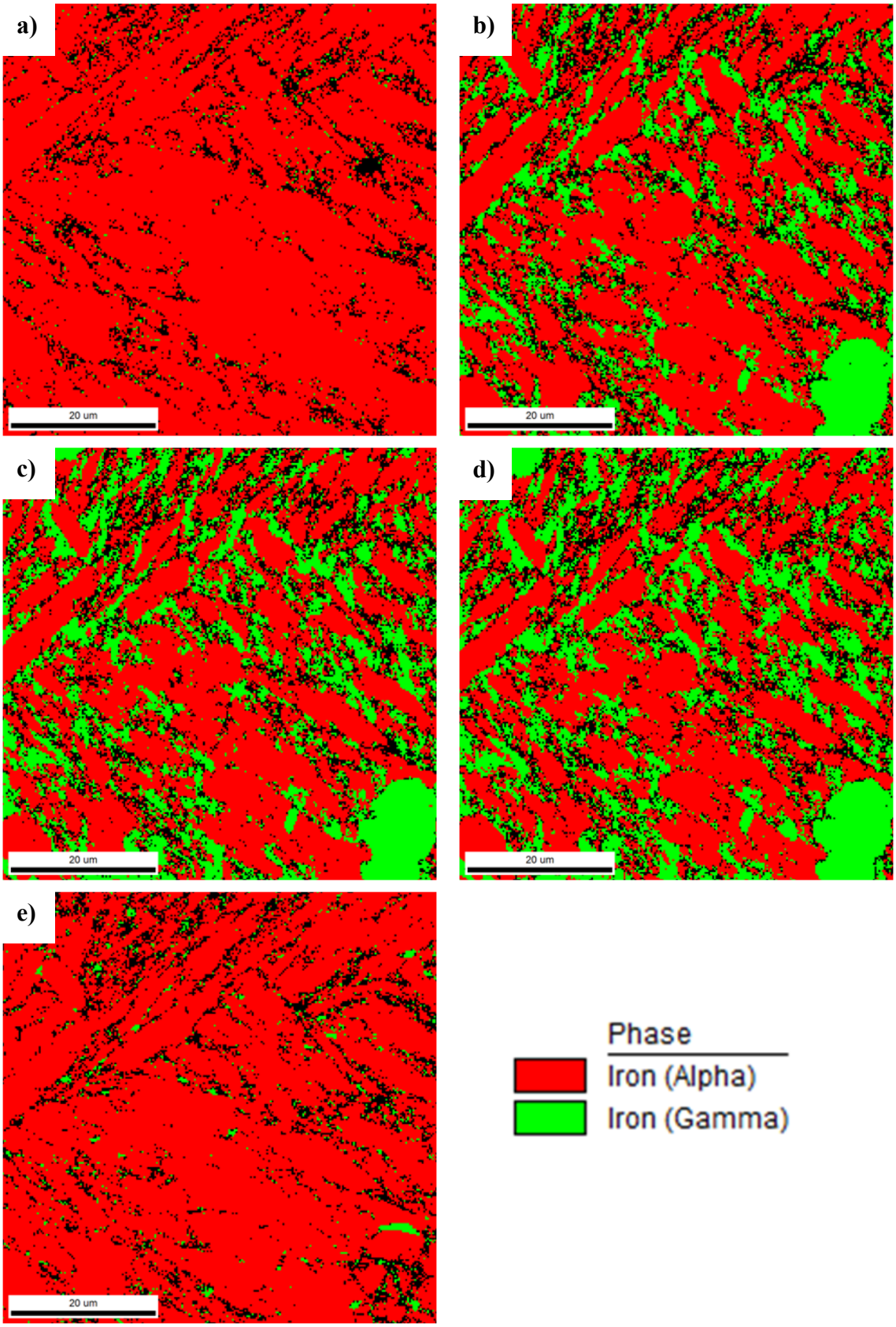


**Figure E.10: Phase maps of the sample heated in situ with a heating rate of 1°C/s to 635°C a) before heating, after b) 9, c) 17 and d) 25 minutes, and e) after relatively slow cooling.**

## Sample Heated Twice to 645°C (9B)

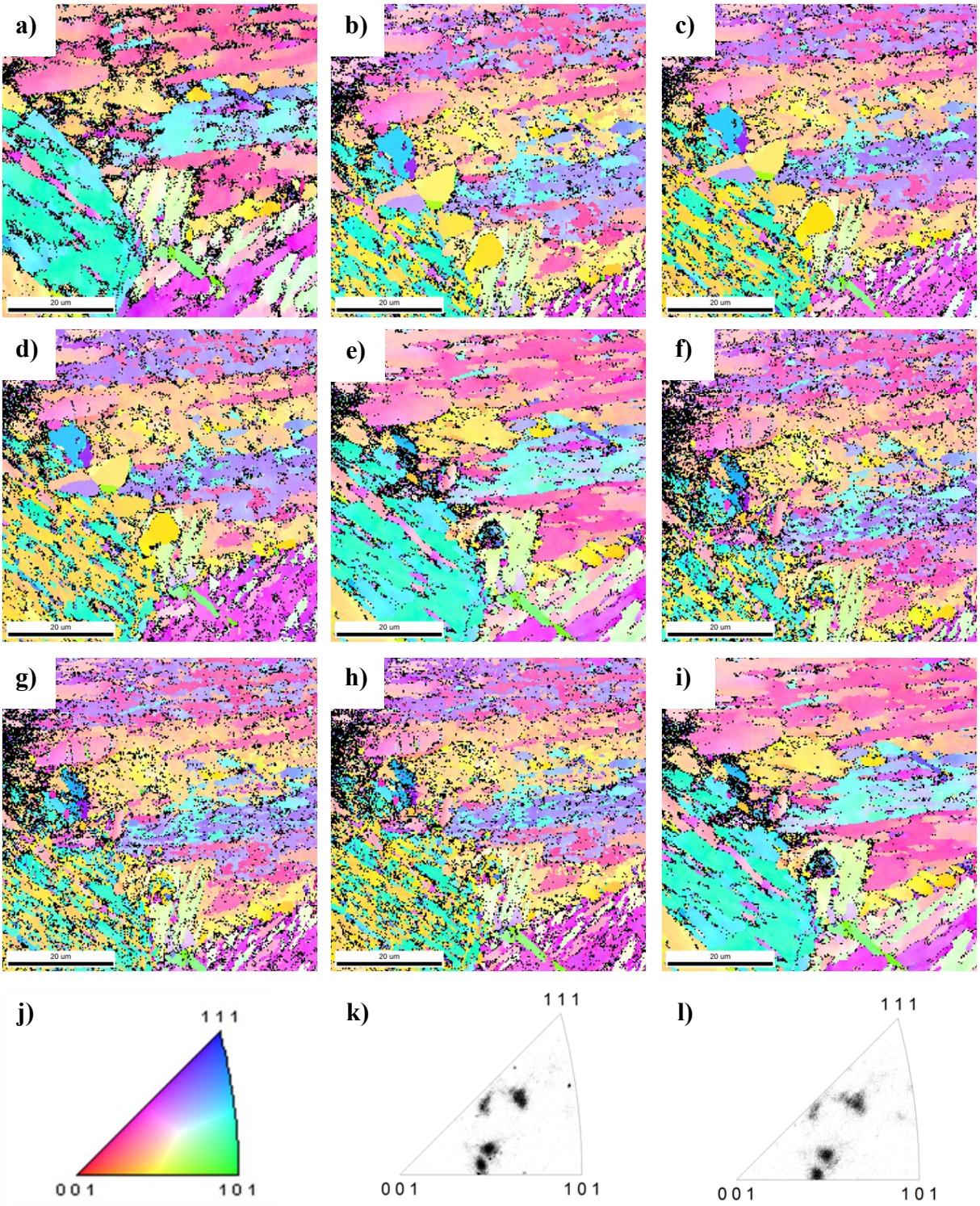


**Figure E.11: IPF maps of the sample heated in situ to 645°C in two cycles. a) Before first heating, after b) 10, c) 18 and d) 26 minutes, e) after relatively slow cooling and also before second heating, after f) 10, g) 17 and h) 25 minutes, and i) after relatively slow cooling after the second heating. The IPF with j) colors and after k) 26 minutes during the first cycle and l) 25 minutes during the second cycle.**

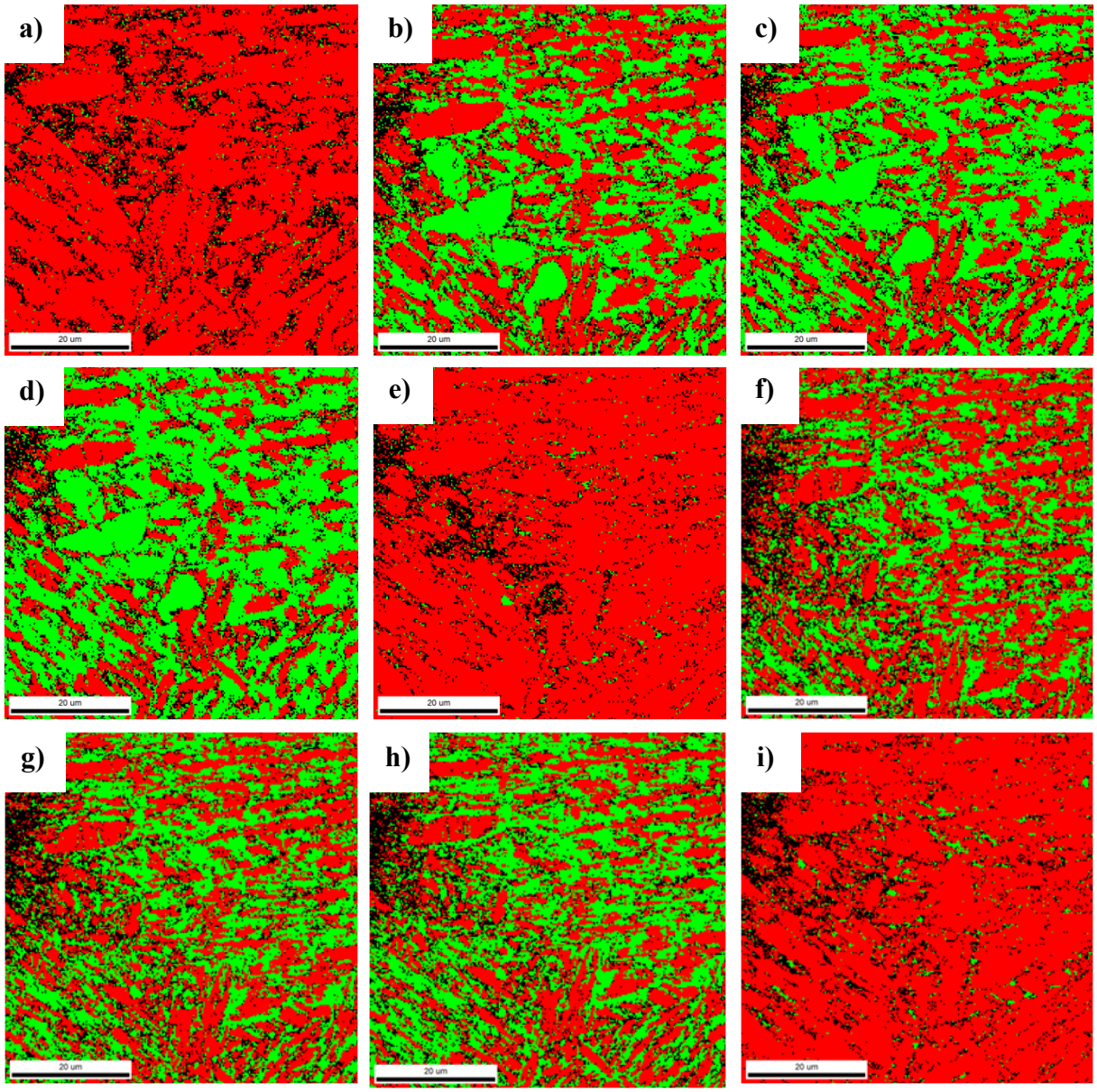


**Figure E.12: Phase maps of the sample heated in situ to 645°C in two cycles. a) Before first heating, after b) 10, c) 18 and d) 26 minutes, e) after relatively slow cooling and also before second heating, after f) 10, g) 17 and h) 25 minutes, and i) after relatively slow cooling after the second heating.**

# Sample Heated to 670°C (11C)

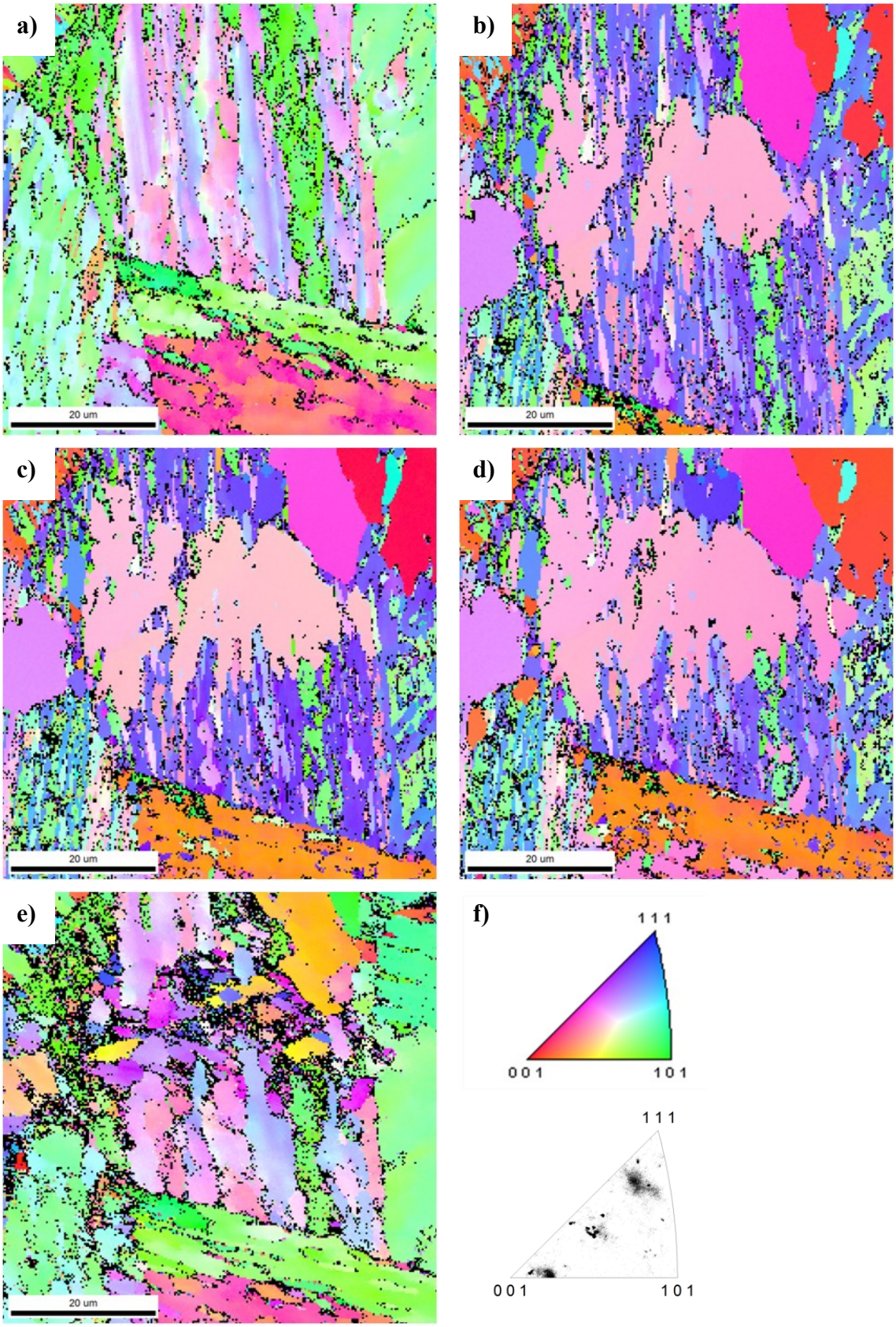


**Figure E.13: IPF maps of the sample heated in situ with a heating rate of 1°C/s to 670°C a) before heating, after b) 9, c) 17 and d) 25 minutes, and e) after relatively slow cooling. f) The IPF of the austenite phase after 25 minutes.**

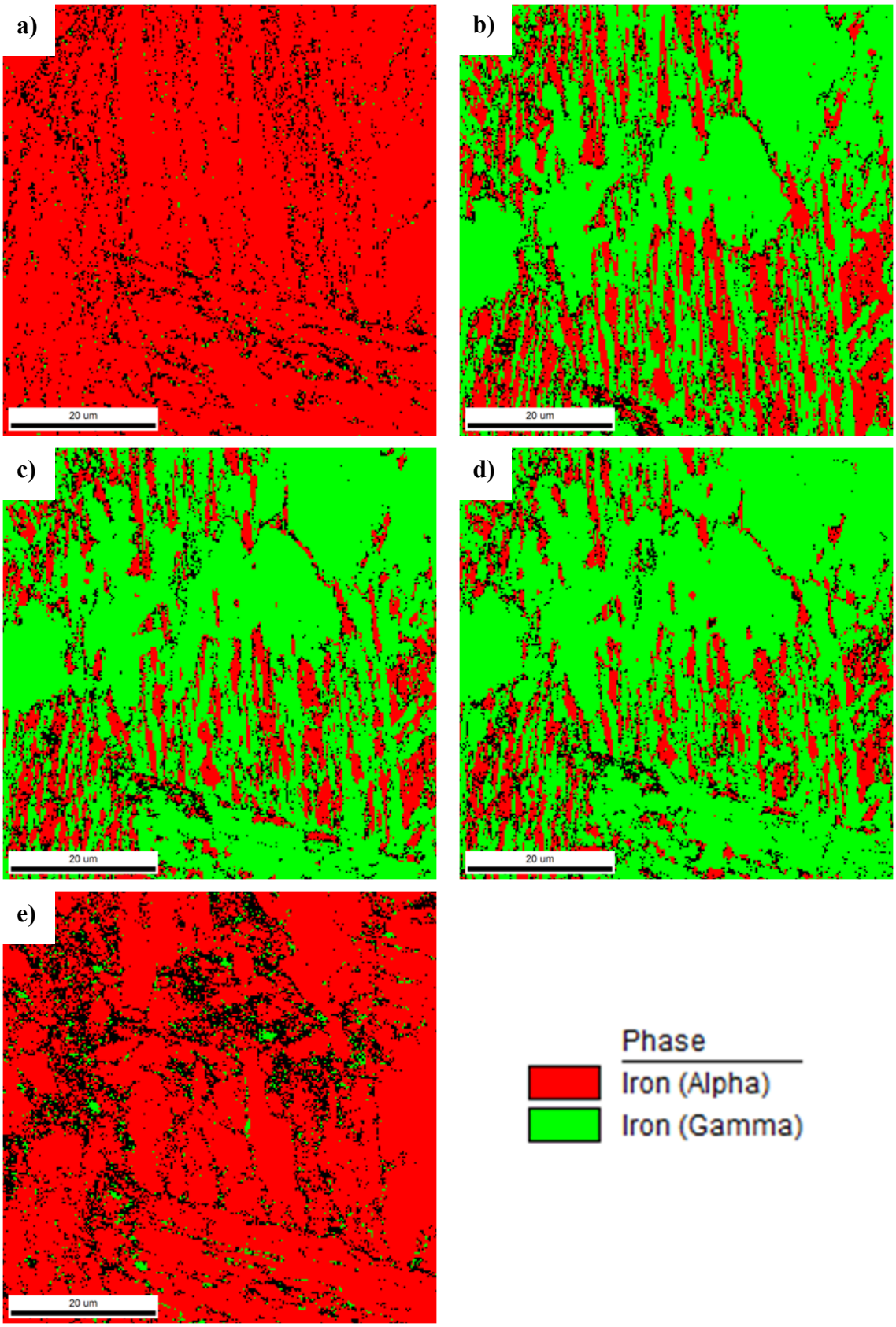


**Figure E.14: Phase maps of the sample heated in situ with a heating rate of 1°C/s to 670°C a) before heating, after b) 9, c) 17 and d) 25 minutes, and e) after relatively slow cooling.**

# Sample Heated to 670°C (11A)

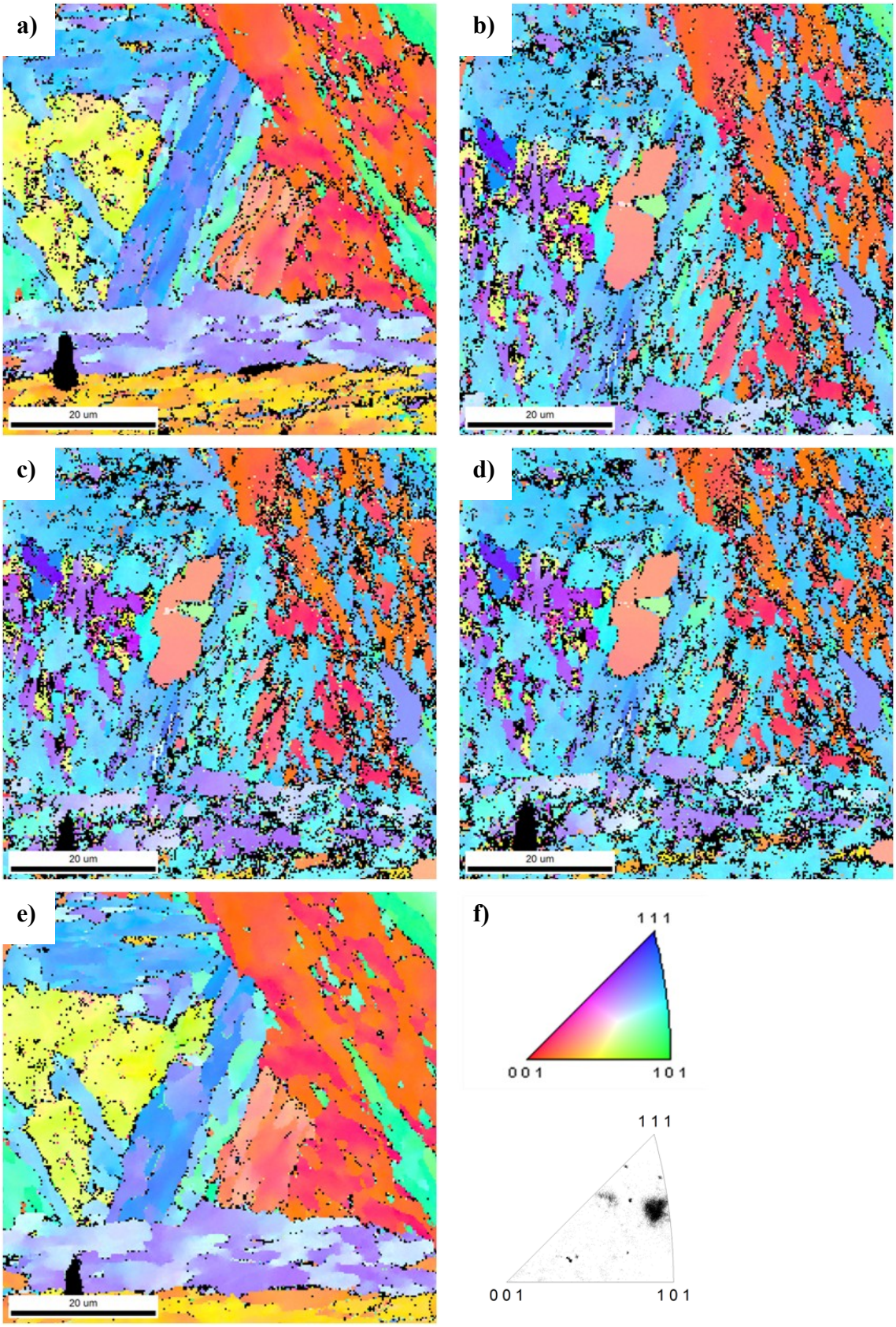


**Figure E.15: IPF maps of the sample heated in situ with a heating rate of 1°C/s to 670°C a) before heating, after b) 10, c) 20 and d) 29 minutes, and e) after relatively slow cooling. f) The IPF of the austenite phase after 29 minutes.**

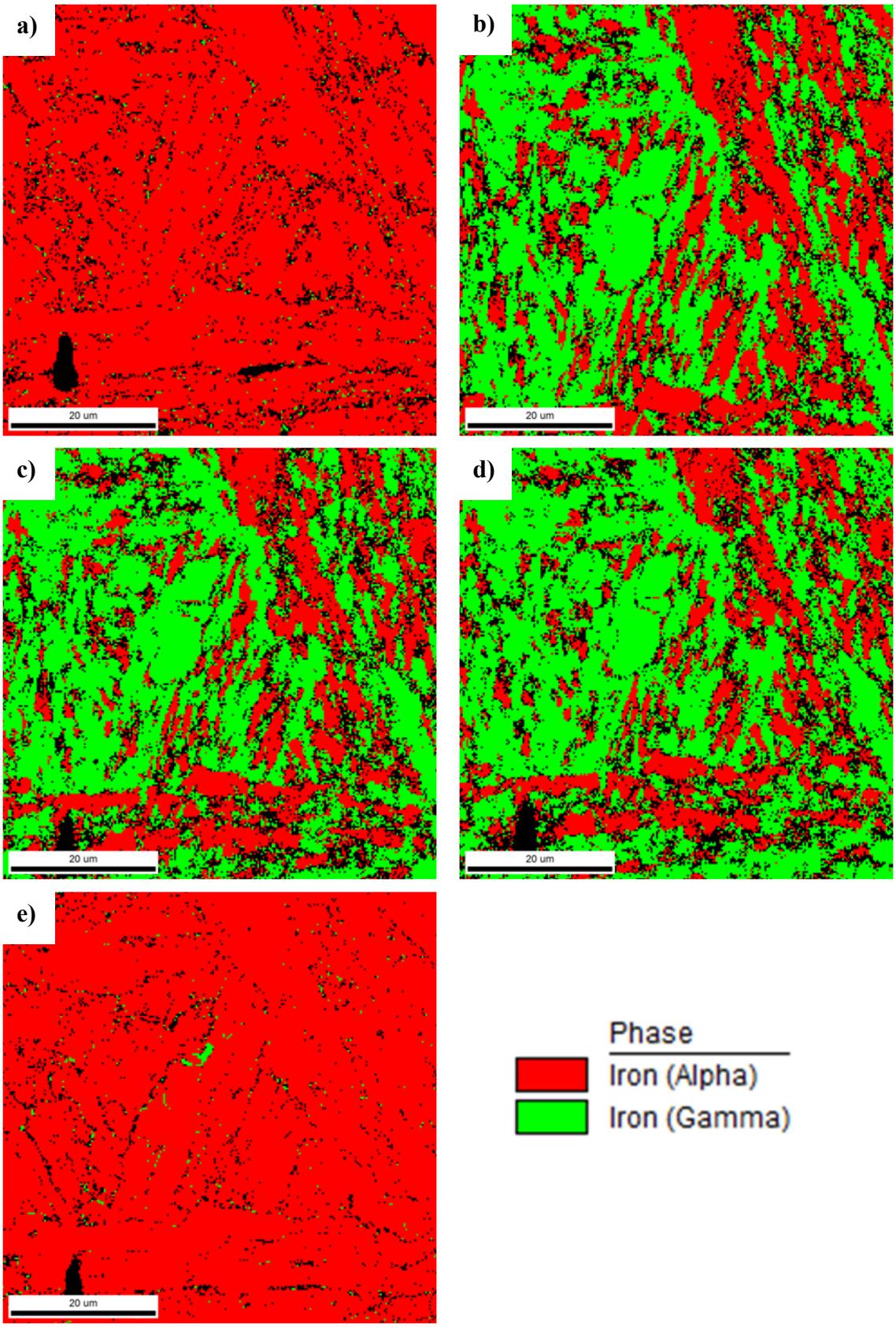


**Figure E.16: Phase maps of the sample heated in situ with a heating rate of 1°C/s to 670°C a) before heating, after b) 10, c) 20 and d) 29 minutes, and e) after relatively slow cooling.**

# Sample Heated to 700°C (8A)

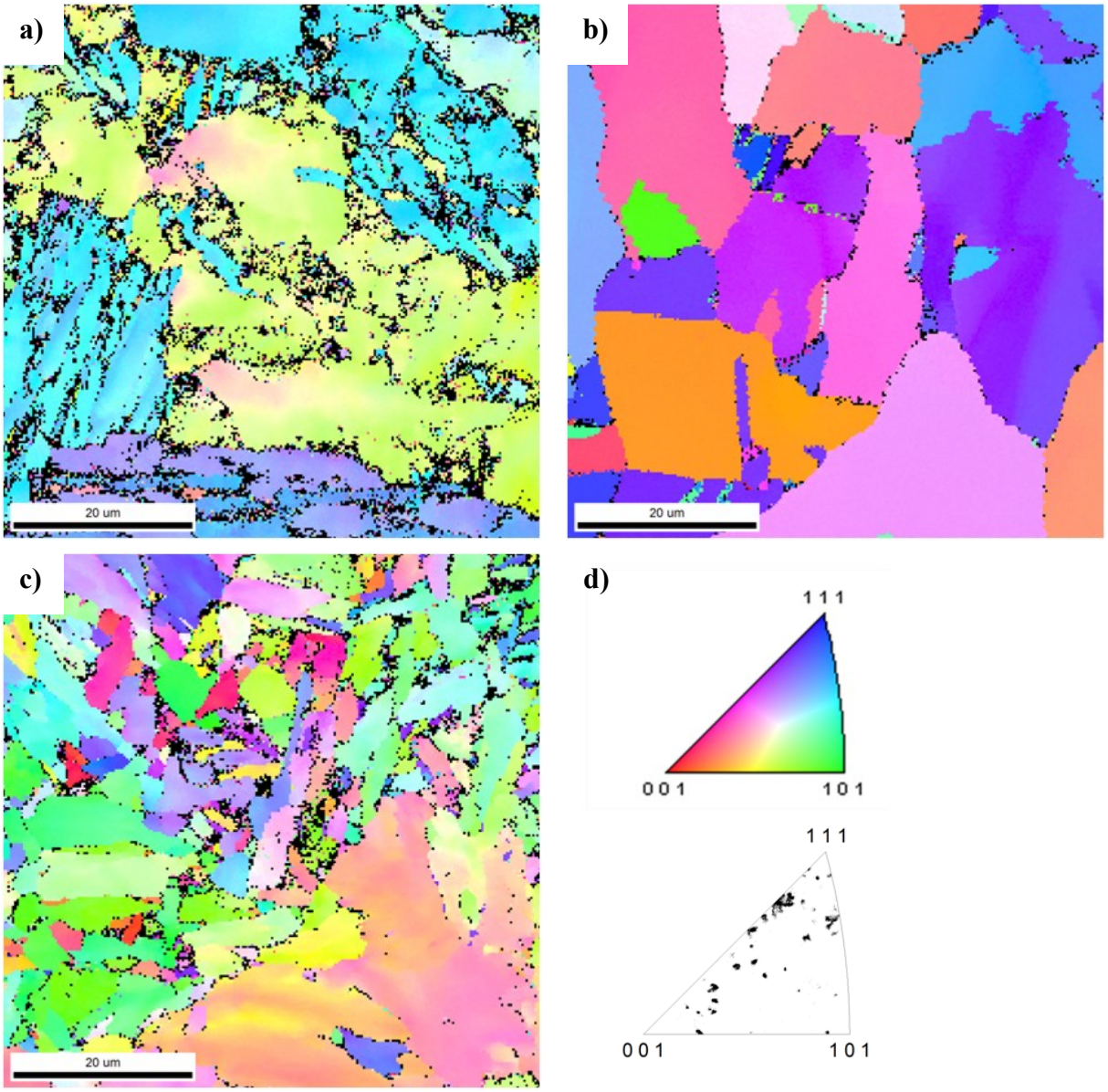


**Figure E.17: IPF maps of the sample heated in situ with a heating rate of 1°C/s to 690°C a) before heating, b) after 10 minutes and c) after relatively slow cooling. The sample is completely recrystallized. This can also be observed in d) the IPF of the austenite phase after 10 minutes.**

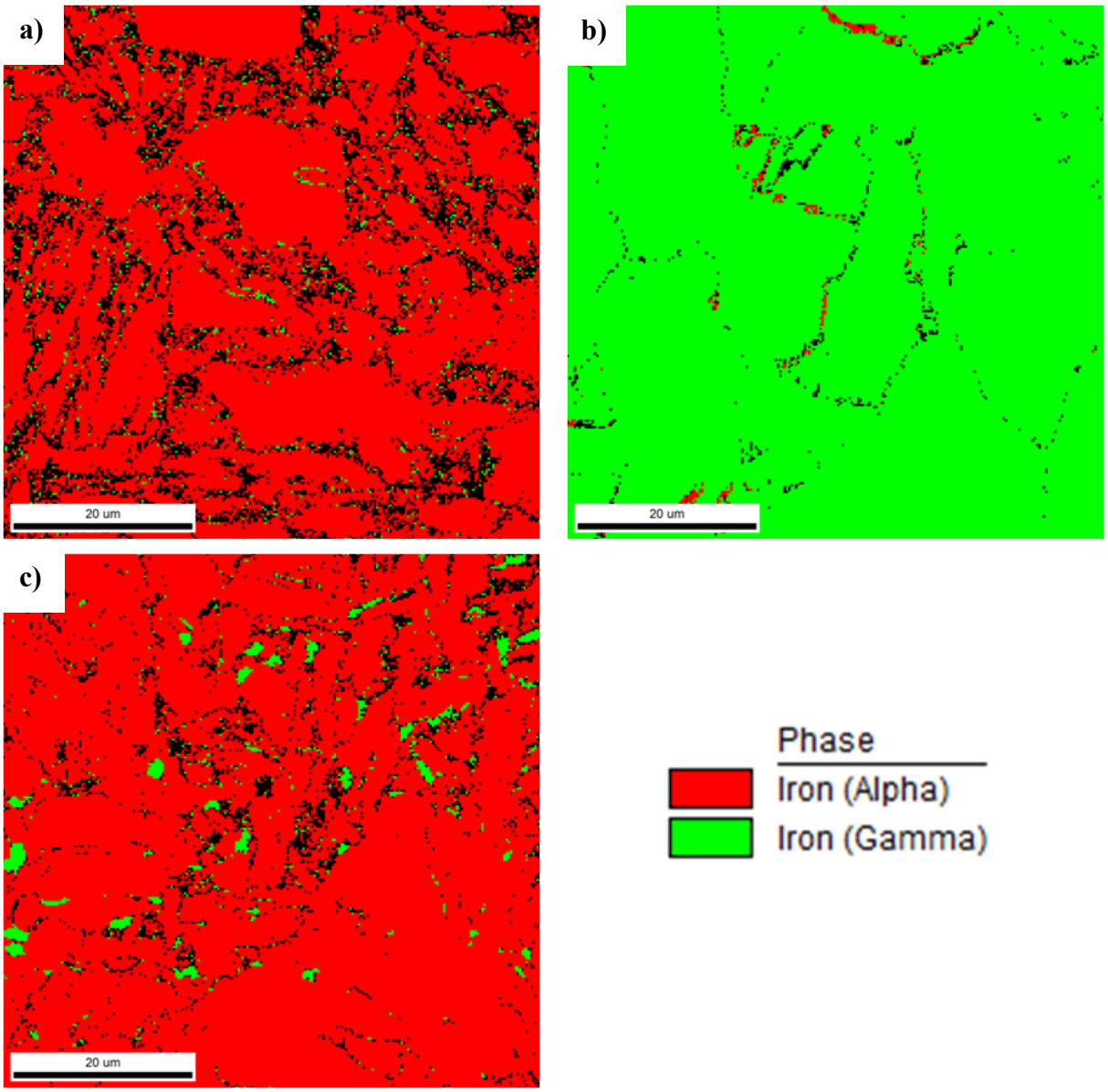


**Figure E.18: Phase maps of the sample heated in situ with a heating rate of 1°C/s to 690°C a) before heating, b) after 10 minutes and c) after relatively slow cooling. The sample is completely recrystallized.**

# Appendix F EBSD: Quality Data

The quality of the scans is evaluated in the following tables based on fraction indexed points as well as average Confidence Index (CI), Fit and Image Quality for the entire scan and the austenite phase. The data for the completely recrystallized scans are emitted. An outtake of the data from the stepwise heating is presented.

**Table F.1: Data from sample 12C heated to 590°C with a heating rate of 1°C/s.**

| **Time [*minutes*]** | Before heating | 10 | 18 | 27 | 35 | After cooling |
|---|---|---|---|---|---|---|
| **Fraction indexed CI≥0.050 [*%*]** | 87.6 | 84.4 | 83.1 | 79.2 | 79.6 | 86.7 |
| ***Entire scan*** | | | | | | |
| **CI** | 0.90 | 0.84 | 0.81 | 0.78 | 0.77 | 0.82 |
| **Fit** | 1.11 | 1.16 | 1.18 | 1.25 | 1.25 | 1.10 |
| **IQ** | 173137 | 319988 | 316781 | 300317 | 301802 | 351641 |
| **Fraction γ [*%*]** | 1.3 | 3.6 | 6.2 | 7.9 | 10.5 | 11.5 |
| ***Austenite phase*** | | | | | | |
| **CI** | 0.08 | 0.13 | 0.22 | 0.23 | 0.32 | 0.42 |
| **Fit** | 1.96 | 1.83 | 1.76 | 1.77 | 1.71 | 1.63 |
| **IQ** | 105732 | 215198 | 221733 | 218965 | 223718 | 247254 |

* Better resolution during first scan, not comparable numbers.

**Table F.2: Data from sample 8C heated to 605°C with a heating rate of 1°C/s.**

| **Time [*minutes*]** | Before heating | 10 | 19 | 28 | 36 | After cooling |
|---|---|---|---|---|---|---|
| **Fraction indexed CI≥0.050 [*%*]** | 76.5 | 86.2 | 85.7 | 84.6 | 84.7 | 89.3 |
| ***Entire scan*** | | | | | | |
| **CI** | 0.80 | 0.79 | 0.77 | 0.76 | 0.77 | 0.82 |
| **Fit** | 1.21 | 1.08 | 1.12 | 1.17 | 1.18 | 1.01 |
| **IQ** | 242547 | 338657 | 331682 | 327876 | 324522 | 354124 |
| **Fraction γ [*%*]** | 3.0 | 9.9 | 15.7 | 19.0 | 22.5 | 11.7 |
| ***Austenite phase*** | | | | | | |
| **CI** | 0.08 | 0.36 | 0.49 | 0.54 | 0.59 | 0.50 |
| **Fit** | 1.93 | 1.57 | 1.50 | 1.49 | 1.47 | 1.42 |
| **IQ** | 176226 | 254885 | 263809 | 268906 | 270258 | 290223 |

**Table F.3: Data from sample 11B heated to 615°C with a heating rate of 1°C/s.**

| **Time [*minutes*]** | Before heating* | 9 | 17 | 26 | After cooling |
|---|---|---|---|---|---|
| **Fraction indexed CI≥0.050 [*%*]** | 85.5 | 85.0 | 83.2 | 83.2 | 84.8 |
| ***Entire scan*** | | | | | |
| **CI** | 0.91 | 0.83 | 0.81 | 0.79 | 0.83 |
| **Fit** | 1.06 | 1.08 | 1.13 | 1.16 | 1.07 |
| **IQ** | 160325 | 286995 | 278107 | 274169 | 286676 |
| **Fraction γ [*%*]** | 1.7 | 9.3 | 15.3 | 19.6 | 11.0 |
| ***Austenite phase*** | | | | | |
| **CI** | 0.09 | 0.39 | 0.50 | 0.57 | 0.50 |
| **Fit** | 1.9 | 1.64 | 1.58 | 1.54 | 1.56 |
| **IQ** | 94759 | 215653 | 222175 | 226592 | 229504 |

* Better resolution during first scan, not comparable numbers.

**Table F.4: Data from sample 9A heated to 625°C with a heating rate of 1°C/s.**

| **Time [*minutes*]** | Before heating | 10 | 19 | 27 | 35 | After cooling |
|---|---|---|---|---|---|---|
| **Fraction indexed CI≥0.050 [*%*]** | 63.1 | 85.3 | 85.3 | 85.3 | 84.3 | 89.4 |
| ***Entire scan*** | | | | | | |
| **CI** | 0.73 | 0.82 | 0.79 | 0.78 | 0.77 | 0.88 |
| **Fit** | 1.42 | 1.19 | 1.20 | 1.21 | 1.25 | 1.06 |
| **IQ** | 216155 | 304268 | 304338 | 301683 | 298569 | 328565 |
| **Fraction γ [*%*]** | 4.5 | 8.6 | 16.4 | 20.0 | 22.6 | 4.9 |
| ***Austenite phase*** | | | | | | |
| **CI** | 0.08 | 0.39 | 0.51 | 0.56 | 0.57 | 0.40 |
| **Fit** | 1.98 | 1.65 | 1.57 | 1.53 | 1.54 | 1.57 |
| **IQ** | 169963 | 246900 | 256173 | 260354 | 260915 | 268201 |

**Table F.5: Data from sample 10B heated to 635°C with a heating rate of 1°C/s.**

| **Time [*minutes*]** | Before heating* | 10 | 18 | 26 | After cooling | ***Other area after cooling*** |
|---|---|---|---|---|---|---|
| **Fraction indexed CI≥0.050 [*%*]** | 90.1 | 88.5 | 87.9 | 87.3 | 87.6 | 86.0 |
| ***Entire scan*** | | | | | | |
| **CI** | 0.89 | 0.85 | 0.83 | 0.83 | 0.86 | 0.81 |
| **Fit** | 1.07 | 1.11 | 1.14 | 1.16 | 1.17 | 1.10 |
| **IQ** | 170795 | 332937 | 322871 | 322983 | 302750 | 341573 |
| **Fraction γ [*%*]** | 1.4 | 8.5 | 13.3 | 17.5 | 3.0 | 16.8 |
| ***Austenite phase*** | | | | | | |
| **CI** | 0.09 | 0.42 | 0.54 | 0.60 | 0.14 | 0.69 |
| **Fit** | 1.91 | 1.61 | 1.54 | 1.50 | 1.82 | 1.24 |
| **IQ** | 109642 | 257382 | 267872 | 271661 | 235858 | 324256 |

* Better resolution during first scan, not comparable numbers.

**Table F.6: Data from sample 12A heated to 635°C with a heating rate of 5°C/s.**

| **Time [*minutes*]** | Before heating* | 10 | 18 | 25 | After cooling |
|---|---|---|---|---|---|
| **Fraction indexed CI≥0.050 [*%*]** | 92.0 | 83.9 | 82.1 | 81.3 | 89.8 |
| ***Entire scan*** | | | | | |
| **CI** | 0.90 | 0.79 | 0.75 | 0.75 | 0.86 |
| **Fit** | 0.99 | 1.21 | 1.27 | 1.30 | 1.06 |
| **IQ** | 183844 | 300524 | 292945 | 284995 | 310831 |
| **Fraction γ [*%*]** | 1.0 | 13.0 | 19.7 | 23.9 | |
| ***Austenite phase*** | | | | | |
| **CI** | 0.09 | 0.45 | 0.55 | 0.62 | 0.25 |
| **Fit** | 1.87 | 1.59 | 1.55 | 1.52 | 1.66 |
| **IQ** | 108654 | 239937 | 245443 | 247270 | 232904 |

* Better resolution during first scan, not comparable numbers.

**Table F.7: Data from sample 10A heated to 640°C with a heating rate of 1°C/s, before the temperature decreased to 635°C.**

| **Time [*minutes*]** | Before heating* | 9 | 17 | 25 | After cooling |
|---|---|---|---|---|---|
| **Fraction indexed CI≥0.050 [*%*]** | 90.1 | 83.7 | 83.8 | 82.9 | 87.2 |
| ***Entire scan*** | | | | | |
| **CI** | 0.90 | 0.76 | 0.75 | 74.0 | 0.86 |
| **Fit** | 1.0 | 1.22 | 1.22 | 1.26 | 1.04 |
| **IQ** | 181660 | 315030 | 309803 | 305108 | 312440 |
| **Fraction γ [*%*]** | 1.2 | 25.5 | 32.0 | 36.8 | 2.9 |
| ***Austenite phase*** | | | | | |
| **CI** | 0.10 | 0.64 | 0.69 | 0.72 | 0.25 |
| **Fit** | 1.84 | 1.38 | 1.34 | 1.36 | 1.67 |
| **IQ** | 106738 | 300664 | 300247 | 299803 | 232358 |

* Better resolution during first scan, not comparable numbers.

**Table F.8: Data from sample 9B during the two heating cycles heated to 645°C, the second heating with a heating rate approximately eight times higher than the first.**

| | **First heating** | | | | | **Second heating** | | | |
|---|---|---|---|---|---|---|---|---|---|
| **Time [*minutes*]** | Before heating* | 10 | 18 | 26 | After first cooling | 10 | 17 | 25 | After second cooling |
| **Fraction indexed CI≥0.050 [*%*]** | 83.9 | 87.7 | 87.6 | 86.3 | 89.3 | 83.0 | 83.7 | 84.3 | 87.2 |
| ***Entire scan*** | | | | | | | | | |
| **CI** | 0.85 | 0.80 | 0.80 | 0.80 | 0.86 | 0.74 | 0.75 | 0.75 | 0.85 |
| **Fit** | 1.19 | 1.20 | 1.23 | 1.26 | 1.03 | 1.28 | 1.29 | 1.3 | 1.09 |
| **IQ** | 151501 | 306384 | 307982 | 301561 | 310692 | 275824 | 279201 | 282427 | 302005 |
| **Fraction γ [*%*]** | 2.0 | 48.6 | 56.2 | 62.8 | 2.2 | 40.1 | 45.7 | 49.3 | 3.7 |
| ***Austenite phase*** | | | | | | | | | |
| **CI** | 0.09 | 0.81 | 0.83 | 0.86 | 0.22 | 0.70 | 0.75 | 0.76 | 0.28 |
| **Fit** | 1.87 | 1.27 | 1.23 | 1.24 | 1.7 | 1.37 | 1.35 | 1.35 | 1.64 |
| **IQ** | 107980 | 30970 | 305847 | 302421 | 230587 | 261021 | 297599 | 271967 | 237784 |

* Better resolution during first scan, not comparable numbers.

**Table F.9: Data from sample 11C heated to 670°C with a heating rate of 1°C/s.**

| **Time [*minutes*]** | Before heating* | 9 | 17 | 25 | After cooling |
|---|---|---|---|---|---|
| **Fraction indexed CI≥0.050 [*%*]** | 91.3 | 90.0 | 90.3 | 89.9 | 82.4 |
| ***Entire scan*** | | | | | |
| **CI** | 0.86 | 0.80 | 0.81 | 0.8 | 0.79 |
| **Fit** | 0.93 | 1.03 | 0.99 | 1.04 | 1.10 |
| **IQ** | 209548 | 418798 | 426442 | 434628 | 305257 |
| **Fraction γ [*%*]** | 0.9 | 69.4 | 77.0 | 81.1 | 3.5 |
| ***Austenite phase*** | | | | | |
| **CI** | 0.09 | 0.85 | 0.86 | 0.86 | 0.17 |
| **Fit** | 1.83 | 0.97 | 0.93 | 0.99 | 1.76 |
| **IQ** | 128079 | 439780 | 445262 | 452406 | 230453 |

* Better resolution during first scan, not comparable numbers.

**Table F.10: Data from sample 11A heated to 670°C with a heating rate of 1°C/s (holding at 350°C for 15 minutes before continuing heating).**

| **Time [*minutes*]** | Before heating* | 10 | 20 | 29 | After cooling |
|---|---|---|---|---|---|
| **Fraction indexed CI≥0.050 [*%*]** | 90.6 | 83.5 | 79.9 | 79.8 | 95.1 |
| ***Entire scan*** | | | | | |
| **CI** | 0.87 | 0.77 | 0.75 | 0.78 | 0.88 |
| **Fit** | 0.96 | 1.20 | 1.27 | 1.29 | 0.87 |
| **IQ** | 188959 | 331311 | 316450 | 312858 | 397152 |
| **Fraction γ [*%*]** | 1.1 | 57.3 | 63.4 | 68.7 | 0.8 |
| ***Austenite phase*** | | | | | |
| **CI** | 0.10 | 0.82 | 0.81 | 0.85 | 0.21 |
| **Fit** | 1.84 | 1.21 | 1.25 | 1.25 | 1.66 |
| **IQ** | 115957 | 334013 | 321510 | 319372 | 314850 |

* Better resolution during first scan, not comparable numbers.

**Table F.11: Data from sample 12B heated stepwise to 605°C with a heating rate of 1°C/s.**

| **Temperature [°*C*] / Time [*minutes*]** | Before heating | 100 / 10 | 550 / 10 | 605 / 6 | 605 / 14 | After cooling |
|---|---|---|---|---|---|---|
| **Fraction indexed CI≥0.050 [*%*]** | 75.0 | 62.8 | 84.5 | 90.3 | 90.6 | 88.6 |
| ***Entire scan*** | | | | | | |
| **CI** | 0.78 | 0.7 | 0.81 | 0.82 | 0.82 | 0.82 |
| **Fit** | 1.19 | 1.36 | 1.09 | 0.95 | 0.96 | 1.01 |
| **IQ** | 250397 | 223403 | 316280 | 379088 | 379319 | 353259 |
| **Fraction γ [*%*]** | 2.9 | 4.9 | 2.9 | 10.7 | 13.5 | 10.6 |
| ***Austenite phase*** | | | | | | |
| **CI** | 0.08 | 0.08 | 0.09 | 0.55 | 0.66 | 0.53 |
| **Fit** | 1.94 | 1.96 | 1.87 | 1.47 | 1.38 | 1.55 |
| **IQ** | 175404 | 171674 | 216104 | 285920 | 296575 | 271680 |

# Appendix G  eZAF Smart Quant Results

The complete report from the eZAF Smart Quant analysis is presented below for one area.

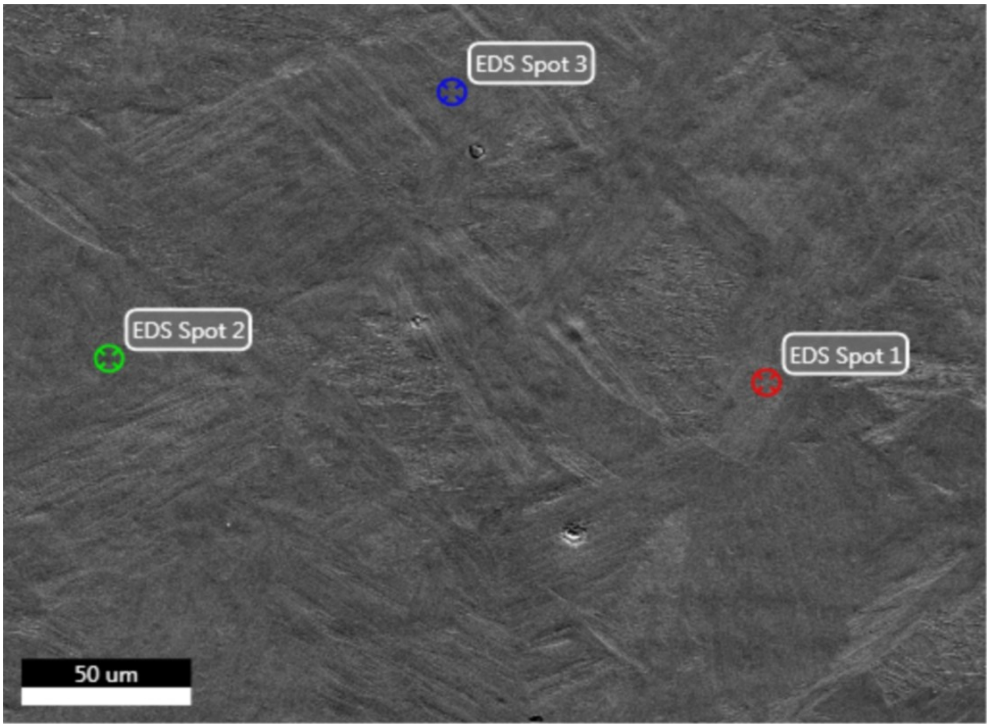


**Figure G.1: Secondary electron image of one of the areas investigated with EDS and point analysis.**

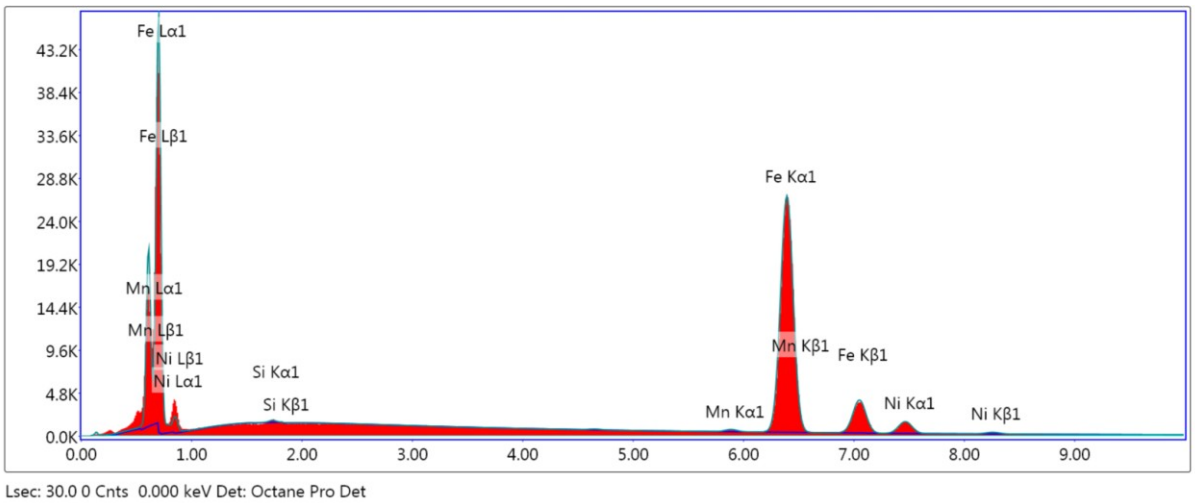


**Figure G.2: The EDS spectrum of spot 1.**

**Table G.1: eZAF Smart Quant Results, spot 1**

| Element | Weight [%] | Atomic [%] | Net Int. | Error [%] | Kratio | Z | R | A | F |
|---|---|---|---|---|---|---|---|---|---|
| SiK | 0.10 | 0.19 | 50.46 | 21.12 | 0.00 | 1.18 | 0.92 | 0.56 | 1 |
| MnK | 0.62 | 0.64 | 108.72 | 18.31 | 0.01 | 0.98 | 0.99 | 1 | 1.11 |
| FeK | 91.20 | 91.47 | 12,147.37 | 2.35 | 0.92 | 1 | 1 | 1 | 1.01 |
| NiK | 8.08 | 7.70 | 655.07 | 5.03 | 0.08 | 1.01 | 1.01 | 0.94 | 1 |

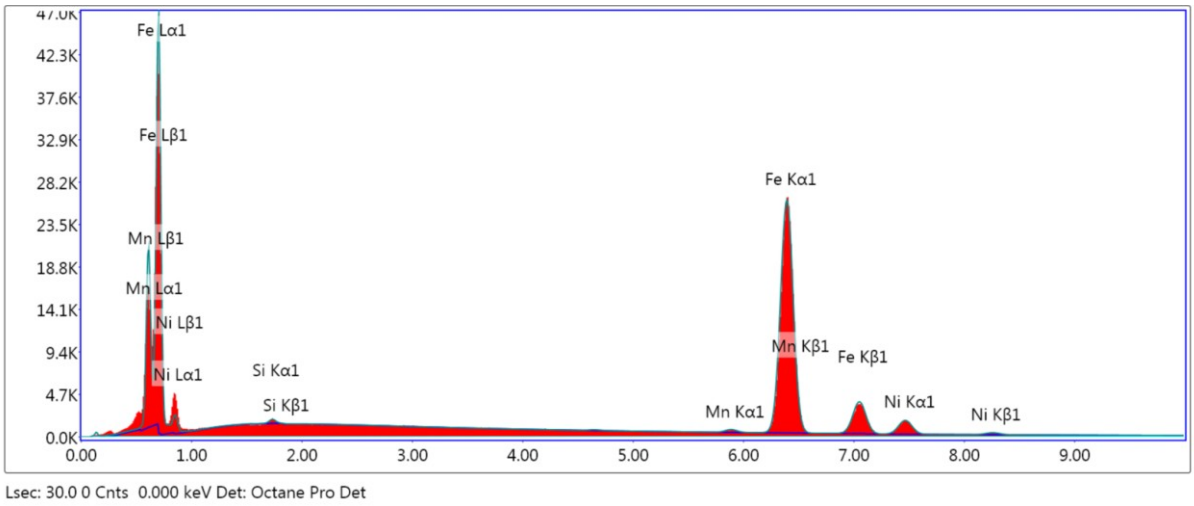


**Figure G.3: The EDS spectrum of spot 2.**

**Table G.2 eZAF Smart Quant Results, spot 2**

| Element | Weight [%] | Atomic [%] | Net Int. | Error [%] | Kratio | Z | R | A | F |
|---|---|---|---|---|---|---|---|---|---|
| SiK | 0.21 | 0.41 | 106.23 | 15.35 | 0.00 | 1.18 | 0.92 | 0.56 | 1 |
| MnK | 0.79 | 0.81 | 137.27 | 13.97 | 0.01 | 0.98 | 0.99 | 1 | 1.11 |
| FeK | 89.60 | 89.82 | 11,872.75 | 2.35 | 0.91 | 1 | 1 | 1 | 1.02 |
| NiK | 9.40 | 8.96 | 757.62 | 4.86 | 0.09 | 1.01 | 1.01 | 0.94 | 1 |

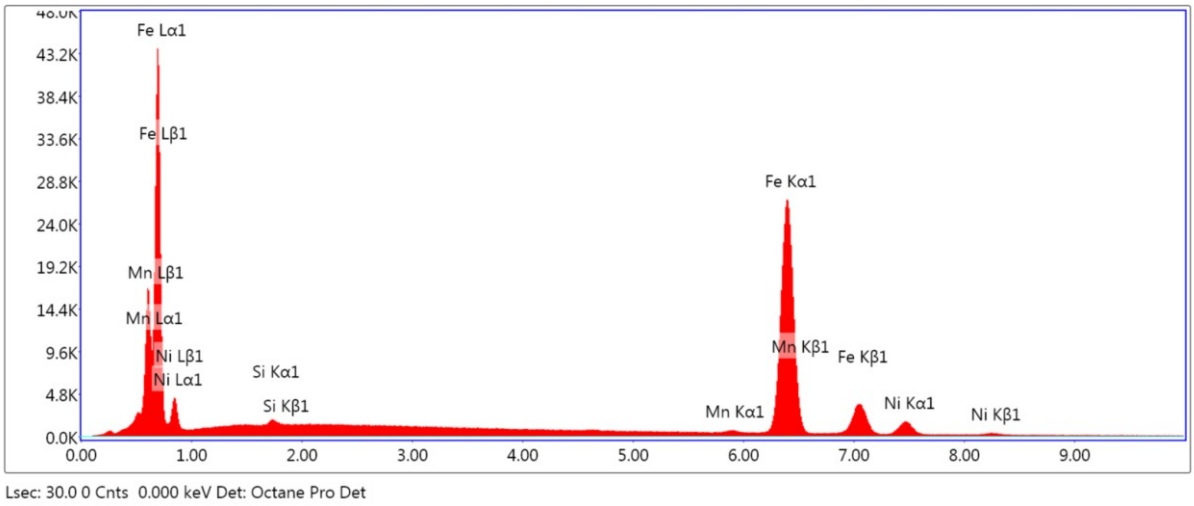


**Figure G.4: The EDS spectrum of spot 3.**

**Table G.3: eZAF Smart Quant Results, spot 3**

| Element | Weight [%] | Atomic [%] | Net Int. | Error [%] | Kratio | Z | R | A | F |
|---|---|---|---|---|---|---|---|---|---|
| SiK | 0.18 | 0.35 | 91.63 | 14.89 | 0.00 | 1.18 | 0.92 | 0.56 | 1 |
| MnK | 0.74 | 0.75 | 128.08 | 15.32 | 0.01 | 0.98 | 0.99 | 1 | 1.11 |
| FeK | 90.34 | 90.56 | 12,003.24 | 2.35 | 0.92 | 1 | 1 | 1 | 1.02 |
| NiK | 8.75 | 8.34 | 707.18 | 4.93 | 0.08 | 1.01 | 1.01 | 0.94 | 1 |